The Pennsylvania State University

The Graduate School

Department of Aerospace Engineering

Computer Prediction of Three-Dimensional Potential Flow Fields in Which Aircraft Propellers Operate

A Thesis in

Aerospace Engineering

by

Stephen Jay Jumper

Submitted in Partial Fulfillment
of the Requirements
for the Degree of

Master of Science

August 1982

Stephen Jay Jumper

NASA-CR-169317) COMPUTER PREDICTION OF N82-32312
THREE-DIMENSIONAL POTENTIAL FLOW FIELDS IN
WHICH AIRCRAFT PROPELLERS OPERATE M.S.
Thesis (Pennsylvania State Univ.) 253 p Unclas
HC A12/MF A01 CSCL 01A G3/02 28936

"Computer Prediction of Three-Dimensional Potential Flow Fields in Which Aircraft Propellers Operate"

Stephen J. Jumper

Master of Science - August 1982

Penn State University

We approve the thesis of Stephen Jay Jumper.

Date of Signature:

_____ _____

Barnes W. McCormick,
Professor and Head of
Aerospace Engineering
Thesis Adviser

_____ _____

Joseph J. Eisenhuth,
Associate Professor of
Aerospace Engineering
Graduate Faculty Reader

_____ _____

Hubert C. Smith,
Assistant Professor of
Aerospace Engineering
Graduate Faculty Reader

ABSTRACT

The flow field in which aircraft propellers must operate is spatially nonuniform due to propeller plane inclination and the presence of the airframe. Such a flow field alters the aerodynamic loading on the propeller blades and may cause excessive blade vibration, stresses, and acoustic noise. In order to design or analyze the performance of a propeller to be used on a given aircraft, the nonuniform flow field at the propeller plane must first be known.

In this study, a computer program was developed to calculate the three-dimensional, steady, incompressible, inviscid, irrotational flow field at the propeller plane (propeller removed) located upstream of an arbitrary airframe geometry. The program uses a horseshoe vortex of known strength to model the wing. All other airframe surfaces are modeled by a network of source panels of unknown strength which is exposed to a uniform free stream and the wing-induced velocity field. By satsifying boundary conditions on each panel (the Neumann problem), relaxed boundary conditions being used on certain panels to simulate inlet inflow, the source strengths are determined. From the known source and wing vortex strengths, the resulting velocity fields on the airframe surface and at the propeller plane are obtained. All program equations are derived in detail, and a brief description of the program structure is presented. A user's manual which fully documents the program is cited in the references.

Computer predictions of the flow on the surface of a sphere and at a propeller plane upstream of the sphere are compared with the exact mathematical solutions. Agreement is good, and correct program operation is verified.

Published experimental data are scarce. However, measured flow field data at a propeller plane of a twin-engine aircraft are present in the literature. Computer predictions for this aircraft are compared with the published test data. Reasonable agreement is observed, further validating the program.

Results of a parametric study are presented which demonstrate wing-induced, aft fuselage-induced, and cowl inlet inflow-induced effects on the flow field at the propeller plane of the single-engine Piper Cherokee PA-28-180 aircraft. Finally, a complete mapping of the computed flow field at the propeller plane of this aircraft is presented. However, no experimental data are available for comparison.

TABLE OF CONTENTS

	Page
ABSTRACT	iii
LIST OF TABLES	viii
LIST OF FIGURES	ix
LIST OF SYMBOLS	xv
ACKNOWLEDGEMENTS	xxviii
Chapter 1: INTRODUCTION	1
1.1 Statement of the Problem and Scope of the Investigation	1
1.2 Previous Investigations	5
Chapter 2: THEORY OF THE POTENTIAL FLOW SOLUTION METHOD	15
2.1 Historical Development	15
2.2 Theoretical Overview	16
2.3 Body Surface Model and Free Stream Velocity Components	18
2.4 Body Panel Source-Induced Velocity Components	20
2.4.1 General case of a nonsymmetric body panel network	20
2.4.2 Special case of a symmetric body panel network	22
2.5 Wing Model Description and Wing-Induced Velocity	24
2.5.1 Horseshoe vortex model and its induced velocity	24
2.5.2 Justification for the use of the horseshoe vortex model	26
2.6 Boundary Condition Equations	27
2.6.1 General case of a nonsymmetric body panel network	27
2.6.2 Special case of a symmetric body panel network	29
2.7 Body Surface Flow Field Velocity and Pressure	31
2.8 Flow Velocities and Flow Angles at the Propeller Plane	32
2.8.1 Cartesian velocity components at a point on the propeller plane	32
2.8.2 Axial, radial, and tangential velocities at a point on the propeller plane	34
2.8.3 Local flow angles at a point on the propeller plane	35
2.9 Three-Dimensional Flow Computer Program Description	36
Chapter 3: TEST CASES OF THE FLOW ABOUT A SPHERE AND THE FLOW ABOUT A SIMPLE FUSELAGE SHAPE	41
3.1 Exact Solution for the Potential Flow About a Sphere	41
3.2 Sphere Surface Pressure Prediction Compared With Exact Solution	42
3.3 Flow Predictions at a Propeller Plane Upstream of a Sphere	42
3.4 Flow Predictions Upstream of a Simple Fuselage Shape and Effects of Ignoring Remote Body Surfaces	44

Page

Chapter 4: MEASURED AND PREDICTED FLOW FIELD RESULTS AT THE LEFT PROPELLER PLANE OF A TWIN-ENGINE AIRCRAFT 46

4.1 Aircraft Geometry, Body Paneling, and Operating Conditions . 46
4.2 Comparisons of Computer-Predicted and Experimentally Measured Flow Quantities at the Left Propeller Plane 49
4.3 Nacelle Inlet Inflow Velocity Effects on the Flow Field at the Left Propeller Plane 51
4.4 Geometry-Induced Contributions Versus Propeller Plane Inclination-Induced Contributions to the Flow Field at the Left Propeller Plane 52

Chapter 5: COMPUTER-PREDICTED FLOW FIELD RESULTS AT THE PROPELLER PLANE OF THE PIPER CHEROKEE PA-28-180 AIRPLANE 56

5.1 Cherokee 180 Airplane Geometry, Body Paneling, and Run Conditions 56
5.2 Aft Fuselage-Induced Effects on the Flow Field at the Propeller Plane of the Cherokee 180 Airplane 58
5.3 Wing Lift-Induced and Dihedral-Induced Effects on the Flow Field at the Propeller Plane of the Cherokee 180 Airplane . 61
5.4 Cowl Inlet Inflow Velocity Effects on the Flow Field at the Propeller Plane of the Cherokee 180 Airplane 64
5.5 Baseline Flow Predictions Over the Entire Propeller Plane of the Cherokee 180 Airplane 66
5.5.1 Model used, purpose of presenting the predictions, and organization of the data 66
5.5.2 Computed azimuthal distributions 68
5.5.3 Computed radial distributions 77

Chapter 6: CONCLUSIONS AND RECOMMENDATIONS 90

REFERENCES 99

Appendix A: BODY SURFACE PANEL CALCULATIONS 102

A.1 Partitioning of the Body Surface 102
A.2 Panel Normal Unit Vector Components 103
A.3 Generation of a Flat Quadrilateral Panel 104
A.4 Surface Area of a Quadrilateral Panel 105
A.5 Control Point on a Quadrilateral Panel 107
A.6 Triangular Panels 107
A.6.1 Triangular panel surface area 108
A.6.2 Triangular panel control point 109

Appendix B: DERIVATION OF FREE STREAM CARTESIAN VELOCITY COMPONENTS 112

Appendix C: COMPUTATION OF VELOCITY COMPONENTS INDUCED BY A STRAIGHT VORTEX FILAMENT OF ARBITRARY ORIENTATION . . . 116

C.1 Geometry of the Arbitrary Vortex Filament 116

Page

Appendix C (cont'd)

C.2 Magnitude of the Total Induced Velocity 118
C.3 Induced Velocity Components 119

Appendix D: TRANSFORMATIONS RELATING THE PROPELLER PLANE AXIS SYSTEM TO THE BODY-FIXED AXIS SYSTEM 121

D.1 Coordinate Transformations 121
D.2 Velocity Component Transformations 124

Appendix E: MEASUREMENT AND MAPPING OF THE PIPER CHEROKEE PA-28-180 COWL AND SPINNER SURFACE GEOMETRY 128

LIST OF TABLES

Table		Page
1	Characteristics of the Twin-Engine Aircraft Flight Conditions for Which Computed and Measured Propeller Plane Flow Field Results Are Presented in Chapter 4	132
2	Characteristics of the Piper Cherokee PA-28-180 Aircraft Configurations for Which Computed Propeller Plane Flow Field Results Are Presented in Chapter 5	133
3	Piper Cherokee PA-28-180 Aircraft Lift Coefficients Corresponding to the Angles of Attack Modeled by the Computer Program	134

LIST OF FIGURES

Figure		Page
1	Body Panel Network and Free Stream Velocity Components	135
2	Edge of a Panel Showing Panel Self-Induced Velocity	136
3	Front View of a Symmetric Body Panel Network	137
4a	Wing Horseshoe Vortex Geometry (Top View)	138
4b	Wing Horseshoe Vortex Geometry (Front View)	138
5	Straight Vortex Filament and Induced Velocity	139
6	Comparison of "Exact" and Approximate Upwash Distributions Upstream of a Flat Plate Airfoil	140
7	Propeller Plane Orientation, Body Orientation, Flow Velocities, and Flow Angles at a Point on the Propeller Plane	141
8	Effect of Angle of Rotational Flow, θ, on Local Propeller Blade Section Angle of Attack	142
9	Organization and Structure of the Three-Dimensional Potential Flow Computer Program	143
10	Sphere in a Uniform Flow	144
11	Surface Pressure Distribution on a Sphere	145
12	Axial Velocity Distribution Along the Upper Vertical Centerline of a Propeller Plane Upstream of a Sphere	146
13	Distributions of Vertical Velocity and Upwash Angle Along the Upper Vertical Centerline of a Propeller Plane Upstream of a Sphere	147
14	Axial Velocity Distribution on the Upper Vertical Centerline of a Propeller Plane Predicted With a Complete Simple Fuselage Shape and With the Isolated Cowling	148
15	Upwash Angle Distribution on the Upper Vertical Centerline of a Propeller Plane Predicted With a Complete Simple Fuselage Shape and With the Isolated Cowling	149
16	Geometric Characteristics of the Twin-Engine Airplane (Source: Reference 15)	150
17a	Twin-Engine Airplane Fuselage Coordinates for the Portions Forward of the Wing Leading Edge (Source: Reference 15)	151

Figure		Page
17b	Twin-Engine Airplane Nacelle Coordinates for the Portions Forward of the Wing Leading Edge (Source: Reference 15)	152
18	Comparison of Computed and Measured Azimuthal Distributions of Axial Velocity at the Left Propeller Plane of the Twin-Engine Airplane	153
19	Comparison of Computed and Measured Azimuthal Distributions of Angle of Rotational Flow at the Left Propeller Plane of the Twin-Engine Airplane	154
20	Comparison of Computed and Measured Radial Distributions of Angle of Rotational Flow at the Left Propeller Plane of the Twin-Engine Airplane	155
21	Comparison of Computed and Measured Radial Distributions of Axial Velocity at the Left Propeller Plane of the Twin-Engine Airplane	156
22	Effect of Change in Nacelle Inlet Inflow Velocity on the Radial Distribution of Flow Angularity at the Left Propeller Plane of the Twin-Engine Airplane	157
23a	Velocity Components at an Isolated Inclined Propeller Plane (Left Side View)	158
23b	Velocity Components at an Isolated Inclined Propeller Plane (Forward View)	158
24	Comparison of Azimuthal Distributions of Flow Angularity at the Left Propeller Plane of the Twin-Engine Airplane Obtained With and Without Airframe Geometry Influences Present	159
25	Comparison of Radial Distributions of Flow Angularity at the Left Propeller Plane of the Twin-Engine Airplane Obtained With and Without Airframe Geometry Influences Present	160
26	Geometric Characteristics of the Piper Cherokee PA-28-180 Airplane (With Short Afterbody Profile Shown)	161
27	Lift Curve for the Piper Cherokee PA-28-180 Airplane	162
28a	Effect of Neglecting the Piper Cherokee 180 Fuselage Geometry (Replaced by a Short Afterbody) on the Computed Azimuthal Distribution of Axial Velocity at the Propeller Plane	163
28b	Effect of Neglecting the Piper Cherokee 180 Fuselage Geometry (Replaced by a Short Afterbody) on the Computed Azimuthal Distribution of Tangential Velocity at the Propeller Plane	164

Figure		Page
28c	Effect of Neglecting the Piper Cherokee 180 Fuselage Geometry (Replaced by a Short Afterbody) on the Computed Azimuthal Distribution of Flow Angularity at the Propeller Plane (α = 2° Case)	165
28d	Effect of Neglecting the Piper Cherokee 180 Fuselage Geometry (Replaced by a Short Afterbody) on the Computed Azimuthal Distribution of Flow Angularity at the Propeller Plane (α = 10° Case)	166
29	Effect of Neglecting the Piper Cherokee 180 Fuselage Geometry (Replaced by a Short Afterbody) on the Computed Radial Distribution of Axial Velocity at the Propeller Plane	167
30a	Effect of Neglecting the Piper Cherokee 180 Wing on the Computed Radial Distribution of Tangential Velocity at the Propeller Plane	168
30b	Effect of Neglecting the Piper Cherokee 180 Wing on the Computed Radial Distribution of Flow Angularity at the Propeller Plane (α = 2° Case)	169
30c	Effect of Neglecting the Piper Cherokee 180 Wing on the Computed Radial Distribution of Flow Angularity at the Propeller Plane (α = 10° Case)	170
31a	Effect of Wing Dihedral on the Computed Radial Distribution of Flow Angularity at the Propeller Plane of the Piper Cherokee 180 (α = 2° Case)	171
31b	Effect of Wing Dihedral on the Computed Radial Distribution of Flow Angularity at the Propeller Plane of the Piper Cherokee 180 (α = 10° Case)	172
32a	Effect of Change in Cowl Inlet Inflow Velocity on the Computed Radial Distribution of Axial Velocity at the Propeller Plane of the Piper Cherokee 180	173
32b	Effect of Change in Cowl Inlet Inflow Velocity on the Computed Radial Distribution of Flow Angularity at the Propeller Plane of the Piper Cherokee 180 (α = 2° Case)	174
32c	Effect of Change in Cowl Inlet Inflow Velocity on the Computed Radial Distribution of Flow Angularity at the Propeller Plane of the Piper Cherokee 180 (α = 10° Case)	175
33a	Computed Azimuthal Distributions of Axial Velocity at the Propeller Plane of the Piper Cherokee 180 (at r/R = 0.35)	176
33b	Computed Azimuthal Distributions of Tangential Velocity at the Propeller Plane of the Piper Cherokee 180 (at r/R = 0.35)	177

Figure		Page
33c	Computed Azimuthal Distributions of Angle of Rotational Flow at the Propeller Plane of the Piper Cherokee 180 (at r/R = 0.35)	178
34a	Computed Azimuthal Distributions of Axial Velocity at the Propeller Plane of the Piper Cherokee 180 (at r/R = 0.5)	179
34b	Computed Azimuthal Distributions of Tangential Velocity at the Propeller Plane of the Piper Cherokee 180 (at r/R = 0.5)	180
34c	Computed Azimuthal Distributions of Angle of Rotational Flow at the Propeller Plane of the Piper Cherokee 180 (at r/R = 0.5)	181
35a	Computed Azimuthal Distributions of Axial Velocity at the Propeller Plane of the Piper Cherokee 180 (at r/R = 0.75)	182
35b	Computed Azimuthal Distributions of Tangential Velocity at the Propeller Plane of the Piper Cherokee 180 (at r/R = 0.75)	183
35c	Computed Azimuthal Distributions of Angle of Rotational Flow at the Propeller Plane of the Piper Cherokee 180 (at r/R = 0.75)	184
36a	Computed Azimuthal Distributions of Axial Velocity at the Propeller Plane of the Piper Cherokee 180 (at r/R = 1.0)	185
36b	Computed Azimuthal Distributions of Tangential Velocity at the Propeller Plane of the Piper Cherokee 180 (at r/R = 1.0)	186
36c	Computed Azimuthal Distributions of Angle of Rotational Flow at the Propeller Plane of the Piper Cherokee 180 (at r/R = 1.0)	187
37a	Computed Radial Distributions of Axial Velocity at the Propeller Plane of the Piper Cherokee 180 (at ψ = 0°)	188
37b	Computed Radial Distributions of Tangential Velocity at the Propeller Plane of the Piper Cherokee 180 (at ψ = 0°)	189
37c	Computed Radial Distributions of Angle of Rotational Flow at the Propeller Plane of the Piper Cherokee 180 (at ψ = 0°)	190
38a	Computed Radial Distributions of Axial Velocity at the Propeller Plane of the Piper Cherokee 180 (at ψ = 45°)	191
38b	Computed Radial Distributions of Tangential Velocity at the Propeller Plane of the Piper Cherokee 180 (at ψ = 45°)	192
38c	Computed Radial Distributions of Angle of Rotational Flow at the Propeller Plane of the Piper Cherokee 180 (at ψ = 45°)	193

Figure		Page
39a	Computed Radial Distributions of Axial Velocity at the Propeller Plane of the Piper Cherokee 180 (at $\psi = 90°$) . . .	194
39b	Computed Radial Distributions of Tangential Velocity at the Propeller Plane of the Piper Cherokee 180 (at $\psi = 90°$) . . .	195
39c	Computed Radial Distributions of Angle of Rotational Flow at the Propeller Plane of the Piper Cherokee 180 (at $\psi = 90°$) .	196
40a	Computed Radial Distributions of Axial Velocity at the Propeller Plane of the Piper Cherokee 180 (at $\psi = 135°$) . .	197
40b	Computed Radial Distributions of Tangential Velocity at the Propeller Plane of the Piper Cherokee 180 (at $\psi = 135°$) . .	198
40c	Computed Radial Distributions of Angle of Rotational Flow at the Propeller Plane of the Piper Cherokee 180 (at $\psi = 135°$) .	199
41a	Computed Radial Distributions of Axial Velocity at the Propeller Plane of the Piper Cherokee 180 (at $\psi = 180°$) . .	200
41b	Computed Radial Distributions of Tangential Velocity at the Propeller Plane of the Piper Cherokee 180 (at $\psi = 180°$) . .	201
41c	Computed Radial Distributions of Angle of Rotational Flow at the Propeller Plane of the Piper Cherokee 180 (at $\psi = 180°$) .	202
42a	Computed Radial Distributions of Axial Velocity at the Propeller Plane of the Piper Cherokee 180 (at $\psi = 225°$) . .	203
42b	Computed Radial Distributions of Tangential Velocity at the Propeller Plane of the Piper Cherokee 180 (at $\psi = 225°$) . .	204
42c	Computed Radial Distributions of Angle of Rotational Flow at the Propeller Plane of the Piper Cherokee 180 (at $\psi = 225°$) .	205
43a	Computed Radial Distributions of Axial Velocity at the Propeller Plane of the Piper Cherokee 180 (at $\psi = 270°$) . .	206
43b	Computed Radial Distributions of Tangential Velocity at the Propeller Plane of the Piper Cherokee 180 (at $\psi = 270°$) . .	207
43c	Computed Radial Distributions of Angle of Rotational Flow at the Propeller Plane of the Piper Cherokee 180 (at $\psi = 270°$) .	208
44a	Computed Radial Distributions of Axial Velocity at the Propeller Plane of the Piper Cherokee 180 (at $\psi = 315°$) . .	209
44b	Computed Radial Distributions of Tangential Velocity at the Propeller Plane of the Piper Cherokee 180 (at $\psi = 315°$) . .	210

Figure		Page
44c	Computed Radial Distributions of Angle of Rotational Flow at the Propeller Plane of the Piper Cherokee 180 (at $\psi = 315°$)	211
A.1a	Periphery Point Input on a Symmetric Body Cross Section	212
A.1b	Periphery Point Input on a Nonsymmetric Body Cross Section	212
A.2	Input Panel Corner Points and Creation of the Outward Normal Vector	213
A.3	Quadrilateral Element With New Coplanar Corner Points	214
A.4	Lengths and Angles Used to Calculate the Area of a Quadrilateral Panel	215
A.5	Control Point Location on a Quadrilateral Panel	216
A.6a	Triangular Panel With Input Points 1 and 2 Coincident (Case a)	217
A.6b	Triangular Panel With Input Points 3 and 4 Coincident (Case b)	217
B.1	Wind Axes and Body-Fixed Axes Initially Coincident	218
B.2	Body-Fixed Axis System Rotations	219
B.3	Free Stream Velocity Components	220
C.1	Geometry and Induced Velocity of a Vortex Filament Having a Specified Location and Orientation in Space	221
D.1	Propeller Plane Shown Initially Noninclined With Respect to the Body-Fixed Axes	222
D.2	Propeller Plane-Fixed Axis System Rotations	223
D.3	View Normal to Propeller Plane in the Thrust Direction (Right-Hand Rotation, ω, of Propeller Assumed for Sign Convention)	224
E.1a	Optical Measurement of Cowl Surface Coordinates (Top View)	225
E.1b	Optical Measurement of Cowl Surface Coordinates (Left Side View)	225

LIST OF SYMBOLS

a	sphere radius
a'	fuselage dimension as shown in Figure 17a
A_{ij}	geometric influence coefficient, on the left side of boundary condition equations, for the effect of panel j on panel i
$[A]$	square matrix of geometric influence coefficients
$[A_{ij}]$	identical to [A]
AA	shorthand notation for $(\mathfrak{x}_2 - \mathfrak{x}_1)$ used in Equation (C.14)
b	wing span
b'	fuselage dimension as shown in Figure 17a
$\vec{B}_1$	diagonal vector on a body panel for obtaining the normal unit vector as shown in Figure A.2
$\vec{B}_2$	diagonal vector on a body panel for obtaining the normal unit vector as shown in Figure A.2
B_{ik}	velocity influence coefficient, on the right side of boundary condition equations, for velocities at panel i associated with the kth body orientation
$[B]$	column matrix of velocity influence coefficients for a single body orientation
$[B_i]$	identical to [B]
$[B_{ik}]$	augmented matrix of velocity influence coefficients with the kth column corresponding to the kth body orientation
BB	shorthand notation for $(\mathfrak{y}_2 - \mathfrak{y}_1)$ used in Equation (C.14)
c	wing root chord or flat plate airfoil chord
c'	fuselage dimension as shown in Figure 17a
C	point on a line containing a vortex filament with coordinates as shown in Figure C.1
C_L	wing lift coefficient corresponding to α
C_{L_k}	wing lift coefficient for the kth body orientation corresponding to α_k

C_p	pressure coefficient
C_{p_i}	surface pressure coefficient at the ith panel control point
C_x, C_y, C_z	x, y, and z coordinates, respectively, of point C as shown in Figure C.1
CC	shorthand notation for $(\hat{z}_2 - \hat{z}_1)$ used in Equation (C.14)
d	distance from each of four noncoplanar input panel corner points to a plane containing a point which is the average of the four input points given by Equation (A.9)
$d\hat{r}$	differential radius used in Equation (13)
$d\hat{S}$	differential body surface area used in Equation (1)
$d\vec{T}$	differential vector lying on a vortex filament as shown in Figure 5
D	an edge point on a triangular panel with coordinates as shown in Figures A.6a and A.6b
D_x, D_y, D_z	x, y, and z coordinates, respectively, of edge point D as shown in Figures A.6a and A.6b
D_1	distance from endpoint 1 of a vortex filament to the point where induced velocity is computed as shown in Figure C.1
D_2	distance from endpoint 2 of a vortex filament to the point where induced velocity is computed as shown in Figure C.1
DE	distance between edge points D and E on a triangular body panel as shown in Figures A.6a and A.6b
E	edge point on a triangular panel with coordinates as shown in Figures A.6a and A.6b
E_x, E_y, E_z	x, y, and z coordinates, respectively, of edge point E as shown in Figures A.6a and A.6b
f	cowl reference length as shown in Figure 14
ff	half the periphery length of a quadrilateral panel defined by Equation (A.13b)
F	cowl or nacelle inlet inflow velocity
F_i	normal velocity component allowed to penetrate body panel i
F(q)	distribution of normal velocity component penetrating the body surface (inflow or outflow) as a function of the generalized surface coordinate q

$\vec{g}$	vector drawn from the point of vortex-induced velocity computation to the vortex filament as shown in Figure 5
G	midpoint on edge RS of a quadrilateral panel with coordinates as shown in Figure A.5
G_x, G_y, G_z	x, y, and z coordinates, respectively, of midpoint G on edge RS as shown in Figure A.5
h	perpendicular distance between a vortex filament line and the point at which velocity is induced as shown in Figure 5
$\vec{h}$	vector of length h directed perpendicular to a vortex filament line from the point at which velocity is induced as shown in Figure C.1
H	midpoint on edge TU of a quadrilateral panel with coordinates as shown in Figure A.5
H_x, H_y, H_z	x, y, and z coordinates, respectively, of midpoint H on edge TU as shown in Figure A.5
i	body panel index number and used as a subscript to identify a quantity associated with the ith body panel
$\vec{i}$, $\vec{j}$, $\vec{k}$	unit vectors along the x, y, and z axes, respectively
i_{image}	subscript referring to the right side image of body panel i in a symmetric panel network
j	body panel index number and used as a subscript to identify a quantity associated with the jth body panel
j_{image}	subscript referring to the right side image of body panel j in a symmetric panel network
J	sequence number of a body cross section used in Appendix A
k	subscript index identifying the body orientation case number in boundary condition equations and also used as a summation index in Equation set (A.10)
L	arbitrary true scale length of all Cartesian axes used in Appendices B and D
m	number of segments in the Weissinger approximation model of a flat plate airfoil as shown in Figure 6 and used as a subscript on quantities pertaining to an m element Weissinger model
M	total number of body orientations, each of which has a separate flow solution and all of which are solved simultaneously

$\vec{n}$	outward drawn unit normal vector
$\vec{n}_i$	outward drawn unit normal vector at the control point of body panel i
n_x, n_y, n_z	x, y, and z components, respectively, of vector $\vec{n}$
n_{x_i}, n_{y_i}, n_{z_i}	x, y, and z components, respectively, of vector $\vec{n}_i$
$\vec{n}_w$	unit vector in the direction of vortex filament-induced velocity at a point as shown in Figure C.1
n_{w_x}, n_{w_y}, n_{w_z}	x, y, and z components, respectively, of vector $\vec{n}_w$
$\vec{n}(P)$	outward drawn unit normal vector at point P on an arbitrary body surface used in Equation (4)
N	total number of body panels
$\vec{N}$	outward normal vector at a body panel used to calculate $\vec{n}$ in Appendix A
N_x, N_y, N_z	x, y, and z components, respectively, of vector $\vec{N}$ used in Appendix A
NP	total number of periphery points defining an entire body cross section as shown in Figure A.1b
P	generalized point on the body surface or a point on the propeller plane
q	generalized body surface position coordinate used in Equation (1)
Q_j	point source strength at the control point of body panel j
r	radial position coordinate of a point on the propeller plane relative to the propeller plane-fixed cylindrical coordinate system as shown in Figures D.1 and D.3
r'	cowling radial dimension used in Figure 17b
$\hat{r}$	radius of an arbitrary sphere concentric about a point source at which the source potential is calculated in Equation (13)
$\bar{r}$	radius coordinate of a polar coordinate system whose origin is at the center of a sphere in a uniform stream as shown in Figure 10
r_{ij}	distance from the control point of panel j to the control point of panel i as shown in Figure 3

$r_{ii_{image}}$	distance from the control point of the right side image of panel i to the control point of panel i on a symmetric body as shown in Figure 3
$r_{ij_{image}}$	distance from the control point of the right side image of panel j to the control point of panel i on a symmetric body as shown in Figure 3
r_{pj}	distance from the control point of panel j to a point P on the propeller plane
r(P,q)	functional expression of the distance from generalized body surface coordinate q to a surface point P used in Equation (1)
R	reference radius of the propeller plane
RS	length of one side of a body panel as shown in Figures A.4, A.5, A.6a, and A.6b
RT	length of a diagonal on a quadrilateral body panel as shown in Figure A.4
RXR	shorthand notation for a quantity defined by Equation (C.17d)
$\vec{s}$	vector colinear with a straight vortex filament as shown in Figure C.1
S	surface area of a body panel
$\hat{S}$	total surface area of an arbitrary body
S_i	surface area of the ith body panel
S_j	surface area of the jth body panel
ST	length of one side of a body panel as shown in Figures A.4, A.5, and A.6b.
SU	length of a diagonal on a quadrilateral body panel or length of one side of a triangular body panel as shown in Figures A.4 and A.6a
t	time
$\vec{T}$	vector coincident with a straight vortex filament whose length equals the filament length and is the vector representation of the filament as shown in Figures 5 and C.1
T	length of vector $\vec{T}$ and thus the vortex filament length used in Appendix C

TR	length of one side of a triangular body panel as shown in Figure A.6b
TU	length of one side of a quadrilateral body panel as shown in Figure A.4
u, v, w	x, y, and z components, respectively, of free stream velocity $\vec{V}$ as shown in Figures 1, 7, and B.3
u_{b_i}, v_{b_i}, w_{b_i}	x, y, and z components, respectively, of the surface flow velocity V_{b_i} at the control point of body panel i
u_f, v_f, w_f	x, y, and z components, respectively, of velocity $\vec{W}$ induced by a straight vortex filament as shown in Figure C.1
u_k, v_k, w_k	x, y, and z components, respectively, of free stream velocity $\vec{V}$ associated with the kth body orientation and defined, using Equations (7) and (8), as functions of α_k, β_k, and η_k
u_p, v_p, w_p	x, y, and z components, respectively, of the resultant flow velocity $\vec{V}_p$ at a point P on the propeller plane as shown in Figure 7
$\bar{u}_p$, $\bar{v}_p$, $\bar{w}_p$	$\bar{x}$, $\bar{y}$, and $\bar{z}$ components, respectively, of the resultant flow velocity $\vec{V}_p$ at a point P on the propeller plane used in Appendix D
u_s, v_s, w_s	x, y, and z components, respectively, of the flow velocity about a sphere in the x - z plane of symmetry
u_{w_i}, v_{w_i}, w_{w_i}	x, y, and z components, respectively, of the velocity $\vec{V}_{w_i}$ induced at the control point of body panel i by the wing horseshoe vortex
$u_{w_{i_k}}$, $v_{w_{i_k}}$, $w_{w_{i_k}}$	x, y, and z components, respectively, of velocity induced at the control point of body panel i by the wing horseshoe vortex operating at C_{L_k} associated with the kth body orientation
u_{w_p}, v_{w_p}, w_{w_p}	x, y, and z components, respectively, of the velocity $\vec{V}_{w_p}$ induced at a point P on the propeller plane by the wing horseshoe vortex
UR	length of one side of a body panel as shown in Figures A.4, A.5, and A.6a
v_{a_p}, v_{r_p}, v_{t_p}	axial, radial, and tangential components, respectively, of the resultant flow velocity at a point P on the propeller plane relative to the propeller plane-fixed cylindrical axis system as shown in Figures 7 and D.3
v_γ	tangential velocity component on the surface of a sphere

V	magnitude of free stream velocity
$\vec{V}$	free stream velocity vector
$\vec{V}_{b_i}$	resultant surface velocity vector at the control point of body panel i
V_{ii}	magnitude of the distributed source self-induced velocity at the control point of body panel i which is always normal to the panel and numerically equal to $V_{n_{ii}}$ as shown in Figure 2
$\vec{V}_{ii}$	vector representation of V_{ii}
$\vec{V}_{ii_{image}}$	velocity vector at the control point of body panel i (normal to the panel) in a symmetric panel network composed of the panel i source self-induced velocity plus the velocity induced by the point source at the image of panel i
$\vec{V}_{ij}$	velocity vector induced at the control point of body panel i by the point source at the control point of body panel j (includes the velocity induced by the point source located at the image of body panel j in a symmetric panel network)
$V_{n_{ii}}$	identical to V_{ii} as shown in Figure 2
$\vec{V}_p$	resultant flow velocity vector at a point P on the propeller plane
$\vec{V}_{pj}$	velocity vector induced at a point P on the propeller plane by the point source at the control point of body panel j
V_r	magnitude of velocity induced radially by a point source at a distance $\hat{r}$ from the source
$\vec{V}_w$	wing-induced velocity vector
$\vec{V}_{w_i}$	velocity vector induced at the control point of body panel i by the wing horseshoe vortex
$\vec{V}_{w_p}$	velocity vector induced at a point P on the propeller plane by the wing horseshoe vortex
$\vec{V}_w(P)$	wing-induced velocity vector at point P on an arbitrary body surface used in Equation (4)
$\vec{V}_w(q)$	wing-induced velocity vector at a generalized surface coordinate q on an arbitrary body

w_1, w_2, w_3, w_4	downwash velocities at the local three-quarter chord position of each of four elements of the Weissinger approximation of a flat plate airfoil shown in Figure 6
$\vec{W}$	total velocity vector induced at a point by a straight vortex filament as shown in Figure C.1
W	magnitude of velocity induced by a straight vortex filament
$\vec{W}_i$	velocity vector induced at a point i by one filament of the wing horseshoe vortex as shown in Figure 5
x, y, z	axes of the body-fixed right-hand Cartesian coordinate system as shown in Figures 1, 7, D.1, and D.2
x', y', z'	axes of a right-hand Cartesian coordinate system with origin at the propeller plane hub each lying parallel to the body-fixed x, y, and z axes, respectively, as shown in Figure D.1
$\bar{x}$, $\bar{y}$, $\bar{z}$	axes of a propeller plane-fixed right-hand Cartesian coordinate system with origin at the propeller plane hub and oriented at angles α_p and β_p with respect to the x'-y'-z' axis system as shown in Figure D.2
$\bar{\bar{x}}$, $\bar{\bar{y}}$, $\bar{\bar{z}}$	axes of a right-hand Cartesian wind axis system used in Appendix B in which axis $\bar{\bar{x}}$ remains directed upstream parallel to the free stream as shown in Figures B.1 and B.3
x*, y*, z*	axes of an intermediate right-hand Cartesian coordinate system used in coordinate transformations in Appendices B and D as shown in Figures B.2 and D.2
$\hat{x}$, $\hat{y}$, $\hat{z}$	x, y, and z coordinates, respectively, of the point at which vortex filament-induced velocity is calculated as shown in Figure C.1
$\hat{\hat{x}}$, $\hat{\hat{y}}$, $\hat{\hat{z}}$	x, y, and z coordinates, respectively, of a point which is the arithmetic average of four input noncoplanar panel corner points with the point lying on the associated flat quadrilateral developed in Appendix A
x_1, y_1, z_1	x, y, and z coordinates, respectively, of the first input body panel corner point as shown in Figures A.2, A.6a, and A.6b
x_2, y_2, z_2	x, y, and z coordinates, respectively, of the second input body panel corner point as shown in Figures A.2, A.6a, and A.6b

x_3, y_3, z_3	x, y, and z coordinates, respectively, of the third input body panel corner point as shown in Figures A.2, A.6a, and A.6b
x_4, y_4, z_4	x, y, and z coordinates, respectively, of the fourth input body panel corner point as shown in Figures A.2, A.6a, and A.6b
$\hat{x}_1$, $\hat{y}_1$, $\hat{z}_1$	x, y, and z coordinates, respectively, of the vortex filament starting point as shown in Figure C.1
$\hat{x}_2$, $\hat{y}_2$, $\hat{z}_2$	x, y, and z coordinates, respectively, of the vortex filament endpoint as shown in Figure C.1
xx, yy, zz	x, y, and z coordinates, respectively, of a corner point on a flat quadrilateral body panel
xx_1, yy_1, zz_1	x, y, and z coordinates, respectively, of the first corner point on a flat quadrilateral body panel defined by Equation set (A.10) and shown in Figure A.3
xx_2, yy_2, zz_2	x, y, and z coordinates, respectively, of the second corner point on a flat quadrilateral body panel defined by Equation set (A.10) and shown in Figure A.3
xx_3, yy_3, zz_3	x, y, and z coordinates, respectively, of the third corner point on a flat quadrilateral body panel defined by Equation set (A.10) and shown in Figure A.3
xx_4, yy_4, zz_4	x, y, and z coordinates, respectively, of the fourth corner point on a flat quadrilateral body panel defined by Equation set (A.10) and shown in Figure A.3
X, Y	coordinates of a point used in axis system transformations in Appendices B and D as shown in Figures B.2 and D.2
X_{hub}, Y_{hub}, Z_{hub}	x, y, and z coordinates, respectively, of the propeller plane hub as shown in Figures 7, D.1, and D.3
X_p, Y_p, Z_p	x, y, and z coordinates, respectively, of a point P on the propeller plane
X_r, Y_r, Z_r	x, y, and z coordinates, respectively, of the wing root quarter chord point as shown in Figures 4a and 4b
XC, YC, ZC	x, y, and z coordinates, respectively, of a body panel control point
XC_i, YC_i, ZC_i	x, y, and z coordinates, respectively, of the ith body panel control point
XC_j, YC_j, ZC_j	x, y, and z coordinates, respectively, of the jth body panel control point

$XC_{i_{image}}$, $YC_{i_{image}}$, $ZC_{i_{image}}$	x, y, and z coordinates, respectively, of the control point on the right side image of body panel i in a symmetric panel network as shown in Figure 3
$XC_{j_{image}}$, $YC_{j_{image}}$, $ZC_{j_{image}}$	x, y, and z coordinates, respectively, of the control point on the right side image of body panel j in a symmetric panel network as shown in Figure 3

<u>Greek Symbols</u>

α	body angle of attack
α_a	flat plate airfoil angle of attack as shown in Figure 6
α_b, α_{b_1}, α_{b_2}	propeller blade section angles of attack defined in Figure 8
α_G	geometric angle of attack of the propeller plane measured from the free stream as shown in Figure 23a
α_k	body angle of attack for the kth body orientation
α_p	installed angle of attack of the propeller plane relative to the body-fixed x axis as shown in Figure 7 and used in Appendix D (positive for thrust axis inclined upward)
$\alpha\alpha$	angle at a corner of a quadrilateral or triangular body panel as shown in Figures A.4 and A.6a
β	body angle of sideslip (positive nose right)
β_k	body angle of sideslip for the kth body orientation (positive nose right)
β_p	installed angle of sideslip of the propeller plane relative to the body-fixed x axis as shown in Figure 7 and used in Appendix D (positive for thrust axis inclined to the right of the body)
$\beta\beta$	angle at a corner of a quadrilateral or triangular body panel as shown in Figures A.4 and A.6b
γ	angular coordinate of a polar coordinate system to define position on a sphere in a uniform stream as shown in Figure 10
Γ	strength of a wing horseshoe vortex and a vortex filament
Γ_1, Γ_2, Γ_3, Γ_4	vortex strengths at the quarter chord position of each of four elements of a Weissinger approximation model of a flat plate airfoil shown in Figure 6
Δ	dihedral angle of wing quarter chord line as shown in Figure 4b

ε	upwash angle at a point P on the propeller plane measured in the x - z plane as shown in Figure 7 (positive for flow directed upward)
η	Euler angle defined by Equation (8) and Equation (B.5)
η_p	Euler angle defined by Equation (40) and Equation (D.5)
θ	angle of rotational flow (apparent not actual rotation) at point P on the propeller plane measured in the blade section plane as shown in Figures 7 and 8 and defined by Equation (48)
$\hat{\theta}_1$	subtended angle at endpoint 1 of a vortex filament as shown in Figures 5 and C.1
$\hat{\theta}_2$	subtended angle at endpoint 2 of a vortex filament as shown in Figures 5 and C.1
λ	angle of outflow at point P on the propeller plane measured in a plane containing the thrust axis and local radius line as shown in Figure 7 and defined by Equation (47) (positive for flow directed radially outward)
Λ	sweep angle of wing quarter chord line as shown in Figure 4a
μ	upwash velocity induced upstream of a flat plate airfoil
μ_m	upwash velocity induced upstream of an m element Weissinger approximation model of a flat plate airfoil as shown in Figure 6
μ_1	upwash velocity induced upstream of a single element Weissinger approximation model of a flat plate airfoil used in Figure 6
π	= 3.1415926...
σ	body panel source strength "density" (strength per unit area) constant over a panel surface
σ_i	source strength "density" (strength per unit area) constant over the surface of body panel i
σ_j	source strength "density" (strength per unit area) constant over the surface of body panel j
$[\sigma]$	matrix of unknown body panel source strength "densities" (strengths per unit area) to be solved using boundary condition equations
$[\sigma_j]$	column matrix of unknown body panel source strength "densities" (strengths per unit area) corresponding to the flow for a single body orientation

$[\sigma_{jk}]$	augmented matrix of unknown body panel source strength "densities" (strengths per unit area) with the kth column containing a set of unknowns corresponding to the flow for the kth body orientation
$\sigma(P)$	value of source strength "density" (strength per unit area) at point P on an arbitrary body surface
$\sigma(q)$	distribution of source strength "density" (strength per unit area) over the surface of an arbitrary body as a function of the generalized surface coordinate q
τ	sidewash angle at a point P on the propeller plane measured in the x - y plane as shown in Figure 7 (positive for flow toward the right (+y) side of the body)
ϕ	scalar velocity potential function
ϕ_j	velocity potential at the control point of body panel j and also used in Equation (13) for the potential at radius $\hat{r}$ from a point source
ϕ_{ij}	velocity potential at the control point of body panel i due to a point source located at the control point of body panel j
ϕ_s	velocity potential function describing the flow about a sphere in a uniform stream defined by Equation (49)
$\phi(P)$	total velocity potential at point P on an arbitrary body surface due to the source strength distribution over the entire surface
χ	distance forward of the leading edge of a flat plate airfoil as shown in Figure 6
χ_A	horizontal distance between transit A and the coordinate origin as shown in Figures E.1a and E.1b
χ_B	horizontal distance between transit B and the coordinate origin as shown in Figure E.1a
$\Delta\chi$	vertical distance between transit B and the coordinate origin as shown in Figure E.1b
ψ	azimuth position angle on the propeller plane measured clockwise from the top when viewed in the thrust direction as shown in Figures 7, D.1, and D.3
ψ_A	horizontal angle measured using transit A as shown in Figure E.1a
ψ_B	horizontal angle measured using transit B as shown in Figure E.1a

ω	angular velocity of a right-hand rotating propeller as indicated in Figures 7, 23b, and D.3
ω_A	vertical angle measured using transit A as shown in Figure E.1b
ω_B	vertical angle measured using transit B as shown in Figure E.1b

<u>Special Symbols</u>

$\int$	integral
$\iint$	double or area integral
Σ	algebraic summation
$\partial/\partial\gamma$	partial derivative in the γ direction
$\partial/\partial n$	normal derivative in the direction outward from and normal to a body surface or panel
d/dt	time derivative
$\partial/\partial x$, $\partial/\partial y$, $\partial/\partial z$	partial derivatives with respect to the body-fixed axes x, y, and z, respectively
∇	$= (\partial/\partial x)\vec{i} + (\partial/\partial y)\vec{j} + (\partial/\partial z)\vec{k}$, the gradient operator in Cartesian coordiantes
∇^2	$= (\partial^2/\partial x^2) + (\partial^2/\partial y^2) + (\partial^2/\partial z^2)$, the Laplacian operator in Cartesian coordinates
$\lvert\ \rvert$	absolute value or vector magnitude
$\cdot$	scalar dot product operator
x	vector cross product operator
$\neq$	"not equal to"

ACKNOWLDGEMENTS

I wish to express my sincere thanks to Dr. Barnes W. McCormick, my thesis adviser, for his advice, guidance, and patience throughout the course of this research and during the preparation of this thesis.

This study was funded by the National Aeronautics and Space Administration under Grant NSG-1308.

Chapter 1

INTRODUCTION

1.1 Statement of the Problem and Scope of the Investigation

Improving the aerodynamic and vibrational characteristics of general aviation aircraft propellers has been an ongoing concern receiving renewed emphasis in recent years. Nearby aircraft structures alter the airflow at the plane of the propeller. This nonuniform flow field in which the propeller operates produces fluctuating aerodynamic blade loadings which increase vibration and fatigue in the propeller structure. Also, the overall aerodynamic performance of the propeller may be reduced. Knowledge of the flow field at the plane of the propeller, as induced by the aircraft structure, enables the propeller designer to match the propeller with the airframe to reduce the severity of these difficulties. Thus, it is desirable to develop an analytic method for predicting the flow field in which the propeller will operate, for any arbitrary aircraft configuration.

In reality, for a tractor propeller, there is a mutual interference between the propeller and airframe. The propeller slipstream produces a disturbed flow of higher velocity which impacts on the structures, nacelles or cowling, immediately behind the propeller. This situation produces extra pressure drag on the airframe which, considered alone, has a detrimental effect on the performance of the propeller-aircraft propulsion system. Simultaneously, however, the airframe components obstruct the flow entering the propeller disk to produce a nonuniform flow field at the propeller plane. The nonuniformity of this flow gives rise to increased propeller vibration. Flow blockage by the airframe can reduce the apparent advance ratio of the propeller and

improve the efficiency of the propeller. However, generally, the mutual interference tends to reduce the propulsive efficiency of the propeller-aircraft combination to an extent not immediately obvious. This mutual interference effect is very difficult to predict analytically and has usually been investigated experimentally.

However, as a starting point in exploring the propeller-aircraft interaction problem, this study confines itself only to examination of the influence of the airframe upon the flow field at the propeller with the propeller removed. It is this airframe interference which is dominant in creating the fluctuating aerodyanmic loads and vibration on the propeller blades. Propeller interference on the airframe and the mutual interference are not considered.

Only tractor propeller-airframe configurations are assumed in this study, as tractor propellers operating in front of the aircraft are more common than pusher propeller configurations. However, the methods presented in this study are applicable to some pusher propeller configurations.

A second assumption is that the flow is incompressible; thus, Mach number effects are not introduced.

Third, steady, inviscid, potential (irrotational) flow is assumed. This assumption is valid for propellers operating upstream of the airframe and not in the wake of any airframe components. Viscosity effects are insignificant in the flow at the forward regions of the airframe with the propeller removed.

The flow field at the plane of the propeller is influenced by several factors. Two factors are aircraft angle of attack and the tilt of the propeller plane relative to the airframe. Many propellers are

mounted with some angle of attack and sideslip relative to the fuselage in order to improve stability. Angle of attack combined with propeller tilt causes the blades to see an azimuthal variation in velocity, and hence, fluctuating loads exist. This situation can exist even in the absence of any airframe interference. A third factor is the forward spacing of the propeller hub from the airframe as well as the vertical and lateral position of the hub relative to the airframe. The influence of the airframe on the propeller flow is lessened if the propeller is spaced farther from it. A last factor influencing the flow at the propeller plane is the shape of the individual airframe components and their positions relative to one another.

Each airframe component has its own type of influence on the propeller plane flow field. The lifting wing upwash creates radial and azimuthal variations in the axial and tangential velocities at the propeller plane. Axial velocity tends to be increased over portions of the propeller plane located above the wing, while axial velocity is decreased over portions below the wing. Nonlifting components, the cowl-fuselage on single-engine configurations and nacelles on multi-engine configurations, tend to block the flow at the propeller. The axial velocity will be less than free stream velocity at the propeller plane, especially at the radial positions near the hub. Also, because these bodies are not usually bodies of revolution and because the propeller hub may not be centered in front of the cowling or nacelle, these bodies can also induce an uneven distribution of radial and tangential velocity components over the propeller plane.

Combining the effects of all the above factors leads to a propeller plane flow field which is fully three-dimensional. The propeller plane

flow field cannot be simplified by assuming axisymmetry or assuming that aircraft components are bodies of revolution.

The purpose of this study is to predict the three-dimensional, steady, incompressible potential flow at the plane of a propeller having any orientation and position in front of an arbitrary nacelle-fuselage-lifting wing combination. Development of a finite element numerical method is presented which calculates the flow on the surfaces of the fuselage and nacelles as well as at the plane of the propeller. This numerical approach is incorporated in a computer program which is described in this thesis.

Numerical predictions of surface pressure and velocity at the propeller plane are compared with exact analytical solutions for a single body in order to check the method.

Little usable experimental data is available in the literature for comparison. However, flow predictions at the propeller plane of a twin-engine aircraft are compared with the published wind tunnel test results for that aircraft.

Computer predictions of the flow field at the propeller plane of a Piper Cherokee PA-28-180 aircraft are presented. However, no experimental flow field data for this aircraft are available for comparison with the predictions.

A parametric study of the flow predictions for the Cherokee aircraft is made to determine the importance of the various airframe components on the flow field at the propeller plane. In particular, the acceptability of neglecting aft portions of the airframe distant from the propeller in making computer predictions is investigated. Also, the effect

of wing dihedral and inlet inflow at the cowl or nacelle upon the flow at the propeller is examined.

1.2 Previous Investigations

Examination of the effects of afterbodies upon propellers has been done since the early 1920's. Most of the early work, prior to 1948, was both theoretical and experimental but was limited to body influences on the steady propeller thrust, torque, and propulsive efficiency rather than unsteady or vibratory loading. In much of this experimental work the actual flow field induced by the body at the propeller was not quantitatively surveyed; rather, the propeller was operated in the flow field and its steady performance measured.

Lesley and Woods (1) performed early wind tunnel tests of propeller-body interaction effects. Steady propeller thrust, torque, and propulsive efficiency were measured with the propeller operating in front of disks and other flat-faced cylindrical afterbodies. Results indicated propulsive efficiency was less for the propeller operating with a slipstream obstruction than for the free operating propeller.

Durand (2) extended the work of Lesley and Woods (1) by use of actual airframe shapes in the propeller slipstream. A cowl-fuselage-high wing combination was tested at various spacings aft of the propeller. Increased propeller-airframe clearance reduced loss of propulsive efficiency, and the influence of the body fell rapidly as clearance increased. Durand concluded propeller-airframe interaction should be a design consideration. Also, use of fuselage shapes producing minimum interaction with the propeller is desirable, or if not possible, maximum propeller-airframe clearance should be used to reduce interaction.

Lock (3) first developed a two-dimensional analytic method for predicting propeller performance under the influence of a slipstream obstruction. The method was limited to a body shape consisting of a spheroidal nose attached to a semi-infinite cylinder aligned parallel to the free-stream velocity. Lock used the exact potential flow solution for the body to get the radial distribution of axial velocity upstream in the propeller plane (propeller removed). The axial velocity defect was incorporated in propeller blade strip theory to calculate the steady propeller performance with body influence.

Lock (4) extended his own previous work. He analyzed the various power wastages by the propeller. To do this, a momentum analysis was used which incorporated the body-induced potential flow axial velocity at the propeller plane. Also, pressure drag on the body nose was used in the power wastage expression. This power loss expression could then be used with either propeller blade strip theory or vortex theory to predict steady performance with body influences.

Lock (5) summarized his previous works. He applied his method to numerical examples involving spheroidal body shapes of various fineness ratios. He compared his predicted performance results with measured test results.

Weick (6) made a limited survey of the axial velocity at the propeller plane of a Sperry Messenger aircraft (propeller removed) in a wind tunnel. At any particular test location in the propeller plane, the ratio of measured axial to free-stream velocity remained constant regardless of the wind tunnel test free-stream velocity. Weick concluded the variation of axial velocity radially f om hub to tip on the propeller plane to be significant and worth much consideration in propeller design.

Lesley and Reid (7) used a VE-7 aircraft fuselage and surveyed the distribution of axial velocity at the propeller plane (propeller removed). At each of three azimuth positions checked, the axial velocity varied from zero at the hub to near free stream at the propeller tip radius. An averaged radial distribution of axial velocity was presented. Next, several propellers of various pitch distribution were tested freely and then in front of the fuselage. Generally, each propeller operated less efficiently when in the presence of the fuselage. Significantly, one propeller having a blade pitch distribution shape similar to the shape of the measured radial distribution of axial velocity in the propeller plane suffered the smallest reduction of efficiency. Lesley and Reid concluded a propeller designed such that each blade section locally attains its optimum angle of attack, at conditions of maximum efficiency, is superior to the conventional constant speed propeller for operation in the presence of a slipstream obstruction.

McHugh and Derring (8) tested several full-scale propellers operating in front of a family of radial engine cowlings having various diameters. Effect of cowling to propeller diameter ratio on the steady propeller performance was investigated. Results were two-fold. First, for cowlings less than one-third the propeller diameter, propulsive efficiency did not vary significantly with variation in cowling diameter. However, as cowling size increased above one-third propeller diameter, propulsive efficiency rapidly decreased. Second, presence of a spinner on the cowling increased propulsive efficiency several percent above that obtained without the spinner.

Stickle, Crigler, and Naiman (9) extensively tested three full-size propellers, each with Clark-Y blade sections, operating in front of

various cowlings. The five body shapes varied from a radial engine cowling without spinner to a very streamlined body having a large spinner. All bodies had circular cross sections and were at zero angle of attack. Flow surveys at the propeller plane of each body (propeller removed) yielded the radial distribution of axial velocity in which the propellers would operate. Powered tests of all propellers operating in these flow fields were made.

For the bodies tested, it was concluded that the change in body drag due to the propeller slipstream negligibly influence propeller performance and could be disregarded. The remaining direct influence of the body-induced flow field on the propeller blade load distribution was dominant.

Their results led to three conclusions. First, the velocity field induced by the body at the propeller plane must be considered when designing the propeller blade pitch distribution. Second, body-induced flow has the strongest influence on the inner blade sections. For round shank blades, reduced axial velocity due to the body alters the drag on the shank and affects efficiency. For blades with shanks having airfoil shaped sections, the reduced velocity increases section angle of attack at the shank sections, so the body causes a change in blade load distribution. Third, efficiency gains obtained with a spinner depend on the velocity at the hub due to the body. The spinner is beneficial if hub velocity is high but not as helpful if hub velocity is low.

Wing-induced effects on propeller loads were examined by Kuhn and Draper (10). A tapered wing semispan was tested with two propellers attached to negligibly small nacelles. When the outboard propeller operated at 90 to 100 percent chord ahead of the leading edge, the propeller

pitching moment was double that produced by the free propeller. However, no lateral propeller force was created. Thus, Kuhn and Draper concluded the wing upwash was not producing significant azimuthal variation in blade forces. Rather, the increased axial velocity induced by the wing over the upper half of the propeller plane and the reduced axial velocity over the lower half were found to cause the pitching moment increase.

With the 1940's came studies examining the vibration of propellers due to oscillatory loads produced when operating in a nonuniform flow field induced by the wing. Such a study was conducted in Great Britain. In part I of the study, Postlethwaite, Carter, Perring, and Diprose (11) made theoretical predictions of vibrating modes in two-, three-, four-, and six-bladed propellers. These propellers were operating upstream in the calculated flow field induced by a wing having Joukowsky airfoil sections. In part II of the study, Forshaw, Squire, and Bigg (12) tested a three-bladed propeller operating in the nonuniform flow field created by blowing a narrow axial jet of air along one propeller plane azimuth location. Measured torsion-bending and whirling-bending vibration modes compared favorably with predictions.

Later, Corson and Miller (13) examined the vibration of a pusher propeller whose blades periodically passed through the wake of a forward body. The reduced axial velocity in the wake was introduced as an instantaneous change of local blade section angle of attack in propeller blade element theory to predict unsteady loading. Actual blade forces were measured also. Blade vibratory stress was increased if the drag of the body (intensity of the wake) increased. Secondly, all else being equal, large diameter propellers experienced less wake-induced stress than smaller diameter propellers.

Most recently (1948 to 1953), the National Advisory Committee for Aeronautics published a series of studies dealing with detailed flow surveys at the plane of the propeller and these flow effects on the oscillatory loads and vibration in the propeller.

Vogely (14) performed flight tests on a propeller inclined to the longitudinal axis of the fuselage. He measured radial and azimuthal blade load distribution and efficiency as affected by propeller thrust axis inclination. He compared theoretical predictions which did not account for any wing-airframe influences on the flow field.

Vogely observed that the pure inclination of the propeller could produce oscillatory loads, and blade stress could be reduced, at a specific aircraft angle of attack, by attaching the propeller to the fuselage with the proper thrust axis inclination. Vogely pointed out that the airframe induces a significant spatially varying flow field in which the propeller operates which can incur further blade load alterations. Vogely concluded that detailed flow angle surveys at the plane of the propeller should be made to obtain accurate results in predicting propeller vibratory loads.

Shortly thereafter, Roberts and Yaggy (15) performed the first very detailed survey of the flow field in the propeller plane (propeller removed) of a twin-engine aircraft. The full-size, unswept wing aircraft was tested in the Ames 40- by 80-foot wind tunnel.

The test conditions run consisted of flaps extended, no flaps, and two different nacelle inlet velocity ratios. For each condition, a series of runs was made over a range of nacelle angles of attack from two to 12 degrees.

Survey points at the left propeller plane were densely distributed over the full radius and at fifteen degree azimuth increments. Several flow quantities were measured at each point. Total local velocity was measured. The local velocity components were measured in terms of two angular quantities; angle of rotational flow was the ratio of local tangential to axial velocity, and angle of outflow was the ratio of local radial to axial velocity. Also, at each point the upwash and sidewash angles, relative to the fuselage, were measured. Measured radial and azimuthal distributions of the flow quantities were presented. The distribution of upwash angle along the horizontal centerline of the propeller plane was plotted.

Measured upwash along the horizontal centerline compared poorly with predicted upwash induced by the isolated wing modeled by lifting line theory. This comparison indicated the fuselage and nacelles contributed greatly to the upwash.

Aerodynamic blade load predictions were made using steady blade element theory and included the nonuniform flow field measurements in terms of instantaneous spacially varying changes in local section angle of attack. Predicted loading varied approximately sinusoidally with azimuth, and when the measured flow field was used in the blade load predictions, those predicted load magnitudes were larger than loads predicted for an inclined propeller operating in free air.

Nacelle inlet velocity ratio was found to influence the flow only at the central region of the propeller plane immediately upstream of the inlet.

Roberts and Yaggy (15) concluded that the angle of rotational flow and, specifically, the upwash angle along the propeller plane horizontal

centerline were the most important quantities in producing the oscillatory blade loading. Also, they concluded it was desirable to develop a theoretical method for predicting the nacelle, fuselage, and wing contributions to the upwash at the propeller plane for any wing-fuselage-nacelle combination.

Testing by Roberts and Yaggy (15) led to two further studies. Using the measured flow field data of Roberts and Yaggy (15) with steady propeller blade element theory, Rogallo, Roberts, and Oldaker (16) computed the airload variation for a propeller operating in the flow field. Based on airload predictions, the first order vibratory blade stresses were calculated. Blade stresses measured on the propeller operating on the twin-engine test aircraft compared favorably with predictions. This study gave two conclusions. First, steady state blade element theory was found adequate for predicting the magnitude and distribution of propeller oscillatory air loads provided the flow field induced by the body at the propeller plane was completely known before hand. Second, these predicted loadings allowed accurate prediction of first order vibratory blade stresses.

Since Roberts and Yaggy (15) had verified that the upwash along the propeller plane horizontal centerline was the most dominant factor in inducing oscillatory blade loads, Yaggy (17) presented a theoretical method for predicting the upwash distribution. Yaggy's method was developed to predict the upwash contributions at the propeller plane due to the fuselage, nacelles, and wing of the test aircraft used in References 15 and 16. Lifting line theory was used for predicting wing-induced upwash. The nacelle was modeled as a simple closed body of revolution for which the exact potential flow could be calculated.

The portion of the fuselage in the vicinity of the propeller plane was modeled as an infinite elliptical cylinder for which an exact upwash expression could be derived from potential flow theory. Net predicted upwash at a point at the propeller plane was taken as the sum of the component contributions. Predicted upwash agreed fairly well with measured results.

Yaggy (17) indicated his method, derived for this specific aircraft, could be extended to other twin-engine aircraft of similar characteristics. The required characteristics were high wing aspect ratio, nacelles of circular cross section, fuselage cross sections resembling an ellipse at the propeller plane region, and that no two body components should be spaced closer than the larger body diameter.

In three remaining publications, work was continued along the lines of the previous work (References 15, 16, and 17). This time the effort was to find the effects of wing sweep on the flow field induced at the propeller plane. Rogallo (18) and Rogallo and McCloud (19) extended the upwash prediction method of Yaggy (17) to the case of a highly swept wing-fuselage-nacelle combination. Rogallo and McCloud (19) also obtained limited experimental results for a swept wing aircraft which were compared with predictions. Also, the swept wing results were compared with upwash measurements made with a similar aircraft having unswept wings.

Hoping to learn more about the effects of wing sweep on propeller vibratory loads, Rogallo and McCloud (20) performed detailed propeller plane flow surveys (propeller removed) with a swept wing-nacelle-fuselage combination. The test was as extensive as that done by Roberts and

Yaggy (15). Wing sweep was found to induce first order vibratory propeller blade loads similar to those attained with an unswept wing.

Since this work of the 1950's, there appears to be no published work presenting detailed propeller plane flow field surveys, or prediction methods. With the exception of Yaggy (17), Rogallo (18), and Rogallo and McCloud (19), whose prediction methods apply only to a small class of similar aircraft, there is no published method for predicting the nonuniform flow field at the propeller plane of an arbitrary wing-fuselage-nacelle combination.

Chapter 2

THEORY OF THE POTENTIAL FLOW SOLUTION METHOD

2.1 Historical Development

With the development of high-speed digital computers in the 1950's and 1960's, it became possible to solve the potential flow about arbitrarily shaped bodies using finite element techniques involving large systems of algebraic equations.

Many such flow solution methods have been advanced since 1958 when Smith and Pierce (21) used source distributions on panels to model bodies of revolution. Hess (22) extended the method to bodies of revolution oriented perpendicular to the free stream flow.

Hess and Smith (23) first solved the flow about nonlifting arbitrary three-dimensional bodies using distributions of sources over the body surface subdivided into discrete panel elements. Smith (24) explained the theory of Hess and Smith (23) and presented sample calculations.

A thorough discussion of the panel element computer methods was done by Hess and Smith (25). They discussed the theoretical details for predicting both two-dimensional and fully three-dimensional potential flow.

Throughout the 1960's and 1970's, many sophisticated computer programs were written to predict the flow about three-dimensional lifting wing-body combinations. Several examples of such work are Hess (26), Woodward, Dvorak, and Geller (27), and Woodward (28). The theory behind these methods is the same, but each uses different singularities over the body panels. Sources, vortices, doublets, or combinations of these singularities have been used in attempts to improve the accuracy of the method.

All of such published computer program packages are limited to body surface velocity, pressure, force, and moment predictions. None of them have been written to calculate the flow at locations, such as at a propeller plane, away from the body surface.

2.2 Theoretical Overview

The method used here involves the solution of the Neumann problem for the potential flow around an arbitrary body-wing combination in a uniform free stream velocity field. Hess (25), Rubbert and Saaris (29), and Hess and Faulkner (30) explain the theory which is also summarized here.

Steady, incompressible, inviscid flow is assumed. Also, irrotationality is assumed. Thus, the velocity field is the negative gradient of a scalar potential function. Three components comprise the velocity field. First is the onset free stream velocity, $\vec{V}$, assumed to be constant everywhere. Second is the velocity induced by the lifting wing, $\vec{V}_w$, if present. Third is the perturbation velocity induced by the body or bodies.

A distribution of source strength density, σ, over the body surface, $\hat{S}$, corresponds to a scalar potential function, ϕ, which satisfies the Laplace equation and whose negative gradient is the velocity at any point. However, the wing surface is not included as part of the body surface. Rather, the wing is modeled by a specified vortex system responsible for the wing-induced velocity. This velocity is thus a known quantity.

At a point P on the body surface, the potential due to a unit strength point source at point q is

$$1/[4\pi r(P,q)] \quad ,$$

where $r(P,q)$ is the distance from q to P. Then if surface $\hat{S}$ has a distribution of source strength density, $\sigma(q)$, the total potential at P, $\phi(P)$, due to the body or bodies is

$$\phi(P) = \iint_{\hat{S}} \frac{\sigma(q)}{4\pi r(P,q)} d\hat{S} \quad , \tag{1}$$

where $d\hat{S}$ is an elemental body surface area. This potential also satisfies the Laplace equation as a consequence of incompressibility:

$$\nabla^2\phi(P) = 0 \quad . \tag{2}$$

Also, due to the irrotationality condition, the perturbation velocity at P is given by $-\nabla\phi(P)$. Thus, the continuity equation may be expressed as

$$\nabla \cdot [-\nabla\phi(P)] = 0 \quad . \tag{3}$$

Equation (1), which satisfies Equations (2) and (3), is used with specified boundary conditions on surface $\hat{S}$ to solve for the unknown $\sigma(q)$.

The boundary conditions are that the normal velocity on the body surface must be some prescribed value, $F(q)$, while the potential, ϕ, at infinity must vanish. Generally, $F(q)$ is zero at locations where $\hat{S}$ is a solid boundary but may be nonzero over areas of the body wall which are considered to be permeable. $F(q)$ is the normal component at point q of the sum of the free stream velocity, $\vec{V}$, the wing-induced velocity, $\vec{V}_w(q)$, and the perturbation velocity given by the negative gradient of Equation (1). Taking the normal derivative of Equation (1), using care in the integration at the singularity of $P = q$ as explained by Hess (25), and combining it with the normal component of $\vec{V}_w$ and $\vec{V}$ gives the following boundary condition equation at point P on $\hat{S}$:

$$\frac{\sigma(P)}{2} - \iint_{\hat{S}} \frac{\partial}{\partial n}\left[\frac{1}{4\pi r(P,q)}\right]\sigma(q)d\hat{S} = -\vec{n}(P) \cdot [\vec{V} + \vec{V}_w(P)] - F(P) \quad , \tag{4}$$

where $\vec{n}(P)$ is the outward unit normal vector to surface $\hat{S}$ at P, and $\partial/\partial n$ denotes the derivative in the direction of $\vec{n}(P)$.

Solving the integral Equation (4) for the unknown σ on the body surface concludes the solution of the complete flow field.

Instead of analytically solving Equation (4), which may be impossible for complex surfaces $\hat{S}$, it is solved numerically by dividing surface $\hat{S}$ into N discrete elements. Applying the surface boundary condition to each of the N elements approximates Equation (4) by a set of N simultaneous linear algebraic equations for the N unknown values of σ. Solving for σ on each surface element completes the flow solution, and the velocity anywhere on or away from the body surface may then be calculated. The details of this numerical method are explained in the remainder of this chapter.

2.3 Body Surface Model and Free Stream Velocity Components

All fuselage and nacelle surfaces are partitioned into a network of N plane triangular and quadrilateral panels. Figure 1 illustrates the panel network on a single body.

S_i denotes the area of the ith panel. The panel control point is denoted by (XC_i, YC_i, ZC_i) and outward unit normal vector by $\vec{n}_i$. Also, on the ith panel there is a constant distribution of source strength density, σ_i (a source strength-per-unit area), see Figure 1. Appendix A provides the details of generating the panel network and obtaining panel areas, control points, and unit normal vectors.

In terms of the body-fixed Cartesian coordinate system, the outward normal unit vector is written as

$$\vec{n}_i = n_{x_i}\vec{i} + n_{y_i}\vec{j} + n_{z_i}\vec{k} \quad . \tag{5}$$

As is also explained in Appendix A, the body surface may be more simply modeled if all body cross sections are symmetric about a common plane of symmetry. In this situation the left (-y) side of the geometry is provided and the right side paneling is a mirror image of the left. Fewer panels need be considered, and this simplifies the problem, as will be explained in later sections of this chapter.

On certain panels, say the ith one, inlet or outlet flow is modeled by specifying a value F_i. F_i equals the amount of velocity allowed to pass normal to and through panel i. F_i, as a positive quantity, represents velocity inward through the panel. F_i, as a negative quantity, represents outflow velocity. A solid boundary panel i has a zero value of F_i which is assumed and need not be specified.

Referring to Figure 1, the body is immersed in a uniform onset velocity, $\vec{V}$, and is oriented in this velocity field with a specified angle of attack, α, and sideslip, β.

Relative to the body-fixed axis system, the body, with orientation α and β, senses three components of the onset free stream velocity expressed vectorially as

$$\vec{V} = u\vec{i} + v\vec{j} + w\vec{k} \quad , \tag{6}$$

where the components are expressed as

$$u = -V \cos \alpha \cos \eta \quad , \tag{7.a}$$

$$v = +V \cos \alpha \sin \eta \quad , \tag{7.b}$$

and

$$w = -V \sin \alpha \quad , \tag{7.c}$$

where V is the free stream velocity magnitude, and Euler angle, η, is expressed as follows:

$$\eta = \tan^{-1}(\tan \beta \cos \alpha) \quad . \tag{8}$$

Appendix B derives the Equations (7) and (8) for the free stream velocity components.

2.4 Body Panel Source-Induced Velocity Components

2.4.1 General case of a nonsymmetric body panel network

Expressions for velocity induced by the source distribution of the ith panel on itself and by all other panels j on the ith panel are developed as follows. Refer to Figure 1 and also Figure 2. On panel i, under consideration, the source strength density σ_i remains distributed over the panel in determining that panel's self-induced velocity. However, in obtaining the velocity induced at panel i by all other panels, j, the source distribution is considered to be lumped into a point source at each of the remote panels j.

As shown in Figure 2, the source strength distribution σ_i produces only a velocity flux normal to panel i. This total velocity flux is numerically equal to the source strength density per unit area:

$$\sigma_i/S_i = 2V_{n_{ii}}/S_i \quad , \tag{9}$$

where $V_{n_{ii}}$ is the normal velocity induced by panel i on itself. This is the quantity of interest and is found to be from Equation (9),

$$V_{n_{ii}} = \frac{\sigma_i}{2} = V_{ii} \quad . \tag{10}$$

To compute velocity induced at panel i by panel j, lump the source strength distribution on j into a point source of strength Q_j given by

$$Q_j = \sigma_j S_j \quad . \tag{11}$$

Q_j, the strength of the point source in three-dimensional space, equals the volume flow rate of the source. On a sphere of radius $\hat{r}$

with the source at the center of the sphere, the source-induced velocity is directed radially and is given using Equation (11) by,

$$V_r = (\sigma_j S_j)/4\pi\hat{r}^2 \quad . \tag{12}$$

V_r equals the negative gradient of the potential, ϕ_j, at radius $\hat{r}$ due to the point source. Conversely, ϕ_j at radius $\hat{r}$ equals the negative of the line integral of V_r from the source to radius $\hat{r}$

$$\phi_j = -\int^{\hat{r}} V_r \, d\hat{r} \quad . \tag{13}$$

Using Equation (12) in Equation (13) and integrating gives the expression for the potential at the control point of panel i due to the source at the control point of panel j as follows:

$$\phi_{ij} = \frac{\sigma_j S_j}{4\pi r_{ij}} \quad , \tag{14}$$

where r_{ij} is the distance from control point j to control point i given by

$$r_{ij} = [(XC_i - XC_j)^2 + (YC_i - YC_j)^2 + (ZC_i - ZC_j)^2]^{1/2} \quad . \tag{15}$$

Then the velocity $\vec{V}_{ij}$ induced at panel i by panel j is the negative gradient of the potential as follows:

$$\vec{V}_{ij} = -\nabla\phi_{ij} = -\frac{\partial\phi_{ij}}{\partial x}\vec{i} - \frac{\partial\phi_{ij}}{\partial y}\vec{j} - \frac{\partial\phi_{ij}}{\partial z}\vec{k} \quad . \tag{16}$$

Substitution of Equations (14) and (15) into Equation (16) gives

$$\vec{V}_{ij} = \frac{\sigma_j S_j}{4\pi r_{ij}^3}[(XC_i - XC_j)\vec{i} + (YC_i - YC_j)\vec{j} + (ZC_i - ZC_j)\vec{k}] \quad , \tag{17}$$

where r_{ij} is given by Equation (15).

Equations (10) and (17) apply to the situation in which all N panels of the body must be considered individually which occurs when the panel network is nonsymmetric.

2.4.2 Special case of a symmetric body panel network

In the special case of body symmetry, each panel on the left (-y) side of the body has a corresponding mirror image panel whose control point differs only by the sign of the y coordinate, see Figure 3. In this situation, Equations (10) and (17) are modified and applied only to the N/2 panels on the left side of the body. The modifications account for the induced effects of the right side "image" panels, and these modified expressions are now derived.

First, Equation (10), for panel self-induced velocity, is modified. In the symmetric body case, the velocity induced on left side panel i by itself, Equation (10), must additionally include the normal component of velocity induced at panel i by a point source at the image of panel i, i_{image}.

Referring to Figure 3, the distance $r_{ii_{image}}$ between panel i and its image is

$$r_{ii_{image}} = 2YC_i \quad . \tag{18}$$

Substitute Equation (18) into (17) and replace point (XC_j, YC_j, ZC_j) by the control point on panel i_{image} to get the total velocity, $\vec{V}_{ii_{image}}$, induced by the point source at i_{image} on panel i. Then get the component of velocity normal to panel i by taking the vector product of $\vec{V}_{ii_{image}}$ and $\vec{n}_i$ using Equation (5). The result is

$$\vec{V}_{ii_{image}} \cdot \vec{n}_i = \frac{\sigma_i S_i YC_i n_{y_i}}{16\pi |YC_i|^3} \quad . \tag{19}$$

Finally, to modify Equation (10) for the effects of the image panel, simply add Equation (19) to the original Equation (10) to give

$$V_{ii} = \frac{\sigma_i}{2}[1 + \frac{S_i YC_i n_{y_i}}{8\pi|YC_i|^3}] \quad , \tag{20}$$

in which panel i is on the left (-y) side of a symmetric panel network. Note, here V_{ii} is the velocity induced normal to panel i by itself and its image panel.

Now a modified form of Equation (17) for velocity induced by remote panels is derived for the case of body panel symmetry. Again refer to Figure 3. At real panel i there is a potential, ϕ, due to the point source at real panel j, and there is also a potential at panel i due to the point source at image panel j. Due to symmetry, the source strength at panel j equals that at j_{image}. Also, note that $YC_j = -YC_{j_{image}}$. Then denoting by $r_{ij_{image}}$ the distance from image panel j to real panel i, write:

$$r_{ij_{image}} = [(XC_i - XC_j)^2 + (YC_i + YC_j)^2 + (ZC_i - ZC_j)^2]^{1/2} \quad . \tag{21}$$

Applying Equation (14) to both panels j and j_{image}, the total potential at panel i is.

$$\phi_{ij} = \frac{\sigma_j S_j}{4\pi r_{ij}} + \frac{\sigma_j S_j}{4\pi r_{ij_{image}}} \quad , \tag{22}$$

where r_{ij} is given by Equation (15), and $r_{ij_{image}}$ is given by Equation (21).

The velocity at panel i due to panels j and j_{image}, $\vec{V}_{ij}$, is found by substituting Equations (15), (21), and (22) into Equation (16). This gives

$$\vec{V}_{ij} = \frac{\sigma_j S_j}{4\pi}\{[\frac{(XC_i - XC_j)}{r_{ij}^3} + \frac{(XC_i - XC_j)}{(r_{ij_{image}})^3}]\,\vec{i} + [\frac{(YC_i - YC_j)}{r_{ij}^3} + \frac{(YC_i + YC_j)}{(r_{ij_{image}})^3}]\,\vec{j}$$

$$+ [\frac{(ZC_i - ZC_j)}{r_{ij}^3} + \frac{(ZC_i - ZC_j)}{(r_{ij_{image}})^3}]\,\vec{k}\} \quad . \tag{23}$$

This equation is the modified version of Equation (17) and is applied only to real panels i and j on the left side of a symmetric panel network.

2.5 Wing Model Description and Wing-Induced Velocity

2.5.1 Horseshoe vortex model and its induced velocity

Should a lifting wing be present on the configuration, the surface of the wing is not modeled with source panels. Rather, it is represented simply by a single horseshoe vortex.

Referring to Figure 4, the wing operates in the free stream velocity, V. Wing span, b, root chord, c, and location of the quarter chord of the wing root, (X_r, Y_r, Z_r), relative to the body-fixed coordinates are specified. Also, the quarter chord line may have some small angles of sweep, Λ, and dihedral, Δ. The horseshoe vortex representation has the bound vortex filaments attached to the quarter chord line. The two trailing vortices are spaced to give the horseshoe a span equal to $\pi b/4$. This spacing represents the mean span between the rolled up vortices trailing from an elliptic wing. These trailing vortices, which actually extend infinitely downstream, are truncated to a length of 100 c for purposes of numerical modeling.

Corresponding to the given body angle of attack, α, the wing lift coefficient, C_L, is specified. C_L is assumed equal to the wing root section lift coefficient. Then the strength of the horseshoe vortex

filaments, Γ, is a constant which equals the total bound circulation at the wing root. Thus, using the Kutta-Joukowski theorem relating lift to bound vortex strength, the horseshoe vortex strength is given by

$$\Gamma = \frac{cC_L V}{2} \quad . \tag{24}$$

Note, Γ is a specified constant and not an unknown. This follows from the assumption used that the wing can influence the flow at the body panels, but the body will not influence the flow over the wing.

At a point i of interest, the velocity induced by the wing horseshoe vortex is given in the body-fixed coordinate system as

$$\vec{V}_{w_i} = u_{w_i}\vec{i} + v_{w_i}\vec{j} + w_{w_i}\vec{k} \quad . \tag{25}$$

The wing-induced velocity is calculated using the Biot-Savart law by applying the law to each of the individual straight vortex filaments, in turn, and summing the individual filament-induced velocities, $\vec{W}$. Referring to Figure 5, the Biot-Savart law for the velocity at point i located distance h from a filament of length $|\vec{T}|$ is given vectorially as

$$\vec{W}_i = \frac{\Gamma}{4\pi}\int_1^2 \frac{\vec{g} \times d\vec{T}}{|\vec{g}|^3} \quad . \tag{26}$$

As shown in McCormick (31), the magnitude of this velocity is given by

$$|\vec{W}_i| = \frac{\Gamma}{4\pi h}(\cos\hat{\theta}_1 + \cos\hat{\theta}_2) \quad . \tag{27}$$

Should a vortex filament pass through or near the point of interest, distance h will be zero or very small causing numerical problems with the Biot-Savart law. Two measures are taken to prevent these problems. First, if distance h is zero, the velocity components induced by the vortex filament are set equal to zero, and the Biot-Savart law, Equation (27), is not used, thus preventing attempted division by zero.

Second, an upper limit is imposed on the magnitude of velocity which a single vortex filament may induce. The upper velocity limit is 20 percent of the free stream velocity. Thus, when distance h is such that Equation (27) yields a velocity magnitude greater than 0.2 V, the induced velocity magnitude $|\vec{W}_i|$ is set equal to 0.2 V, and velocity components are adjusted accordingly.

Choice of 0.2 V for the velocity limit was made because this approximates the value of downwash velocity at the root three-quarter chord location of a wing with flat plate airfoil sections having an aspect ratio of 3 and operating at $C_L = 2.0$, as calculated by thin airfoil theory. Thus, at body panels near the wing root region, where calculations with Equation (27) will likely require the use of the velocity limit, 0.2 V is an appropriate velocity limit.

Appendix C presents expressions employing the Biot-Savart law and the 0.2 V velocity limit rule used by a computer subroutine to calculate the induced velocity at any point due to a straight vortex filament having any specified orientation.

2.5.2 Justification for the use of the horseshoe vortex model

To show the validity of using a simple horseshoe vortex model instead of more complicated vortex lattice or lifting line models, a thin airfoil will be investigated.

A flat plate airfoil with the vortex attached at the quarter chord represents the two-dimensional case of a horseshoe vortex. Using Weissinger's approximation, the upwash velocity, μ, may be calculated. Analagous to a more exact finite wing model using a vortex lattice, the flat plate airfoil may be modeled using m segments, each with a vortex

at the segment quarter chord. Weissinger's approximation applied to each element can be used to solve more accurately the upwash, μ_m, ahead of the airfoil.

Figure 6 compares the upwash at various upstream positions, χ/c, of the single element airfoil to that for a multi-element airfoil having $m = 100$ segments. Comparing the approximate to the nearly exact model, there is a 13 percent difference in upwash at points at $\chi/c = 0.4$. Typical twin engine aircraft propellers are positioned approximately at $\chi/c = 1.0$, where the upwash difference has dropped to 3.6 percent. Typical single engine aircraft have propellers positioned approximately 1.5 chords or more ahead of the wing. As Figure 6 shows, the upwash difference is 2.0 percent or less at those positions.

As the main purpose of this study is to predict the flow at an upstream propeller plane, Figure 6 indicates that the use of the single bound vortex (horseshoe vortex) representation of the wing is justified.

2.6 Boundary Condition Equations

2.6.1 General case of a nonsymmetric body panel network

Each point source potential, Equation (14), on the body vanishes at infinity which satisfies one of two boundary conditions.

The other boundary condition is applied to each panel on the body. This condition is that the normal component of velocity at the control point of each ith panel must vanish or equal a specified value of inflow velocity, F_i, through the panel. The velocity at the panel is composed of free stream, wing-induced, and all N panel-induced velocity contributions. For the ith panel, the surface boundary condition is given as

$$\vec{V}_{w_i} \cdot \vec{n}_i + \left[\sum_{\substack{j=1 \\ (j\neq i)}}^{N} \vec{V}_{ij} \cdot \vec{n}_i\right] + V_{if} + \vec{V} \cdot \vec{n}_i = \begin{cases} 0, & \text{solid boundary} \\ -F_i, & \text{relaxed boundary} \end{cases}, \quad (28)$$

where F_i is a positive value if it is inflow velocity and negative if outflow velocity. By substitution of Equations (5), (6), (10), (17), and (25) into Equation (28), the boundary condition on panel i becomes

$$\sigma_i + \frac{1}{2\pi} \sum_{\substack{j=1 \\ (j \neq i)}}^{N} \frac{\sigma_j S_j}{r_{ij}^3} \{ (XC_i - XC_j) n_{x_i} + (YC_i - YC_j) n_{y_i} + (ZC_i - ZC_j) n_{z_i} \}$$

$$= -2[(u + u_{w_i}) n_{x_i} + (v + v_{w_i}) n_{y_i} + (w + w_{w_i}) n_{z_i}]$$

$$+ \begin{cases} 0, \text{ solid boundary} \\ -2F_i, \text{ relaxed boundary} \end{cases} . \tag{29}$$

By writing Equation (29) for each of the N body panels, a set of N simultaneous linear algebraic equations is formed in which the source strengths, σ, are unknowns. In matrix notation, this set is expressed as

$$[A_{ij}][\sigma_j] = [B_i] \quad i, j = 1, 2, 3, \ldots N \quad . \tag{30}$$

Note, the [B] matrix containing the wing-induced velocity components and free-stream velocity components is the only quantity directly dependent upon the input values of α and β (Equations (7) and (8)) and C_L. The matrix [A] consists of geometric parameters and is unaltered by α, β, and C_L variations.

A given input combination of α, β, and C_L will result in a particular flow solution, $[\sigma]$ matrix. Assuming there are M total input combinations of α, β, and C_L, the system of boundary condition equations can be augmented to contain M sets of [B] coefficients and M sets of unknowns $[\sigma_j]$. Denoting by subscript k the kth input combination α_k, β_k, and C_{L_k}, Equation set (30) can be expressed in matrix notation as

$$[A_{ij}][\sigma_{jk}] = [B_{ik}] \quad , \tag{31.a}$$

where in accordance with Equation (29) the coefficients are

$$A_{ij} = 1, \text{ for } (i = j);\ i, j = 1, 2, 3 \ldots N \quad ,$$

$$A_{ij} = \frac{S_j}{2\pi r_{ij}^3}[(XC_i - XC_j)n_{x_i} + (YC_i - YC_j)n_{y_i} + (ZC_i - ZC_j)n_{z_i}] \quad ,$$

$$\text{for } (i \neq j);\ i, j = 1, 2, 3 \ldots N \quad , \tag{31.b}$$

and

$$B_{ik} = -2[(u_k + u_{w_{i_k}})n_{x_i} + (v_k + v_{w_{i_k}})n_{y_i} + (w_k + w_{w_{i_k}})n_{z_i}]$$

$$+ \begin{cases} 0, \text{ solid boundary} \\ -2F_i, \text{ relaxed boundary} \end{cases} ,$$

$$\text{for } i = 1, 2, 3 \ldots N; \text{ and } k = 1, 2, 3 \ldots M \quad , \tag{31.c}$$

where F_i is a positive value if it is inflow velocity and negative if outflow velocity with r_{ij} given by Equation (15); u_k, v_k, and w_k are direct functions of α_k and β_k by Equations (7) and (8). Also, $u_{w_{i_k}}$, $v_{w_{i_k}}$, and $w_{w_{i_k}}$ are the wing-induced components at panel i for the wing operating at C_{L_k} as per Section 2.5 of this chapter.

Equation set (31) represents the augmented set of N simultaneous equations to be solved for M different sets of N source strengths, σ. With all σ values known, the flow around the body will have been solved for each of the M input body orientations.

2.6.2 Special case of a symmetric body panel network

In the case of a symmetrically paneled body, only the N/2 panels on the left (-y) side of the configuration need be considered. In this case only a half-size system of N/2 simultaneous equations must be solved. Analagous to Equation set (31), this half-size system of boundary condition equations is written by substituting Equations (5), (6), (20), (23), and (25) into Equation (28). However, summations are only made to N/2 rather than to N. The half-size system in matrix form is

$$[A_{ij}][\sigma_{jk}] = [B_{ik}] \quad , \tag{32.a}$$

where

$$A_{ij} = [1 + \frac{S_i YC_i n_{y_i}}{8\pi |YC_i|^3}] \quad , \text{ for } (i = j);\ i = 1, 2, 3 \ldots N/2 \ , \tag{32.b}$$

$$A_{ij} = \frac{S_j}{2\pi}\{[\frac{1}{r_{ij}}]^3[(XC_i - XC_j)n_{x_i} + (YC_i - YC_j)n_{y_i} + (ZC_i - ZC_j)n_{z_i}]$$

$$+ [\frac{1}{r_{ij_{image}}}]^3[(XC_i - XC_j)n_{x_i} + (YC_i + YC_j)n_{y_i} + (ZC_i - ZC_j)n_{z_i}]\} \quad ,$$

$$\text{for } (i \neq j);\ i, j = 1, 2, 3 \ldots N/2 \quad , \tag{32.c}$$

and

$$B_{ik} = -2[(u_k + u_{w_{i_k}})n_{x_i} + (v_k + v_{w_{i_k}})n_{y_i} + (w_k + w_{w_{i_k}})n_{z_i}]$$

$$+ \begin{cases} 0, \text{ solid boundary} \\ -2F_i, \text{ relaxed boundary} \end{cases} , \text{ for } \begin{matrix} i = 1, 2, 3 \ldots N/2 \text{ and} \\ k = 1, 2, 3 \ldots M \end{matrix} \ , \tag{32.d}$$

where index i represents body panels on the left side of the configuration and where F_i is a positive value if it is inflow velocity and negative if outflow velocity. Also, r_{ij} is given by Equation (15) and $r_{ij_{image}}$ is given by Equation (21). Components u_k, v_k, and w_k are functions of α_k and β_k by Equations (7) and (8). Also, $u_{w_{i_k}}$, $v_{w_{i_k}}$, and $w_{w_{i_k}}$ are wing-induced components at left side panel i due to a wing operating at C_{L_k} as per Section 2.5 of this chapter.

Equation set (32) is solved for M sets of unknown source strengths, σ, on each of the N/2 left side body panels. The solutions on the right side image panels match those on the left side. The flow around the body will then have been solved for each of the M input body orientations.

2.7 Body Surface Flow Field Velocity and Pressure

Having solved the system of Equations (31) or (32) for the M sets of unknown panel source strengths, σ, the resulting flow velocity and pressure at each of the N panel control points is calculated using expressions developed below.

In the following, assume only one set of N solutions, σ, has been solved. That is, set M equal to one in the equation sets (31) and (32).

At the ith panel control point (XC_i, YC_i, ZC_i), the resultant flow velocity vector, $\vec{V}_{b_i}$, is denoted by its body-fixed Cartesian axis components as

$$\vec{V}_{b_i} = u_{b_i}\,\vec{i} + v_{b_i}\,\vec{j} + w_{b_i}\,\vec{k} \quad . \tag{33}$$

This resultant velocity is the sum of the free stream, wing-induced, panel self-induced, and remote panel-induced velocities;

$$\vec{V}_{b_i} = \vec{V} + \vec{V}_{w_i} + \vec{V}_{ii} + \sum_{\substack{j=1 \\ (j\neq i)}}^{N} \vec{V}_{ij} \quad . \tag{34}$$

The self-induced velocity, $\vec{V}_{ii}$, is always directed normal to panel i. Thus, its Cartesian components are the scalar multiples of the unit normal vector at panel i. Using Equations (5) and (10), $\vec{V}_{ii}$ is given in vector notation by

$$\vec{V}_{ii} = \frac{\sigma_i}{2}\,n_{x_i}\,\vec{i} + \frac{\sigma_i}{2}\,n_{y_i}\,\vec{j} + \frac{\sigma_i}{2}\,n_{z_i}\,\vec{k} \quad . \tag{35}$$

Substitute Equations (6), (25), (35), and (17) for $\vec{V}$, $\vec{V}_{w_i}$, $\vec{V}_{ii}$, and $\vec{V}_{ij}$, respectively, in Equation (34) for the resultant velocity $\vec{V}_{b_i}$ at panel i. Then according to Equation (33) the Cartesian components of $\vec{V}_{b_i}$ on the ith panel are

$$u_{b_i} = (u + u_{w_i}) + \frac{\sigma_i}{2}\,n_{x_i} + \sum_{\substack{j=1 \\ (j\neq i)}}^{N} \frac{S_j\sigma_j}{4\pi}\left[\frac{XC_i - XC_j}{r_{ij}^{3}}\right] \quad , \tag{36.a}$$

$$v_{b_i} = (v + v_{w_i}) + \frac{\sigma_i}{2} n_{y_i} + \sum_{\substack{j=1 \\ (j \neq i)}}^{N} \frac{S_j \sigma_j}{4\pi} \left[\frac{YC_i - YC_j}{r_{ij}^3} \right] , \tag{36.b}$$

and

$$w_{b_i} = (w + w_{w_i}) + \frac{\sigma_i}{2} n_{z_i} + \sum_{\substack{j=1 \\ (j \neq i)}}^{N} \frac{S_j \sigma_j}{4\pi} \left[\frac{ZC_i - ZC_j}{r_{ij}^3} \right] , \tag{36.c}$$

where u, v, and w are given by Equations (7) and (8) and where r_{ij} is given by Equation (15).

The magnitude of the total surface velocity at panel i is

$$|\vec{V}_{b_i}| = [u_{b_i}^2 + v_{b_i}^2 + w_{b_i}^2]^{1/2} . \tag{37}$$

Lastly, the pressure coefficient at the control point of panel i is given, using Equation (37) and free stream velocity, V, by

$$C_{p_i} = 1.0 - \left[\frac{|\vec{V}_{b_i}|}{V} \right]^2 . \tag{38}$$

Use of Equations (36), (37), and (38) on each of the N body panels completely defines the surface potential flow for a particular combination of body angle of attack, α, sideslip, β, and wing C_L.

2.8 Flow Velocities and Flow Angles at the Propeller Plane

2.8.1 Cartesian velocity components at a point on the propeller plane

The propeller plane of radius R is centered at a point (X_{hub}, Y_{hub}, Z_{hub}) relative to the body-fixed coordinate system. In general, the propeller plane is skewed with an angle of attack, α_p, and sideslip, β_p, relative to the body-fixed axes, see Figure 7. Although the propeller itself is not present, a right-hand sense of rotation in the propeller plane is assumed for velocity sign convention.

As indicated in Figure 7, a point P on the propeller plane has the specified radial and azimuthal position (r, ψ) in a propeller plane cylindrical axis system. The cylindrical coordinates (r, ψ) of point P are transformed to corresponding body-fixed Cartesian axis coordinates (X_p, Y_p, Z_p) using the following expressions which are fully derived in Appendix D:

$$X_p = -r[\sin\psi \cos\alpha_p \sin\eta_p + \cos\psi \sin\alpha_p] + X_{hub} \quad , \tag{39.a}$$

$$Y_p = [r \sin\psi \cos\eta_p] + Y_{hub} \quad , \tag{39.b}$$

and

$$Z_p = r[\sin\psi \sin\alpha_p \sin\eta_p - \cos\psi \cos\alpha_p] + Z_{hub} \quad , \tag{39.c}$$

where Euler angle, η_p, is given by

$$\eta_p = \tan^{-1}[\tan\beta_p \cos\alpha_p] \quad . \tag{40}$$

The total flow velocity vector, $\vec{V}_p$, at point (X_p, Y_p, Z_p) is denoted by its body-fixed Cartesian components as

$$\vec{V}_p = u_p \vec{i} + v_p \vec{j} + w_p \vec{k} \quad . \tag{41}$$

$\vec{V}_p$ is the vector sum of the free stream, wing-induced, and panel source-induced velocities, $\vec{V}_{pj}$, at the point P on the propeller plane;

$$\vec{V}_p = \vec{V} + \vec{V}_{w_p} + \sum_{j=1}^{N} \vec{V}_{pj} \quad . \tag{42}$$

Equations (6), (25), and (17) may be substituted for $\vec{V}$, $\vec{V}_{w_p}$, and $\vec{V}_{pj}$, respectively, in Equation (42) if all i subscripts are replaced by p and if point (XC_i, YC_i, ZC_i) is replaced by (X_p, Y_p, Z_p). After making the aforementioned substitutions into Equation (42), the Cartesian components of the net flow velocity at point P on the propeller plane shown in Figure 7 are given as follows:

$$u_p = u + u_{w_p} + \sum_{j=1}^{N} \frac{S_j \sigma_j}{4\pi} \left[\frac{X_p - XC_j}{r_{pj}^3} \right] , \tag{43.a}$$

$$v_p = v + v_{w_p} + \sum_{j=1}^{N} \frac{S_j \sigma_j}{4\pi} \left[\frac{Y_p - YC_j}{r_{pj}^3} \right] , \tag{43.b}$$

and

$$w_p = w + w_{w_p} + \sum_{j=1}^{N} \frac{S_j \sigma_j}{4\pi} \left[\frac{Z_p - ZC_j}{r_{pj}^3} \right] , \tag{43.c}$$

where u, v, and w are given by Equations (7) and (8), and

$$r_{pj} = [(X_p - XC_j)^2 + (Y_p - YC_j)^2 + (Z_p - ZC_j)^2]^{1/2} . \tag{43.d}$$

2.8.2 Axial, radial, and tangential velocities at a point on the propeller plane

At point P on the propeller plane, the Cartesian velocity components u_p, v_p, and w_p of Equations (43) may, by the following transformations, be converted into axial, radial, and tangential components, v_{a_p}, v_{r_p}, and v_{t_p}, respectively:

$$v_{a_p} = [\cos \alpha_p \cos \eta_p]u_p + [\sin \eta_p]v_p - [\sin \alpha_p \cos \eta_p]w_p , \tag{44.a}$$

$$v_{r_p} = -[\sin \alpha_p \cos \psi + \cos \alpha_p \sin \eta_p \sin\psi]u_p + [\cos \eta_p \sin \psi]v_p + [\sin \alpha_p \sin \eta_p \sin \psi - \cos \alpha_p \cos \psi]w_p , \tag{44.b}$$

and

$$v_{t_p} = [\sin \alpha_p \sin \psi - \cos \alpha_p \sin \eta_p \cos \psi]u_p + [\cos \eta_p \cos \psi]v_p + [\cos \alpha_p \sin \psi + \sin \alpha_p \sin \eta_p \cos \psi]w_p , \tag{44.c}$$

where η_p is given by Equation (40), and ψ is the azimuth position angle of point P.

As indicated in Figure 7, v_{a_p} is directed positive in the thrust direction perpendicular to the propeller plane. v_{r_p} is directed positive

radially outward in the propeller plane. v_{t_p} is directed in-plane perpendicular to v_{r_p} and positive when directed clockwise around the propeller plane hub. Appendix D gives the complete derivation of transformation Equations (44).

2.8.3 Local flow angles at a point on the propeller plane

The velocity components at point P on the propeller plane may be expressed in terms of four flow angles. These are angles of upwash, sidewash, outflow, and rotational flow denoted by ε, τ, λ, and θ, respectively, and are functions of u_p, v_p, and w_p given by

$$\varepsilon = \tan^{-1}\left[\frac{w_p}{u_p}\right] \tag{45}$$

and

$$\tau = \tan^{-1}\left[\frac{-v_p}{u_p}\right] \tag{46}$$

such that ε is positive when the flow is directed locally upward toward the negative z axis, and τ is positive when the flow is directly locally to the right toward the positive y axis.

The angles of outflow and rotational flow at point P are measured with respect to the propeller plane and were first defined by Roberts and Yaggy (15). These angles are functions of v_{a_p}, v_{r_p}, and v_{t_p} given, respectively, by

$$\lambda = \tan^{-1}\left[\frac{v_{r_p}}{-v_{a_p}}\right] \tag{47}$$

and

$$\theta = \tan^{-1}\left[\frac{v_{t_p}}{-v_{a_p}}\right] \quad . \tag{48}$$

As shown in Figure 7, angle of outflow, λ, lies in a plane containing the thrust axis and radius line to the point P. λ is positive when the local flow has a component directed radially outward. Angle of rotational flow, θ, indicates the apparent tangential or rotational sense of the local flow at the propeller plane. θ is measured from a line parallel to the thrust axis and lies in the plane perpendicular to the radius line to the point. That is, θ is an angle which would appear in the propeller blade section diagram at that point. For sign convention, a right-hand propeller rotation is assumed, so a positive value of θ corresponds to an effective decrease in local blade section angle of attack from that encountered by the propeller operating freely in a uniform flow. A negative value of θ corresponds to an increase in the local section angle of attack. Figure 8 illustrates the effect of θ on the angle of attack of a blade section at radius, r, on a propeller rotating at an angular velocity of ω.

2.9 Three-Dimensional Flow Computer Program Description

A computer program has been written which solves the subsonic potential flow about any arbitrary three-dimensional body-wing combination using the theory presented in this chapter. The surface geometry of the body, or group of bodies, must be provided in an organized set of discrete points. Geometry of the wing, if present, as well as the location and orientation of a propeller must be specified. Then for each specified combination of body angle of attack, sideslip, and wing C_L, the program calculates the velocity and pressure coefficient at points on the body surface. Lastly, the program calculates the flow velocities and flow angles at each point in a mesh of points on the plane of the propeller.

Figure 9 presents the organizational structure of the program. It consists of fourteen subroutines each handling a major portion of the problem and linked by a main calling program. The program is coded in Fortran for use on the IBM 370/OS 360 computer system at The Pennsylvania State University.

The program has been dimensioned to various sizes, the largest of which is capable of handling N = 2596 body panels and M = 6 combinations of α, β, and C_L.

Several features have been incorporated. First is the symmetric input option feature (NSYMET = 0) which requires the input of only the left side of a symmetric body geometry. Image geometry is computed automatically and the program must solve a problem only half as large as would occur with a nonsymmetric configuration.

Second, due to the massive amounts of input surface geometry required, a geometry check run feature (NCALC = 1) has been included. This feature is used when a new body geometry is being tried. The program generates and prints the panel geometry network which allows the user to check for errors in paneling data and allows the user to identify the sequence numbers of panels to be characterized as inflow and outflow panels. Flow calculations, which consume most of the computer time, are not made during a geometry check run thus reducing the amount of computing time which would have been wasted if flow calculations had been attempted with geometry data containing errors.

Third, a feature (NPUNCH = 1) allows punched output to be produced. This feature, if selected, produces a punched card deck containing identifying information and propeller plane flow field data including axial and tangential velocity components at each point on the propeller

plane. These output cards are formatted for direct application as input data cards in the propeller performance analysis program of Aljabri (32).

Because of the vast amounts of storage required by the program, it is necessary to store the system of boundary condition equations, Equations (31) or (32), on an auxiliary sequential scratch disk file. A second auxiliary file is also needed for printing certain output data. As a result, the system of equations cannot be solved by matrix inversion or other direct methods, but instead requires the use of iterative methods. The method of Gauss-Siedel iteration is used in this program.

Additionally, because of the use of auxiliary files, slower program execution occurs. Thus, it has been found useful to compile the program into a highly efficient machine language deck using the Fortran H, optimization level = 2, compiler available at The Pennsylvania State University. Actual jobs are performed by running this compiled machine language program. Execution time conserved by this technique can often mean the difference between success and failure in completion of the flow solution.

The purpose of each subroutine is given very briefly below.

INPUT reads and stores all input data. It also checks for certain input errors.

VCOMP calculates the set of free stream velocity components using Equations (7) and (8) for each input set of α and β.

EULER calculates angles η and η_p using Equations (8) and (40), respectively.

WGEOM generates the wing horseshoe vortex geometry based on input wing geometry if a wing is present in the configuration.

PANEL generates the body panel network. It calculates all panel areas, control points, and unit normal vectors using the methods and

formulas given in Appendix A. It assigns a sequence number to each panel and counts the total number of panels. PANEL also generates image panels and establishes a system for matching "real" and "image" panels on symmetric configurations.

COFSYM generates the matrices of coefficients, [A] and [B], for the half-size system of boundary condition equations, Equation set (32), used in the case of body symmetry.

SOLSYM solves Equation set (32) for M sets of N/2 unknown panel source strengths using Gauss-Siedel iteration.

COEFIC generates the matrices of coefficients, [A] and [B], for the full-size system of boundary condition equations, Equation set (31), used when the configuration is not symmetrically paneled.

SOLVE solves Equation set (31) for M sets of N unknown panel source strengths using Gauss-Siedel iteration.

WINGV calculates the velocity components induced at a point by the wing horseshoe vortex. It uses subroutine VORTEX, below.

VORTEX calculates the magnitude and components of velocity induced at a point by a straight vortex filament. Formulas given in Appendix C are used.

VELOCI calculates and prints the surface flow velocity and pressure coefficient at each panel control point using Equations (36), (37), and (38).

VPROPS calculates the propeller plane flow field. It first calculates and prints u_p, v_p, and w_p using Equation set (43) at each point on the propeller plane. Second, it calculates and prints v_{a_p}, v_{r_p}, and v_{t_p} using Equation set (44) at each point. Also, it calculates, using subroutine ANGLES, and prints flow angles ε, τ, λ, and θ using Equations

(45) through (48) at each point. Third, if desired, it punches values v_{a_p}, v_{t_p}, and other data on output cards for each point.

ANGLES calculates flow angles ε, τ, λ, and θ for each point on the propeller plane using Equations (45) through (48).

A user's manual, Jumper (33), has been written which gives a complete description of program input and output. Also, the manual presents all necessary operating instructions and contains a complete program listing.

However, the user's manual contains an older version of subroutine VORTEX which incorporates a quantity called h_{min} and which does not use the computational formulas given in Appendix C.

Subroutine VORTEX listed in Jumper (33) should be modified by deleting the expressions and logic pertaining to h_{min} and then reorganizing the expressions to conform with the equations given in Appendix C.

An errata sheet to the user's manual has been written which describes all changes necessary to make expressions in subroutine VORTEX, originally printed in the manual, conform with the formulas found in Appendix C of this thesis.

Chapter 3

TEST CASES OF THE FLOW ABOUT A SPHERE AND THE FLOW ABOUT A SIMPLE FUSELAGE SHAPE

3.1 Exact Solution for the Potential Flow About a Sphere

To ensure the three-dimensional potential flow computer program functions properly, the test case of the flow about a sphere has been used for comparison, because the exact solution for this flow exists.

Figure 10 shows the cross sectional view of a sphere of radius, a, in a uniform velocity field, V. In terms of the polar coordinates, the velocity potential for this flow may be derived by mathematical solution of the Laplace equation. Also, the potential is found in Milne-Thomson (34) and is given by

$$\phi_s = V[\bar{r} + \frac{a^3}{2\bar{r}^2}]\cos\gamma \quad . \tag{49}$$

On the sphere surface, only the tangential velocity component exists and is found, using Equation (49), to be

$$v_\gamma = -[\frac{1}{\bar{r}}\frac{\partial\phi_s}{\partial\gamma}]_{\text{at } \bar{r}=a} = \frac{3}{2} V \sin\gamma \quad . \tag{50}$$

Then, using Equation (50) in the definition of pressure coefficient, Equation (38), the sphere surface pressure coefficient distribution is

$$C_p = 1 - \frac{9}{4}[\sin\gamma]^2 \quad . \tag{51}$$

The velocity potential may be rewritten in terms of the body-fixed Cartesian axes shown in Figure 10. The potential becomes

$$\phi_s = V[1 + \frac{a^3}{2[(x+a)^2 + z^2]^{3/2}}](x + a) \quad . \tag{52}$$

To get the Cartesian velocity components anywhere on the x-z plane in Figure 10, the negative gradient of Equation (52) is taken. These x, y, and z components of velocity are given, respectively, by

$$u_s = \left[\frac{2a^3(x + a)^2 - a^3z^2}{2[(x + a)^2 + z^2]^{5/2}} - 1\right]V \quad , \tag{53.a}$$

$$v_s = 0 \quad , \tag{53.b}$$

and

$$w_s = \frac{3}{2}\left[\frac{a^3(x + a)z}{[(x + a)^2 + z^2]^{5/2}}\right]V \quad . \tag{53.c}$$

3.2 Sphere Surface Pressure Prediction Compared With Exact Solution

A sphere was modeled using ten equally spaced cross sections to generate 120 panels, and the flow was solved using the three-dimensional flow program. Figure 11 compares the predicted and exact, Equation (51), pressure distributions. Agreement is excellent over the entire surface with only a minute deviation near $\gamma = 90$ degrees. This result verifies that the computer program functions properly.

3.3 Flow Predictions at a Propeller Plane Upstream of a Sphere

In addition to surface flow predictions, the flow velocities and angles were predicted at untilted propeller planes centered in front of the sphere. Results were predicted for two propeller plane-sphere spacings. Figure 12 gives the axial velocity distribution along the upper centerline of the propeller plane for both spacings tested and compares the results with the exact solutions, Equation (53.a). Figure 13 presents the distribution of vertical velocity compared with the exact solution of Equation (53.c). Additionally, this figure combines

the axial and vertical velocity distributions by showing the corresponding upwash angle distributions.

The results in both Figures 12 and 13 show excellent agreement between predictions and exact theory for both spacings at radial positions beyond 0.6 sphere radii. At positions inside this radius, the predictions deviate from the exact results. The deviation in upwash angle is the most pronounced. It is seen that as the propeller plane-sphere spacing increases, the computer predictions improve along the entire radius.

At the inner regions of the propeller plane, the sphere surface is comparatively close to the plane, and the flow is dominated by the influence of the nearby front ring of body panels. To points at the inner radii of the propeller plane, which are near the body surface, the body panel network appears rather coarse and does not present as accurate a representation of the true body surface shape as is presented to points more distant from the body. This results in deviations of the predicted flow from the exact solution, at the inner radii of the propeller plane. However, at points at larger radii on the propeller plane, local panel domination diminishes, and the overall panel network more closely resembles a sphere. Thus, the computer predictions improve at points farther from the body surface.

Thus, it appears that in using the computer program for propeller plane flow predictions, the flow is most sensitive to the body surfaces nearest to the propeller plane, and care must be taken to panel these surface regions densely and accurately.

3.4 Flow Predictions Upstream of a Simple Fuselage Shape and Effects of Ignoring Remote Body Surfaces

Because the three-dimensional flow computer program requires large amounts of tedious body panel geometry input, it is desirable to reduce as much as possible the amount of this input without sacrificing accuracy in the propeller plane flow predictions.

To examine the effect of neglecting remote regions of the body in predicting the flow at the propeller plane, a simplistic fuselage shape was used. This fuselage profile is shown in exact scale proportions in Figure 14. The cowl and tailcone have circular cross sections, while the cabin region has "pear-shaped" cross sections. A propeller plane is untilted and centered in front of the cowl with a spacing of 7.8 percent of the cowl length, f.

Figure 14 compares axial velocity distributions at the propeller plane predicted by the computer program with the complete fuselage modeled and with cabin and tail removed. As might be expected, with the cabin and tail removed there is less flow obstruction, and a slight increase in the magnitude of axial velocity occurs. The velocity distribution with the isolated cowling varies as much as 1.6 percent from the distribution predicted with the complete fuselage. This change in axial velocity considered alone might seem unacceptable. However, as the axial velocity changes so does the radial velocity component. Thus, as Figure 15 shows, the flow angularity, presented in terms of upwash angle, at the propeller plane changes only slightly by removal of the aft portions of the fuselage. Flow angularity shows the combined effect of all velocity components and can be considered a more useful parameter for describing the flow field as it would influence a propeller.

Results in Figure 15 thus indicate that in modeling a fuselage for propeller plane flow predictions, the body regions remote from the propeller, such as the tail and cabin, can be ignored without seriously affecting flow predictions.

Paneling only the cowling of a typical single-engine aircraft fuselage should be sufficiently accurate for making flow predictions at the propeller plane. This will greatly simplify computer program input and decrease run time and cost.

The effect of neglecting aft portions of a fuselage of an actual aircraft will be shown later in Chapter 5.

Chapter 4

MEASURED AND PREDICTED FLOW FIELD RESULTS AT THE LEFT PROPELLER PLANE OF A TWIN-ENGINE AIRCRAFT

4.1 Aircraft Geometry, Body Paneling, and Operating Conditions

Roberts and Yaggy (15) conducted extensive wind tunnel tests in which the flow velocities and flow angles were measured at the left propeller plane (propeller removed) of the twin-engine aircraft shown in Figure 16. Because the experimental data was presented in detail, flow predictions for this aircraft were made using the three-dimensional potential flow computer program. Comparisons of computer predictions with the published experimental results were conducted to further check the accuracy of the computer program.

Figure 16 shows a three-view drawing of the aircraft including overall dimensions and the orientation of the left propeller plane. Figures 17a and 17b present in detail the cross section geometry of the fuselage and nacelle surfaces located foreward of the wing leading edge.

To generate the body paneling input data required by the computer program, the data in Figures 17a and 17b was used to obtain the paneling accuracy needed at the foreward body surfaces, which are in proximity to the propeller plane. At regions aft of the wing leading edge, which are more distant from the propeller plane, the surface geometry at a given longitudinal position was estimated by taking the cross section shapes shown in Figures 17a and 17b and scaling them to the dimensions indicated by the views in Figure 16. This produced a body paneling network of sufficient detail in the aft regions.

Initially, the computer program was run using the wing vortex model and body paneling over the entire surface of the fuselage and nacelles. Unfortunately, with the body surfaces completely paneled, the program

failed to converge. Apparently, the matrix of boundary condition equations generated by the complete body panel network was not diagonally dominant or for some other reason was not solvable by the Gauss-Siedel iterative method employed by the program. Thus, it was necessary to reduce the complexity of the paneling network by excluding certain portions of the aircraft geometry.

Finally, after several trails, a simplified body panel network was devised which gave successful computer solution convergence. The wing vortex geometry was modeled as before. However, the right nacelle and aft portion of the fuselage were eliminated from the paneling network. Only the left nacelle and the fuselage nose, the crosshatched region in Figure 16, remained paneled. As previous results in Chapter 3 indicate, ignoring the right nacelle and aft fuselage, which are remote from the left propeller, should not significantly diminish the accuracy of the flow field predictions at the left propeller plane. The simplified left nacelle-fuselage nose paneling network consisted of 424 panels and required the use of the nonsymmetric input option of the program.

To match the aircraft flight conditions of Roberts and Yaggy (15), the computer model required a simulation of the engine cooling air flow through the left nacelle. All panels covering the nacelle inlet face were assigned a known constant inflow velocity, F, normal to and passing through the panels thus simulating inflow of engine cooling air. However, no cooling air outflow panels were specified. To obey the law of continuity, it was assumed that the cooling air was exhausted infinitely far downstream or at the extreme aft location on the nacelle such that the exhaust air influence on the flow field at the propeller plane would be negligible. Based on this assumption, the presence of exhaust air could be ignored; thus, it was not simulated.

Table 1 summarizes the various flight conditions modeled using the computer program. Flight conditions 1, 2, and 3 on the table were also tested by Roberts and Yaggy (15). Flight conditions 4, 5, and 6 used a value of nacelle inlet inflow velocity which was not wind tunnel tested, and these conditions were run on the computer to investigate the effects of the inflow velocity parameter on the flow at the propeller plane.

Table 1 also lists the geometric characteristics which remained constant for all flight conditions, including sideslip angle β, propeller plane reference radius R, and propeller plane orientation angles, α_p and β_p.

The installed propeller sideslip angle, β_p, is zero for this aircraft. However, there existed a confusion about the value of the installed angle of attack, α_p, of the propeller plane. Roberts and Yaggy (15) conducted their experiments in the belief the propeller plane was not tilted downward with respect to the fuselage; that is, α_p was believed to be zero. All of the experimental data was presented as a function of α_G, the geometric angle of attack of the propeller plane from the free stream, which under the assumption of zero α_p would also equal the aircraft angle of attack. However, Yaggy (17) later reported that following test publications by Roberts and himself (15) it was found the propeller plane had actually been oriented with a downward tilt of two degrees ($\alpha_p = -2$ degrees) during the testing. Discovery of this fact did not alter the measured results but produced an error in the presentation of the data in Roberts and Yaggy (15). In the published test results, data presented for a specified propeller plane angle of attack of α_G, believed to equal the aircraft angle of attack α, are actually data corresponding to a propeller plane angle of attack of α_G but at an aircraft angle of attack equal to $\alpha_G + 2$ degrees. Similarly the published C_L values tested cor-

respond to the aircraft angle of attack of $\alpha_G + 2$ degrees. Therefore, as Table 1 indicates, to model a wind tunnel test performed at a published propeller plane angle of attack of α_G, it was necessary to perform the corresponding computer run using an input aircraft angle of attack of $\alpha = \alpha_G + 2.0$ degrees.

4.2 Comparisons of Computer-Predicted and Experimentally Measured Flow Quantities at the Left Propeller Plane

Figure 18 presents azimuthal distributions of axial velocity at the 75 percent radius position for two extremes of body angle of attack. For the angle of attack of two degrees, there is fair agreement between computations and experiment. Agreement is much better for the 12 degree angle of attack case particularly at azimuths near the vertical centerline of the propeller plane. For both angles of attack, the computed distribution shapes agree well with the measured shapes.

Figure 19 presents azimuthal distributions of flow angularity at the 75 percent radius position corresponding to the velocities in Figure 18. Additionally, Figure 19 contains a set of curves for a midrange angle of attack of six degrees. Again the agreement between calculated and measured distributions is good and improves with increasing angle of attack. The ability of the program to accurately predict the flow for higher angles of attack is good in that propeller vibration, which is more severe at higher angles of attack, may be more accurately calculated using the predicted flow field. Generally, in Figure 19, the flow angularity predictions differ by approximately only one degree from the measured values, and at most only a three degree difference is seen for an angle of attack of two degrees.

As explained by Roberts and Yaggy (15), the extremes in flow angularity occur near the horizontal centerline (near the 90 and 270 degree azimuths) of the propeller plane. The flow field near these azimuths produces the peak vibratory loading on the propeller blades. Additionally, along the inboard horizontal centerline of the left propeller plane, increased flow angularity is encountered due to the increased wing upwash in that region as well as due to the influence of the fuselage nose near the inboard tip of the propeller plane. Thus, the ability to predict the flow along the horizontal centerline is of value for anticipating vibration problems of propellers operating in the flow field.

Radial distributions of angle of rotational flow along the inboard horizontal centerline (90 degree azimuth) of the left propeller plane are shown in Figure 20. Over the outer radii beyond 0.25R, where a propeller blade would be more heavily loaded, computed flow angularity distributions agree well with the measured distributions particularly at the lower angles of attack. Increased flow angularity induced near the tip radius by the fuselage nose may be seen on this figure and has been accurately predicted for the angle of attack of 12 degrees. However, computed and measured distributions diverge at radii less than the nacelle inlet radius in Figure 20. Fortunately, any weakness in prediction ability at these inner radii is not extremely bothersome, because a propeller blade is lightly or negligibly loaded at these radii. Propeller performance or loading calculations for blades operating in the predicted flow field of Figure 20 should not be seriously affected by some inaccuracy in flow field predictions at the inner radii. Disagreement between measured and computed flow angularity in the propeller plane hub region may be due to some shortcomings in the inlet inflow velocity modeling

technique used by the computer program. Inlet inflow velocity effects are examined later in this chapter.

Figure 21 shows the axial velocity distributions along the inboard horizontal centerline for angles of attack of two and 12 degrees corresponding to the flow angles of Figure 20. The predicted and measured velocities agree well to approximately the 30 percent radius position. Beyond the 30 percent radius position, the computer program overpredicts the axial velocity. The computer program modeled the wing vortex system, but the actual wing surface geometry was not paneled. Thus, wing thickness effects were not introduced into the calculations. Any retardation of the axial velocity along the horizontal centerline which may exist due to wing thickness blockage effects would not be reflected in the computer predictions. This may account for the overpredictions of axial velocity in Figure 21.

It is apparent from Figures 18 through 21 that the potential flow computer program satisfactorily calculated the flow field at the propeller plane of the twin-engine aircraft despite the necessary deletion of a large portion of the airframe geometry from the computer model.

4.3 Nacelle Inlet Inflow Velocity Effects on the Flow Field at the Left Propeller Plane

Additional computer predictions at the twin-engine aircraft propeller plane were made in which the nacelle inlet velocity ratio, F/V, was changed from a value of 0.29, used in the wind tunnel tests, to a value of 0.10. Figure 22 demonstrates the effects of varying the inflow velocity ratio. Plotted are computed radial distributions of angle of rotational flow along the inboard horizontal centerline (90 degree azimuth) of the left propeller plane. As the figure shows, changing F/V produces large changes in the flow field only at the hub region directly upstream

of the nacelle inlet. However, the flow field is nearly unaltered at radii greater than the inlet radius. These results match the experimental findings of Roberts and Yaggy (15).

That changing of the value of F/V produces large flow field changes only in the hub region, where propeller blade loadings are minimal, is fortunate. This result indicates that the actual choice of F/V value used in the computer simulation of inlet inflow should not be critical in regard to its ultimate effect on calculated blade loadings, because changing F/V will provide major flow prediction changes only near the hub such that changes in loading and vibration of a blade operating in the flow field will be slight.

4.4 Geometry-Induced Contributions Versus Propeller Plane Inclination-Induced Contributions to the Flow Field at the Left Propeller Plane

The flow field at the propeller plane is composed of two contributions. These are the contribution due to pure propeller plane inclination and that due to the influence of the airframe. It is of interest to examine these two contributions to gain insights into the relative signifigance of each.

At the plane of an isolated propeller inclined to an angle of attack, α_G, from the free stream, the free stream velocity contributes azimuthally varying radial and tangential velocity components as shown in Figures 23a and 23b. An expression for the azimuthal variation of flow angularity, in terms of angle of rotational flow θ, at the isolated inclined propeller plane may be obtained by inserting the velocity components of Figures 23a and 23b into Equation (48). The resulting expression applicable to an isolated inclined propeller plane is

$$\theta = \tan^{-1}(-\tan \alpha_G \sin \psi) \quad . \tag{54}$$

Flow field predictions produced by the computer program contain both the airframe-induced and propeller plane inclination-induced contributions. By comparing the flow angularity distribution at an isolated inclined propeller plane, Equation (54), with the corresponding distribution obtained from the computer program predictions incorporating both the inclination and airframe effects, the airframe-induced flow contribution contained in the computer results is highlighted.

Figure 24 presents such a comparison applied to the left propeller plane of the twin-engine airplane. In this figure the azimuthal variations in angle of rotational flow at the 75 percent radial station are presented for both high and low aircraft angles of attack. As the figure indicates, for an aircraft angle of attack of two degrees, the propeller plane inclination, α_G, is zero. Thus, the isolated propeller plane, in the absence of airframe effects, experiences no flow angularity. The corresponding curve produced by the computer program shows that the introduction of the wing-fuselage nose-left nacelle geometry at two degrees of angle of attack produces a nonsymmetric distribution of flow angularity with a peak magnitude of nearly two degrees occurring at the 90 degree azimuth position.

For an aircraft angle of attack of 12 degrees, the isolated propeller plane inclination is ten degrees. With a ten degree inclination, flow angularity for the isolated propeller plane, as shown in Figure 24, is symmetrically distributed in a periodic fashion about the azimuth with a maximum flow angularity magnitude of ten degrees at the horizontal centerline azimuths of 90 and 270 degrees. The corresponding curve calculated by the computer program indicates that the addition of the airframe geometry at an angle of attack of 12 degrees produces greater and more dis-

torted flow angularity. Geometry influences have shifted the flow distribution curve to the left. Increased upwash introduced by the airframe geometry is reflected by the greater amplitudes of θ in the computer program prediction. Also, the airframe induces more upwash over the inboard half of the left propeller plane than over the outboard half. This is indicated by greater θ amplitudes in the vicinity of the 90 degree azimuth than in the vicinity of the 270 degree azimuth.

Figure 25, like Figure 24, also compares the effects of geometry influences and propeller plane inclination influences. In this figure, radial distributions of angle of rotational flow along the inboard horizontal centerline, 90 degree azimuth, on the left propeller plane are plotted. Because the isolated inclined propeller plane experiences no radial variation in the flow field, as indicated by Equation (54), the flow angularity due to inclination is a constant for each angle of attack in Figure 25. For an aircraft angle of attack of two degrees, the propeller plane inclination with respect to the free stream is zero, and the isolated propeller plane experiences no flow angularity, as indicated by the uppermost plot in Figure 25. As the corresponding computer-predicted plot shows, the aircraft geometry at a two degree angle of attack induces upwash, particularly strong near the hub due to the nacelle, which produces peak flow angularity magnitudes of nearly 5.5 degrees.

As shown in Figure 25, for an aircraft angle of attack of 12 degrees, the isolated propeller plane inclination is ten degrees. Thus, a blade in this isolated propeller plane would experience a ten degree flow angularity at the horizontal centerline equivalent to a uniform blade pitch increase of ten degrees. The corresponding computer program predictions for a 12 degree angle of attack indicate a large increase in upwash due

to the presence of the airframe geometry. Increased upwash corresponds to negative values of θ in Figure 25. The nacelle is seen to induce the greatest upwash in the hub region, while a less but nearly constant flow angularity due mostly to wing-induced upwash is seen at the midrange radii. Finally, increased flow angularity is induced by the fuselage nose near the tip radius in the lowermost plot in Figure 25.

As Figures 24 and 25 demonstrate, the influence of the airframe geometry on the flow at the propeller plane is very evident. The inclusion of geometry effects yields more flow angularity and flow field distortion than exists when only the propeller plane inclination-induced flow is present.

Chapter 5

COMPUTER-PREDICTED FLOW FIELD RESULTS AT THE PROPELLER PLANE OF THE PIPER CHEROKEE PA-28-180 AIRPLANE

5.1 Cherokee 180 Airplane Geometry, Body Paneling, and Run Conditions

A Piper Cherokee PA-28-180 is owned by the Aerospace Engineering Department of The Pennsylvania State University. Because this airplane was readily available for research use, computer predictions of the flow at the propeller plane (propeller removed) were made for it.

In this chapter, results of parametric studies are presented which show the effects of cowl inlet inflow, wing lift, wing dihedral, and aft fuselage geometry deletion on the computed potential flow field at the propeller plane. Additionally, a series of figures is included which provides a mapping of the computed flow field over the entire propeller plane of the baseline Cherokee 180 configuration for a range of fuselage angles of attack.

Figure 26 presents the geometric characteristics of the single-engine, fixed-gear Cherokee 180 airplane. Though not indicated in Figure 26, the propeller is mounted on the airplane such that the propeller plane is inclined, with respect to the fuselage, downward and to the right by the angular amounts given in Table 2. As noted in Figure 26, due to the sideward inclination of the propeller plane, the propeller hub position is shifted a distance of 0.0228 propeller radii to the right of the fuselage plane of symmetry.

Computer panel input for all portions of the fuselage aft of the firewall was obtained from detailed cross section geometry descriptions found on aircraft drawings supplied by the aircraft manufacturer. However, all of the cowling surfaces are constructed of fiberglass. As a result,

the manufacturer has no detailed cross sectional drawings for any of the cowling geometry foreward of the firewall. Therefore, in order to generate the computer paneling model of the cowling and spinner, it was necessary to physically measure the cowling and spinner surface geometry of the Univeristy-owned Cherokee airplane.

Measurement of the cowling and spinner surface coordinates was performed by triangulation using surveying transits. Three-view drawings of the cowling and spinner were made from the measurements. From these drawings, the computer paneling model of the cowling and spinner was generated. The process of measuring and mapping this geometry is described further in Appendix E.

None of the tail or wing surfaces were paneled. However, the wing was simulated by the horseshoe vortex model used in the computer program. Also, none of the landing gear were included in the computer input model.

Figure 27 presents flight test-measured aircraft lift coefficients as a function of fuselage angle of attack. C_L values from this figure were assumed to be equivalent to wing lift coefficients and were used as program input for wing-on computations.

Two different aircraft body paneling networks have been created. The first network includes the cowl-fuselage combination. The second network is the same as the first one, except the fuselage geometry aft of the firewall has been replaced by a short, streamlined afterbody. This short afterbody is illustrated in Figure 26. The second panel network was used for computer predictions at the propeller plane from which the effects of ignoring aft fuselage geometry-induced flow could be determined.

During preliminary testing of a Cherokee 180 wind tunnel model, a cowl inlet inflow velocity ratio, F/V, of 0.2 was measured. This value of F/V was accepted as the baseline input value for computer runs.

Initially, the cowl inlet geometry was precisely paneled producing a closed concave panel surface covering the inlet. Unfortunately, the iterative solution process of the computer program failed to converge because of this concave panel surface. To correct this problem, while maintaining a simulation of inlet inflow, the concave inlet paneling was replaced by a planar membrane of panels placed over the inlet opening. Each of the panels in this membrane was identified as an inlet panel and assigned a value inlet inflow velocity ratio, F/V, to model the inlet inflow.

The spinner paneling also created a problem on early computer runs. Initially, the spinner geometry was included and paneled as a discrete closed body positioned upstream of the cowl inlet panels. In each attempt, the presence of the spinner paneling caused program failure manifested by divergence of the iterative solution process. As a result, the spinner paneling was deleted from the paneling networks, and all computer predictions for the Cherokee 180 were made with the spinner off.

Table 2 describes the various configurations which were used as program input. Additionally, Table 3 lists the values of wing lift coefficient, taken from Figure 27, which were used as program input. Results from computer runs involving all of these configurations are presented in the remainder of this chapter.

5.2 Aft Fuselage-Induced Effects on the Flow Field at the Propeller Plane of the Cherokee 180 Airplane

A study was made to determine how much the accuracy of flow predictions at the propeller plane of the Cherokee 180 airplane was reduced by

deletion of the aft fuselage geometry, that geometry aft of the firewall, from the computer panel modeling. Acceptability of neglecting the aft fuselage geometry would permit the creation of a computer model containing fewer panels, thereby decreasing computing time and cost. This study also was performed to verify the results of aft fuselage paneling deletion previously presented for the arbitrary fuselage in Chapter 3.

Fuselage-off computer flow predictions were made using the Cherokee cowl-short afterbody paneling network and the input parameters of Configuration 6 in Table 2. Effectively, the use of the short afterbody eliminates the windshield geometry and thus reduces the frontal area of the paneled configuration. The cowl-short afterbody geometry contains fewer panels than the cowl-fuselage geometry and is less expensive to run on the computer. Additional fuselage-on flow predictions were made using the cowl-fuselage paneling network and the input parameters of Configuration 1 in Table 2.

Comparisons of the fuselage-on predictions with fuselage-off predictions were made to determine the significance of the aft fuselage contribution to the flow at the propeller plane. Figure 28a compares fuselage-on and fuselage-off azimuthal distributions of predicted axial velocity. Regardless of the body angle of attack, α, the axial velocity magnitude is increased at all azimuths due to the reduced flow blockage realized by deletion of the aft fuselage. As the figure shows, the fuselage-off overprediction of axial velocity is no more than 1.0 to 2.5 percent of the free stream velocity.

Removal of the aft fuselage geometry produces slightly increased upwash predictions at the propeller plane. This increase is reflected in the fuselage-off tangential velocity distributions in Figure 28b. At

the lower body angle of attack, α, deletion of the aft fuselage changes the tangential velocity field everywhere except near the vertical centerline azimuths of zero and 180 degrees. However, the tangential velocity distribution for a body angle of attack of ten degrees is less affected by aft fuselage removal, since noticeable changes occur only near the horizontal centerline azimuth positions.

Figures 28c and 28d present the flow angularity distributions corresponding to the previously examined axial and tangential velocity predictions for body angles of attack, α, of two and ten degrees, respectively. At the lower angle of attack, Figure 28c, deletion of the aft fuselage geometry results in no more than a 0.3 degree change in predicted flow angularity at any azimuth. At the higher angle of attack, Figure 28d, fuselage-off computations produce no discernable change in the flow angularity distribution.

The upper vertical centerline of the propeller plane is located directly upstream of the windshield surface on the aft fuselage. Therefore, presumably, the largest fuselage-induced axial velocity contributions at the propeller plane would occur along the upper vertical centerline. Figure 29 presents fuselage-on-predicted and fuselage-off-predicted radial distributions of axial velocity along the upper vertical centerline position (the zero degree azimuth) for high and low fuselage angles of attack. Even at this azimuth position, where fuselage influences should be strongest, no more than a three percent overprediction of the axial velocity magnitude results from deleting the aft fuselage computer paneling.

For a typical single-engine aircraft geometry such as the Cherokee 180, greater accuracy in the flow predictions at the propeller plane is achieved by including the aft fuselage geometry in the computer model.

However, as the results of this subsection indicate, deletion of the aft fuselage geometry from the computer model results in a decrease of only a few percent in the accuracy of flow field predictions at the propeller plane for a typical single-engine airplane. Specifically, flow angularity predictions are negligibly affected, particularly at high angles of attack, by aft fuselage geometry deletion. Also, axial velocity overpredictions of no more than three percent can be expected should the computer paneling exclude the aft fuselage geometry.

The advantage of computer time and cost savings realized by using a fuselage-off panel model may offset the disadvantage of slightly reduced flow prediction accuracy. However, if increased accuracy in flow predictions is desired, the aft fuselage should be included in the computer panel model.

5.3 Wing Lift-Induced and Dihedral-Induced Effects on the Flow Field at the Propeller Plane of the Cherokee 180 Airplane

To determine if it is important to include the wing geometry in the computer model of a single-engine airplane for predicting flow at the propeller plane, two computer runs were made with the Cherokee 180. The first computer run was made at both high and low fuselage angles of attack using the complete cowl-fuselage-wing input geometry (spinner removed). The second run was the same as the first, except that the wing geometry was deleted from the model. The models for these two runs correspond to Configurations 1 and 5, respectively, in Table 2.

Wing lift-induced upwash in the vicinity of the horizontal centerline is the most significant wing contribution to the flow at the propeller plane which affects cyclic propeller blade loads and vibration. Thus, comparisons of wing-off-predicted and wing-on-predicted radial distribu-

tions of tangential velocity and angle of rotational flow near the horizontal centerline would indicate how much the wing-induced upwash contributes to the flow field.

Such comparisons are presented in Figures 30a, 30b, and 30c for radial distributions of flow quantities along the 90 degree azimuth position (near the horizontal centerline) of the Cherokee propeller plane using results from the two computer runs. It should be noted that because the Cherokee propeller is oriented with vertical and sideward inclinations, α_p and β_p, the 90 degree azimuth position is a few degrees below the actual horizontal centerline rather than coincident with it.

At the 90 degree azimuth, negative tangential velocities, as in Figure 30a, are indicative of upwash. In Figure 30a, the wing-induced upwash increases the magnitude of the tangential velocity by nearly the same amount at all radii for a given fuselage angle of attack, α. This magnitude increase is on the order of two percent of the free stream velocity for a fuselage angle of attack of two degrees, corresponding to a cruise flight condition. However, for a fuselage angle of attack of ten degrees (a high lift, takeoff flight condition), wing-induced increase in the magnitude of the tangential velocity is as much as 6.5 percent of the free stream velocity.

Figure 30b presents the wing-on and wing-off predictions of angle of rotational flow associated with the velocities in Figure 30a for a fuselage angle of attack of two degrees. The wing is seen to increase the flow angularity at all radii. A one to two degree increase is observed at radii greater than the cowl inlet radius, the important radii where the propeller blade is heavily loaded. For a fuselage angle of attack of ten degrees, Figure 30c indicates wing-induced flow angularity increases of two to four degrees at radii greater than the inlet radius.

It is evident from Figures 30a, 30b, and 30c that the wing of a typical single-engine airplane such as the Cherokee 180 makes a sizeable contribution to the flow field at the propeller plane even for low fuselage angles of attack. Clearly, to ensure more accuracy in the flow predictions at the propeller plane, particularly for high fuselage angles of attack, the wing geometry must be included in the computer input model.

Having determined the necessity of including the wing geometry in the computer model, the effect of wing dihedral on the computer-predicted flow at the propeller plane is of interest. Concern about dihedral-induced effects on the flow field was raised during construction of a wind tunnel model of the Cherokee 180 to be used in experimental phases of this research. To simplify model construction, it was desirous to build the wing without dihedral, but it was first necessary to determine if dihedral removal would have a negligible effect upon the flow field at the propeller plane, to be experimentally measured.

In an effort to determine the size of the wing dihedral-induced contribution to the flow at the propeller plane, two computer runs were made. The first run employed the Cherokee cowl-fuselage-wing model with wing dihedral included (Configuration 1 in Table 2). The second run was made using no dihedral (Configuration 4 in Table 2).

Results of the two computer runs are compared in Figures 31a and 31b. These figures present radial distributions of flow angularity along the 90 degree azimuth position for two different fuselage angles of attack. For a fuselage angle of attack of two degrees, Figure 31a indicates that there is no discernable dihedral-induced contribution to flow angularity except at the innermost radii, which are embedded within the spinner on the actual aircraft and are not important. However, for a

fuselage angle of attack of ten degrees (Figure 31b), flow angularity is increased at all radii if wing dihedral is not modeled. Dihedral-induced decreases in flow angularity of as much as two degrees are observed near the 75 percent radial position.

Obviously, wing dihedral can be deleted from the computer model for low fuselage angles of attack, and little loss in flow prediction accuracy will result. However, for high fuselage angles of attack, the high wing lift magnifies the dihedral-induced contribution to the flow at the propeller plane. Hence, the actual wing dihedral should be included in the computer model to provide increased accuracy in the flow predictions for higher fuselage angles of attack. Therefore, in general, modeling the wing dihedral is advisable.

5.4 Cowl Inlet Inflow Velocity Effects on the Flow Field at the Propeller Plane of the Cherokee 180 Airplane

Investigation of inlet inflow effects on the flow at the propeller plane first performed in Chapter 4 for the twin-engine airplane was continued for the single-engine Cherokee 180 airplane. The study was done to determine the sensitivity of flow at the propeller plane to changes in cowl inlet inflow velocity.

Using the Cherokee cowl-fuselage-wing computer model, three computer runs were made, each using a different value of cowl inlet inflow velocity ratio, F/V, for input. The first run used the baseline F/V value of 0.2 (Configuration 1 in Table 2) which was previously measured in wind tunnel tests of the Cherokee 180. In the second run, F/V was decreased to 0.1 (Configuration 2 in Table 2). F/V was increased to 0.4 in the third run (Configuation 3 in Table 2).

In Figures 32a, 32b, and 32c, results obtained using the various inlet inflow velocity ratios are compared for both low and high fuselage

angles of attack. Radial distributions of axial velocity obtained using the three inlet inflow velocity ratios are presented in Figure 32a. For both fuselage angles of attack, changing F/V is seen to produce significant changes in axial velocity only at radii less than the local cowl inlet radius, positions which are directly upstream of the inlet. By reducing F/V from the baseline value to a value of 0.1, the cowling becomes more like a bluff body at the inlet face, and axial flow blockage at the inner radii on the propeller plane is increased. Conversely, by increasing F/V from the baseline value of 0.2 to a value of 0.4, axial flow blockage at the propeller plane is greatly reduced. In fact, axial flow blockage appears to decrease almost linearly with increasing F/V at the inner radii. At radii beyond the cowl inlet radius, locations in which the propeller blades are heavily loaded, changing F/V has little effect on the axial velocity. In fact, changing F/V produces no discernible change in axial velocity at locations beyond the 43 percent radial position.

Radial distributions of flow angularity obtained using the various inlet inflow velocity ratios are presented in Figures 32b and 32c for fuselage angles of attack of two and ten degrees, respectively. Reasons for the strange oscillatory behavior of the flow angularity distributions at the inner radii seen in these two figures are given later in subsection 5.5.3. In both figures, it is seen that changes in F/V greatly alter the flow angularity only at the inner radii directly upstream of the cowl inlet. Flow angularity increases as F/V decreases. At radii beyond the cowl inlet radius, where the propeller blades are most heavily loaded, flow angularity is little affected by changes in F/V. Beyond the 50 percent radial position, changing F/V does not noticeably change the flow angularity in either of the Figures 32b or 32c.

The major result observed in this study of inflow effects is that changing the input value of inflow velocity ratio, F/V, greatly affects the predicted flow field only at the region of the propeller plane directly upstream of the inlet. This finding agrees with the computer-predicted results presented in Chapter 4 for the twin-engine airplane and agrees with the experimental results of Roberts and Yaggy (15).

The flow field at the hub region directly upstream of the cowl inlet has much less affect on the overall propeller vibration and performance than does the flow field outside of the hub region. Therefore, any inaccuracies in the flow field predictions at the hub region are not extremely distressing. Thus, insofar as overall propeller performance and vibration are affected by the flow at the propeller plane, the choice of inlet inflow velocity ratio, F/V, used to make the flow predictions is not extremely critical.

To maximize flow prediction accuracy, the actual value of inlet inflow velocity should be specified in the computer program input. But, if the actual value of F/V is not known, an approximation of the value should suffice.

5.5 Baseline Flow Predictions Over the Entire Propeller Plane of the Cherokee 180 Airplane

5.5.1 Model used, purpose of presenting the predictions, and organization of the data

In this final section, this chapter presents a series of figures providing a complete description of the flow field over the entire propeller plane of the Piper Cherokee 180 based on computer predictions. The predictions were made using the baseline cowl-wing-fuselage (spinner-off) computer model (Configuration 1 in Table 2).

Effects of aft fuselage modeling, wing modeling, and cowl inlet inflow velocity on the flow predictions at the propeller plane of the Cherokee 180, a typical single-engine airplane, were examined in previous sections of this chapter. To obtain the most accurate flow predictions, it was shown that the computer model must: include the aft fuselage paneling; include the wing (and dihedral); and employ a value of inlet inflow velocity closely matching the expected in-flight value.

Because the baseline Cherokee computer model incorporates the aforementioned characteristics, it is the most realistic of the six model configurations listed in Table 2. Thus, of all flow predictions from the six models, those made using the baseline model are the most accurate. Hence, the flow field predictions obtained using the baseline model were selected for presentation in this section.

There is a two-fold purpose in presenting these computer predictions. First, the information is presented as a general example of the flow field at the propeller plane of an actual single-engine light aircraft. Second, although there are no experimental data currently available for comparison with these predictions to guage the computer prediction accuracy, these predictions are also presented to serve as a data base for use during subsequent experimental phases of the research project of which the work described in this thesis is but a part.

The series of flow predictions has been divided into two groups presented in the following two subsections, the first including only the azimuthal distributions of flow parameters, and the second including only the radial distributions.

5.5.2 Computed azimuthal distributions

Figures 33, 34, 35, and 36 present azimuthal distributions of flow field parameters at respective radial positions, r/R, of 0.35, 0.5, 0.75, and 1.0 on the propeller plane of the Cherokee 180. Parts a, b, and c of each of the four figures consist of distributions of axial velocity, tangential velocity, and angle of rotational flow, respectively.

It is instructive to examine these predicted distributions by discussing a single flow parameter at a time, plotted on the same part of each of the four figures. In this manner, all axial velocity distributions will be examined, then all the tangential velocity distributions, and last, all the distributions of angle of rotational flow.

First, consider the axial velocity distributions, Figures 33a, 34a, 35a, and 36a. At any fixed radius, the azimuthal variation of axial velocity magnitude is seen to increase with increasing fuselage angle of attack. However, the shapes of the velocity distributions at any particular radius are similar for all fuselage angles of attack. With increasing radius, the axial velocity distributions flatten and deviate less from the freestream velocity; thus, a reduction in body-induced flow blockage occurs as radius increases.

For any fixed radius, Figures 33a, 34a, 35a, or 36a, minimum axial flow blockage occurs in the region along the upper vertical centerline (zero degree azimuth position) of the propeller plane for any fuselage angle of attack. This region extends up and away from the cowling. In fact, at higher fuselage angles of attack, some axial flow acceleration occurs at the upper vertical centerline region. This accelerated flow region encompasses a larger azimuth range as radius increases.

Regardless of radial position, axial flow blockage increases at azimuths away from the upper vertical centerline region. In Figures 34a, 35a, and 36a, greatest flow blockage occurs in a region centered about the lower vertical centerline (180 degree azimuth position). At the 0.35 radial station, Figure 33a, two flow blockage peaks occur, one near the 120 degree azimuth position and the other near the 240 degree azimuth position. At this inner radius, these two azimuth positions are directly upstream of and nearest to the cowl surface, hence the peak flow blockage at these locations. Note, however, that due to the installed angle of sidetilt, β_p, of the propeller plane to the right, the left half-plane is positioned slightly farther from the cowl than is the right half-plane. Thus, in Figure 33a, the flow blockage near the 120 degree azimuth (on the right half-plane) is greater than that near the 240 degree azimuth. Similarly, for all the distributions in Figures 34a, 35a, and 36a, maximum axial flow blockage occurs at azimuths on the right half-plane due to the installed angle of sidetilt, β_p.

Second, consider the tangential velocity distributions, Figures 33b, 34b, 35b, and 36b. Ideally, as previously seen in Figure 23b, for an isolated propeller plane with an inclination, α_G, from the free stream, the tangential velocity varies sinusoidally with azimuth and does not vary with radius. However, the tangential velocity distributions for the Cherokee propeller plane are distorted sinusoids which also vary with radius.

At the 35 percent radial position, Figure 33b, small oscillatory irregularities exist on each of the tangential velocity plots. These irregularities are primarily a result of cowl-induced effects, which quickly diminish with increasing distance from the cowl. That these

C-3

small irregularities are cowl-induced is evident, since these irregularities are not observed in the tangential velocity plots for the outer radii, Figures 34b, 35b, and 36b.

At the upper and lower vertical centerline positions (zero and 180 degree azimuths, respectively), the tangential velocities would be zero if the hub of the propeller plane was located on the fuselage plane of symmetry and if there was no installed sidetilt, β_p, of the propeller plane. However, the hub of the Cherokee propeller plane is offset to the right of the plane of symmetry due to the installed sidetilt, β_p, of the propeller plane. As a result of the offset, the upper and lower vertical centerline positions are immersed in a cowl-induced right-directed sidewash. Additionally, a right-directed sidewash only due to the right sideward inclination, β_p, of the propeller plane exists at the vertical centerline positions. The net sidewash corresponds to positive and negative tangential velocity components at the zero degree and 180 degree azimuths, respectively, noted in Figures 33b, 34b, 35b, and 36b.

Peaks in the tangential velocity profiles at the 35 percent radial position, Figure 33b, are much steeper and sharper than the peaks in the profiles at the other radii. At the 35 percent radial station, narrow regions centered about the 75 and 285 degree azimuths, where the velocity peaks occur, lie directly upstream of and are very close to the inlet face of the cowl. Thus, cowl-induced effects are intense in the two narrow regions. Hence, the peaks in the velocity profiles in Figure 33b tend to be very sharp. However, at the 50, 75, and 100 percent radial positions, there are no regions on the propeller plane which lie directly upstream of or as close to the inlet face of the cowl. Cowl-induced effects are small or negligible at these radii. Hence, the peaks in the

velocity profiles in Figures 34b, 35b, and 36b assume rounder, more sinusoidal shapes.

For a fixed fuselage angle of attack, small shifts in the azimuthal location of the tangential velocity peaks in Figures 33b, 34b, 35b, and 36b occur as radial position changes. Partly because of wing dihedral, the azimuthal position of the maximum wing-induced flow changes as radius changes. This dihedral effect, combined with the effect of decreasing cowl-induced flow at larger radii, produces the azimuthal shifts in the locations of the tangential velocity peaks as radius changes.

Also, for any fixed radius, shifts in the azimuthal location of the tangential velocity peaks in Figures 33b, 34b, 35b, and 36b occur as fuselage angle of attack varies. Apparently, changes in wing lift as well as changes in cowl-induced flow with changing fuselage angle of attack also contribute to azimuthal shifts in the locations of tangential velocity peaks.

Upwash at an isolated inclined propeller plane is greatest along the right and left horizontal centerlines (90 and 270 degree azimuths, respectively). Thus, as Figure 23b indicates, tangential velocity is minimum at the 90 degree azimuth and maximum at the 270 degree azimuth for an isolated propeller plane. However, at the propeller plane of the Cherokee 180, Figures 33b, 34b, 35b, and 36b, the peak minimum and peak maximum tangential velocities are not azimuthally positioned 180 degrees apart and occur near but not on the horizontal centerline. This is primarily due to the position of the hub of the propeller plane relative to the cowling.

Additionally, the peak magnitudes at the left half-plane and right half-plane azimuth positions in each of the plots in Figures 33b, 34b,

35b, and 36b are not equal. This inequality is due to the installed propeller plane sidetilt angle, β_p. Due to β_p, the region near the right horizontal centerline is slightly closer to the airframe than is the region near the left horizontal centerline. Upwash tends to be greater on the right half-plane than on the left. Consequently, in each of the plotted distributions, the peak positive tangential velocity is slightly larger in magnitude than is the peak negative velocity.

Comparing Figures 33b, 34b, 35b, and 36b, it is seen that the cowl-induced and wing-induced effects on the tangential velocity distributions for a fixed fuselage angle of attack diminish with increasing radius. At the 35 percent radial station, Figure 33b, wing-induced and cowl-induced upwash are greatest and create the largest peak magnitudes of tangential velocity. As radius increases (Figures 34b, 35b, and 36b, respectively), peak tangential velocity magnitudes decrease. The decrease is mainly due to decreased cowl-induced upwash, though it also is due to the slight decrease in wing-induced upwash at the outer radii. However, wing-induced upwash remains a significant contributor to the tangential velocity variation even at the tip radius (Figure 36b). In Figure 36b, the wing-induced effects are clearly evident in the tangential velocity distribution for the fuselage angle of attack of four degrees. At this fuselage angle of attack, the propeller plane itself has no vertical inclination from the free stream, so the tangential velocity profile in Figure 36b for this fuselage angle of attack contains no vertical inclination-induced contributions. Hence, the sinusoidal variation of this tangential velocity profile is due almost entirely to wing-induced upwash at the 100 percent radial position.

With the presence of the airframe-induced upwash, the peak magnitudes of tangential velocity at the propeller plane of the Cherokee 180 are significantly greater than the peak magnitudes which would exist at the same propeller plane operating in isolation, out of the influences of the airframe. The airframe-induced increases in tangential velocity can be demonstrated by examples in which a comparison is made between the tangential velocities at the propeller plane of the Cherokee 180, Figures 33b, 34b, 35b, and 36b and the tangential velocities at an isolated propeller plane having the same inclination from the free stream.

Take for one example an isolated propeller plane having a geometric angle of attack, α_G, of six degrees from the free stream. Because α_p is -4 degrees and β_p is three degrees for the Cherokee propeller plane, α_G for the Cherokee propeller plane is approximately six degrees when the fuselage angle of attack, α, is ten degrees. Using the expression for v_{t_p} in Figure 23b, the minimum and maximum tangential velocity ratios for the isolated propeller plane with α_G equal to six degrees are -0.1455 and +0.1455, respectively. However, as seen in Figure 33b, 34b, 35b, and 36b for a fuselage angle of attack of ten degrees, the corresponding Cherokee propeller plane experiences peak magnitudes of tangential velocity ratio far in excess of 0.1455 at all radii. The excesses are due entirely to airframe-induced effects.

For a second example, consider an isolated inclined propeller plane which is perpendicular to the free stream. That is, α_G is zero degrees. For this isolated propeller plane, the tangential velocity is everywhere equal to zero. The corresponding Cherokee propeller plane is the one for which the fuselage angle of attack, α, is four degrees. In contrast to the nonexistent tangential velocities on the isolated propeller plane,

the plots in Figures 33b, 34b, 35b, and 36b for α equal to four degrees indicate nonzero tangential velocities on the propeller plane of the Cherokee. Though sidetilt, β_p, contributes somewhat to these nonzero tangential velocities, most of the nonzero contributions are due to the airframe-induced flow.

Third and finally in this subsection, consider the azimuthal distributions of angle of rotational flow, θ, in Figures 33c, 34c, 35c, and 36c. These figures present azimuthal variations of flow angularity corresponding to the previously examined axial and tangential velocity variations.

As a reminder, θ is a function of the ratio of local tangential to local axial velocity as given in Equation (48) in Chapter 2 and is an angle lying in the plane of the local section of a propeller blade rotating in the propeller plane. For a given propeller rotational speed, the local blade section angle of attack decreases as θ increases as Figure 8 indicates. Thus, Figures 33c, 34c, 35c, and 36c each qualitatively indicate the azimuthal variation in angle of attack of blade sections at the given radius on the Cherokee propeller operating in the flowfield for a given fuselage angle of attack.

As indicated in Figures 33c, 34c, 35c, and 36c for any fixed radius, azimuthal variation of flow angularity increases with increasing fuselage angle of attack. These increases in azimuthal variation of flow angularity are due to the combined effects of increased airframe-induced upwash and increased propeller plane inclination resulting from increased fuselage angle of attack.

Comparing Figures 33c, 34c, 35c, and 36c, the azimuthal variation of flow angularity increases as radial position decreases. Increasing

cowl-induced upwash with decreasing radius is the primary cause of this trend in the flow angularity distributions. Thus, in the plotted distributions, a peak θ magnitude as large as 35 degrees is observed in the distribution at the 35 percent radial position for a fuselage angle of attack of ten degrees. Conversely, a peak θ magnitude as small as three degrees is observed at the 100 percent radial position for a fuselage angle of attack of two degrees.

As seen in Figures 33c, 34c, 35c, and 36c, the combined effects of cowl-induced flow, wing-induced upwash and propeller plane inclination shift the azimuthal positions of the maximum and minimum θ values on the plotted distributions as changes in radial position and fuselage angle of attack occur. For an isolated inclined propeller plane, experiencing no airframe-induced effects, maximum and minimum θ values would occur exactly at the left and right horizontal centerlines, respectively (the 270 and 90 degree azimuths, respectively). On all the plotted θ distributions at the Cherokee propeller plane with the exception of the plots in Figures 35c and 36c for angles of attack of two and four degrees, the maximum and minimum θ values, though shifting slightly in azimuthal position, remain in the vicinity of the left and right horizontal centerline, respectively.

However, in the distributions of θ for fuselage angles of attack of two and four degrees at the two outer radii, Figures 35c and 36c, the maximum and minimum values of θ do not occur near the horizontal centerline. Instead, they occur near the upper and lower vertical centerlines, respectively (near the zero and 180 degree azimuths, respectively). These shifts of maximum and minimum θ values to the vertical centerline positions are due to the effect of the installed sideward inclination, β_p,

of the propeller plane. At the outer radii at fuselage angles of attack of two and four degrees, the effect of sideward inclination, β_p, of the propeller plane outweighs the effects of wing-induced upwash, cowl-induced flow, and vertical inclination, α_p, of the propeller plane.

The following example, involving an isolated inclined propeller plane, shows the significance of the airframe-induced contribution to the flow angularity at the propeller plane of the Cherokee. On an isolated propeller plane having an inclination, α_G, of six degrees from the free stream, a peak magnitude of θ equal to six degrees occurs at the 90 and 270 degree azimuths for any radius, as computed using Equation (54) in Chapter 4. For a fuselage angle of attack, α, of ten degrees, the propeller plane of the Cherokee has an inclination, α_G, from the free stream of approximately six degrees. Therefore, θ values on the isolated propeller plane having an inclination, α_G, of six degrees when compared with the θ values observed on the propeller plane of the Cherokee for a fuselage angle of attack, α, of ten degrees will reveal the airframe-induced contribution to the observed θ values on the propeller plane of the Cherokee. For a fuselage angle of attack, α, of ten degrees, distributions in Figures 33c, 34c, 35c, and 36c exhibit peak magnitudes of θ equal to 34.7, 18.6, 12.7, and 10.8 degrees, respectively. Each of these peak magnitudes is greater than the six degree value existing on the isolated inclined propeller plane solely because the airframe-induced flow at the propeller plane of the Cherokee is present.

A striking illustration of airframe-induced effects on the flow at the propeller plane of the Cherokee is obtained if the flow angularity increase at the 75 percent radial position, evident in the foregoing example, is reexpressed in terms of an increase in the angle of attack of a

propeller blade section operating at that radial position. Operating in the propeller plane of the Cherokee, the propeller blade would experience a maximum angle of attack when at the 112 degree azimuth position, since the minimum angle of rotational flow, -12.7 degrees, occurs at that azimuth (refer to the distribution in Figure 35c for a fuselage angle of attack of ten degrees). However, operating in the isolated inclined propeller plane of the foregoing example, the blade section would experience a maximum angle of attack when at the 90 degree azimuth position where the minimum angle of rotational flow, -6 degrees, occurs. Assuming that in both propeller planes the propeller is operating at an advance ratio of 1.2, the decrease in minimum θ from -6 degrees to -12.7 degrees indicates the following concerning change in blade section angle of attack: when operating in the flow field at the Cherokee propeller plane, Figure 35c, the blade section at the 75 percent radial station attains a maximum angle of attack which is 16.96 degrees greater than the maximum angle of attack attained when the propeller operates in the isolated inclined propeller plane. This increase of 16.96 degrees is entirely due to the airframe-induced contribution to the flow angularity at the propeller plane of the Cherokee.

This concludes discussion of the azimuthal distributions of the predicted flow parameters at the propeller plane of the Cherokee. In the following subsection, the radial distributions of the flow parameters are discussed.

5.5.3 Computed radial distributions

Figures 37 through 44 present radial distributions of flow field parameters at fixed azimuth positions, ψ, of zero through 315 degrees in increments of 45 degrees, respectively, on the propeller plane of the

Cherokee 180. Parts a, b, and c of each figure consist of distributions of axial velocity, tangential velocity, and angle of rotational flow, respectively. Predictions for five values of fuselage angle of attack are included in each figure.

Indicated in each figure is the local radial position of the periphery of the cowl inlet. The radius of the inlet varies with azimuth, because the inlet opening is elongated, and the hub of the propeller plane is positioned to the right of the plane of symmetry. At any azimuth, the local cowl inlet radius is approximately equal to the maximum local radial extent of the cowl inlet face, the region on the cowl surface which is nearest to the propeller plane. Thus, the local radial position of the inlet on the figures acts as a reference point, indicating the radial extent of those cowl surfaces proximal to the propeller plane.

Before discussing in detail each of the distributions of the various flow parameters, the erratic behavior observed at the inner radii on almost every plotted distribution in Figure 37a through 44c should be discussed. In the hub region at radii less than the local cowl inlet radius, the predicted distributions in all figures, with the exception of Figure 37a, exhibit unexpected characteristics. The axial velocity profiles have strange peaks or oscillations in this region. The distributions of tangential velocity and angle of rotational flow are extremely oscillatory in the hub region.

This unexpected erratic nature of the predicted radial distributions probably occurs for two reasons. First, for reasons previously given in the first section of this chapter, the spinner geometry was omitted from the final computer model used to make the flow predictions presented

throughout this chapter. Absence of the spinner probably accounts for most of the erratic nature of the distributions inside the ten percent radial position. However, on the actual Cherokee 180, the region on the propeller plane at positions less than the ten percent radial position is buried within the spinner. Thus, the predicted flow inside the ten percent radial position in each of Figures 37a through 44c is nonexistant, and in reality should be ignored.

Second, possible shortcomings in the paneling mesh at the region of the cowl inlet may have caused problems in the predictions at the hub region on the propeller plane. The maximum length of some of the panels on the inlet face of the cowl in the computer model is greater than or nearly equal to the length of the spacing between the propeller plane and the cowl inlet face. Thus, the paneling mesh at the cowl inlet region may be too coarse to produce accurate flow prediction in the hub region of the propeller plane. The phenomenon of oscillatory flow distributions at the hub region of the propeller plane due to excessive coarseness of the paneling mesh was previously observed in the results pertaining to flow upstream of a sphere in Chapter 3. The same phenomenon is probably occurring in Figure 37a through 44c for the Cherokee 180.

Regardless of the causes, any inaccuracies in the flow predictions out to a radial position of 20 to 30 percent on the propeller plane of the Cherokee are not of extreme concern, because a propeller blade is not heavily loaded at these inner radii. Inaccuracies in the flow predictions at these inner radii would have a minimal impact upon loading and vibration of propeller blades operating in the flow field presented in Figures 37a through 44c. Note, the foregoing discussion on the erratic distributions at the inner radii is also applicable to the distributions in Figures 30a through 32c.

In the remainder of this subsection, as was done in the previous subsection for the azimuthal distributions, the predicted radial distributions in Figures 37 through 44 will be examined in detail. In turn, the group of axial velocity profiles, the group of tangential velocity profiles, and the group of profiles of angle of rotational flow will be discussed.

First, consider the radial distributions of axial velocity plotted in part a of each of Figures 37 through 44. In each of these figures, airframe-induced blockage of axial flow is plainly evident. This blockage is greatest at radial positions directly upstream of the cowling, radii less than the local cowl inlet radius, with axial velocities as low as 20 to 35 percent of the free stream velocity existing there. At all azimuths, the airframe-induced blockage of axial flow diminishes rapidly as radius increases, since the blockage is nearly entirely due to the fuselage (particularly the cowl). Little wing-induced blockage occurs.

At azimuths of zero, 45, and 315 degrees (Figures 37a, 38a, and 44a, respectively) on the upper half-plane, the cowl-induced axial flow blockage diminishes more radily than at any other azimuth. Because the hub of the Cherokee propeller plane is situated upstream of the upper portion of the cowl inlet face, little of the propeller plane at these three azimuths lies directly upstream of any cowl surfaces. Hence, cowl-induced blockage is only severe at positions less than the 20 to 25 percent radial positions in Figures 37a, 38a, and 44a. Beyond the 25 percent radial position, axial velocities in these three figures quickly return, asymptotically, to the free stream value. In fact, at higher fuselage angles of attack, axial velocity in Figures 37a, 38a, and 44a is accelerated to a value greater than the free stream velocity at regions just beyond the

cowl inlet radius. However, the axial velocity returns to the free stream value as radius continues to increase.

Because the propeller plane has an installed inclination, β_p, to the right, the 45 degree azimuth position is rotated toward the cowl and wing, while the 315 degree azimuth position is rotated away from the cowl and wing. Consequently, the cowl-induced flow blockage at the inner radii in Figure 38a is greater than the blockage at the inner radii in Figure 44a. Conversely, at the outer radii, flow blockage is less in Figure 38a than in Figure 44a. This is due to the existence of slightly higher wing-induced axial flow at the 45 degree azimuth than at the 315 degree azimuth as a consequence of the sideward inclination, β_p.

At azimuths of 135, 180, and 225 degrees (Figures 40a, 41a, and 42a, respectively), on the lower half-plane, cowl-induced axial flow blockage diminishes much less rapidly with increasing radius than it diminishes at azimuths on the upper half-plane, previously examined. Because a large area of the lower half-plane lies directly upstream of the cowl, significant cowl-induced flow blockage occurs over the entire radius at these three azimuths with a three to seven percent reduction of axial velocity below the free stream value remaining at the tip radius in each of Figures 40a, 41a, and 42a. Though some wing-induced axial flow blockage occurs at the outer radii in these three figures, most of the blockage at the outer radii is cowl-induced. Also, in contrast to the behavior previously noted at azimuths on the upper-half plane, axial flow blockage at azimuths of 135, 180, and 225 degrees, on the lower half-plane, increases with increasing fuselage angle of attack, α.

Due to the installed propeller plane inclination, β_p, to the right, the 135 degree azimuth position is rotated toward the cowl and wing,

while the 225 degree azimuth position is rotated away from the cowl and wing. Consequently, axial flow blockage at the 135 degree azimuth position, Figure 40a, is slightly greater than the blockage at the 225 degree azimuth position, Figure 42a, at any particular radius for any fuselage angle of attack, α.

At the 90 and 270 degree azimuth positions (near the right and left horizontal centerlines, respectively, of the propeller plane) in Figures 39a and 43a, respectively, cowl-induced axial flow blockage is smaller in magnitude and less extensive (radially) than the blockage at the three azimuths on the lower half-plane, previously examined. In Figures 39a and 43a, cowl-induced axial flow reduction is significant (more than five percent of the free stream velocity) out to approximately the 70 percent radial position. At the tip radius in Figures 39a and 43a, the cowl-induced reduction in axial velocity is not more than two percent of the free stream velocity.

At any particular radius, axial flow blockage at the 90 degree azimuth position, Figure 39a, is slightly greater than the blockage at the 270 degree azimuth position, Figure 43a. The greater blockage near the right horizontal centerline is a consequence of the installed propeller plane inclination, β_p, which causes the 90 degree azimuth position to lie closer to the cowl than does the 270 degree azimuth position.

As Figures 39a and 43a also show, the axial velocity profiles near the right and left horizontal centerlines of the propeller plane are little affected by changes in fuselage angle of attack, α.

Second, consider the radial distributions of tangential velocity plotted in part b of each of Figures 37 through 44. As previously observed in the radial distributions of axial velocity, airframe-induced

tangential velocity contributions also decrease most rapidly with increasing radius at the zero, 45, and 315 degree azimuths (Figures 37b, 38b, and 44b, respectively), on the upper half-plane. At azimuths of 90, 135, 180, 225, and 270 degrees (Figures 39b, 40b, 41b, 42b, and 43b, respectively), lying near the horizontal centerline or in the lower half-plane, airframe-induced tangential velocity contributions decrease less rapidly with increasing radius than at the three azimuths on the upper half-plane. At azimuths near the horizontal centerline and on the lower half-plane, fairly large airframe-induced tangential velocity contributions are observed as far outboard as the 60 percent radial position and beyond. Conversely, at azimuths of zero, 45, and 315 degrees, airframe-induced contributions (predominantly cowl-induced contributions) are fairly large only at positions inboard of the 60 percent radial position.

Large airframe-induced tangential velocity contributions are more extensive on the lower half-plane than on the upper half-plane for two reasons. One reason is that most of the frontal area of the cowl lies directly downstream of the lower half-plane, so large cowl-induced effects persist at outer radii. The other reason is that wing-induced upwash, which is strong at all radial positions, heavily contributes to the tangential velocties at the 90, 135, 225, and 270 degree azimuth locations.

Ideally, tangential velocity would be nonexistant along the upper and lower vertical centerlines (zero and 180 degree azimuths, respectively) if the hub of the propeller plane was located on the fuselage plane of symmetry and if there was no installed sideward inclination, β_p, of the propeller plane. However, the hub of the propeller plane of the Cherokee is located slightly to the right of the fuselage plane of

symmetry, and an inclination, β_p, to the right does exist. Hence, the vertical centerline of the propeller plane lies in a region at which a small right-directed sidewash exists. This sidewash field yields small positive tangential velocities at the zero degree azimuth position (Figure 37b) and yields small negative tangential velocities at the 180 degree azimuth position (Figure 41b). In Figure 37b, the tangential velocity distribution at the region inboard of the 25 percent radial position is due to the cowl-induced sidewash, a consequence of the location of the hub of the propeller plane. The nearly constant distribution outboard of the 25 percent radial position is largely due to the sidewash component created by the installed sidetilt, β_p. In Figure 41b, tangential velocity resulting from cowl-induced sidewash persists over nearly the entire radius. The nearly constant distribution of velocity noted at the tip radius is a result of the installed sidetilt, β_p, of the propeller plane.

At azimuth positions of 45, 90, and 135 degrees (Figures 38b, 39b, and 40b, respectively), on the right half-plane, negative tangential velocities are produced by a positive upwash field. Hence, with increasing fuselage angles of attack, α, larger negative tangential velocities occur at each radius at these three azimuths, because wing-induced and propeller plane inclination-induced upwash contributions increase with increasing α. Conversely, at azimuth positions of 225, 270, and 315 degrees (Figures 42b, 43b, and 44b, respectively), on the left half-plane, positive tangential velocities are produced by a positive upwash field. Hence, tangential velocities increase with increasing fuselage angle of attack, α, at each radius at these three azimuths.

Upwash makes a maximum contribution to tangential velocity along the horizontal centerline of the propeller plane, and it makes no con-

tribution to tangential velocity along the vertical centerline. Hence, as comparison of part b of each of Figures 37 through 44 illustrates, the greatest change in tangential velocity per unit change in fuselage angle of attack, α, at any particular radius occurs at the 90 and 270 degree azimuths, which are nearest to the horizontal centerline of the propeller plane of the Cherokee.

Third and finally, consider the radial distributions of angle of rotational flow, θ, plotted in part c of each of Figures 37 through 44. In each of these figures, the flow angularity is greatest in the hub region at radii less than the local cowl inlet radius at any azimuth. Reasons for the oscillatory, erratic nature of each of the θ distributions in the hub region were previously stated at the beginning of this subsection. That negative values of θ exist on the right half-plane (azimuths less than 180 degrees) and positive values of θ exist on the left half-plane indicates the presence of upwash over the entire propeller plane of the Cherokee at all fuselage angles of attack for which flow predictions are presented.

Comparing all the plots of θ in part c of each of Figures 37 through 44, it is seen that flow angularity is generally slightly greater on the right half-plane than on the left half-plane. On the right half-plane, a magnitude of θ as large as 58.5 degrees is predicted (at the 135 degree azimuth position for a fuselage angle of attack, α, of ten degrees). On the left half-plane, however, a magnitude of θ only as large as 53.5 degrees is predicted (at the 270 degree azimuth position for a fuselage angle of attack, α, of ten degrees). That flow angularity is slightly greater on the right half-plane than on the left half-plane is attributable to the existence of the installed right-directed sidetilt, β_p, of

the propeller plane of the Cherokee. Due to β_p, the right half-plane lies slightly closer to the airframe than the left half-plane does. Hence, airframe-induced contributions to flow angularity are larger on the right half-plane of the propeller than on the left half-plane.

Figures 37c and 41c clearly show the effect of the installed sidetilt angle, β_p, of the propeller plane on the flow angularity at the upper and lower vertical centerline azimuths (zero and 180 degrees), respectively. At the zero degree azimuth position, cowl-induced flow angularity is evident out to the 40 percent radial position and slightly varies with changes in fuselage angle of attack, α. This slight variation occurs because the hub of the propeller plane is positioned slightly to the right of the fuselage plane of symmetry in a region of cowl-induced sidewash which slightly changes as fuselage angle of attack, α, changes. However, wing-induced flow angularity is negligible at this azimuth. Hence, beyond the 40 percent radial position, airframe-induced flow angularity is insignificant, and θ remains fixed at three degrees for all fuselage angles of attack due to the installed propeller plane sidetilt angle, β_p, of three degrees to the right. Similarly, airframe-induced contributions to θ at the 180 degree azimuth position (Figure 41c) are negligible beyond the 85 percent radial position. Hence, at this radial position, θ remains fixed at -3 degrees, commensurate with the three degree value of propeller plane sidetilt angle, β_p, to the right.

At the six azimuth positions not on the vertical centerline of the propeller plane (Figures 38c, 39c, 40c, 42c, 43c, and 44c), flow angularity increases with increasing fuselage angle of attack, α, at any radius. At the inner radii at these azimuths, an increase in fuselage

angle of attack, α, of two degrees produces flow angularity increases greatly in excess of two degrees, because extra flow contributions induced by the cowl exist at these radii. At the outer radii, however, a two degree increase in fuselage angle of attack, α, produces flow angularity increases of only 1.5 to 3.5 degrees, because only the wing-induced upwash and vertical propeller plane inclination-induced upwash are important contributors to flow angularity at these radii. Of course, the wing-induced upwash and vertical propeller plane inclination-induced upwash make the greatest contribution to angle of rotational flow, θ, at the horizontal centerline azimuths. Of all the azimuth positions for which results are plotted, consequently, it is at the 90 and 270 degree azimuth positions (Figures 39c and 43c), nearest to the horizontal centerline of the propeller plane of the Cherokee, that the increase in flow angularity per unit increase in fuselage angle of attack, α, at the tip radius is greatest.

The significance of the wing-induced contribution to flow angularity (θ) may be discerned at the tip radius at the 90 and 270 degree azimuths (Figures 39c and 43c, respectively) by comparing the flow field at the propeller plane of the Cherokee for a given vertical propeller plane inclination from the free stream with the flow field at an isolated propeller plane having nearly the same vertical inclination from the free stream. Due to the combined effects of the installed inclination angles, α_p and β_p, the propeller plane of the Cherokee has a vertical inclination, α_G, from the free stream which is approximately four degrees less than the corresponding fuselage angle of attack, α. Therefore, the plotted flow results at the propeller plane of the Cherokee for a specified value of fuselage angle of attack, α, should be compared with flow results at

an isolated propeller plane having a vertical inclination, α_G, from the free stream equal to α - 4 degrees. Then the flow results at the outer radii of the propeller plane of the Cherokee will differ from the results at the isolated propeller plane by an amount only due to the wing-induced contribution. At the 90 degree azimuth position on the isolated propeller plane for vertical inclinations, α_G, from the free stream of -2, zero, two, four, and six degrees, the angles of rotational flow, θ, are constant at all radii and are equal to 2.0, 0.0, -2.0, -4.0, and -6.0 degrees, respectively (computed using Equation (54) in Chapter 4). However, at the tip radius at the 90 degree azimuth position on the propeller plane of the Cherokee (Figure 39c) for the corresponding fuselage angles of attack, α, of two, four six, eight, and ten degrees, the angles of rotational flow, θ, are equal to 0.7, -2.0, -4.5, -7.2, and -9.8 degrees, respectively. Comparing the results at the two propeller planes, the discrepancy between the set of values of θ for the isolated propeller plane and the set of values for the propeller plane of the Cherokee is solely due to the wing-induced contribution to the flow angularity at the propeller plane of the Cherokee for each fuselage angle of attack, α. A similar comparison can be made for the 270 degree azimuth position. At the 270 degree azimuth position on the isolated propeller plane for vertical inclinations, α_G, from the free stream of -2, zero, two, four, and six degrees, the angles of rotational flow, θ, are constant at all radii and are equal to -2.0, 0.0, 2.0, 4.0 and 6.0 degrees, respectively. However, at the tip radius at the 270 degree azimuth on the propeller plane of the Cherokee (Figure 43c) for the corresponding fuselage angles of attack, α, of two, four, six, eight, and ten degrees, the angles of rotational flow, θ, are equal to -0.7, 1.8, 4.6, 7.1, and 9.6 degrees,

respectively. Comparing the results at the two propeller planes at the 270 degree azimuth, the discrepancy between the two sets of values of θ is solely due to the wing-induced contribution to the flow angularity at the propeller plane of the Cherokee. The foregoing examples for the two azimuth positions indicate that the wing-induced contribution to the flow angularity is substantial.

It is apparent from the series of figures presented in this subsection and the preceding subsection that the flow field at the propeller plane of the Cherokee 180 airplane is, indeed, very nonuniform. Obviously when a propeller is operating in this flow field, the spanwise (radial) loading on the blades is greatly altered, and substantial azimuthal variations in blade loading occur. Vibratory stresses in the blades certainly are increased because of this nonuniform flow field. This concludes the discussion of the baseline flow field predictions at the propeller plane of the Cherokee 180 airplane.

Chapter 6

CONCLUSIONS AND RECOMMENDATIONS

A computer program has been developed which computes the three-dimensional, steady, incompressible, inviscid, potential flow field at a propeller plane (propeller removed) positioned with any installed inclination upstream of an arbitrary airframe geometry.

Based upon the results of the flow field predictions made for the sphere, twin-engine airframe, and single-engine Piper Cherokee airframe geometries, four conclusions can be drawn regarding the overall capabilities of the computer program. Seven more conclusions regarding the nature of the flow at the propeller plane and regarding computer program input modeling for increased accuracy of the flow predictions at the propeller plane can also be made. The latter seven conclusions are based upon all the flow prediction results, in general, and upon the results of the parametric studies, in particular.

1. For a simple wingless geometry such as a sphere, the computer program yields excellent predictions of the surface flow. Also, accurate predictions of the flow field at a propeller plane upstream of such a geometry are obtained using the program.

2. For a typical twin-engine aircraft configuration, the program provides very good predictions of velocity profile shapes at the propeller plane despite the deletion of aft and remote fuselage and nacelle surfaces from the computer model used for the computations. Reasonable predictions of velocity magnitude at the propeller plane are obtained using the program for such a configuration based on comparisons with experimental data.

3. For a typical single-engine aircraft configuration, the program provides reasonable predictions of the flow field at the propeller plane.

This conclusion is based upon judgements of the quality of the single-engine Cherokee aircraft predictions which are extrapolations from the observed quality of the twin-engine aircraft predictions. However, the absence of experimental data for comparison precludes making more specific conclusions regarding the computer program capabilities for single-engine aircraft.

4. In general, for the typical airframe geometries considered, the flow field predictions at any propeller plane obtained from the computer program are more accurate at the outer radii than at the inner radii. There is room for improvement in the computer predictions at the innermost (hub region) radii.

5. Flow fields at propeller planes upstream of typical airframe geometries do, indeed, exhibit a high degree of flow angularity and spatial nonuniformity as the plotted flow predictions for the twin-engine and single-engine configurations clearly illustrate.

6. Though pure inclination of the propeller plane alone is an important contributor to the angularity and azimuthal nonuniformity of the flow at the propeller plane, the airframe-induced effects are equally important or even more important contributors to the flow angularity and are much more important contributors to the spatial nonuniformity of the flow field. This conclusion is based upon the comparisons between the propeller plane flow field results obtained airframe-absent and the corresponding results obtained airframe-present for both the single-engine and twin-engine aircraft configurations.

7. The wing must be included in the computer model if greatest prediction accuracy from the program is to be achieved. This conclusion is based on the computer predictions for the typical aircraft configura-

tions which indicate the wing significantly contributes to the flow field at the propeller plane, particularly in the region near the horizontal centerline.

8. The actual wing dihedral should always be incorporated in computer models to help maximize the accuracy of the flow predictions. This conclusion can be inferred from the observation at the propeller plane for higher fuselage angles of attack that flow predictions made using the actual wing dihedral appreciably differ from the flow predictions made using no dihedral.

9. For maximum accuracy of the flow field predictions at the propeller plane, all of the remote component and aft fuselage geometries must be included in the paneling input model to the computer program. However, fairly good results, which are but a few percent less accurate, can be obtained should such remote and aft geometries be excluded from the panel model. This is revealed by the studies of aft fuselage effects conducted for the simple arbitrary fuselage configuration and for the single-engine Cherokee aircraft configuration. The benefits of computing cost savings realized by deleting such geometry components from the computer model may offset the disadvantages of the slight decrease in flow prediction accuracy which results. The user may need to strike a compromise between computing costs and prediction accuracy when deciding on the size and complexity of paneling models to use.

10. Given the airframe components to be paneled in the computer model, the accuracy of the flow predictions depends on the distribution and sizing of surface panels in the model. The paneling mesh must be extremely fine and dense over the airframe surfaces immediately aft of the propeller plane in order to improve the accuracy of the flow predictions at the propeller plane, particularly in the hub region.

11. If the true inlet inflow velocity for program input is not known, an approximate value is satisfactory and its use will have only a minimal impact on the overall accuracy of the flow predictions at the propeller plane. This conclusion is inferred from the observation that changes in the specified inlet inflow velocity ratio induce noticeable changes in the propeller plane flow field only at the small hub region directly upstream of the inlet. Thus, any inaccuracies in the predicted flow field due to the input of an approximate value of inlet inflow velocity ratio would have only a very small or negligible impact on the overall performance of a propeller operating in the flow field.

Recommendations for future work include the following eight items.

1. Experimental measurements of the flow field at the propeller plane of the Piper Cherokee PA-28-180 aircraft should be obtained and compared with baseline flow field predictions from the computer program which have been presented in this thesis. Such comparisons would provide a definitive check of the program capabilities for typical single-engine aircraft configurations. Wind tunnel testing would be the best approach, as flow field data at the propeller plane (propeller removed) could be gathered and directly compared with the existing baseline predictions. Flight testing, however, could not be done propeller-off but could be done power-off and would require making measurements at a plane just downstream of the actual propeller plane. If flight test data were the only kind obtainable, computer predictions for comparison could be made at the plane, just downstream of the actual propeller plane, where the flight test data were taken.

2. The iterative solution method currently employed by the flow prediction program, Jumper (33), should be replaced by a direct matrix

solution method. Such a program modification would completely eliminate solution divergence problems such as those which were encountered during this study when attempts were made to model concave inlet surfaces, airframes including spinners, and remote components of the twin-engine airframe geometry. This program modification could be easily implemented by replacing the current subroutines SOLVE and SOLSYM, both of which use Gauss-Siedel iteration to solve a system of equations, by new subroutines of the same names which perform a direct matrix solution process such as matrix inversion or Gaussian elimination. However, as a result of this change, a larger computer having more memory would be required to run the program.

3. As the generation of the paneling input and checking for paneling errors is the most tedious task faced by a user of the flow prediction program, a graphics package capable of generating three-dimensional perspective drawings of the input paneling geometry should be added to the current version of the program. Such a graphics package would greatly facilitate the process of finding and correcting paneling errors, a process which must be performed before the comparatively costly flow prediction steps of the computer program can be allowed to proceed.

4. Flow field predictions for the Piper Cherokee PA-28-180 model with the input spinner paneling included should be obtained. Comparisons of these predictions with the currently existing baseline predictions would indicate if inclusion of the spinner geometry is necessary for improved accuracy of flow field predictions in the hub region of the propeller plane. With the spinner included as a discrete body in the input paneling network for the Cherokee 180 airplane, all prediction attempts using the current version of the program have, to date, failed due to

iterative solution divergence. However, solutions for this airframe-spinner combination could be successfully obtained by direct solution through the use of the program modified as described in Recommendation 2. Alternatively, if the airframe-spinner model were modified by fairing the spinner and cowl geometries to form a single body, the current version of the program could be used and iterative solution divergence probably would not occur.

5. Further parametric studies should be done to determine the effects on the propeller plane flow field due to changes in the propeller plane inclination angles, α_p and β_p; changes in the spacing between the cowl and propeller plane or between the nacelle and propeller plane; and changes in the lateral and vertical positions of the propeller plane with respect to the airframe. Such studies could be done with either the twin-engine airplane configuration or the single-engine Cherokee airplane configuration. Also, these studies could be done by using either the current version of the flow prediction program or a version modified as discussed in Recommendation 2.

6. The current version of the flow prediction program, Jumper (33), which solves for the flow field at the propeller plane (propeller removed), should be modified to allow the inclusion of propeller interaction effects in solving for the airframe-induced flow field at the propeller plane. The theory underlying the current flow prediction program permits the existence of an onset velocity field, impinging the body, which is spatially varying provided the velocity field is steady. By introducing a known quasi-steady propeller wake (propeller-induced flow field) as part of such a spatially varying onset velocity field impinging the panel model of the airframe in the computer program, the resulting flow field

predictions at the propeller plane would incorporate propeller interaction effects. Though the current computer code does not accomodate a spatially varying onset velocity field, the program could be changed fairly easily to do so by modifying the boundary condition equations (generated by subroutines COEFIC and COFSYM) and by modifying the program input (subroutine INPUT). This would be the next step toward addressing the mutual airframe-propeller interaction problem.

7. In conjunction with Recommendation 6 for incorporating propeller interaction effects in the solution of the airframe-induced flow field at the propeller plane, a computer program should be obtained or written which will generate a quasi-steady wake downstream of a propeller having an arbitrary nonuniform aerodynamic loading. This program would generate the spatially nonuniform onset velocity field for use as input to the propeller plane flow field prediction program modified as discussed in Recommendation 6. Perhaps a vortex lattice method could be employed by such a program.

8. After modifying the flow prediction program to accomodate propeller interaction effects (Recommendation 6) and after developing a propeller wake prediction program (Recommendation 7), the problem of computing the propeller plane flow field, propeller loads, and propeller performance for a complete airframe-propeller combination including mutual propeller-airframe interference effects should be addressed. One possibility for addressing this problem is an iterative scheme utilizing the propeller performance prediction program, Aljabri (32); the flow prediction program, Jumper (33), modified to include propeller interaction effects as described in Recommendation 6; and a propeller wake prediction program, Recommendation 7. Such an iterative scheme might include the following steps (a through e).

a. For the airframe immersed in a uniform onset velocity field (no propeller interaction effects), compute the airframe-induced flow field at the propeller plane (propeller removed) as has been done in this thesis, but use the modified flow prediction program.

b. Using the resulting nonuniform propeller plane flow field from Step a for input, compute the propeller performance and loading using the program of Aljabri (32) and compute the quasi-steady propeller-induced flow field using a propeller wake prediction program.

c. Create a quasi-steady, spatially nonuniform onset velocity field by incorporating the propeller wake results from Step b. Then using this nonuniform onset velocity field for input to the modified flow prediction program, recompute the flow field at the propeller plane. This time, however, propeller interaction effects will have been incorporated in the flow field solution.

d. Repeat Step b, but use for input the resulting propeller plane flow field from Step c. The results would consist of the computed propeller performance, loading, and wake with mutual propeller-airframe interaction effects entering into the solutions. Repeat Step c, but use for input the results obtained from the repeat of Step b. The result would be the computed propeller plane flow field with mutual propeller-airframe interaction effects entering into the solution.

e. Repeat, in an iterative fashion, the cycle described in Step d until some desired convergence criteria are met.

Completion of the iterations would yield the final propeller plane flow field; the airframe surface flow field; and the propeller performance, loading, and wake results for the airframe-propeller combination with mutual propeller-airframe interaction effects accounted for.

Developing such an iterative procedure would go a long way toward achieving the ultimate goal of this ongoing NASA-sponsored project of which the work described in this thesis is but a part. That goal is to develop the capability of designing aircraft propellers attuned to possess optimum performance, vibration, and noise characteristics when operating in combination with a specific airframe configuration.

REFERENCES

1. Lesley, E. P. and Woods, B. M., "The Effect of Slipstream Obstructions on Air Propellers," NACA TR177, 1923.

2. Durand, W. F., "Interation Between Air Propellers and Airplane Structures," NACA TR 235, 1926.

3. Lock, C. N. H., "Analysis of Experiments on an Airscrew in Various Positions Within the Nose of a Tractor Body," ARC Reports and Memoranda No. 1120, 1927.

4. Lock, C. N. H., "The Effect of Body Interference on the Efficiency of an Airscrew," ARC Reports and Memoranda No. 1238, December 1928.

5. Lock, C. N. H., "Theory of Airscrew Body Interference. Application to Experiments on a Body of Fineness Ratio 3.0 With Tractor Airscrew," ARC Reports and Memoranda No. 1378, May 1930, Revised May 1932.

6. Weick, Fred E., "The Effect of the Sperry Messenger Fuselage on the Airflow at the Propeller Plane," NACA TN 274, January 1928.

7. Lesley, E. P. and Reid, E. G., "Tests of Five Metal Model Propellers With Various Pitch Distributions in a Free Stream and in Combination With a Model VE-7 Fuselage," NACA TR 326, 1929.

8. McHugh, James G. and Derring, Eldridge H., "The Effect of Nacelle-Propeller Diameter Ratio on Body Interference and on Propeller and Cooling Characteristics," NACA TR 680, 1938.

9. Stickle, George W., Crigler, John L. and Naiman, Irven, "Effect of Body Nose Shape on the Propulsive Efficiency of a Propeller," NACA TR 725, 1941.

10. Kuhn, Richard E. and Draper, John W., "Investigation of the Aerodynamic Characteristics of a Model Wing-Propeller Combination and of the Wing and Propeller Separately at Angles of Attack up to 90°," NACA TR 1263, 1956.

11. Postlethwaite, F., Carter, B. C., Perring, W. G. A., and Diprose, K. V., "Vibration of Propellers Due to Aerodynamic Forces. Part I: Permissible Proximity of a Propeller to the Leading Edge of a Wing, as Decided by Propeller Blade Vibration," ARC Reports and Memoranda No. 2054, April 1942.

12. Forshaw, J. R., Squire, H. B., and Bigg, F. J., "Vibration of Propellers Due to Aerodynamic Forces. Part II: Vibration of Propellers due to Non-Uniform Inflow," ARC Reports and Memoranda No. 2054, April 1942.

13. Corson, Blake W. Jr. and Miller, Mason F., "Consideration of Wake Excited Vibratory Stress in a Pusher Propeller," NACA ARCL 4B28 (WRL-146), February 1944.

14. Vogely, A. W., "Calculation of the Effect of Thrust-Axis Inclination on Propeller Disk Loading and Comparison With Flight Measurements," NACA TN 1721, October 1948.

15. Roberts, John C. and Yaggy, Paul F., "A Survey of the Flow at the Plane of the Propeller of a Twin-Engine Airplane," NACA TN 2192, September 1950.

16. Rogallo, Vernon L., Roberts, John C., and Oldaker, Merritt R., "Vibratory Stresses in Propellers Operating in the Flow Field of a Wing-Nacelle-Fuselage Combination," NACA TN 2308, March 1951.

17. Yaggy, Paul F., "A Method for Predicting the Upwash Angles Induced at the Propeller Plane of a Combination of Bodies With an Unswept Wing," NACA TN 2528, October 1951.

18. Rogallo, Vernon L., "Effects of Wing Sweep on the Upwash at the Propeller Planes of Multiengine Airplanes," NACA TN 2795, September 1952.

19. Rogallo, Vernon L. and McCloud, John L. III, "Calculations of Upwash in the Region Above or Below the Wing-Chord Planes of Swept-Back Wing-Fuselage-Nacelle Combinations," NACA TN 2894, February 1953.

20. Rogallo, Vernon L. and McCloud, John L. III, "Surveys of the Flow Fields at the Propeller Planes of Six 40° Sweptback Wing-Fuselage-Nacelle Combinations," NACA TN 2957, June 1953.

21. Smith, A. M. O. and Pierce, Jesse, "Exact Solution of the Neumann Problem. Calculation of Non-Circulatory Plane and Axially Symmetric Flows About or Within Arbitrary Boundaries," Third U.S. National Congress of Applied Mechanics, Brown University, 1958.

22. Hess, John L. "Calculation of Potential Flow About Bodies of Revolution Having Axes Perpendicular to the Free-Stream Direction," Journal of the Aerospace Sciences, Vol. 29, No. 6, June 1962.

23. Hess, J. L. and Smith, A. M. O., "Calculation of Nonlifting Potential Flow About Arbitrary Three Dimensional Bodies," Douglas Aircraft Co., Long Beach, Calif., Report ES40622, 1962.

24. Smith, A. M. O., "Incompressible Flow About Bodies of Arbitrary Shape," IAS National Summer Meeting, Los Angeles, Calif., IAS Paper No. 62-143, June 19-22, 1962.

25. Hess, J. L. and Smith, A. M. O., "Calculation of Potential Flow About Arbitrary Bodies," in Progress in Aeronautical Sciences, Pergamon Press, New York, Vol. 8, 1967, pp. 1-138.

26. Hess, John L., "Calculation of Potential Flow About Arbitrary Three-Dimensional Lifting Bodies. Phase I: Final Report," Douglas Aircraft Co., McDonnell Douglas Corp., Long Beach, Calif., Report MDC-J0545, December 1969.

27. Woodward, F. A., Dvorak, F. A., and Geller, E. W., "A Computer Program for Three-Dimensional Lifting Bodies in Subsonic Inviscid Flow," U.S. Army Air Mobility Research and Development Laboratory, Fort Eustis, Va., Final Report USAAMRDL-TR-74-18, April 1974.

28. Woodward, F. A., "An Improved Method for the Aerodynamic Analaysis of Wing-Body-Tail Configurations in Subsonic and Supersonic Flow. Part I: Theory and Application," NACA CR2228, May 1973.

29. Rubbert, P. E. and Saaris, G. R., "Review and Evaluation of a Three-Dimensional Lifting Potential Flow Analysis Method for Arbitrary Configurations," AIAA 10th Aerospace Sciences Meeting, San Diego, Calif. AIAA Paper No. 72-188, January 17-19, 1972.

30. Hess, John L. and Faulkner, Suzanne M., "Determination of Low Speed Interference Effects by Superposition," AGARD Report CP-71-71, 1971.

31. McCormick, Barnes W. Jr., Aerodynamics of V/STOL Flight, Academic Press, Inc., New York, 1967, p. 28.

32. Aljabri, Abdulla S., "Prediction of Propeller Performance and Loading in Uniform and Nonuniform Flowfields," M.S. Thesis, The Pennsylvania State University, November 1978.

33. Jumper, Stephen J., "Computer Prediction of Three-Dimensional Potential Flow Fields in Which Aircraft Propellers Operate. (Computer Program Description and Users Manual)," The Pennsylvania State University, Department of Aerospace Engineering, Report PSU-AERO-R-79/80-25, August 1979.

34. Milne-Thomson, L. M. Theoretical Hydrodynamics, Fifth Edition, The Macmillan Co., New York, 1968, p. 488.

Appendix A

BODY SURFACE PANEL CALCULATIONS

Presented here is the method of partitioning the body surface into a network of N panels. Also, formulas for normal unit vector components and panel surface areas are presented. These methods and formulas follow the techniques used by Woodward, Dvorak, and Geller (27). Additionally, formulas for panel control point coordinates are given. All point coordinates are relative to a single body-fixed Cartesian axis system.

A.1 Partitioning of the Body Surface

A body-fixed Cartesian coordinate system is defined with positive x toward the front of the body, positive y to the right, and positive z downward. In general, the origin of the coordinate system may be located anywhere within or outside the body. However, for a body with left-right symmetry, the origin must lie somewhere on the plane of symmetry if the advantages of body symmetry are to be obtained.

The body is divided into a series of cross sections of a constant or nearly constant x coordinate. Cross sections are specified and numbered in sequence from front to aft on the body.

The Jth cross section is defined by NP discrete periphery points. As Figure A.1b shows, for the general nonsymmetric body cross section, all NP points are specified in sequence beginning near the top of the section and moving clockwise around the section, as viewed toward the rear of the body, ending with a repeat of the first point.

For the special symmetric case, Figure A.1a, in which all cross sections are symmetric about plane y = 0, only (NP + 1)/2 points need be specified in sequence starting at the top centerline and moving around

the left (-y) side of the section to the bottom centerline. The computer program automatically generates the image points on the other side of the plane of symmetry. However, if body sideslip is nonzero, a symmetric body must be input in the same manner as a nonsymmetric body.

Between adjacent cross sections, a ring of panels is generated by pairing corresponding points on each section. For example, the first and second points on section J are paired with the first and second points on section J + 1 to produce the first panel on the ring. Generally, panels are four-sided, but triangular panels are created by repeated descriptions of a single periphery point. The sequence of specifying points is such as to ensure that normal unit vectors, calculated below, will be outwardly directed from the body.

This systematic partitioning produces a network of N panels over the entire body (N/2 panels on each side of a symmetric body).

A.2 Panel Normal Unit Vector Components

Figure A.2 shows a typical panel created between cross sections J and J + 1. Identify the input corner points by 1, 2, 3, and 4 as shown on the figure. Define the two diagonal vectors, $\vec{B}_1$ and $\vec{B}_2$, given by

$$\vec{B}_1 = (x_4 - x_1)\vec{i} + (y_4 - y_1)\vec{j} + (z_4 - z_1)\vec{k} \tag{A.1}$$

and

$$\vec{B}_2 = (x_3 - x_2)\vec{i} + (y_3 - y_2)\vec{j} + (z_3 - z_2)\vec{k} \quad . \tag{A.2}$$

The vector cross product, $(\vec{B}_1 \times \vec{B}_2)$, produces a vector, $\vec{N}$, which is directed outward from and normal to the panel and is given by

$$\vec{N} = N_x\vec{i} + N_y\vec{j} + N_z\vec{k} \quad , \tag{A.3}$$

where the components are

$$N_x = [(y_4 - y_1)(z_3 - z_2) - (y_3 - y_2)(z_4 - z_1)] , \qquad (A.4a)$$

$$N_y = [(x_3 - x_2)(z_4 - z_1) - (x_4 - x_1)(z_3 - z_2)] , \qquad (A.4b)$$

and

$$N_z = [(x_4 - x_1)(y_3 - y_2) - (x_3 - x_2)(y_4 - y_1)] , \qquad (A.4c)$$

and where the magnitude is given by

$$|\vec{N}| = (N_x^{\,2} + N_y^{\,2} + N_z^{\,2})^{1/2} \quad . \qquad (A.5)$$

Finally, the outward drawn normal unit vector, $\vec{n}$, is vector $\vec{N}$ divided by its own length, $|\vec{N}|$. Thus, in terms of the corner points, $\vec{n}$ is given by

$$\vec{n} = n_x\vec{i} + n_y\vec{j} + n_z\vec{k} \qquad (A.6)$$

with components given by

$$n_x = \frac{N_x}{|\vec{N}|} , \qquad (A.7a)$$

$$n_y = \frac{N_y}{|\vec{N}|} , \qquad (A.7b)$$

and

$$n_z = \frac{N_z}{|\vec{N}|} , \qquad (A.7c)$$

where N_x, N_y, N_z, and $|\vec{N}|$ are given in Equations (A.4) and (A.5).

A.3 Generation of a Flat Quadrilateral Panel

In general, the four input corner points will not be coplanar. It is necessary to have a flat panel for which the surface area is calculable. Define the plane of this flat panel as one which is orthogonal to unit vector $\vec{n}$ and contains a point $(\hat{x}, \hat{y}, \hat{z})$ whose coordinates are the average of the four input points. Thus,

$$\hat{x} = \frac{1}{4}(x_1 + x_2 + x_3 + x_4) \quad , \tag{A.8a}$$

$$\hat{y} = \frac{1}{4}(y_1 + y_2 + y_3 + y_4) \quad , \tag{A.8b}$$

and

$$\hat{z} = \frac{1}{4}(z_1 + z_2 + z_3 + z_4) \quad . \tag{A.8c}$$

All input corner points 1, 2, 3, and 4 are of equal distance, d, from this plane. Distance d is given by

$$d = |n_x(\hat{x} - x_2) + n_y(\hat{y} - y_2) + n_z(\hat{z} - z_2)| \quad , \tag{A.9}$$

where $\hat{x}$, $\hat{y}$, and $\hat{z}$ are given in Equation set (A.8).

Input points 1, 2, 3, and 4 are projected distance d onto the new plane. Denote the new coplanar point coordinates as xx, yy, and zz. Then

$$xx_k = \begin{cases} (x_k - n_x d) & , \quad k = 1 \text{ or } 4 \\ (x_k + n_x d) & , \quad k = 2 \text{ or } 3 \quad ; \end{cases} \tag{A.10a}$$

$$yy_k = \begin{cases} (y_k - n_y d) & , \quad k = 1 \text{ or } 4 \\ (y_k + n_y d) & , \quad k = 2 \text{ or } 3 \quad ; \end{cases} \tag{A.10b}$$

and

$$zz_k = \begin{cases} (z_k - n_z d) & , \quad k = 1 \text{ or } 4 \\ (z_k + n_z d) & , \quad k = 2 \text{ or } 3 \end{cases} \tag{A.10c}$$

are the new coplanar points lying on the corners of the flat quadrilateral element. Figure A.3 shows this quadrilateral.

A.4 Surface Area of a Quadrilateral Panel

Figure A.4 shows the flat quadrilateral element with the new corner points given by Equation set (A.10). The sides of the quadrilateral have

lengths RS, ST, TU, and UR, and the diagonals have lengths RT and SU. Angles at corners 1 and 3 are denoted by αα and ββ, respectively.

In terms of the corner point coordinates, these six lengths are given by

$$RS = [(xx_1 - xx_3)^2 + (yy_1 - yy_3)^2 + (zz_1 - zz_3)^2]^{1/2} \quad , \text{(A.11a)}$$

$$ST = [(xx_1 - xx_2)^2 + (yy_1 - yy_2)^2 + (zz_1 - zz_2)^2]^{1/2} \quad , \text{(A.11b)}$$

$$TU = [(xx_4 - xx_2)^2 + (yy_4 - yy_2)^2 + (zz_4 - zz_2)^2]^{1/2} \quad , \text{(A.11c)}$$

$$UR = [(xx_3 - xx_4)^2 + (yy_3 - yy_4)^2 + (zz_3 - zz_4)^2]^{1/2} \quad , \text{(A.11d)}$$

$$RT = [(xx_2 - xx_3)^2 + (yy_2 - yy_3)^2 + (zz_2 - zz_3)^2]^{1/2} \quad , \text{(A.11e)}$$

and

$$SU = [(xx_4 - xx_1)^2 + (yy_4 - yy_1)^2 + (zz_4 - zz_1)^2]^{1/2} \quad . \text{(A.11f)}$$

Using the cosine law of triangles, the angles are given by

$$\alpha\alpha = \cos^{-1}[\frac{RS^2 + ST^2 - RT^2}{2(RS)(ST)}] \qquad \text{(A.12a)}$$

and

$$\beta\beta = \cos^{-1}[\frac{UR^2 + RS^2 - SU^2}{2(UR)(RS)}] \quad . \qquad \text{(A.12b)}$$

Finally, the panel area, S, is given by the formula for the area of a general plane quadrilateral as follows:

$$S = [(ff - RS)(ff - ST)(ff - TU)(ff - UR) - (RS)(ST)(TU)(UR)\cos^2(\frac{\alpha\alpha + \beta\beta}{2})]^{1/2} \qquad \text{(A.13a)}$$

where

$$ff = \frac{1}{2}(RS + ST + TU + UR) \quad , \qquad \text{(A.13b)}$$

and the other quantities are given by Equation sets (A.11) and (A.12).

A.5 Control Point on a Quadrilateral Panel

For the flat quadrilateral panel, the control point (XC, YC, ZC) is located at the intersection of two lines bisecting opposite sides of the panel, see Figure A.5. Define points (G_x, G_y, G_z) and (H_x, H_y, H_z) as the midpoints of panel edges RS and TU, respectively. In terms of the corner points, coordinates of points G and H are given by

$$G_x = \frac{1}{2}(xx_1 + xx_3) \quad , \tag{A.14a}$$

$$G_y = \frac{1}{2}(yy_1 + yy_3) \quad , \tag{A.14b}$$

$$G_z = \frac{1}{2}(zz_1 + zz_3) \quad , \tag{A.14c}$$

$$H_x = \frac{1}{2}(xx_2 + xx_4) \quad , \tag{A.14d}$$

$$H_y = \frac{1}{2}(yy_2 + yy_4) \quad , \tag{A.14e}$$

and

$$H_z = \frac{1}{2}(zz_2 + zz_4) \quad . \tag{A.14f}$$

Coordinates of control point (XC, YC, ZC) are then given by

$$XC = \frac{1}{2}(G_x + H_x) \quad , \tag{A.15a}$$

$$YC = \frac{1}{2}(G_y + H_y) \quad , \tag{A.15b}$$

and

$$ZC = \frac{1}{2}(G_z + H_z) \quad , \tag{A.15c}$$

where G_x, G_y, G_z, H_x, H_y, and H_z are given by Equation set (A.14).

A.6 Triangular Panels

As Figures A.6a and A.6b show, a triangular panel is generated if input points 1 and 2 are equal (this is Case a) or if points 3 and 4 are equal (this is Case b).

For triangular panels, the outward normal unit vector, $\vec{n}$, is calculated as described in Section A.2.

The input points themselves are coplanar for triangular panels, so the procedure for finding average coplanar corner points, Section A.3, is unnecessary.

The formulas for calculating surface area and control point coordinates of triangular panels differ from those used for quadrilateral panels and are described in the remaining two subsections.

A.6.1 Triangular panel surface area

For each case of a triangular panel, Case a (with the vertex at points 1 and 2) and Case b (with the vertex at points 3 and 4), a different set of expressions for panel area, S, is used.

First, consider the triangle, Case a, see Figure A.6a. Define the base length as UR and the side lengths as RS and SU. The angle at the vertex is $\alpha\alpha$. In terms of corner point coordinates, the three edge lengths are given by

$$RS = [(x_3 - x_1)^2 + (y_3 - y_1)^2 + (z_3 - z_1)^2]^{1/2} \quad , \quad (A.16a)$$

$$SU = [(x_4 - x_1)^2 + (y_4 - y_1)^2 + (z_4 - z_1)^2]^{1/2} \quad , \quad (A.16b)$$

and

$$UR = [(x_4 - x_3)^2 + (y_4 - y_3)^2 + (z_4 - z_3)^2]^{1/2} \quad . \quad (A.16c)$$

Using the law of cosines, the angle $\alpha\alpha$ is given by

$$\alpha\alpha = \cos^{-1}\left[\frac{(RS)^2 + (SU)^2 - (UR)^2}{2(RS)(SU)}\right] \quad . \quad (A.17)$$

Finally, using the area formula for a general triangle, the surface area, S, is

$$S = \frac{1}{2}(RS)(SU)\sin(\alpha\alpha) \quad , \quad (A.18)$$

where RS, SU, and $\alpha\alpha$ are given by Equations (A.16) and (A.17), respectively.

Second, consider the triangle, Case b, see Figure A.6b. Define the base length as ST and the side lengths as RS and TR. The angle at the vertex is $\beta\beta$. In terms of corner point coordinates, the three edge lengths are given by

$$RS = [(x_3 - x_1)^2 + (y_3 - y_1)^2 + (z_3 - z_1)^2]^{1/2} \quad , \quad (A.19a)$$

$$ST = [(x_2 - x_1)^2 + (y_2 - y_1)^2 + (z_2 - z_1)^2]^{1/2} \quad , \quad (A.19b)$$

and

$$TR = [(x_3 - x_2)^2 + (y_3 - y_2)^2 + (z_3 - z_2)^2]^{1/2} \quad . \quad (A.19c)$$

Angle $\beta\beta$ is given, using the law of cosines, as

$$\beta\beta = \cos^{-1}[\frac{(RS)^2 + (TR)^2 - (ST)^2}{2(RS)(TR)}] \quad . \quad (A.20)$$

Then the surface area, S, is given by the area formula for a general triangle as follows:

$$S = \frac{1}{2}(RS)(TR)\sin(\beta\beta) \quad , \quad (A.21)$$

where RS, TR, and $\beta\beta$ are given, respectively, by Equations (A.19) and (A.20).

A.6.2 Triangular panel control point

As with area formulas, the formulas for control point coordinates for the triangular panel, Case a, differ slightly from those for the other triangular panel, Case b.

First, consider the triangular panel, Case a, see Figure A.6a. The control point (XC, YC, ZC) is at the area centroid which is located midway along line segment DE. Line DE intersects each panel edge one-

third the way from the base of the triangle. Thus, points (D_x, D_y, D_z) and (E_x, E_y, E_z) are functions of the corner points as follows:

$$D_x = x_3 + \frac{1}{3}(x_1 - x_3) \quad , \tag{A.22a}$$

$$D_y = y_3 + \frac{1}{3}(y_1 - y_3) \quad , \tag{A.22b}$$

$$D_z = z_3 + \frac{1}{3}(z_1 - z_3) \quad , \tag{A.22c}$$

$$E_x = x_4 + \frac{1}{3}(x_1 - x_4) \quad , \tag{A.22d}$$

$$E_y = y_4 + \frac{1}{3}(y_1 - y_4) \quad , \tag{A.22e}$$

and

$$E_z = z_4 + \frac{1}{3}(z_1 - z_4) \quad . \tag{A.22f}$$

Then in terms of Equation set (A.22), the coordinates of the control point for the triangular panel, Case a, are given by

$$XC = \frac{1}{2}(D_x + E_x) \quad , \tag{A.23a}$$

$$YC = \frac{1}{2}(D_y + E_y) \quad , \tag{A.23b}$$

and

$$ZC = \frac{1}{2}(D_z + E_z) \quad . \tag{A.23c}$$

Second, consider the triangular panel, Case b, shown in Figure A.6b. Following the notation of Case a, the control point (XC, YC, ZC) is situated at the area centroid, which lies midway along line segment DE. Line DE intersects each panel edge one-third the way from the base of the triangle. In terms of corner point coordinates, the coordinates of points (D_x, D_y, D_z) and (E_x, E_y, E_z) are given as follows:

$$D_x = x_1 + \frac{1}{3}(x_3 - x_1) \quad , \tag{A.24a}$$

$$D_y = y_1 + \frac{1}{3}(y_3 - y_1) \quad , \tag{A.24b}$$

$$D_z = z_1 + \frac{1}{3}(z_3 - z_1) \quad , \tag{A.24c}$$

$$E_x = x_2 + \frac{1}{3}(x_3 - x_2) \quad , \tag{A.24d}$$

$$E_y = y_2 + \frac{1}{3}(y_3 - y_2) \quad , \tag{A.24e}$$

and

$$E_z = z_2 + \frac{1}{3}(z_3 - z_2) \quad . \tag{A.24f}$$

Finally, in terms of Equation set (A.24), the control point coordinates for the triangular panel, Case b, are given by

$$XC = \frac{1}{2}(D_x + E_x) \quad , \tag{A.25a}$$

$$YC = \frac{1}{2}(D_y + E_y) \quad , \tag{A.25b}$$

and

$$ZC = \frac{1}{2}(D_z + E_z) \quad . \tag{A.25c}$$

Appendix B

DERIVATION OF FREE STREAM CARTESIAN VELOCITY COMPONENTS

Denote by V the magnitude of the free stream velocity. Define a wind Cartesian axis system, $\bar{\bar{x}}$, $\bar{\bar{y}}$, $\bar{\bar{z}}$, in which V is always directed along the negative $\bar{\bar{x}}$ axis as in Figure B.1. Next, define by x, y, and z the body-fixed Cartesian axes whose origin coincides with the wind axes origin. Then for a body having no angle of attack, α, or sideslip, β, the body axes are coincident with the wind axes. This is shown in Figure B.1.

For the general case of the body having an angle of attack, α, and sideslip, β, it is necessary to derive expressions for free stream components, u, v, and w, along the x, y, and z axes, respectively. With the body and wind axes initially coincident, a pair of rotations is made. See Figure B.2. First, a rotation of α about the $\bar{\bar{y}}$ axis is made. Denote the resulting intermediate set of axes by x*, y*, and z*. Second, a rotation of η about the z* axis is made resulting in the body axes, x, y, and z, in their final position with angle of attack, α, and sideslip β. Angle η is chosen so as to produce the desired sideslip angle, β, as viewed in the $\bar{\bar{x}}$ - $\bar{\bar{y}}$ plane. These rotations yield relations between the $\bar{\bar{x}}$, $\bar{\bar{y}}$, $\bar{\bar{z}}$ system and the x, y, z system. Then derivation with respect to time of the axis transformations yields velocities u, v, and w as functions of V, α, and β.

Figures B.2a, B.2b, and B.2c show the angular rotations and show the resulting projected lengths of all three sets of axes in three different views. For scale, the axes have a true arbitrary length, L.

It is first necessary to derive the expression for angle η as a function of α and β. Refer to Figure B.2a, showing the $\bar{\bar{x}}$ - $\bar{\bar{y}}$ plane and

portraying β in its true arc. In this view, axes x^*, y^*, x, and y project onto an ellipse given by the equation

$$[\frac{\bar{\bar{x}}}{L \cos \alpha}]^2 + [\frac{\bar{\bar{y}}}{L}]^2 = 1 \quad . \tag{B.1}$$

In Figure B.2a, the projection of axis x ends at point (X,Y) on the ellipse. Coordinates of point (X,Y) thus satisfy the following three relationships:

$$[\frac{X}{L \cos \alpha}]^2 + [\frac{Y}{L}]^2 = 1 \quad , \tag{B.2}$$

$$X = L \cos \alpha \cos \eta \ , \tag{B.3}$$

and

$$\tan \beta = \frac{Y}{X} \quad . \tag{B.4}$$

Combining Equations (B.2) and (B.3) with Equation (B.4) gives the following desired result:

$$\eta = \tan^{-1}(\tan \beta \cos \alpha) \quad . \tag{B.5}$$

As seen in Figure B.2b, the rotation of η about z^* yields the following relations between axis sets x^*, y^*, z^* and x, y, z:

$$x^* = x \cos \eta - y \sin \eta \ , \tag{B.6a}$$

$$y^* = x \sin \eta + y \cos \eta \ , \tag{B.6b}$$

and

$$z^* = z \quad . \tag{B.6c}$$

Then as shown in Figure B.2c, rotation of α about $\bar{\bar{y}}$ yields the following relations between axis sets $\bar{\bar{x}}$, $\bar{\bar{y}}$, $\bar{\bar{z}}$ and x^*, y^*, z^*:

$$\bar{\bar{x}} = x^* \cos \alpha + z^* \sin \alpha \ , \tag{B.7a}$$

$$\bar{\bar{y}} = y^* \quad , \tag{B.7b}$$

and

$$\bar{\bar{z}} = z^* \cos \alpha - x^* \sin \alpha \ . \tag{B.7c}$$

Equation set (B.6) is substituted for x^*, y^*, and z^* in Equation set (B.7), and the resulting system is inverted using Cramer's rule. This gives the final relations between the wind axes, $\bar{\bar{x}}$, $\bar{\bar{y}}$, and $\bar{\bar{z}}$, and the rotated body axes, x, y, and z, as follows:

$$x = (\cos\alpha\cos\eta)\bar{\bar{x}} + (\sin\eta)\bar{\bar{y}} - (\sin\alpha\cos\eta)\bar{\bar{z}} \quad , \tag{B.8a}$$

$$y = -(\cos\alpha\sin\eta)\bar{\bar{x}} + (\cos\eta)\bar{\bar{y}} + (\sin\alpha\sin\eta)\bar{\bar{z}} \quad , \tag{B.8b}$$

and

$$z = (\sin\alpha)\bar{\bar{x}} + (\cos\alpha)\bar{\bar{z}} \quad . \tag{B.8c}$$

The time derivative along each axis gives the velocity component parallel to each axis. By definition of the orientation of the wind axes with the free stream, the following holds:

$$\frac{d\bar{\bar{x}}}{dt} = -V \tag{B.9}$$

and

$$\frac{d\bar{\bar{y}}}{dt} = \frac{d\bar{\bar{z}}}{dt} = 0 \quad . \tag{B.10}$$

Also, define the following:

$$u = \frac{dx}{dt} \quad , \tag{B.11a}$$

$$v = \frac{dy}{dt} \quad , \tag{B.11b}$$

and

$$w = \frac{dz}{dt} \quad . \tag{B.11c}$$

Derivation with respect to time of Equation set (B.8) and substitution of Equations (B.9), (B.10), and (B.11) give

$$u = -V\cos\alpha\cos\eta \ , \tag{B.12a}$$

$$v = V\cos\alpha\sin\eta \ , \tag{B.12b}$$

and

$$w = -V\sin\alpha \ , \tag{B.12c}$$

where η is given by Equation (B.5).

Equation set (B.12) gives the body Cartesian components of the free stream velocity for the body at angle of attack, α, and sideslip, β. These components are illustrated in Figure B.3.

Appendix C

COMPUTATION OF VELOCITY COMPONENTS INDUCED BY A STRAIGHT VORTEX FILAMENT OF ARBITRARY ORIENTATION

This appendix derives the formulas used by a computer subroutine to calculate the Cartesian velocity components at some specified point, $(\hat{x}, \hat{y}, \hat{z})$, which are induced by a straight vortex filament of finite length. The Biot-Savart law is used to obtain the velocity magnitude, and special precautions are used to circumvent numerical difficulties inherent in the Biot-Savart law.

C.1 Geometry of the Arbitrary Vortex Filament

Refer to Figure C.1. The vortex filament of strength, Γ, starts at point 1, having coordinates $(\hat{x}_1, \hat{y}_1, \hat{z}_1)$, and ends at point 2, having coordinates $(\hat{x}_2, \hat{y}_2, \hat{z}_2)$; both endpoints and Γ are specified. The vortex filament coincides with a vector, $\vec{T}$, given by

$$\vec{T} = (\hat{x}_2 - \hat{x}_1)\vec{i} + (\hat{y}_2 - \hat{y}_1)\vec{j} + (\hat{z}_2 - \hat{z}_1)\vec{k} \qquad (C.1)$$

of length, T, given by

$$T = [(\hat{x}_2 - \hat{x}_1)^2 + (\hat{y}_2 - \hat{y}_1)^2 + (\hat{z}_2 - \hat{z}_1)^2]^{1/2} \quad . \qquad (C.2)$$

Specify the point, $(\hat{x}, \hat{y}, \hat{z})$, at which induced velocities are to be found. There exists a point C, having coordinates (C_x, C_y, C_z), coordinates to be determined, positioned on the line containing the vortex filament such that a vector, $\vec{h}$, from $(\hat{x}, \hat{y}, \hat{z})$ to (C_x, C_y, C_z) is perpendicular to the filament. $\vec{h}$ is given by

$$\vec{h} = (C_x - \hat{x})\vec{i} + (C_y - \hat{y})\vec{j} + (C_z - \hat{z})\vec{k} \qquad (C.3)$$

and has a length, h, given by

$$h = [(C_x - \hat{x})^2 + (C_y - \hat{y})^2 + (C_z - \hat{z})^2]^{1/2} \quad . \qquad (C.4)$$

Denote by $\vec{s}$ a vector between point 1 and point C expressed as

$$\vec{s} = (C_x - \hat{x}_1)\vec{i} + (C_y - \hat{y}_1)\vec{j} + (C_z - \hat{z}_1)\vec{k} \quad . \qquad (C.5)$$

Lines D1 and D2 connect point $(\hat{x}, \hat{y}, \hat{z})$ with the vortex starting point and endpoint, respectively. Their lengths are given by the following:

$$D1 = [(\hat{x} - \hat{x}_1)^2 + (\hat{y} - \hat{y}_1)^2 + (\hat{z} - \hat{z}_1)^2]^{1/2} \qquad (C.6)$$

and

$$D2 = [(\hat{x} - \hat{x}_2)^2 + (\hat{y} - \hat{y}_2)^2 + (\hat{z} - \hat{z}_2)^2]^{1/2} \quad . \qquad (C.7)$$

D1 and D2 intersect the vortex at angles $\hat{\theta}_1$ and $\hat{\theta}_2$, respectively. Using the law of cosines for triangles, these angles are given in terms of previously defined quantities as

$$\cos \hat{\theta}_1 = \frac{T^2 + D1^2 - D2^2}{2(T)(D1)} \qquad (C.8)$$

and

$$\cos \hat{\theta}_2 = \frac{T^2 + D2^2 - D1^2}{2(T)(D2)} \quad . \qquad (C.9)$$

It remains to find the coordinates C_x, C_y, and C_z of point C in terms of the given geometry. As Figure C.1 shows, vectors $\vec{s}$ and $\vec{T}$ are colinear. Thus, the vector cross product, $(\vec{s} \times \vec{T})$, is zero as is each component of the vector $(\vec{s} \times \vec{T})$. This vector cross product is performed using Equations (C.1) and (C.5), and each component of the resulting vector is equated with zero. The result is a set of three equations for the unknown values of C_x, C_y, and C_z as follows:

$$0 + (\hat{z}_2 - \hat{z}_1)C_y - (\hat{y}_2 - \hat{y}_1)C_z = [\hat{y}_1(\hat{z}_2 - \hat{z}_1) - \hat{z}_1(\hat{y}_2 - \hat{y}_1)], \qquad (C.10)$$

$$-(\hat{z}_2 - \hat{z}_1)C_x + 0 + (\hat{x}_2 - \hat{x}_1)C_z = [\hat{z}_1(\hat{x}_2 - \hat{x}_1) - \hat{x}_1(\hat{z}_2 - \hat{z}_1)] \quad , \qquad (C.11)$$

and

$$(\hat{y}_2 - \hat{y}_1)C_x - (\hat{x}_2 - \hat{x}_1)C_y + 0 = [\hat{x}_1(\hat{y}_2 - \hat{y}_1) - \hat{y}_1(\hat{x}_2 - \hat{x}_1)]. \qquad (C.12)$$

However, the above three equations form an indeterminant system. A fourth independent equation is required to solve for C_x, C_y, and C_z. Because vectors $\vec{h}$ and $\vec{T}$ are orthogonal, their scaler product, $(\vec{h} \cdot \vec{T})$, is zero. Using Equations (C.1) and (C.3) in the scaler product and equating with zero gives a fourth equation containing unknowns C_x, C_y, and C_z as follows:

$$(\hat{x}_2 - \hat{x}_1)C_x + (\hat{y}_2 - \hat{y}_1)C_y + (\hat{z}_2 - \hat{z}_1)C_z = [\hat{x}(\hat{x}_2 - \hat{x}_1) + \hat{y}(\hat{y}_2 - \hat{y}_1) + \hat{z}(\hat{z}_2 - \hat{z}_1)] \quad . \tag{C.13}$$

Simultaneous solution of Equations (C.11), (C.12), and (C.13) for unknowns C_x, C_y, and C_z, using Cramer's rule, gives the following results:

$$C_x = \frac{\{\hat{x}(AA)^2 + \hat{x}_1[(BB)^2 + (CC)^2] + AA[BB(\hat{y} - \hat{y}_1) + CC(\hat{z} - \hat{z}_1)]\}}{(AA)^2 + (BB)^2 + (CC)^2}, \tag{C.14a}$$

$$C_y = \frac{\{\hat{y}(BB)^2 + \hat{y}_1[(AA)^2 + (CC)^2] + BB[AA(\hat{x} - \hat{x}_1) + CC(\hat{z} - \hat{z}_1)]\}}{(AA)^2 + (BB)^2 + (CC)^2}, \tag{C.14b}$$

and

$$C_z = \frac{\{\hat{z}(CC)^2 + \hat{z}_1[(AA)^2 + (BB)^2] + CC[AA(\hat{x} - \hat{x}_1) + BB(\hat{y} - \hat{y}_1)]\}}{(AA)^2 + (BB)^2 + (CC)^2}, \tag{C.14c}$$

where $AA = (\hat{x}_2 - \hat{x}_1)$, $BB = (\hat{y}_2 - \hat{y}_1)$, and $CC = (\hat{z}_2 - \hat{z}_1)$.

C.2 Magnitude of the Total Induced Velocity

Denote by W the magnitude of the total velocity induced at point $(\hat{x}, \hat{y}, \hat{z})$ by the vortex filament. When this point lies on the line containing the filament, length h is zero. In this case, W is fixed at zero and the Biot-Savart law is not used.

When length h is nonzero, the Biot-Savart law is used to calculate W. To ensure that W is not unrealistically large, it is checked to see

if it is larger than a maximum velocity limit. This velocity limit equals 20 percent of the free stream velocity, V. Should W be found larger than the limit velocity, W is set equal to the limit value, and that is the value used to obtain the velocity components.

In summary, velocity W is calculated using one of the following equations:

$$W = 0 \ , \quad \text{if } h = 0 \ ; \tag{C.15a}$$

$$W = \frac{\Gamma}{4\pi h}(\cos \hat{\theta}_1 + \cos \hat{\theta}_2) \ , \quad \text{if } h \neq 0 \ ; \tag{C.15b}$$

or

$$W = 0.2V \ , \quad \text{if } W \text{ [by Equation (C.15b)]} > 0.2V \ , \tag{C.15b}$$

where V is the magnitude of the free stream velocity and all other quantities have been defined previously.

C.3 Induced Velocity Components

At point $(\hat{x}, \hat{y}, \hat{z})$ the induced velocity vector, $\vec{W}$, is directed normal to the plane containing $\vec{T}$ and $\vec{h}$. Define a unit vector, $\vec{n}_w$, which is also normal to the plane containing $\vec{T}$ and $\vec{h}$ and has the same direction as $\vec{W}$, see Figure C.1. The vector cross product $(\vec{h} \times \vec{T})$ is also a vector normal to the plane containing $\vec{T}$ and $\vec{h}$. Therefore, $\vec{n}_w$ can be given by

$$\vec{n}_w = \frac{(\vec{h} \times \vec{T})}{|\vec{h} \times \vec{T}|} \ . \tag{C.16}$$

Substitution of Equations (C.1) and (C.3) into (C.16) yields the following expressions for the components of $\vec{n}_w$:

$$n_{w_x} = \frac{1}{RXR}[CC(C_y - \hat{y}) - BB(C_z - \hat{z})] \ , \tag{C.17a}$$

$$n_{w_y} = \frac{1}{RXR}[AA(C_z - \hat{z}) - CC(C_x - \hat{x})] \ , \tag{C.17b}$$

and

$$n_{w_z} = \frac{1}{RXR}[BB(C_x - \hat{x}) - AA(C_y - \hat{y})] \ , \tag{C.17c}$$

where

$$RXR = \{[CC(C_y - \hat{y}) - BB(C_z - \hat{z})]^2 + [AA(C_z - \hat{z}) - CC(C_x - \hat{x})]^2 + [BB(C_x - \hat{x}) - AA(C_y - \hat{y})]^2\}^{1/2} \quad , \tag{C.17d}$$

and where $AA = (\hat{x}_2 - \hat{x}_1)$, $BB = (\hat{y}_2 - \hat{y}_1)$, $CC = (\hat{z}_2 - \hat{z}_1)$, and C_x, C_y, and C_z are given by Equation set (C.14). Express the induced velocity vector in terms of its Cartesian components as follows:

$$\vec{W} = u_f\vec{i} + v_f\vec{j} + w_f\vec{k} \quad . \tag{C.18}$$

These components are shown in Figure C.1. Because $\vec{W}$ coincides with unit vector $\vec{n}_w$, the following holds:

$$\vec{n}_w = \frac{\vec{W}}{W} \quad . \tag{C.19}$$

Equations (C.15), (C.18), and (C.17) are substituted for W, $\vec{W}$, and components of $\vec{n}_w$, respectively, in Equation (C.19). By comparing like terms on each side of the resulting equality, it follows that the desired components of the vortex filament-induced velocity are given by

$$u_f = n_{w_x}W \quad , \tag{C.20a}$$

$$v_f = n_{w_y}W \quad , \tag{C.20b}$$

and

$$w_f = n_{w_z}W \quad . \tag{C.20c}$$

Appendix D

TRANSFORMATIONS RELATING THE PROPELLER PLANE AXIS SYSTEM TO THE BODY-FIXED AXIS SYSTEM

D.1 Coordinate Transformations

Denote by $\bar{x}$, $\bar{y}$, and $\bar{z}$ the Cartesian coordinate axes which remain attached to the propeller plane. Positive $\bar{x}$ is directed along the propeller axis of rotation in the thrust direction as in Figure D.1. A point, P, on the propeller plane is positioned relative to a cylindrical coordinate system, $r - \psi$, where azimuth angle, ψ, is measured clockwise from the negative $\bar{z}$ axis. Also denote by x', y', and z' three Cartesian axes which remain parallel to the body-fixed axes, x, y, and z, but which are displaced to a point (X_{hub}, Y_{hub}, Z_{hub}) relative to the body-fixed axes. Figure D.1 shows all the axis systems and shows the propeller plane initially without angle of attack, α_p, or sideslip, β_p. In this situation the $\bar{x}$, $\bar{y}$, and $\bar{z}$ axes are coincident with the x', y', and z' axes, respectively.

For the general case of the propeller plane oriented at some combination of angle of attack, α_p, and sideslip, β_p, relative to the body, it is necessary to express the $r - \psi$ coordinate system, attached to the propeller plane, in terms of the body-fixed axes, x, y, and z.

With the $\bar{x}$, $\bar{y}$, and $\bar{z}$ axes initially coincident with the x', y', and z' axes, a pair of rotations is made, see Figure D.2. First, a rotation of α_p about the y' axis is made. Denote the resulting intermediate set of axes by x*, y*, and z*. Second, a rotation of η_p about the z* axis is made resulting in the propeller plane-fixed axes, $\bar{x}$, $\bar{y}$, and $\bar{z}$, in their final skewed orientation with angle of attack, α_p, and sideslip, β_p, with respect to the x', y', and z' axes. Angle η_p is chosen so as

to produce the desired sideslip angle, β_p, as viewed in the $x' - y'$ plane. Once transformations between the skewed $\bar{x}$, $\bar{y}$, and $\bar{z}$ axes and the x', y', and z' axes have been obtained, the final transformations between the $r - \psi$ and $x - y - z$ axis systems are then obtained.

Figures D.2a, D.2b, and D.2c show the two angular rotations and show the resulting projected lengths of all four sets of Cartesian axes in three different views. For scale, the axes have a true arbitrary length, L.

It is first necessary to derive the expression for angle η_p as a function of α_p and β_p. Refer to Figure D.2a, showing the $x' - y'$ plane and portraying β_p in its true arc. In this view, axes x^*, y^*, $\bar{x}$, and $\bar{y}$ project onto an ellipse given by the equation

$$[\frac{x'}{L \cos \alpha_p}]^2 + [\frac{y'}{L}]^2 = 1 \quad . \tag{D.1}$$

In Figure D.2a, the projection of axis $\bar{x}$ ends at point (X, Y) on the ellipse. Coordinates of point (X, Y) thus satisfy the following three relationships:

$$[\frac{X}{L \cos \alpha_p}]^2 + [\frac{Y}{L}]^2 = 1 \quad , \tag{D.2}$$

$$X = L \cos \alpha_p \cos \eta_p \quad , \tag{D.3}$$

and

$$\tan \beta_p = \frac{Y}{X} \quad . \tag{D.4}$$

Combining Equations (D.2) and (D.3) with Equation (D.4) gives

$$\eta_p = \tan^{-1}(\tan \beta_p \cos \alpha_p) \quad , \tag{D.5}$$

which is the desired function relating η_p to α_p and β_p.

As seen in Figure D.2b, the rotation of η_p about z^* yields the following relationships between axis sets x^*, y^*, z^* and $\bar{x}$, $\bar{y}$, $\bar{z}$:

$$x^* = \bar{x} \cos \eta_p - y \sin \eta_p \quad , \tag{D.6a}$$

$$y^* = \bar{x} \sin \eta_p + \bar{y} \cos \eta_p \quad , \tag{D.6b}$$

and

$$z^* = \bar{z} \quad . \tag{D.6c}$$

As shown in Figure D.2c, rotation of α_p about y' yields the following relationships between axis sets x', y', z' and x*, y*, z*:

$$x' = x^* \cos \alpha_p + z^* \sin \alpha_p \quad , \tag{D.7a}$$

$$y' = y^* \quad , \tag{D.7b}$$

and

$$z' = z^* \cos \alpha_p - x^* \sin \alpha_p \quad . \tag{D.7c}$$

Axes x', y', and z' are displaced to point (X_{hub}, Y_{hub}, Z_{hub}) relative to the body-fixed axes x, y, and z, so the following applies:

$$x = x' + X_{hub} \quad , \tag{D.8a}$$

$$y = y' + Y_{hub} \quad , \tag{D.8b}$$

and

$$z = z' + Z_{hub} \quad . \tag{D.8c}$$

Equation set (D.6) is substituted into Equation set (D.7) to eliminate x*, y*, and z*. Then, substitution into Equation set (D.8) produces the following relationships between the body-fixed axes, x, y, and z, and the propeller plane-fixed axes, $\bar{x}$, $\bar{y}$, and $\bar{z}$:

$$x = (\cos \alpha_p \cos \eta_p)\bar{x} - (\cos \alpha_p \sin \eta_p)\bar{y} + (\sin \alpha_p)\bar{z} + X_{hub} \quad , \tag{D.9a}$$

$$y = (\sin \eta_p)\bar{x} + (\cos \eta_p)\bar{y} + Y_{hub} \quad , \tag{D.9b}$$

and

$$z = -(\sin \alpha_p \cos \eta_p)\bar{x} + (\sin \alpha_p \sin \eta_p)\bar{y} + (\cos \alpha_p)\bar{z} + Z_{hub} \quad . \tag{D.9c}$$

As shown in Figure D.3, the cylindrical coordinate system, r - ψ, on the propeller plane is related to the propeller plane-fixed $\bar{x}$, $\bar{y}$, and

$\bar{z}$ axes as follows:

$$\bar{x} = 0 \quad \text{(on the propeller plane)} \quad , \tag{D.10a}$$

$$\bar{y} = r \sin \psi \quad , \tag{D.10b}$$

and

$$\bar{z} = -r \cos \psi \quad . \tag{D.10c}$$

Equation set (D.10) is substituted into Equation set (D.9). Then point P, at coordinates (r, ψ) on the propeller plane, has corresponding Cartesian coordinates (X_p, Y_p, Z_p) in the body-fixed axis system given by

$$X_p = -r(\sin \psi \cos \alpha_p \sin \eta_p + \cos \psi \sin \alpha_p) + X_{hub} \quad , \tag{D.11a}$$

$$Y_p = r(\sin \psi \cos \eta_p) + Y_{hub} \quad , \tag{D.11b}$$

and

$$Z_p = r(\sin \psi \sin \alpha_p \sin \eta_p - \cos \psi \cos \alpha_p) + Z_{hub} \quad , \tag{D.11c}$$

where η_p is given by Equation (D.5).

Equation set (D.11) is the resulting transformation from the propeller plane-fixed cylindrical coordinates to the body-fixed Cartesian coordinates for a point on a propeller plane centered at $(X_{hub}, Y_{hub}, Z_{hub})$ and tilted with an angle of attack, α_p, and sideslip, β_p, relative to the body-fixed axes.

D.2 Velocity Component Transformations

It is necessary to derive transformations which convert Cartesian velocity components, u_p, v_p, and w_p, at point P on the propeller plane, relative to the body-fixed axes, into corresponding cylindrical system velocity components, v_{a_p}, v_{r_p}, and v_{t_p}. As shown in Figure D.3, v_{a_p}, v_{r_p}, and v_{t_p} are axial, radial, and tangential velocity components, respectively, with the axial component directed normal to the propeller

plane and positive in the thrust direction (into the figure). Tangential velocity, v_{t_p}, at P is in-plane and positive if it follows the right-hand rotation of a propeller. v_{r_p} is in-plane and positive radially outward.

Equation set (D.9) is inverted using Cramer's rule giving expressions relating the propeller plane-fixed axes, $\bar{x}$, $\bar{y}$, and $\bar{z}$ to the body-fixed axes, x, y, and z, as follows:

$$\bar{x} = (\cos \alpha_p \cos \eta_p)(x - X_{hub}) + (\sin \eta_p)(y - Y_{hub}) - (\sin \alpha_p \cos \eta_p)(z - Z_{hub}) \quad , \tag{D.12a}$$

$$\bar{y} = -(\cos \alpha_p \sin \eta_p)(x - X_{hub}) + (\cos \eta_p)(y - Y_{hub}) + (\sin \alpha_p \sin \eta_p)(z - Z_{hub}) \quad , \tag{D.12b}$$

and

$$\bar{z} = (\sin \alpha_p)(x - X_{hub}) + (\cos \alpha_p)(z - Z_{hub}) \quad . \tag{D.12c}$$

At a point on the propeller plane, the velocity components, u_p, v_p, and w_p, relative to the body-fixed Cartesian axis system are given by the following time derivatives:

$$u_p = \frac{dx}{dt} \quad , \tag{D.13a}$$

$$v_p = \frac{dy}{dt} \quad , \tag{D.13b}$$

and

$$w_p = \frac{dz}{dt} \quad . \tag{D.13c}$$

Similarly, the velocity components, $\bar{u}_p$, $\bar{v}_p$, and $\bar{w}_p$, relative to the propeller plane-fixed Cartesian axis system are given by time derivatives as follows:

$$\bar{u}_p = \frac{d\bar{x}}{dt} \quad , \tag{D.14a}$$

$$\bar{v}_p = \frac{d\bar{y}}{dt} \quad , \tag{D.14b}$$

and

$$\bar{w}_p = \frac{d\bar{z}}{dt} \quad . \tag{D.14c}$$

The time derivative of Equation set (D.12) is taken and Equations (D.13) and (D.14) are substituted. Observe that the derivatives of X_{hub}, Y_{hub}, and Z_{hub} vanish. The result is a set of relations transforming the velocity components, u_p, v_p, and w_p, into components, $\bar{u}_p$, $\bar{v}_p$, and $\bar{w}_p$, as follows:

$$\bar{u}_p = (\cos \alpha_p \cos \eta_p)u_p + (\sin \eta_p)v_p - (\sin \alpha_p \cos \eta_p)w_p \quad , \tag{D.15a}$$

$$\bar{v}_p = -(\cos \alpha_p \sin \eta_p)u_p + (\cos \eta_p)v_p + (\sin \alpha_p \sin \eta_p)w_p \quad , \tag{D.15b}$$

and

$$\bar{w}_p = (\sin \alpha_p)u_p + (\cos \alpha_p)w_p \quad . \tag{D.15c}$$

As indicated in Figure D.3, propeller plane-fixed Cartesian velocity components, $\bar{u}_p$, $\bar{v}_p$, and $\bar{w}_p$, are related to the corresponding axial, radial, and tangential velocities, v_{a_p}, v_{r_p}, and v_{t_p}, at point P as follows:

$$v_{a_p} = \bar{u}_p \quad , \tag{D.16a}$$

$$v_{r_p} = (\sin \psi)\bar{v}_p - (\cos \psi)\bar{w}_p \quad , \tag{D.16b}$$

and

$$v_{t_p} = (\cos \psi)\bar{v}_p + (\sin \psi)\bar{w}_p \quad . \tag{D.16c}$$

Finally, Equation set (D.15) is substituted into Equation set (D.16). This produces the following relationships:

$$v_{a_p} = (\cos \alpha_p \cos \eta_p)u_p + (\sin \eta_p)v_p - (\sin \alpha_p \cos \eta_p)w_p \quad , \tag{D.17a}$$

$$v_{r_p} = -(\sin \alpha_p \cos \psi + \cos \alpha_p \sin \eta_p \sin \psi)u_p + (\cos \eta_p \sin \psi)v_p$$
$$+ (\sin \alpha_p \sin \eta_p \sin \psi - \cos \alpha_p \cos \psi)w_p \quad , \tag{D.17b}$$

and

$$v_{t_p} = (\sin \alpha_p \sin \psi - \cos \alpha_p \sin \eta_p \cos \psi)u_p + (\cos \eta_p \cos \psi)v_p + (\cos \alpha_p \sin \psi + \sin \alpha_p \sin \eta_p \cos \psi)w_p \ , \quad \text{(D.17c)}$$

where η_p is given by Equation (D.5). For a point P at position (r, ψ) on the propeller plane, Equations (D.17) are the desired relations which transform the body-fixed Cartesian velocity components at P, u_p, v_p, and w_p, into the corresponding axial, radial, and tangential velocity components, v_{a_p}, v_{r_p}, and v_{t_p}, relative to the propeller plane-fixed cylindrical coordinate system.

Appendix E

MEASUREMENT AND MAPPING OF THE PIPER CHEROKEE PA-28-180 COWL AND SPINNER SURFACE GEOMETRY

No manufacturer-supplied detail drawings of the cowl and spinner exist for the Piper Cherokee PA-28-180. As these airframe components are proximate to the propeller plane, a detailed description of these surface shapes was important for creating a good computer paneling model. Therefore, to obtain this description the only recourse was to physically measure the cowl and spinner geometry on an actual aircraft. Direct measurement of this geometry on The Pennsylvania State University-owned Cherokee 180 research airplane, tail number N907PS, was conducted. This measurement process is described in this appendix.

Measurement by triangulation was performed using two precision surveying transits, both capable of angular measurement to within a tolerance of ± 20 seconds of arc. Figures E.1a and E.1b schematically illustrate the deployment of the two transits, identified as transit A and transit B.

Parked on a flat surface, the aircraft fuselage was jacked to the horizontal position. The horizontal position was determined by placing a level on the reference leveling screws located on the exterior of the fuselage beneath the pilot's window as shown in Figure E.1b.

Transit A was positioned on the fuselage plane of symmetry at a distance of approximately 30 percent wing span forward of the spinner. As shown in Figure E.1b, transit A was vertically positioned such that the horizontal line of sight intersected the spinner near its tip. This intersection point, on the plane of symmetry, was marked and designated as the coordinate origin for all measurements. The horizontal distance X_A between transit A and the origin was precisely measured.

Next, using sightings from transit A, transit B was positioned directly to the left of the coordinate origin at a precisely measured horizontal distance χ_B as shown in Figure E.1a. Thus, the lines of sight of both transits, viewed from above, intersected at a right angle at the origin. The height above ground of transit B was slightly less than the height of the origin. The vertical distance $\Delta\chi$ between the origin and transit B was measured. Knowledge of χ_A, χ_B, and $\Delta\chi$ completely determined the transit positions with respect to the origin, and the transits were then ready for use.

The cowl and spinner surfaces were prepared for measurement by covering the left half of both with a mesh of tiny adhesive paper target points. These paper targets were visually placed in a series of rows of nearly constant x coordinate such that a row of points approximately defined a body cross section. The target points were closely spaced at the forward end of the cowling and at other regions of extreme surface curvature. Target points were more thinly spaced at regions on the cowl where the surface was less convoluted.

After placement of the surface targets, actual measurement was begun. As shown in Figures E.1a and E.1b, a measurement consisted of simultaneous sightings on a surface target point by transits A and B. While sighted on a target, the horizontal angles ψ_A and ψ_B were recorded. Also, the vertical angles ω_A and ω_B were recorded. This process was repeated for all target points on the left side of the cowl and spinner.

Transit B was then moved directly across to the right side of the spinner origin point. Additional target points were placed on ducts and surface features found only on the right half of the cowl. Further sightings were made to measure these target points. This concluded the gathering of data.

Using the measured lengths χ_A, χ_B, and $\Delta\chi$, as well as the four angles ψ_A, ψ_B, ω_A, and ω_B, associated with a target point, trigonometry was applied to calculate the Cartesian coordinates of the target point relative to the spinner origin. By using a computer program, this trigonometric analysis was rapidly completed for the hundreds of target points. The result was a discrete point description of the cowl and spinner geometry in Cartesian coordinates.

Preliminary three-view cowl and spinner drawings were made using the measured surface points. As previously stated, the target points had been positioned visually in a series of rows, each row lying approximately at a constant x coordinate. Of course, analysis of the data revealed that points on a given row were not precisely aligned at a single x coordinate. Therefore, the measured surface points on each row were shifted slightly until all rows fell on contours of constant x coordinate and thus defined true cross sections. Guided by the preliminary three-view drawings, the data point shifting was done carefully using cubic spline interpolation.

Final three-view cowl and spinner drawings were made using the shifted surface points. The front view of these drawings afforded detailed descriptions of geometry cross sections.

Surface coordinates from the final three-view drawings were used to generate cowl and spinner input computer paneling. To produce a symmetric cowl paneling network, small irregular cowl surface features, such as engine exhaust pipes and small intake ducts, were ignored.

The manufacturer-defined Cherokee 180 aircraft coordinate origin, used in all existing drawings of fuselage geometry, aft of the firewall, did not coincide with the arbitrarily chosen cowl-spinner coordinate

origin. Therefore, to properly mate the measured cowl-spinner geometry with the remaining aircraft geometry, coordinates of all geometry on manufacturer-supplied drawings were converted to the measured cowl-spinner coordinate system. Thus, all aircraft input geometry, including the cowl, fuselage, and spinner paneling, for the flow prediction program was referenced to the chosen coordinate origin indicated in Figures E.1a and E.1b.

Table 1

Characteristics of the Twin-Engine Aircraft Flight Conditions for Which Computed and Measured Propeller Plane Flow Field Results Are Presented in Chapter 4

Flight condition	Installed propeller plane vertical tilt, α_p (degrees)	Aircraft angle of attack, α (degrees)	Propeller plane angle of attack, $\alpha_G = \alpha + \alpha_p$ (degrees)	Wing C_L	Nacelle inlet velocity ratio, F/V
1	-2.0	2.0	0.0	0.32	0.29
2	-2.0	6.0	4.0	0.60	0.29
3	-2.0	12.0	10.0	1.03	0.29
4	-2.0	2.0	0.0	0.32	0.10
5	-2.0	6.0	4.0	0.60	0.10
6	-2.0	12.0	10.0	1.03	0.10

Characteristics fixed for all flight conditions:

Aircraft angle of sideslip, $\beta \doteq 0.0$ degrees

Installed propeller plane lateral tilt, $\beta_p = 0.0$ degrees

Propeller plane reference radius, R = 2.3368 meters

Notes:

1. All flight conditions were computed; only conditions 1, 2, and 3 were tested by Roberts and Yaggy (15).
2. All computer runs modeled the wing vortex; the body panel network modeled only the left nacelle and foreward fuselage (shown crosshatched in Figure 16) using N = 424 panels.

Table 2

Characteristics of the Piper Cherokee PA-28-180 Aircraft Configurations for Which Computed Propeller Plane Flow Field Results Are Presented in Chapter 5

Configuration	Panel network	Wing modeled	Dihedral modeled	Aircraft angles of attack, α (degrees)	Cowl inlet velocity ratio, F/V
1	cowl - fuselage	yes	yes	2.0, 4.0, 6.0, 8.0, and 10.0	0.2
2	cowl - fuselage	yes	yes	2.0 and 10.0	0.1
3	cowl - fuselage	yes	yes	2.0 and 10.0	0.4
4	cowl - fuselage	yes	no	2.0 and 10.0	0.2
5	cowl - fuselage	no	---	2.0 and 10.0	0.2
6	cowl - short afterbody	yes	yes	2.0 and 10.0	0.2

Characteristics fixed for all flight conditions:

Aircraft angle of sideslip, β = 0.0 degrees

Installed propeller plane vertical tilt angle, α_p = -4.0 degrees

Installed propeller plane lateral tilt angle, β_p = 3.0 degrees

Propeller plane reference radius, R = 0.9652 meters

Notes:

1. C_L values corresponding to the α values are listed in Table 3.
2. Propeller spinner and landing gear geometry were not paneled in any of the configurations.
3. Configuration 1 is the baseline against which all other configurations are compared.
4. All configurations were symmetric; numbers 1 to 5 each used N = 968 panels; number 6 used N = 824 panels.

Table 3

Piper Cherokee PA-28-180 Aircraft Lift Coefficients Corresponding to the Angles of Attack Modeled by the Computer Program

Fuselage angle of attack, α (degrees)	C_L (from Figure 27)
2.0	0.385
4.0	0.568
6.0	0.751
8.0	0.934
10.0	1.116

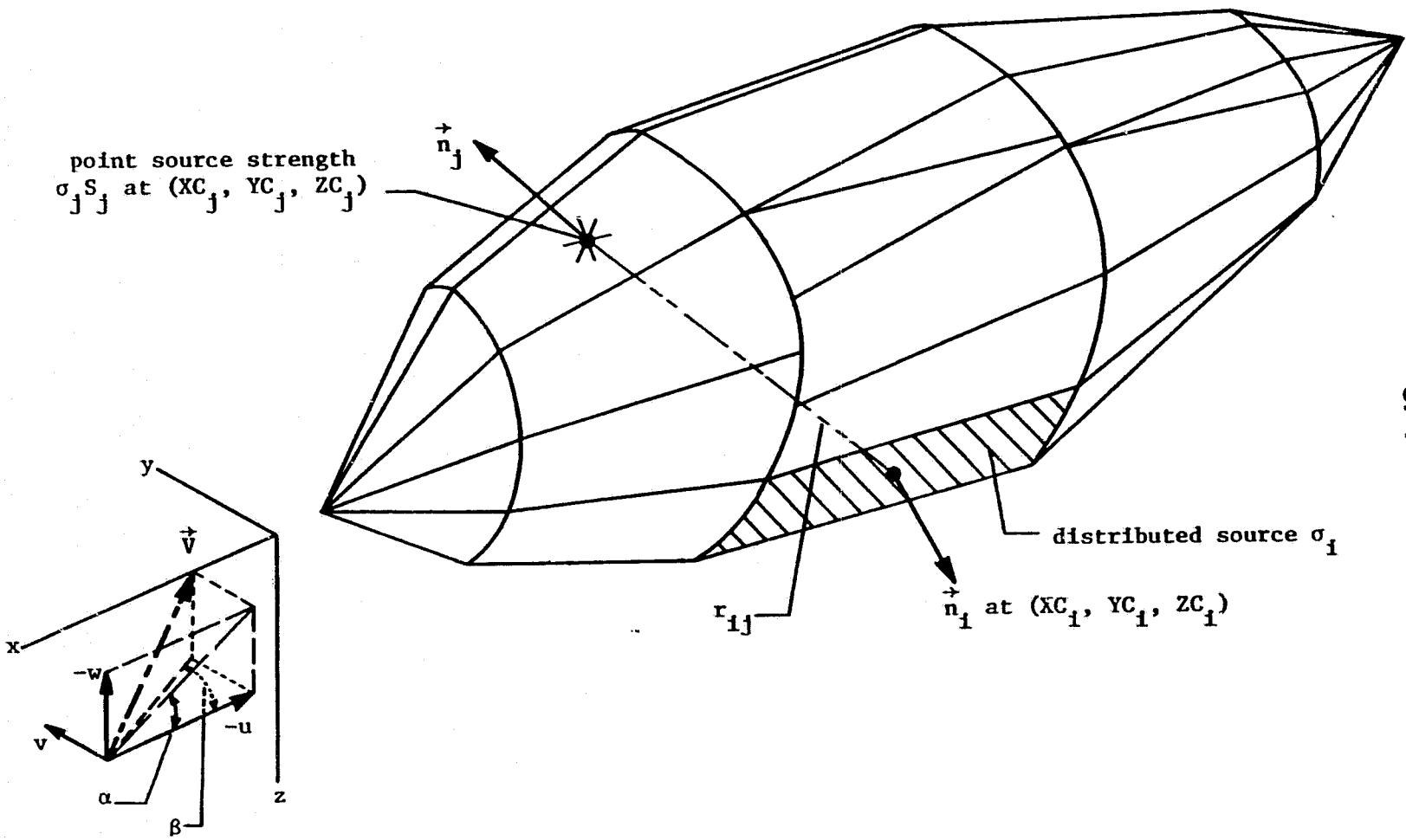

Figure 1. Body Panel Network and Free Stream Velocity Components

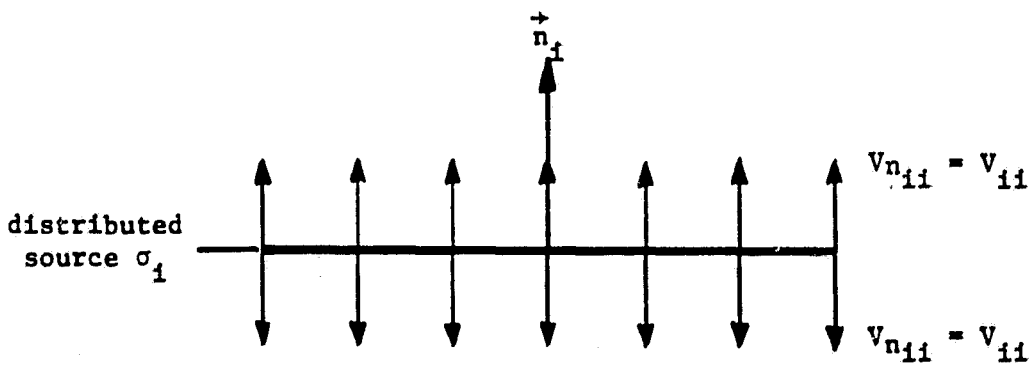

Figure 2. Edge of a Panel Showing Panel Self-Induced Velocity

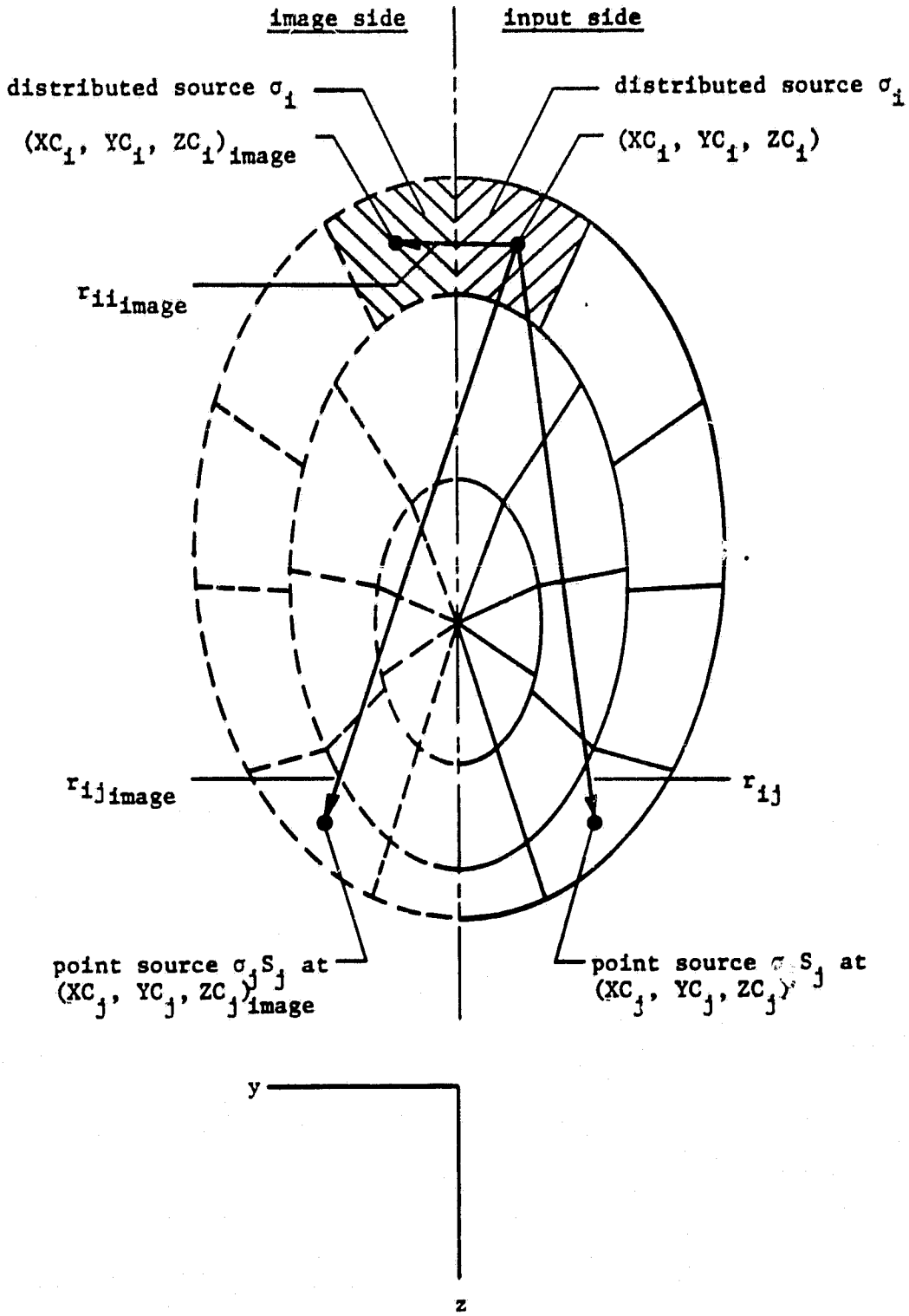

Figure 3. Front View of a Symmetric Body Panel Network

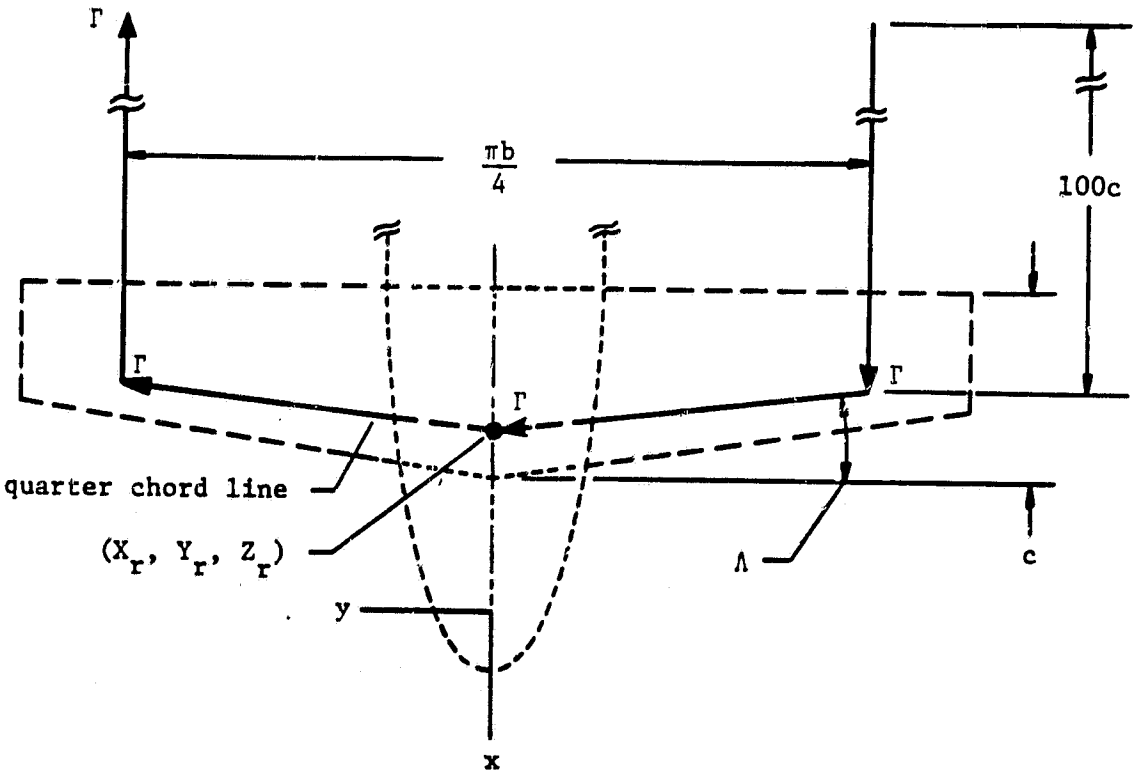

Figure 4a. Wing Horseshoe Vortex Geometry (Top View)

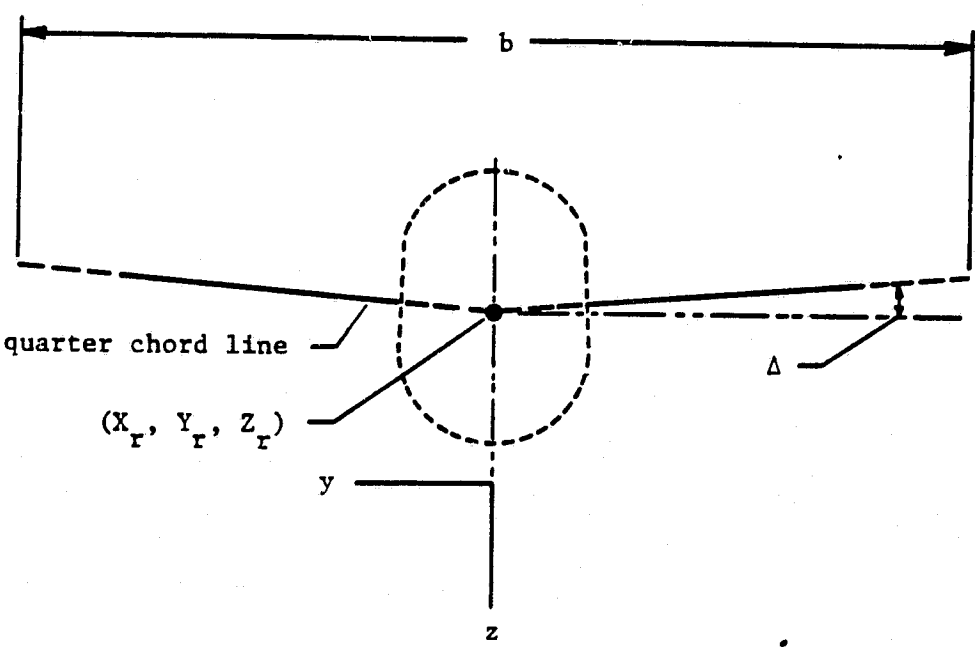

Figure 4b. Wing Horseshoe Vortex Geometry (Front View)

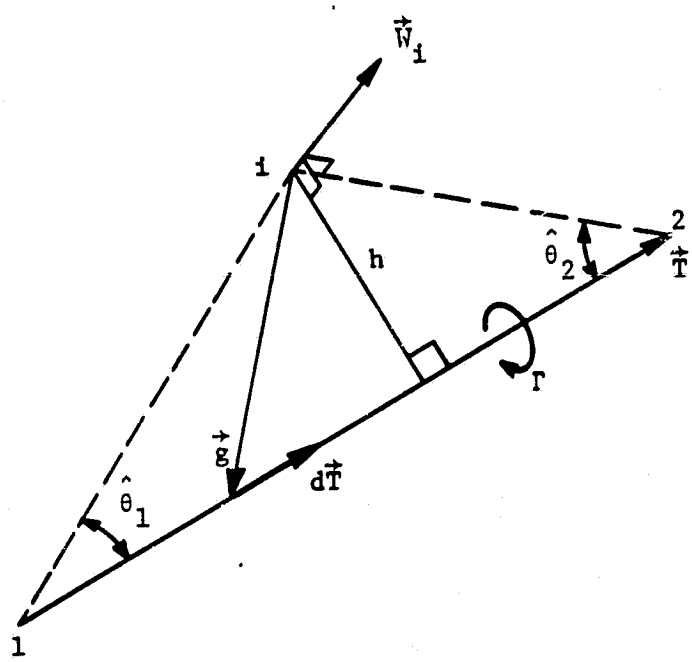

Figure 5. Straight Vortex Filament and Induced Velocity

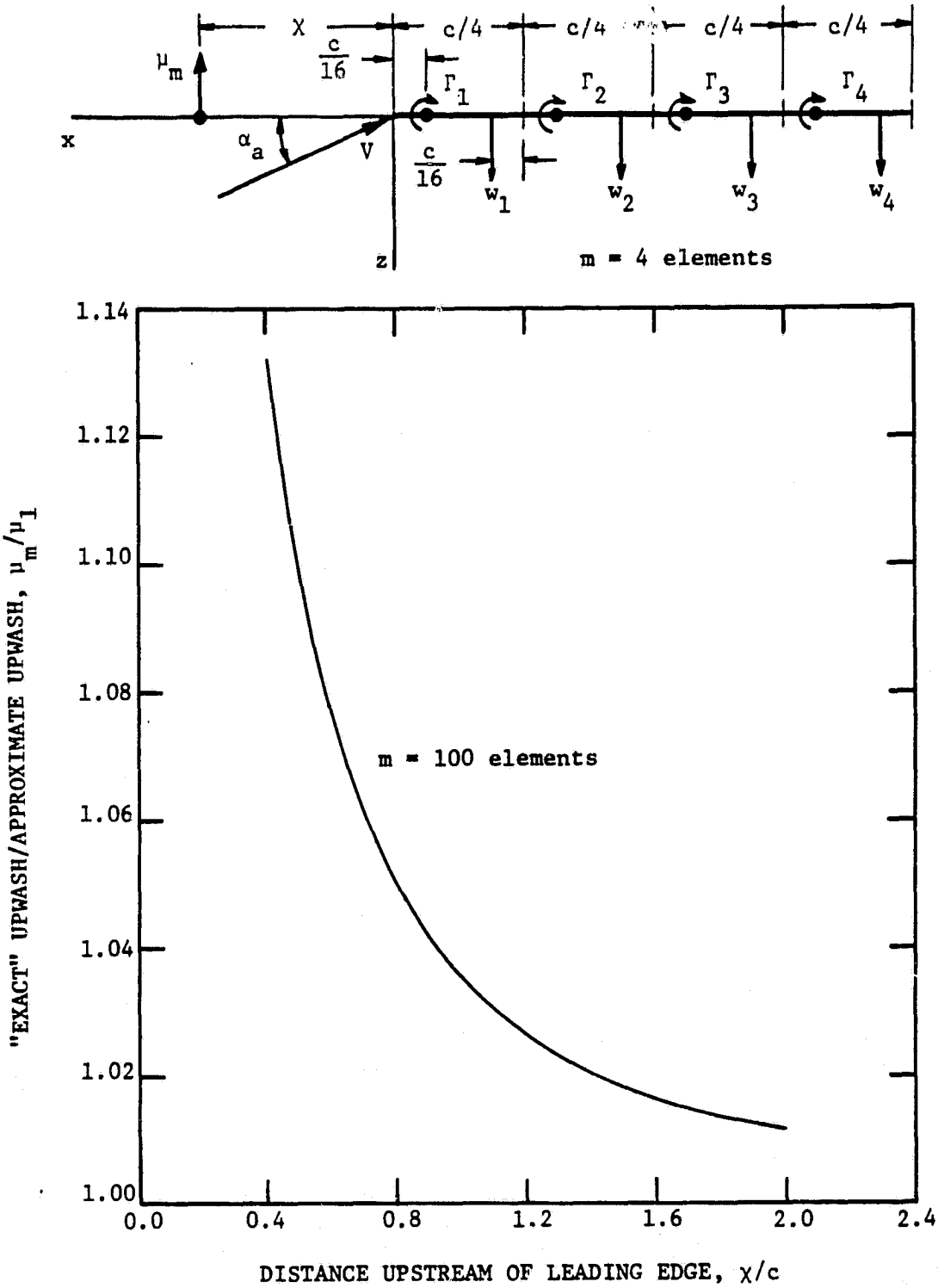

Figure 6. Comparison of "Exact" and Approximate Upwash Distributions Upstream of a Flat Plate Airfoil

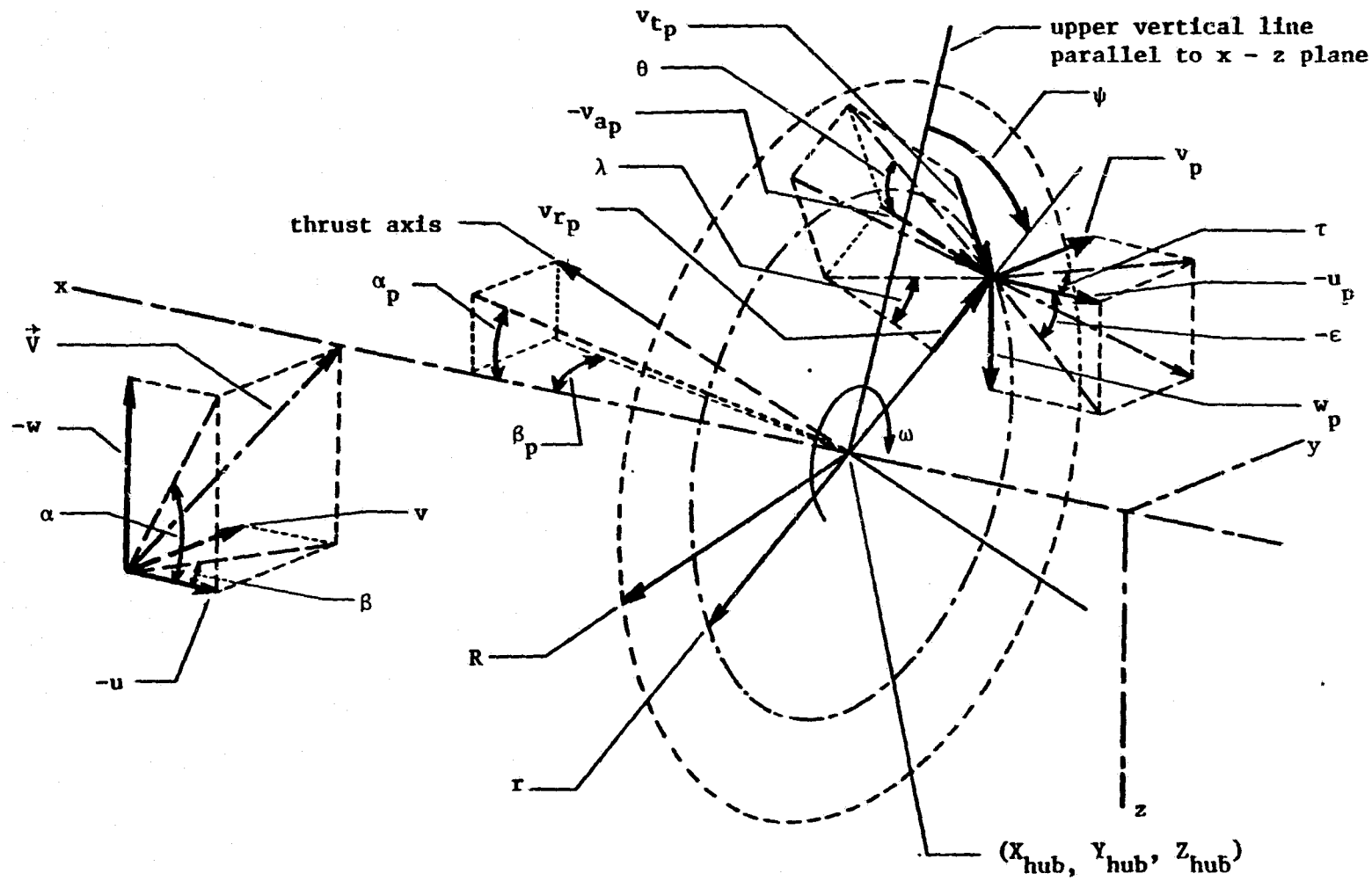

Figure 7. Propeller Plane Orientation, Body Orientation, Flow Velocities, and Flow Angles at a Point on the Propeller Plane

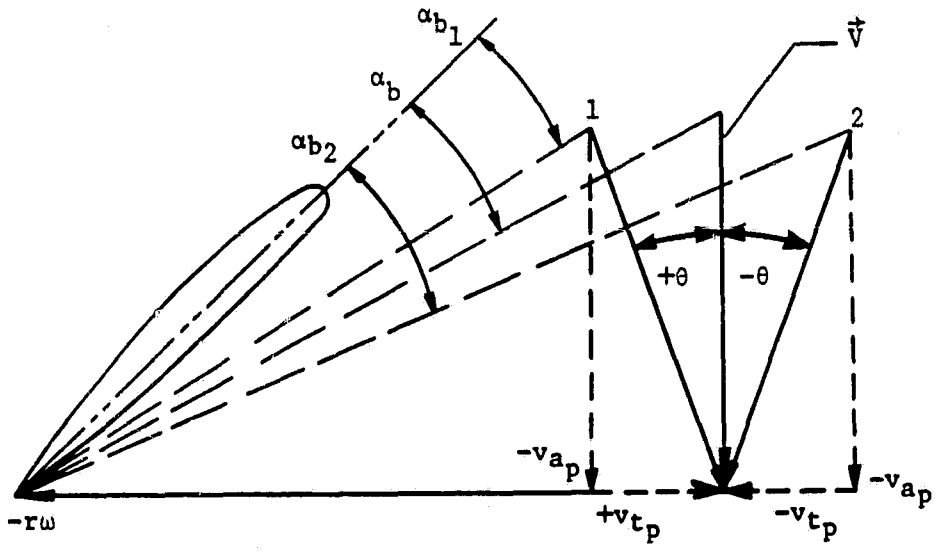

Figure 8. Effect of Angle of Rotational Flow, θ, on Local Propeller Blade Section Angle of Attack

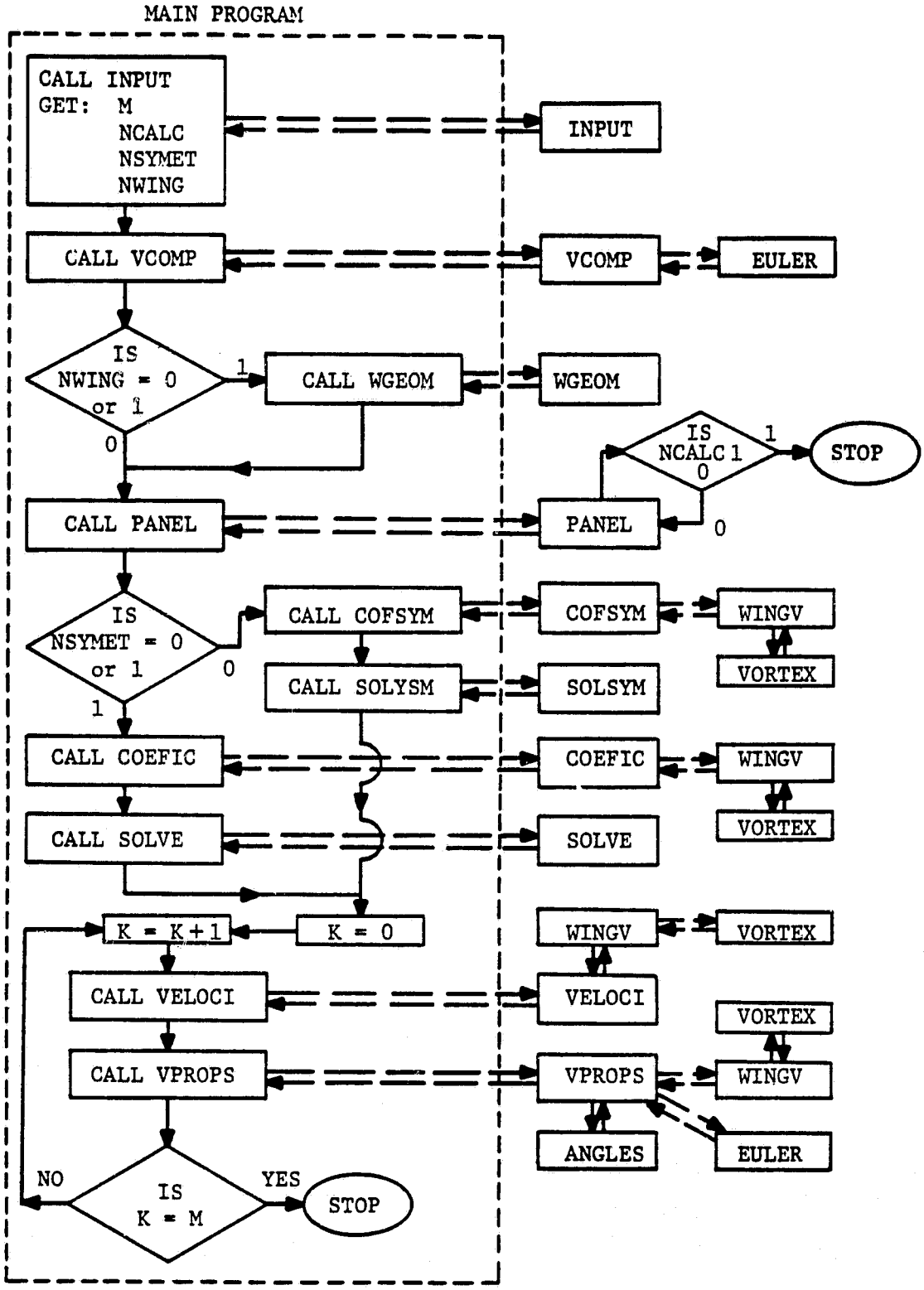

Figure 9. Organization and Structure of the Three-Dimensional Potential Flow Computer Program

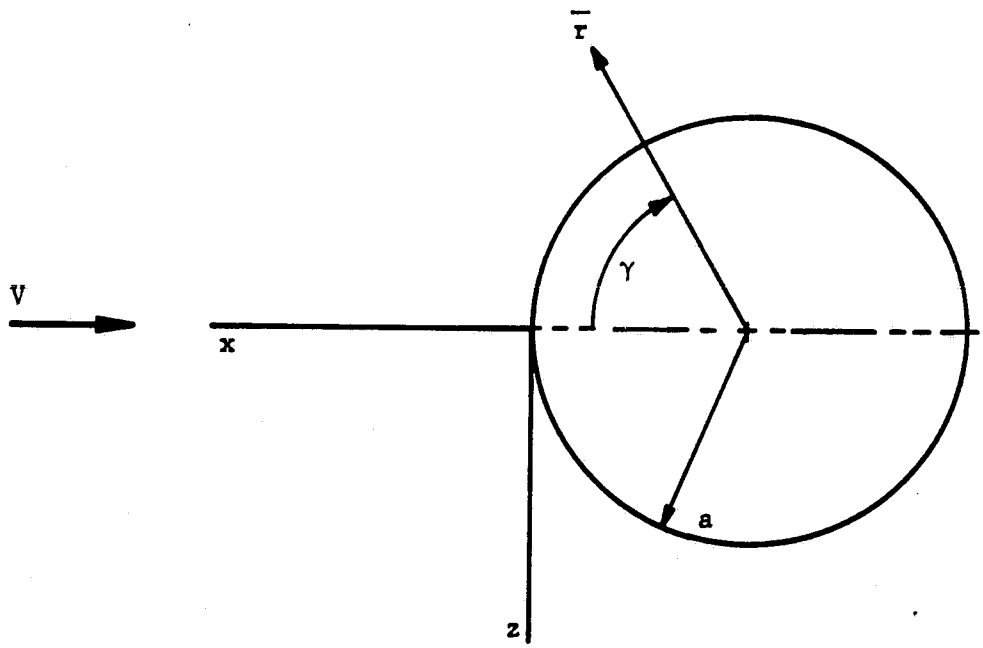

Figure 10. Sphere in a Uniform Flow

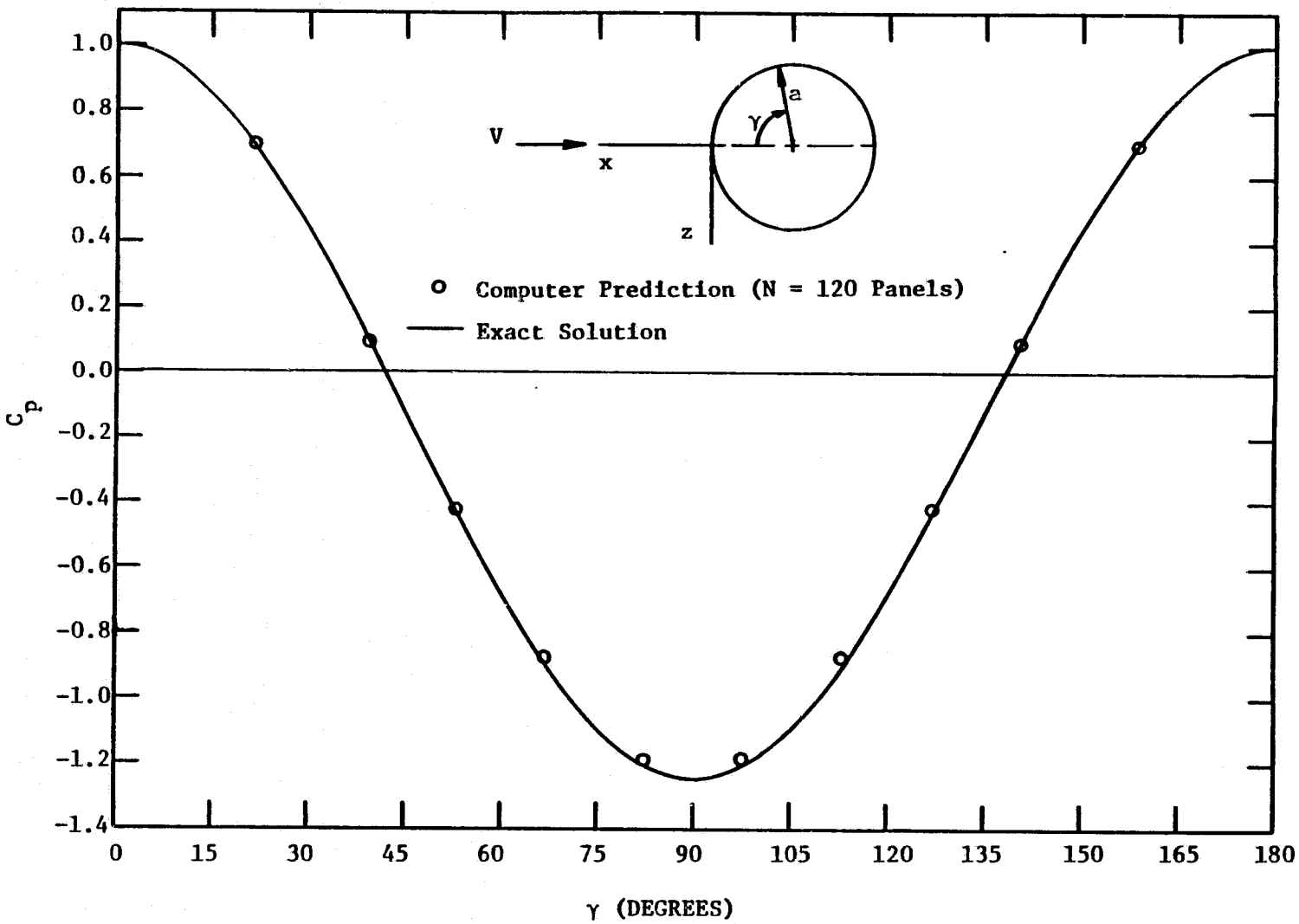

Figure 11. Surface Pressure Distribution on a Sphere

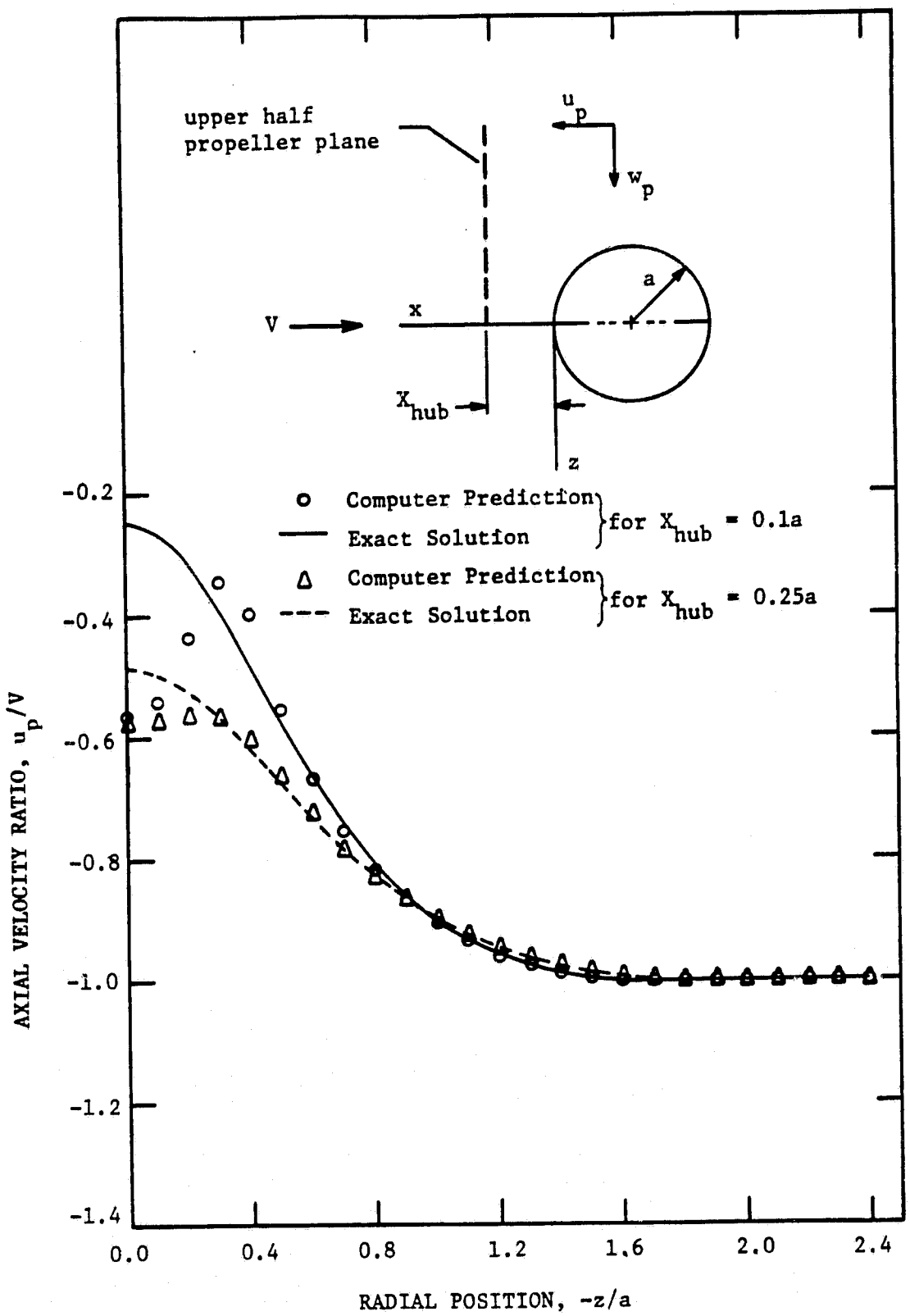

Figure 12. Axial Velocity Distribution Along the Upper Vertical Centerline of a Propeller Plane Upstream of a Sphere

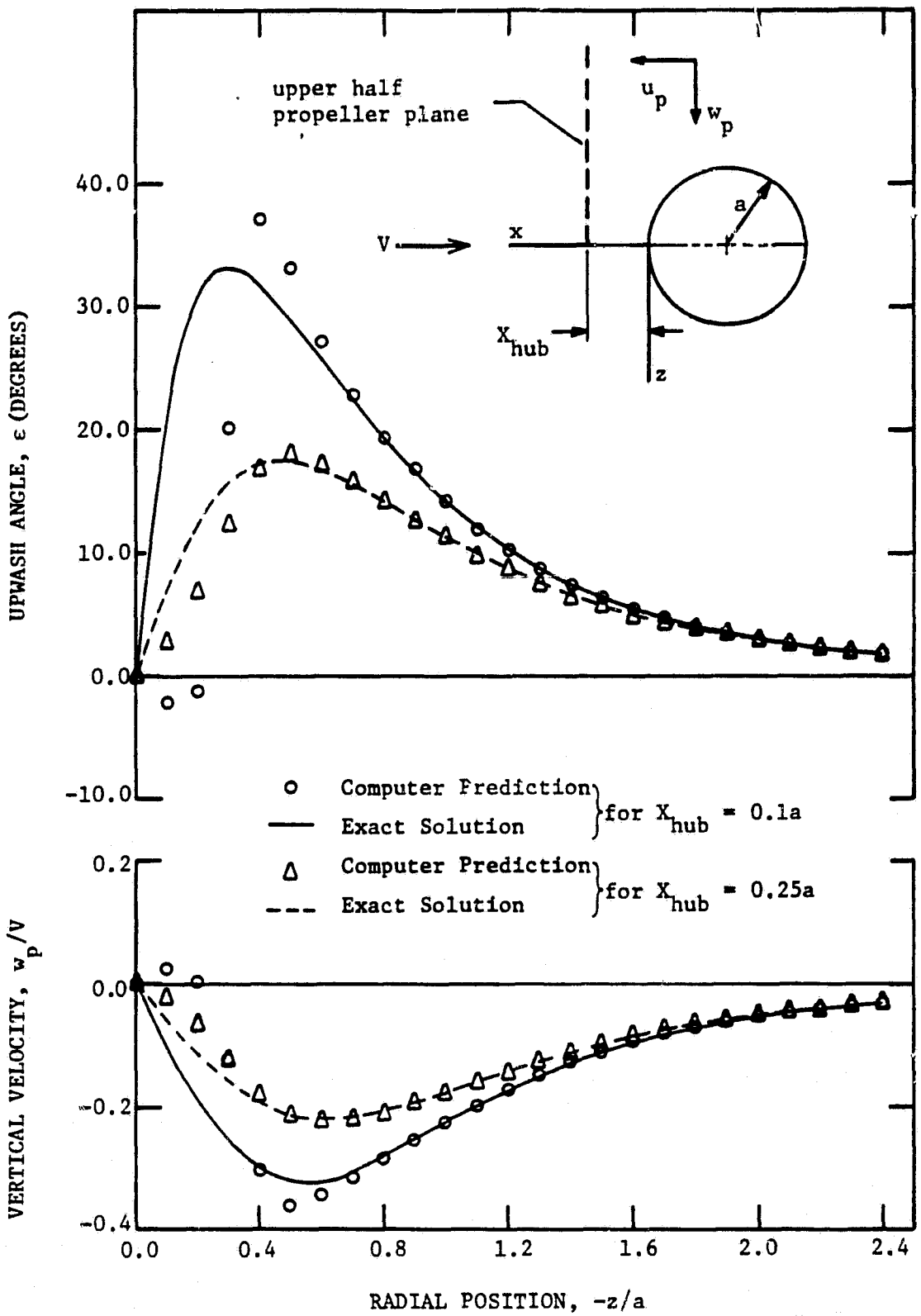

Figure 13. Distributions of Vertical Velocity and Upwash Angle Along the Upper Vertical Centerline of a Propeller Plane Upstream of a Sphere

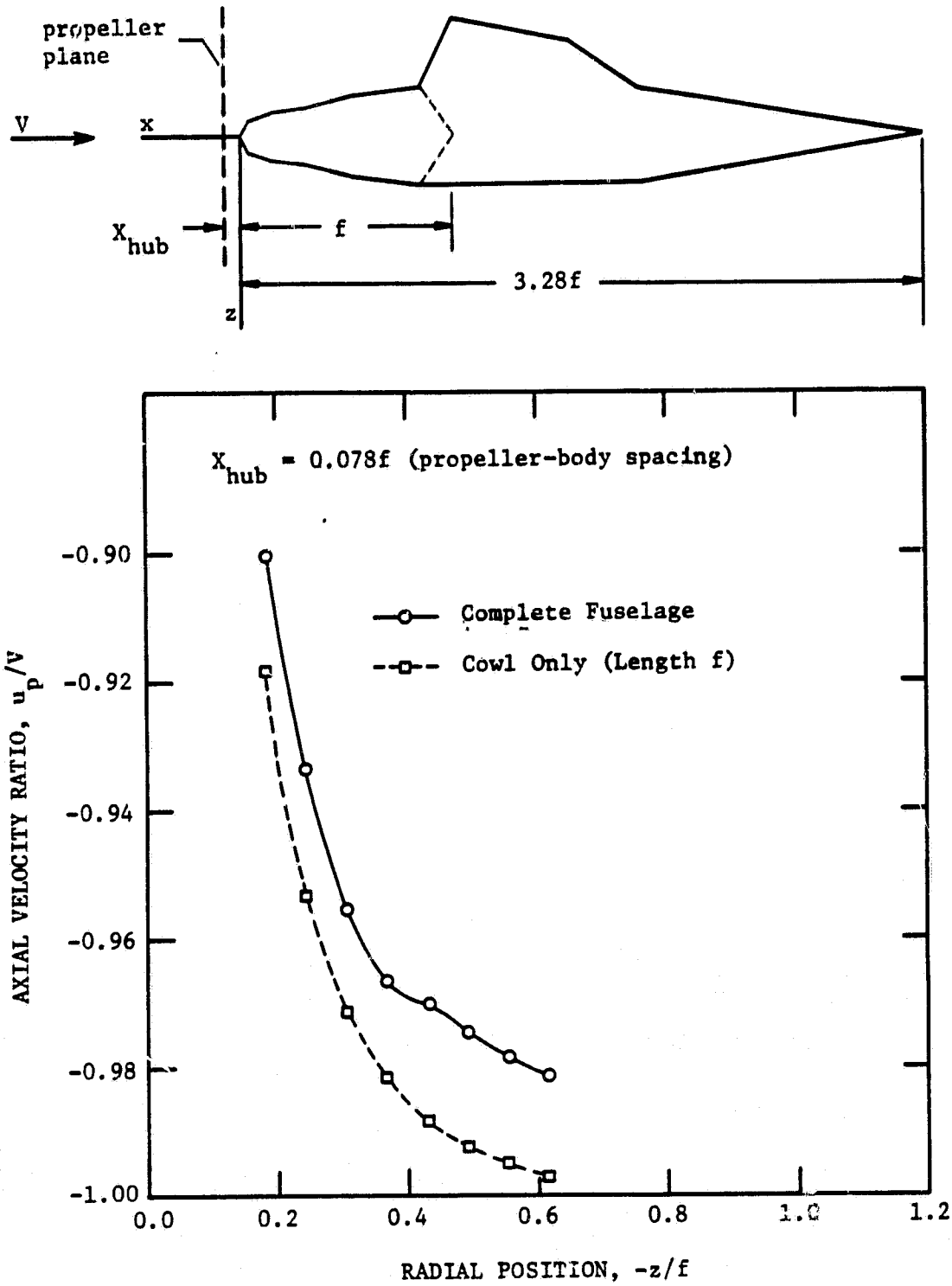

Figure 14. Axial Velocity Distribution on the Upper Vertical Centerline of a Propeller Plane Predicted With a Complete Simple Fuselage Shape and With the Isolated Cowling

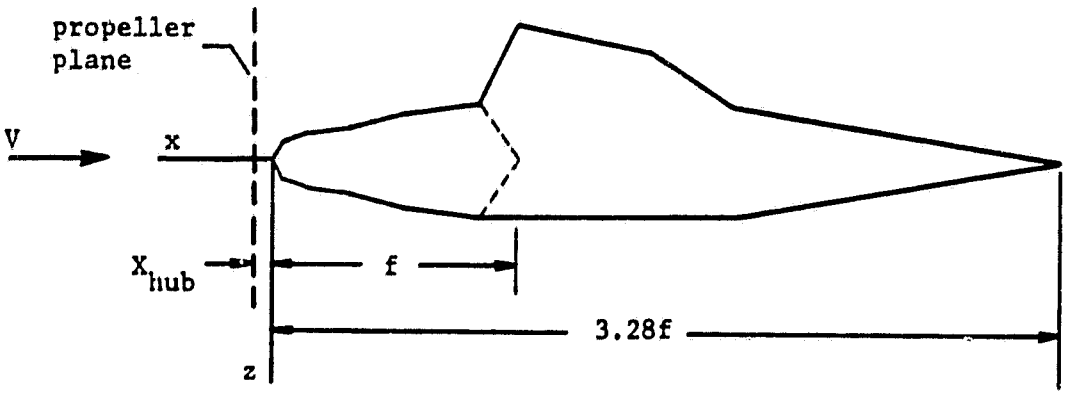

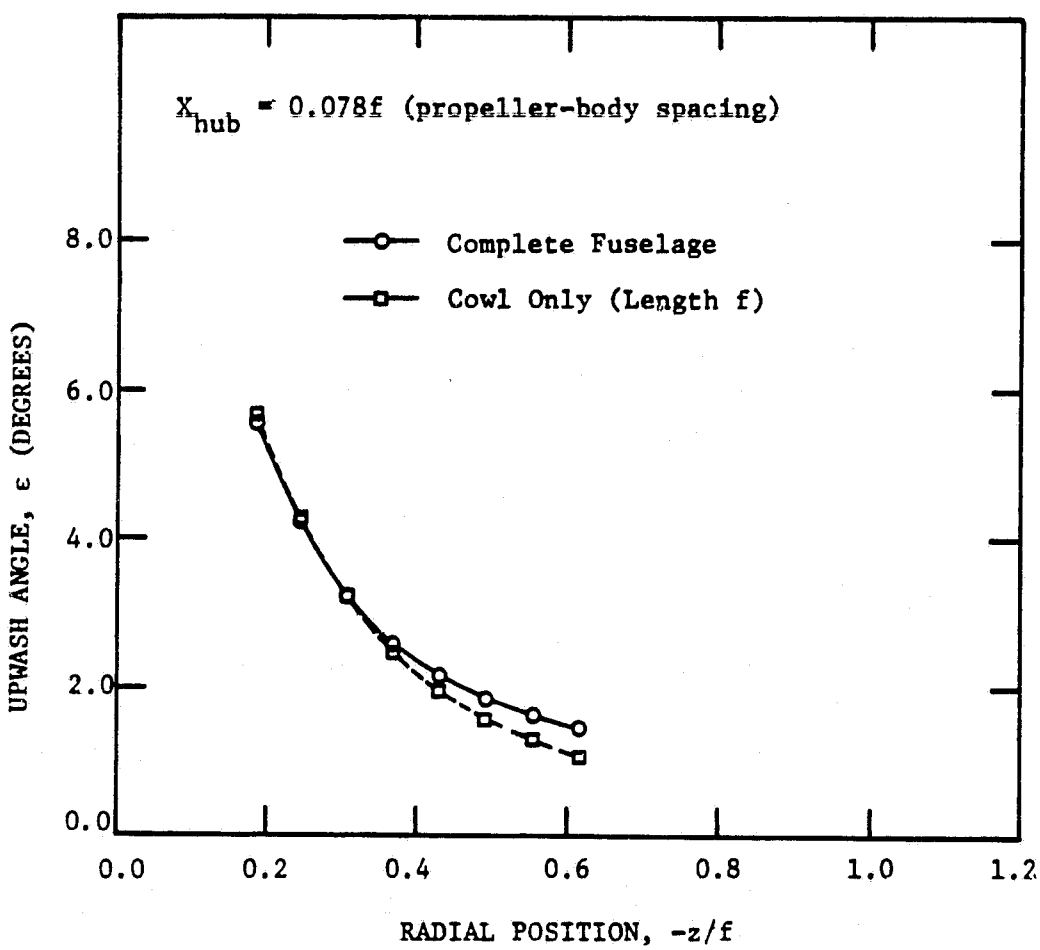

Figure 15. Upwash Angle Distribution on the Upper Vertical Centerline of a Propeller Plane Predicted With a Complete Simple Fuselage Shape and With the Isolated Cowling

All dimensions are in meters unless otherwise noted.

Root section NACA 23015
Tip section NACA 23012

Only the left nacelle and forward fuselage (crosshatched in plan view) were paneled.

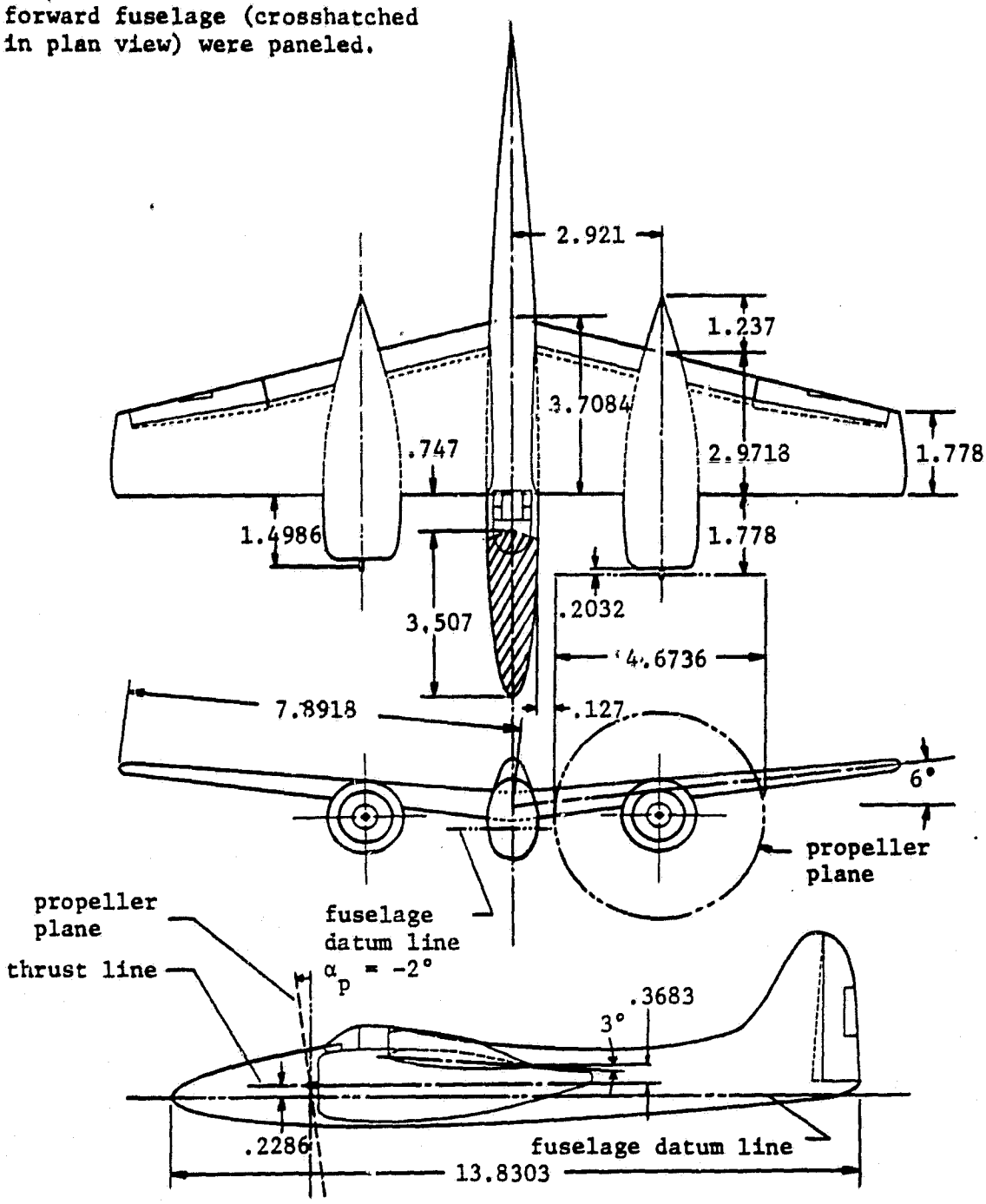

Figure 16. Geometric Characteristics of the Twin-Engine Airplane (Source: Reference 15)

ORIGINAL PAGE IS
OF POOR QUALITY

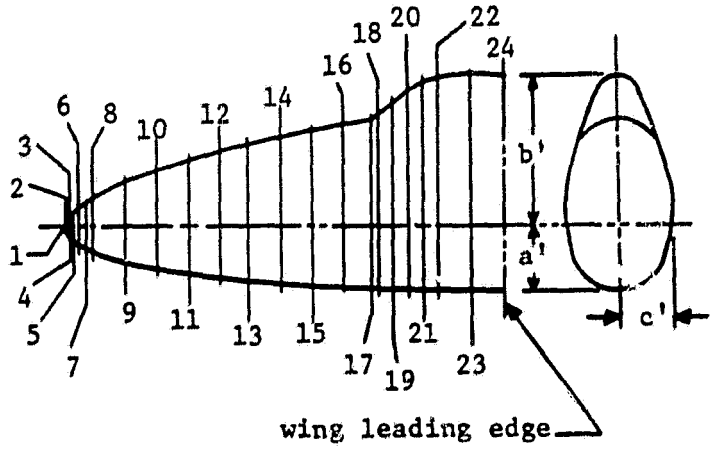

STATION NUMBER	FUSELAGE COORDINATES (METERS)			
	DISTANCE AFT	a'	b'	c'
1	0.00000	0.00000	0.00000	0.00000
2	0.02540	0.07620	0.05842	0.06350
3	0.05080	0.11430	0.08890	0.08890
4	0.07620	0.13462	0.12192	0.11430
5	0.10160	0.16002	0.14732	0.12700
6	0.15240	0.19050	0.18796	0.15748
7	0.22860	0.22352	0.23876	0.19304
8	0.30480	0.25400	0.28702	0.21590
9	0.60960	0.34290	0.43180	0.29210
10	0.91440	0.41656	0.54610	0.34544
11	1.21920	0.46228	0.64770	0.39370
12	1.52400	0.49530	0.73152	0.42164
13	1.82880	0.52832	0.81280	0.44704
14	2.13360	0.55372	0.87376	0.47244
15	2.43840	0.57404	0.93472	0.48768
16	2.74320	0.59182	0.99060	0.50292
17	2.99720	0.59944	1.03378	0.51054
18	3.04800	0.59944	1.06680	0.51054
19	3.20040	0.60706	1.19380	0.51308
20	3.35280	0.60960	1.31064	0.51562
21	3.50520	0.61214	1.40208	0.51816
22	3.65760	0.61468	1.44780	0.52070
23	3.96240	0.61722	1.47320	0.52578
24	4.25450	0.61722	1.46050	0.53086

Figure 17a. Twin-Engine Airplane Fuselage Coordinates for the Portions Forward of the Wing Leading Edge (Source: Reference 15)

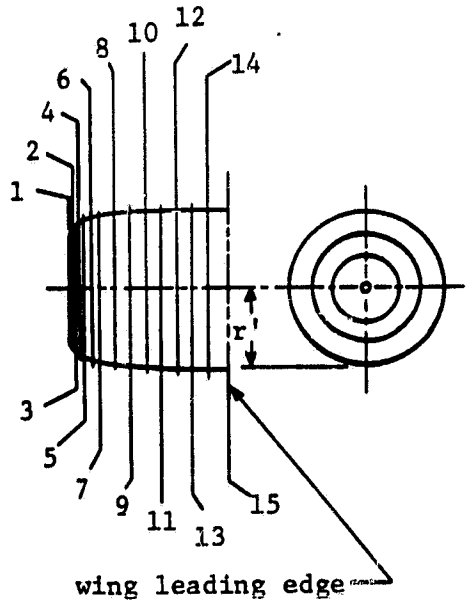

STATION NUMBER	NACELLE COORDINATES (METERS)	
	DISTANCE AFT	r'
1	0.0000	0.54610
2	0.0254	0.58420
3	0.0508	0.60960
4	0.1016	0.63500
5	0.1524	0.66040
6	0.2286	0.68580
7	0.3048	0.70612
8	0.4572	0.72390
9	0.6096	0.73660
10	0.7620	0.74930
11	0.9144	0.75184
12	1.0668	0.75438
13	1.2192	0.75692
14	1.3716	0.75692
15	1.5748	0.75692

Figure 17b. Twin-Engine Airplane Nacelle Coordinates for the Portions Forward of the Wing Leading Edge (Source: Reference 15)

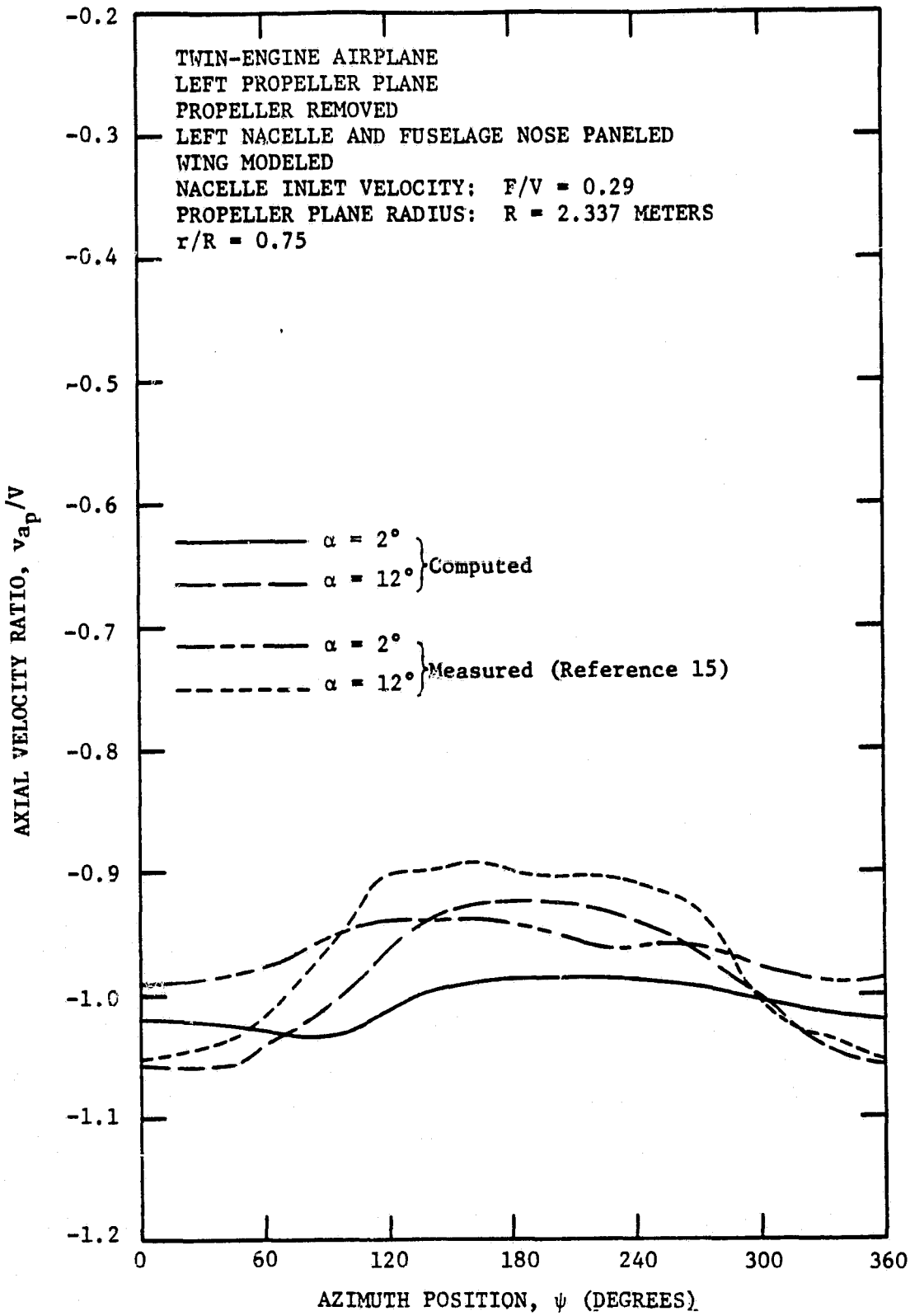

Figure 18. Comparison of Computed and Measured Azimuthal Distributions of Axial Velocity at the Left Propeller Plane of the Twin-Engine Airplane

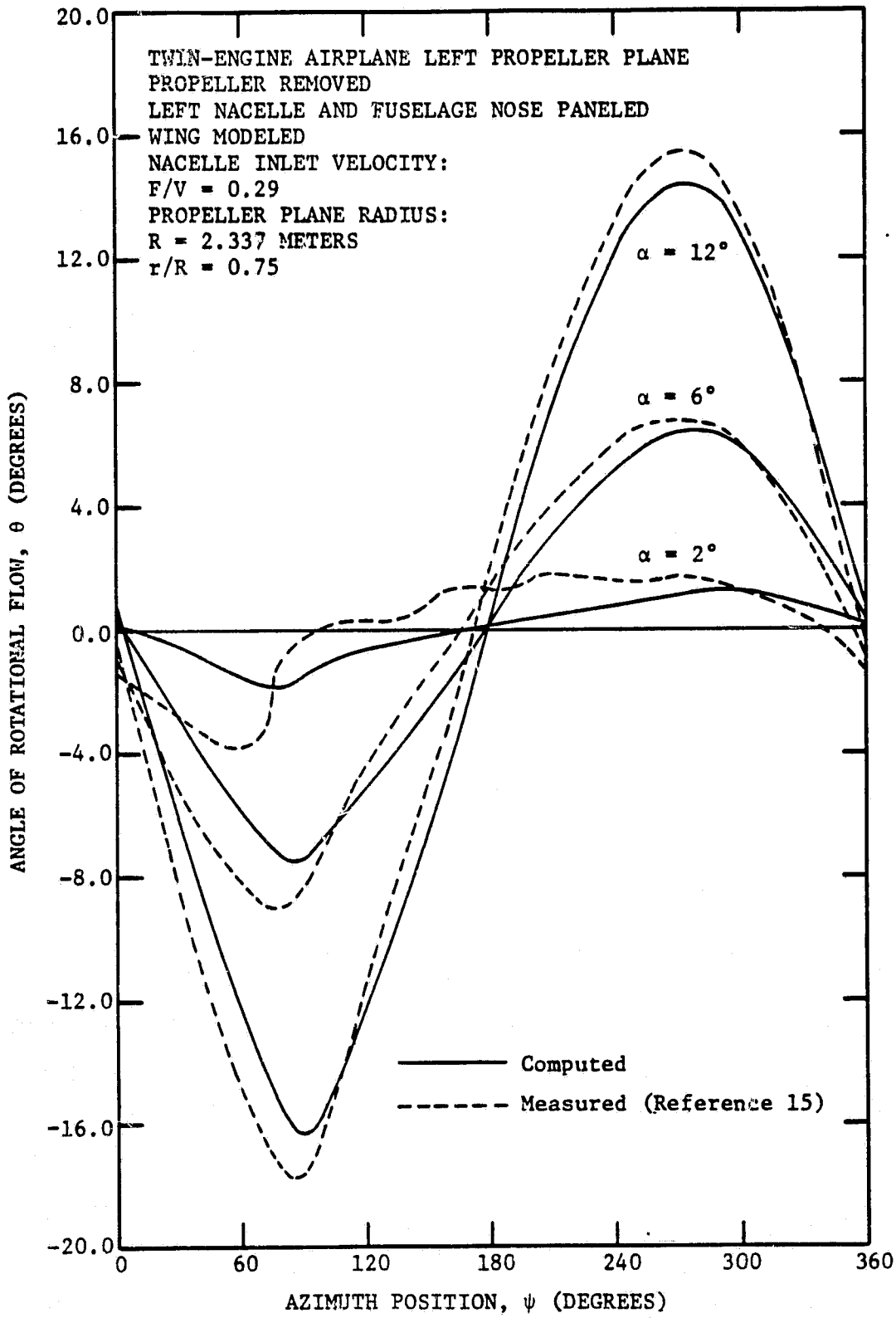

Figure 19. Comparison of Computed and Measured Azimuthal Distributions of Angle of Rotational Flow at the Left Propeller Plane of the Twin-Engine Airplane

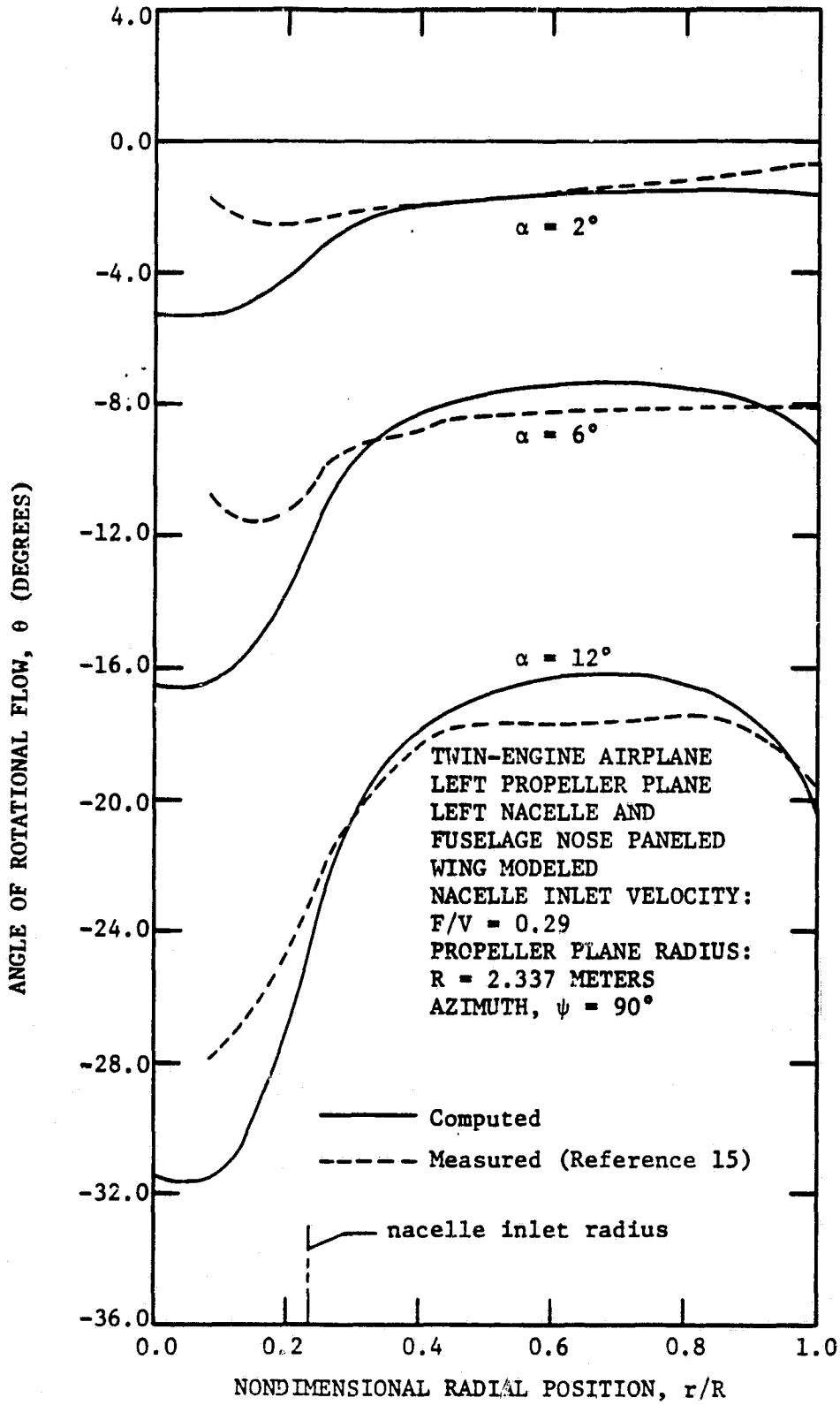

Figure 20. Comparison of Computed and Measured Radial Distributions of Angle of Rotational Flow at the Left Propeller Plane of the Twin-Engine Airplane

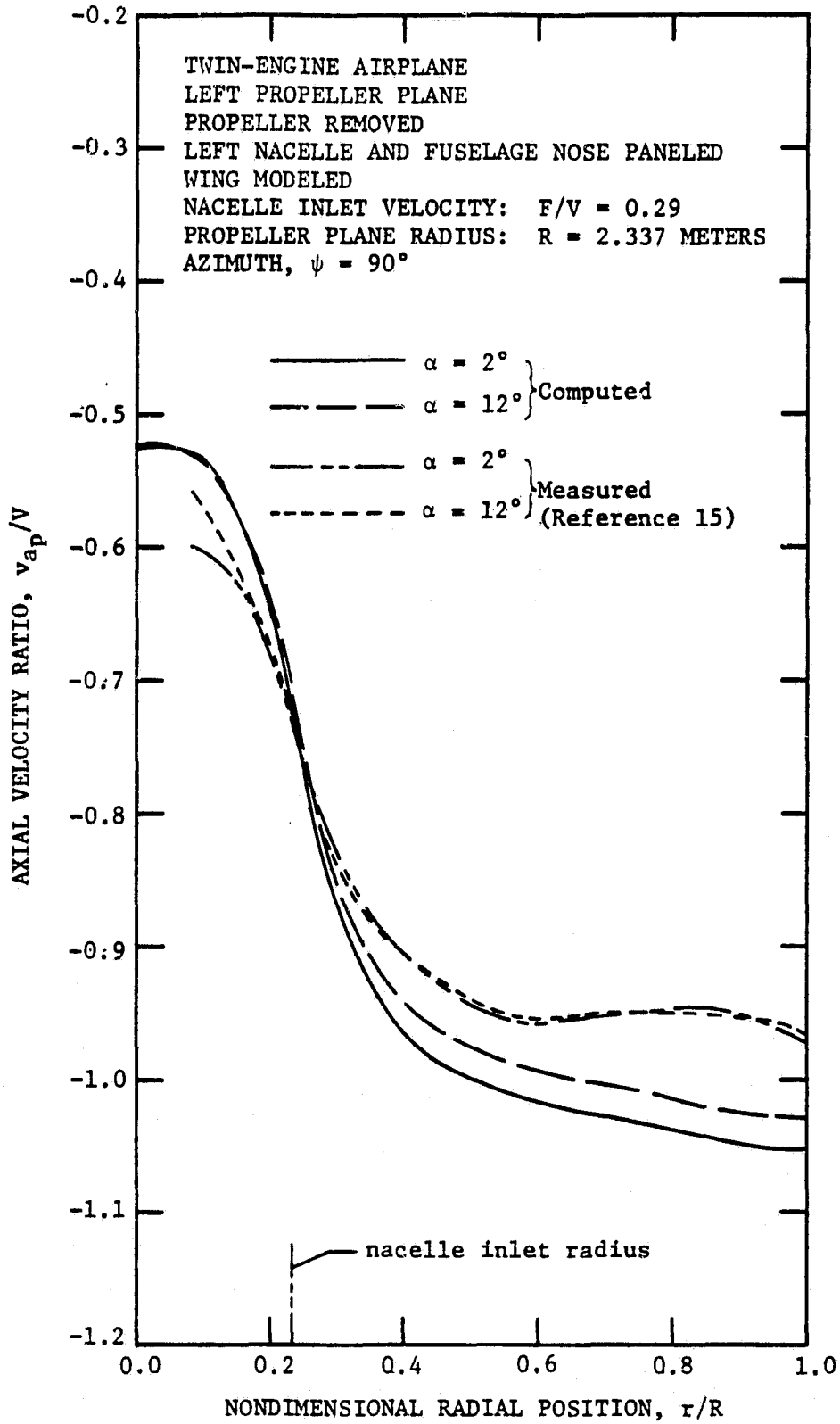

Figure 21. Comparison of Computed and Measured Radial Distributions of Axial Velocity at the Left Propeller Plane of the Twin-Engine Airplane

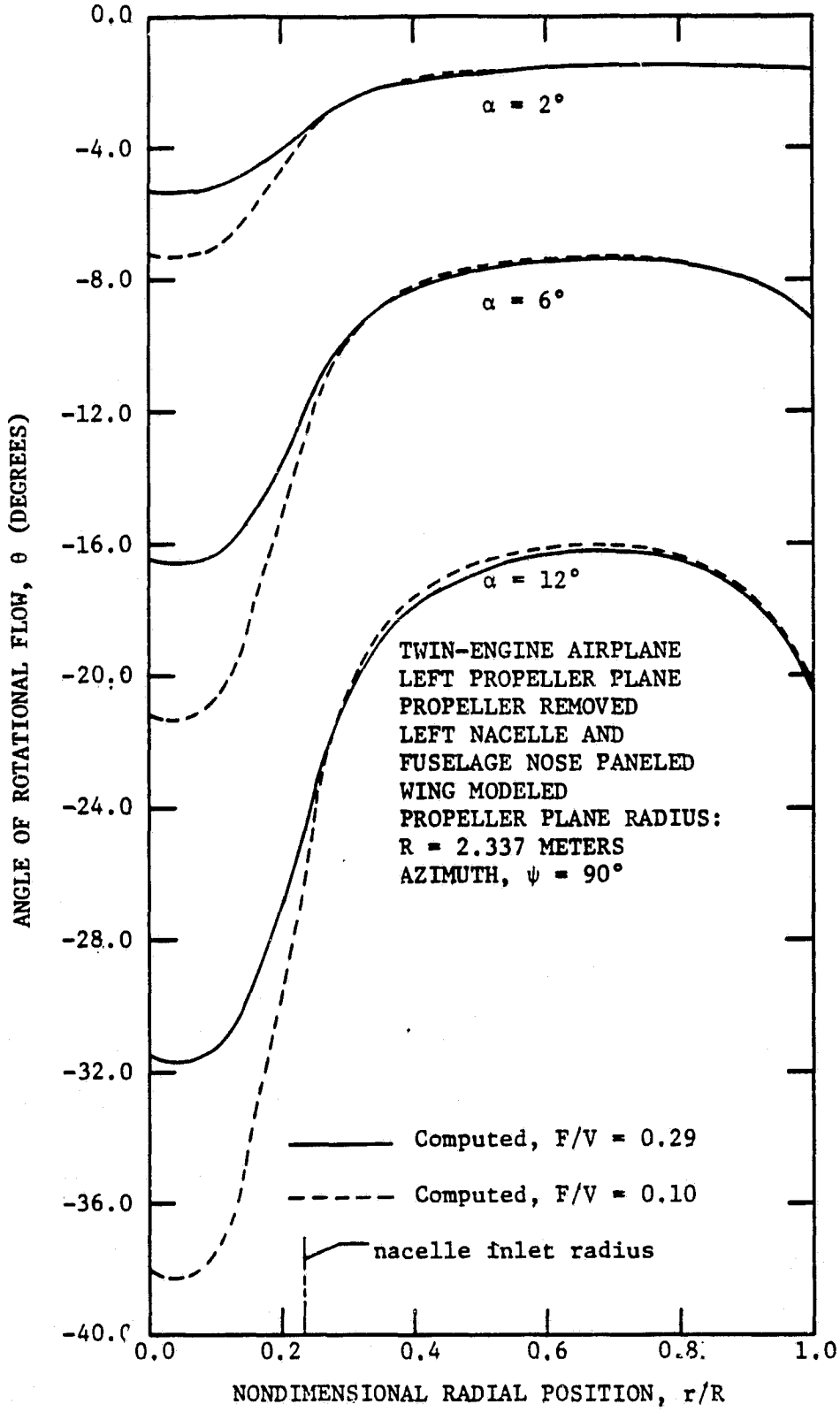

Figure 22. Effect of Change in Nacelle Inlet Inflow Velocity on the Radial Distribution of Flow Angularity at the Left Propeller Plane of the Twin-Engine Airplane

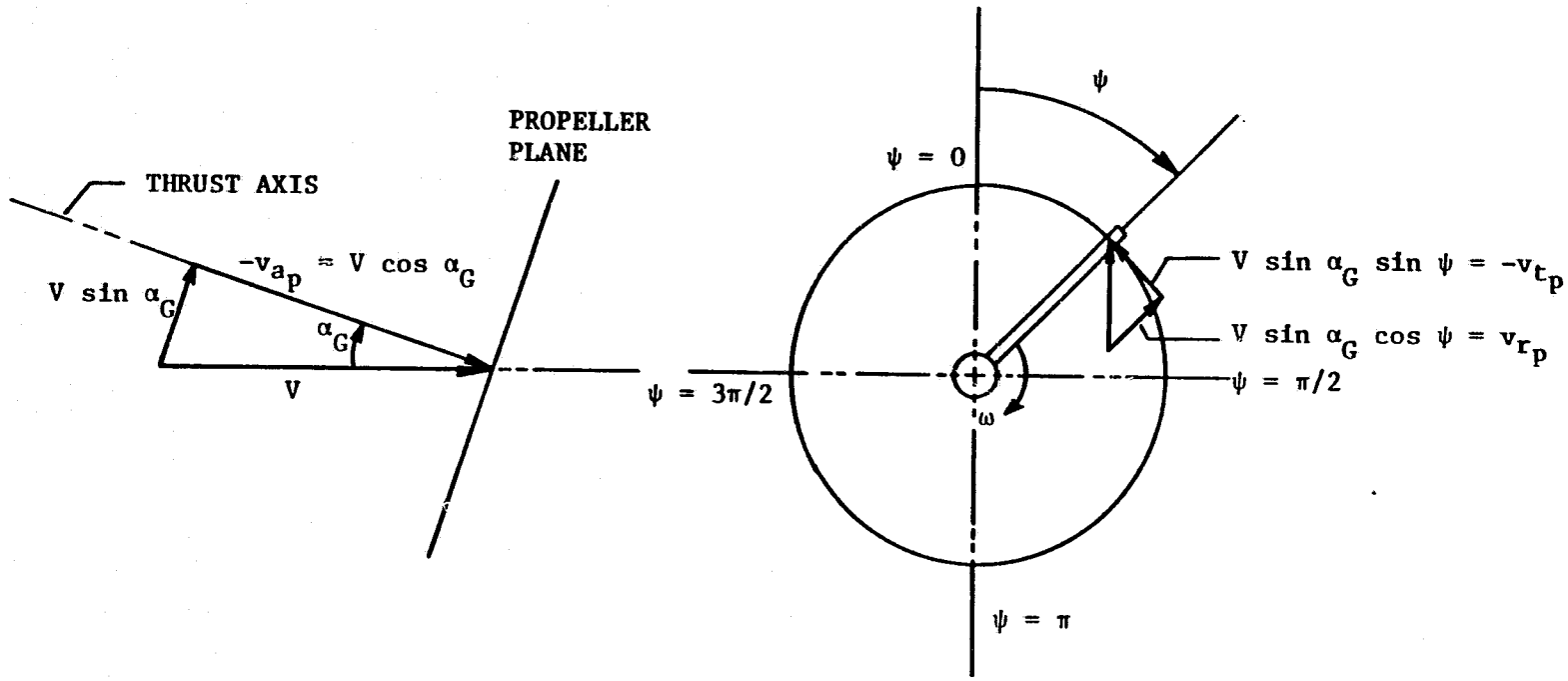

Figure 23a. Velocity Components at an Isolated Inclined Propeller Plane (Left Side View)

Figure 23b. Velocity Components at an Isolated Inclined Propeller Plane (Forward View)

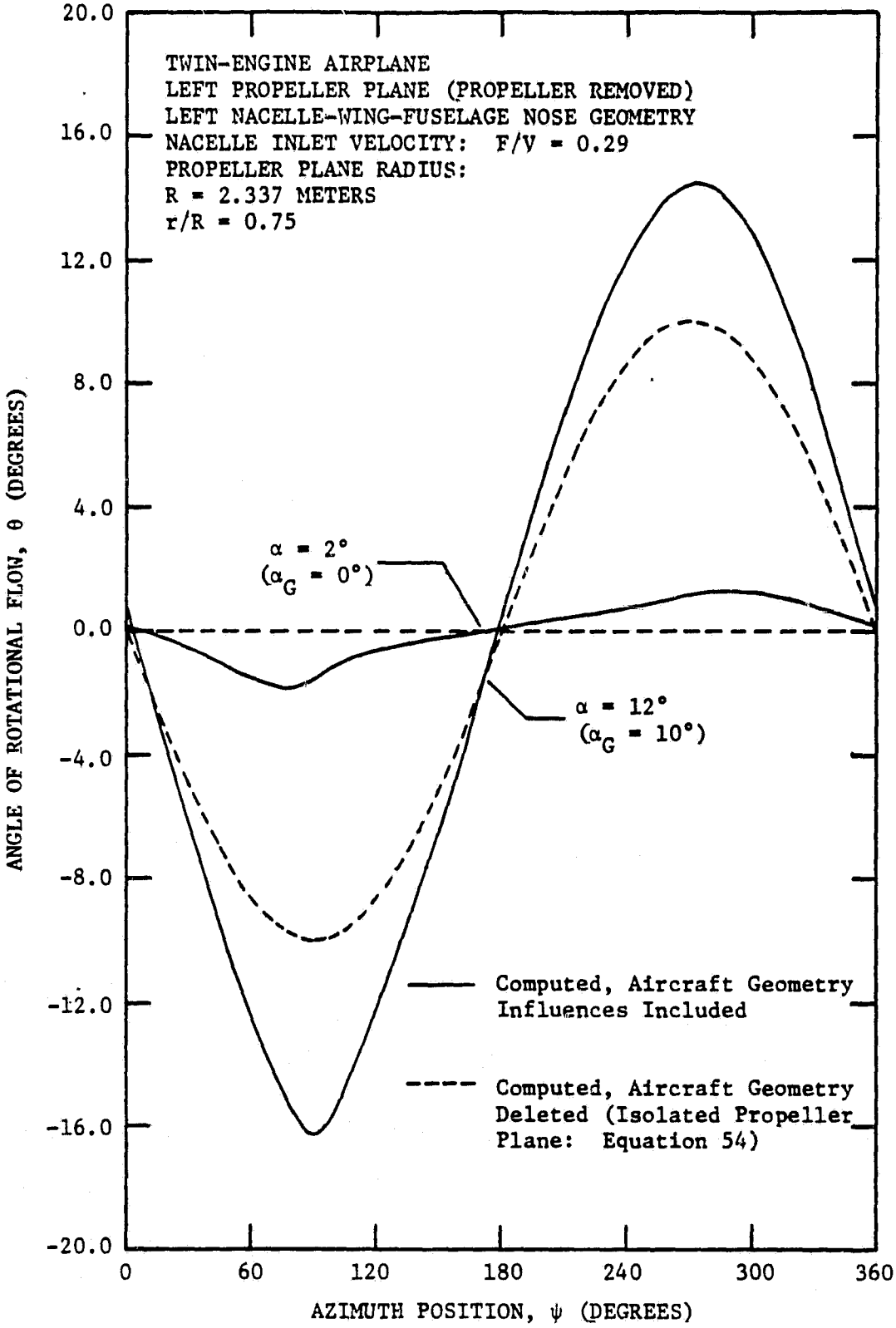

Figure 24. Comparison of Azimuthal Distributions of Flow Angularity at the Left Propeller Plane of the Twin-Engine Airplane Obtained With and Without Airframe Geometry Influences Present

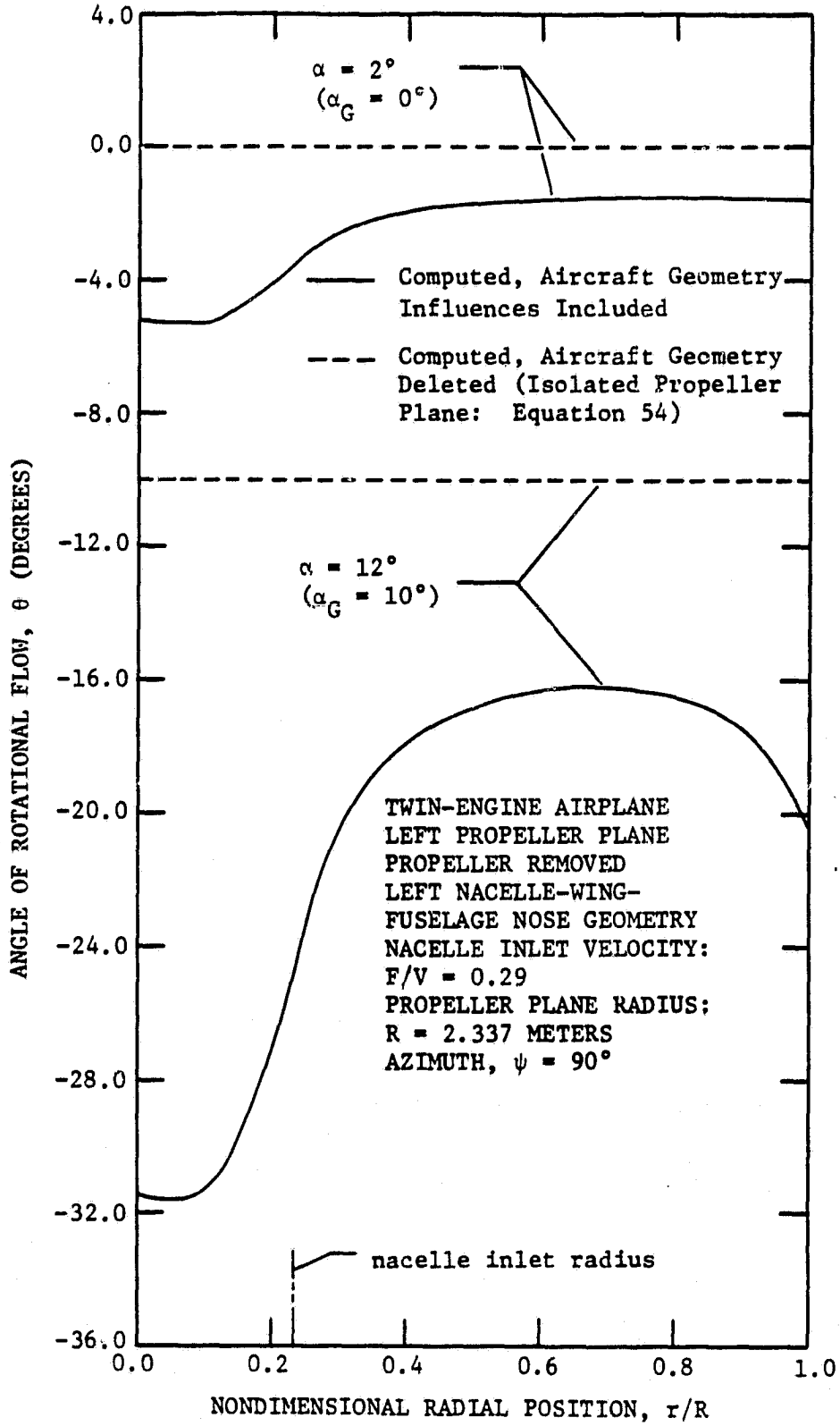

Figure 25. Comparison of Radial Distributions of Flow Angularity at the Left Propeller Plane of the Twin-Engine Airplane Obtained With and Without Airframe Geometry Influences Present

Note: Propeller hub position is 0.0228 propeller radii to the right of the fuselage plane of symmetry due to propeller plane inclination.

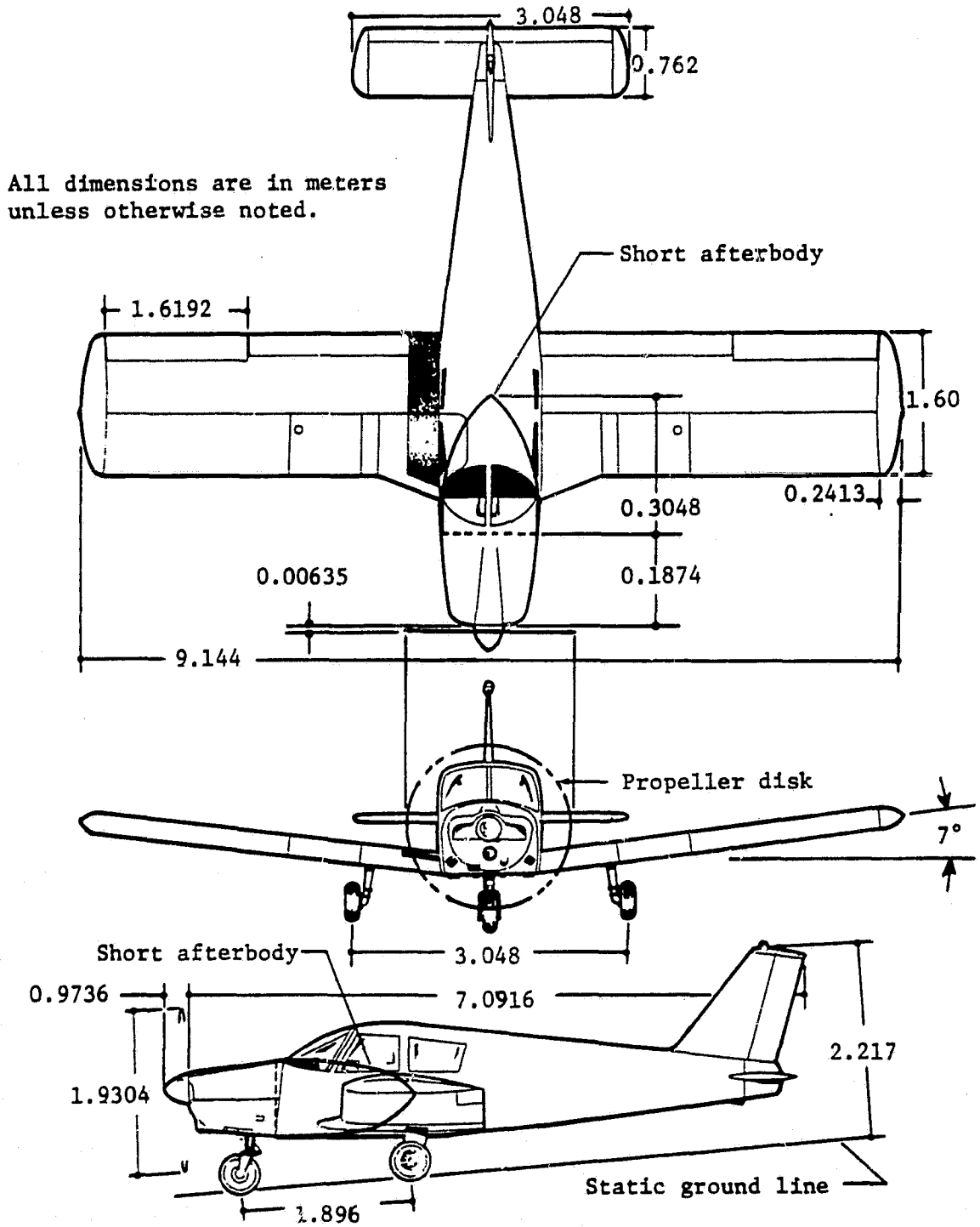

Figure 26. Geometric Characteristics of the Piper Cherokee PA-28-180 Airplane (With Short Afterbody Profile Shown)

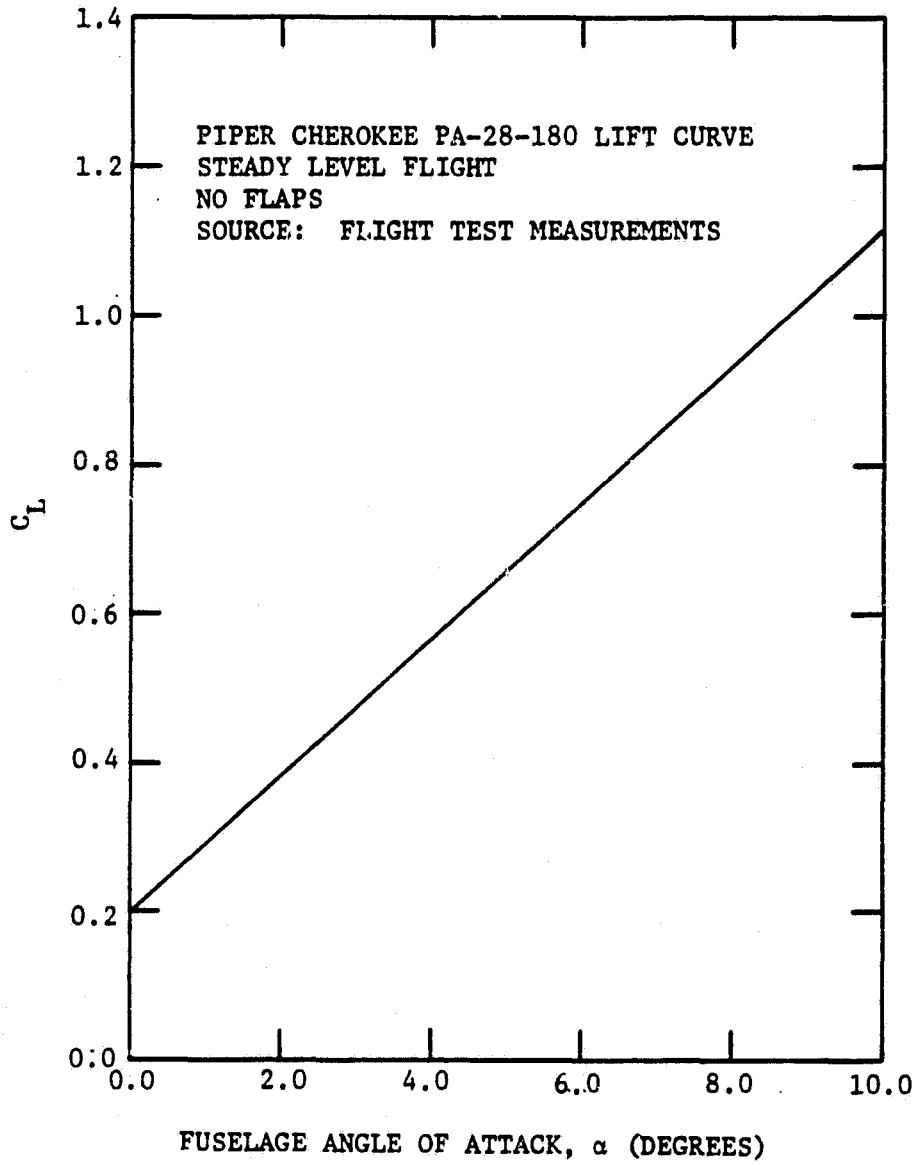

Figure 27. Lift Curve for the Piper Cherokee PA-28-180 Airplane

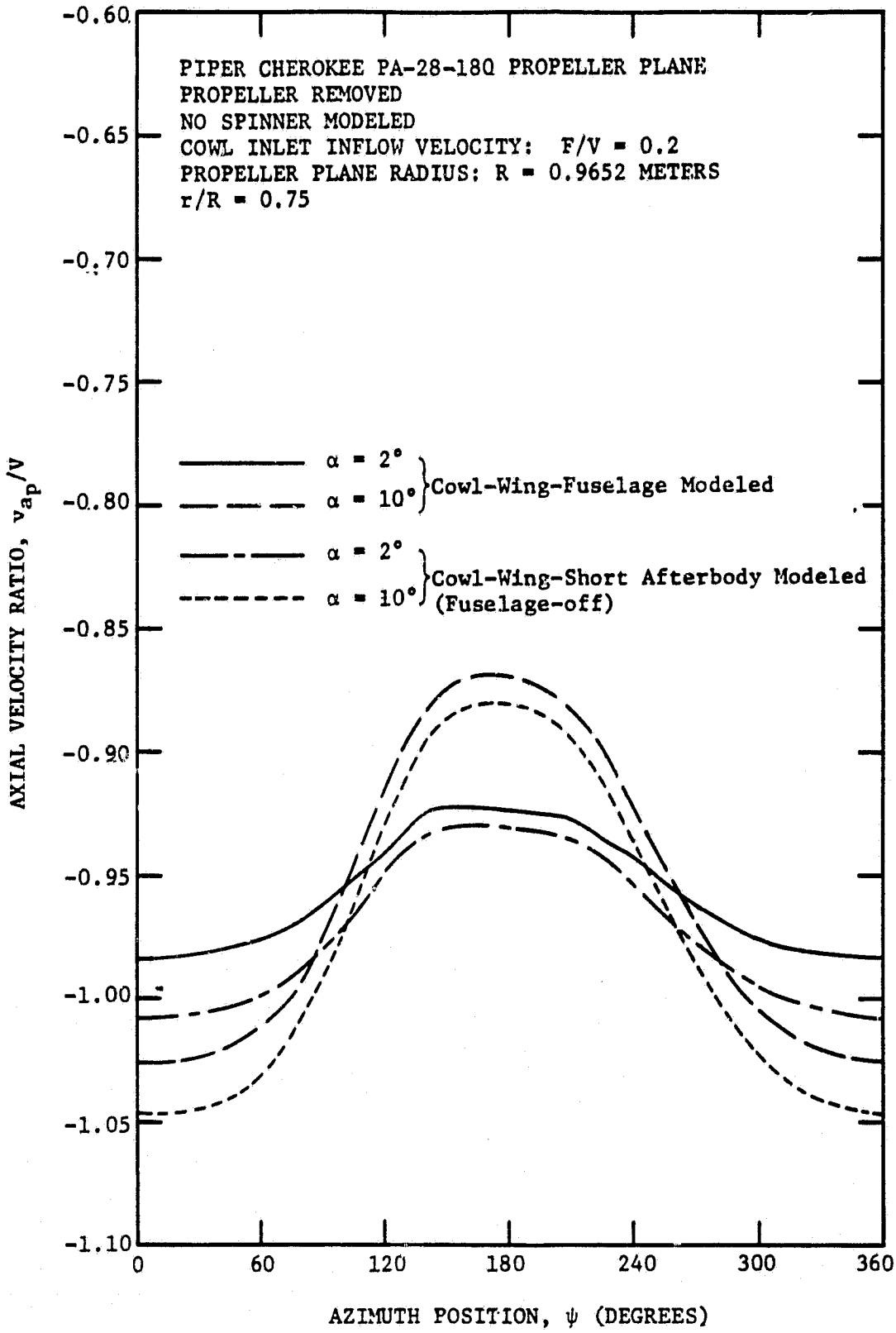

Figure 28a. Effect of Neglecting the Piper Cherokee 180 Fuselage Geometry (Replaced by a Short Afterbody) on the Computed Azimuthal Distribution of Axial Velocity at the Propeller Plane

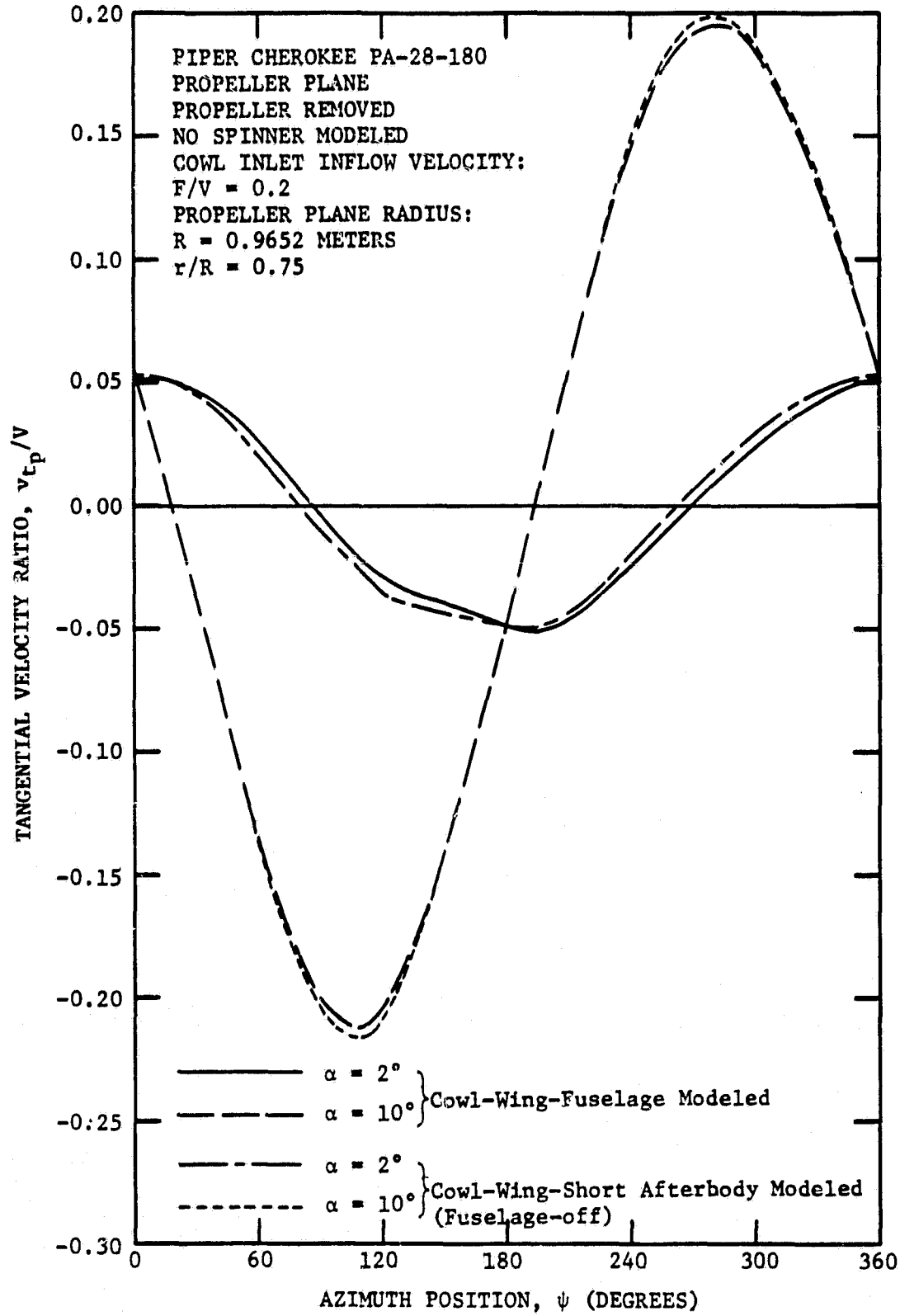

Figure 28b. Effect of Neglecting the Piper Cherokee 180 Fuselage Geometry (Replaced by a Short Afterbody) on the Computed Azimuthal Distribution of Tangential Velocity at the Propeller Plane

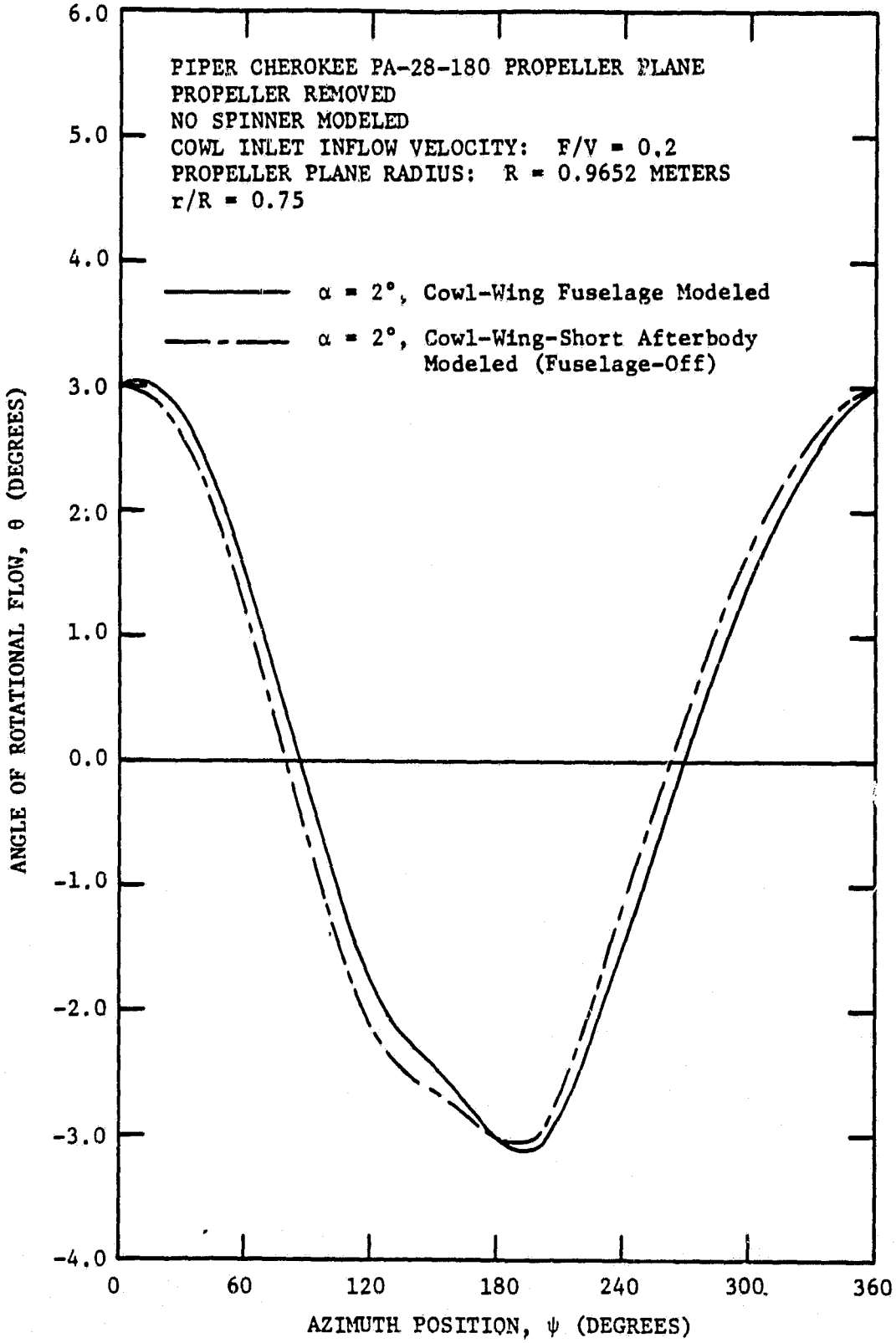

Figure 28c. Effect of Neglecting the Piper Cherokee 180 Fuselage Geometry (Replaced by a Short Afterbody) on the Computed Azimuthal Distribution of Flow Angularity at the Propeller Plane ($\alpha = 2°$ Case)

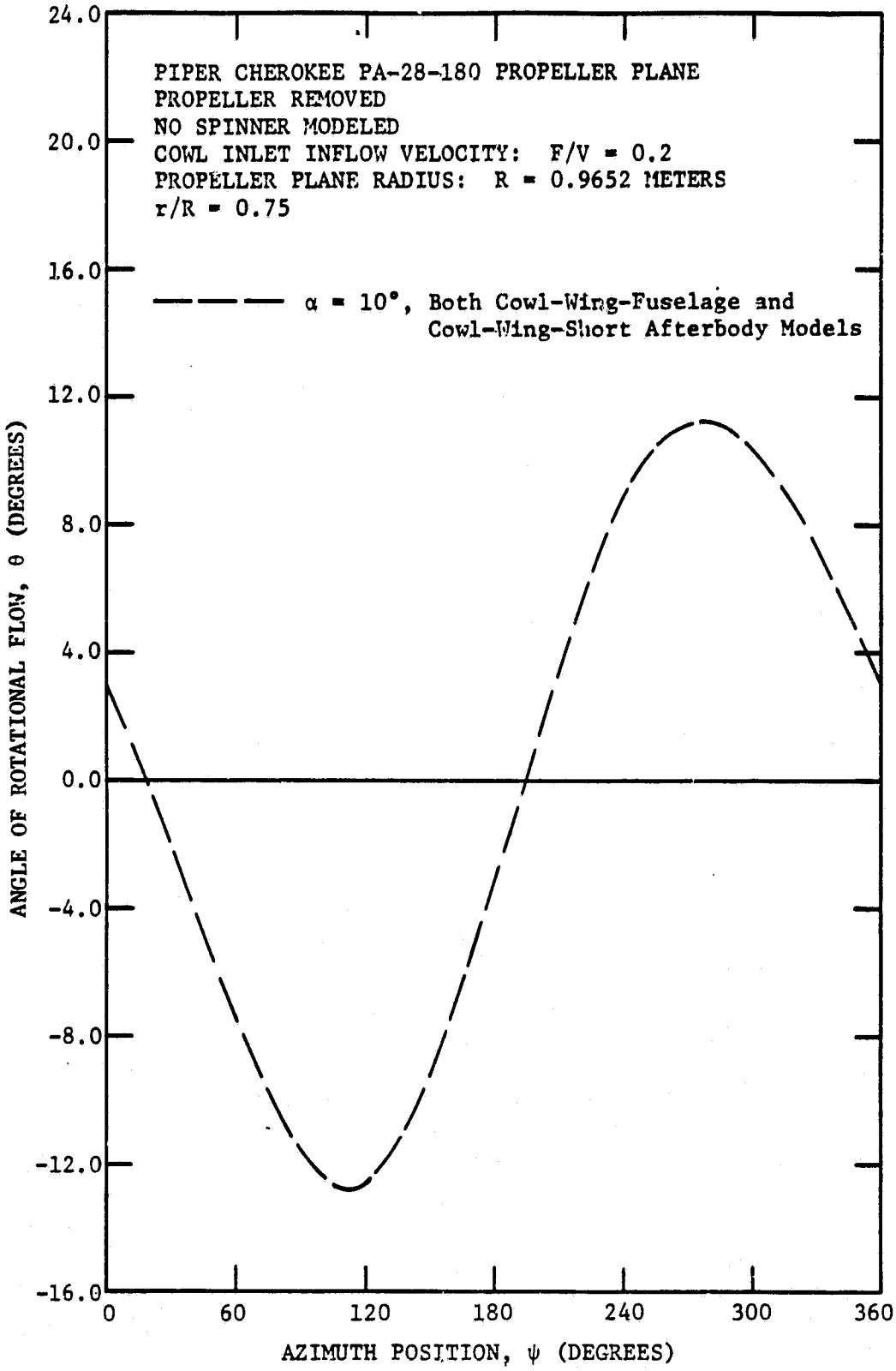

Figure 28d. Effect of Neglecting the Piper Cherokee 180 Fuselage Geometry (Replaced by a Short Afterbody) on the Computed Azimuthal Distribution of Flow Angularity at the Propeller Plane (α = 10° Case)

C-3

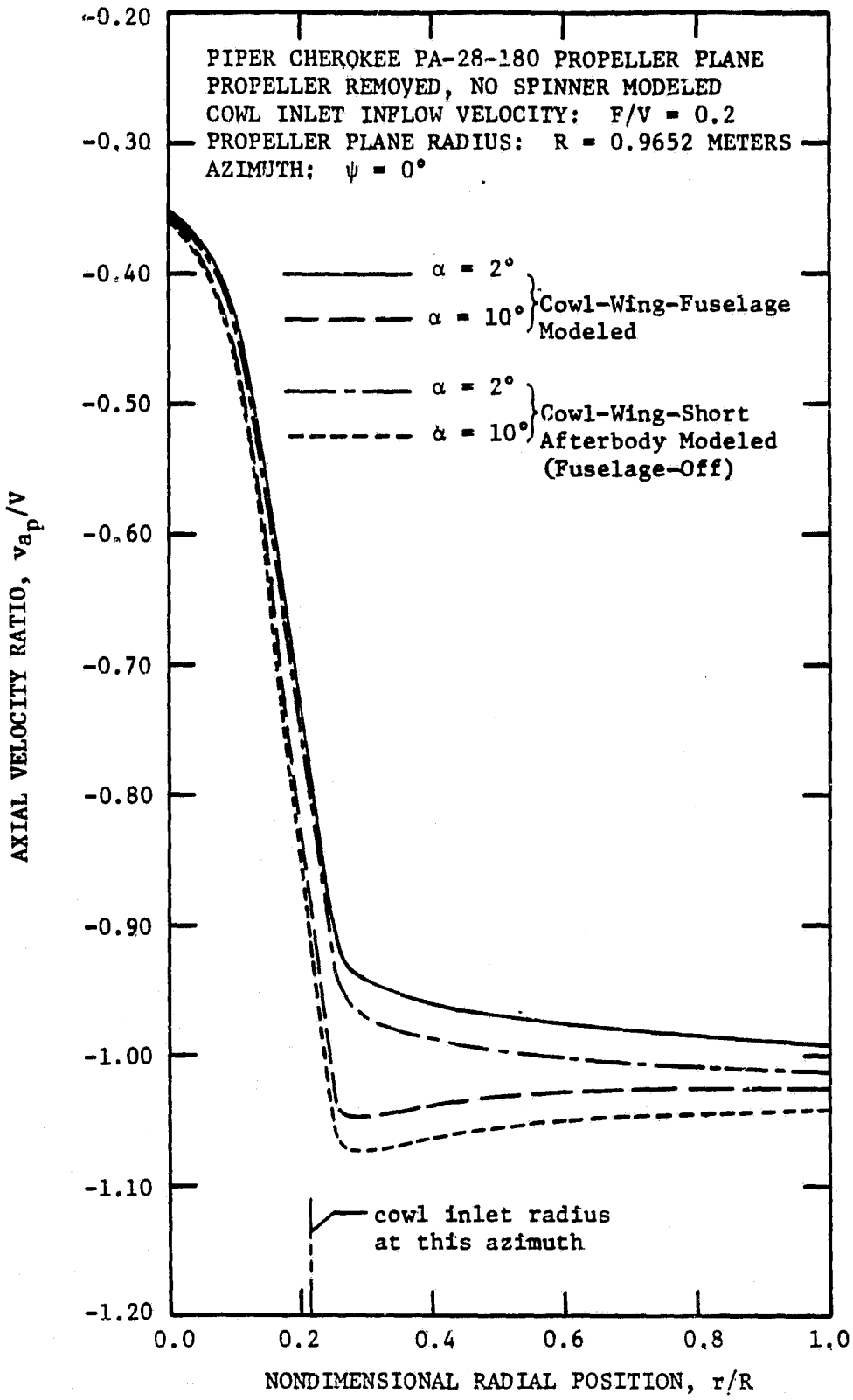

Figure 29. Effect of Neglecting the Piper Cherokee 180 Fuselage Geometry (Replaced by a Short Afterbody) on the Computed Radial Distribution of Axial Velocity at the Propeller Plane

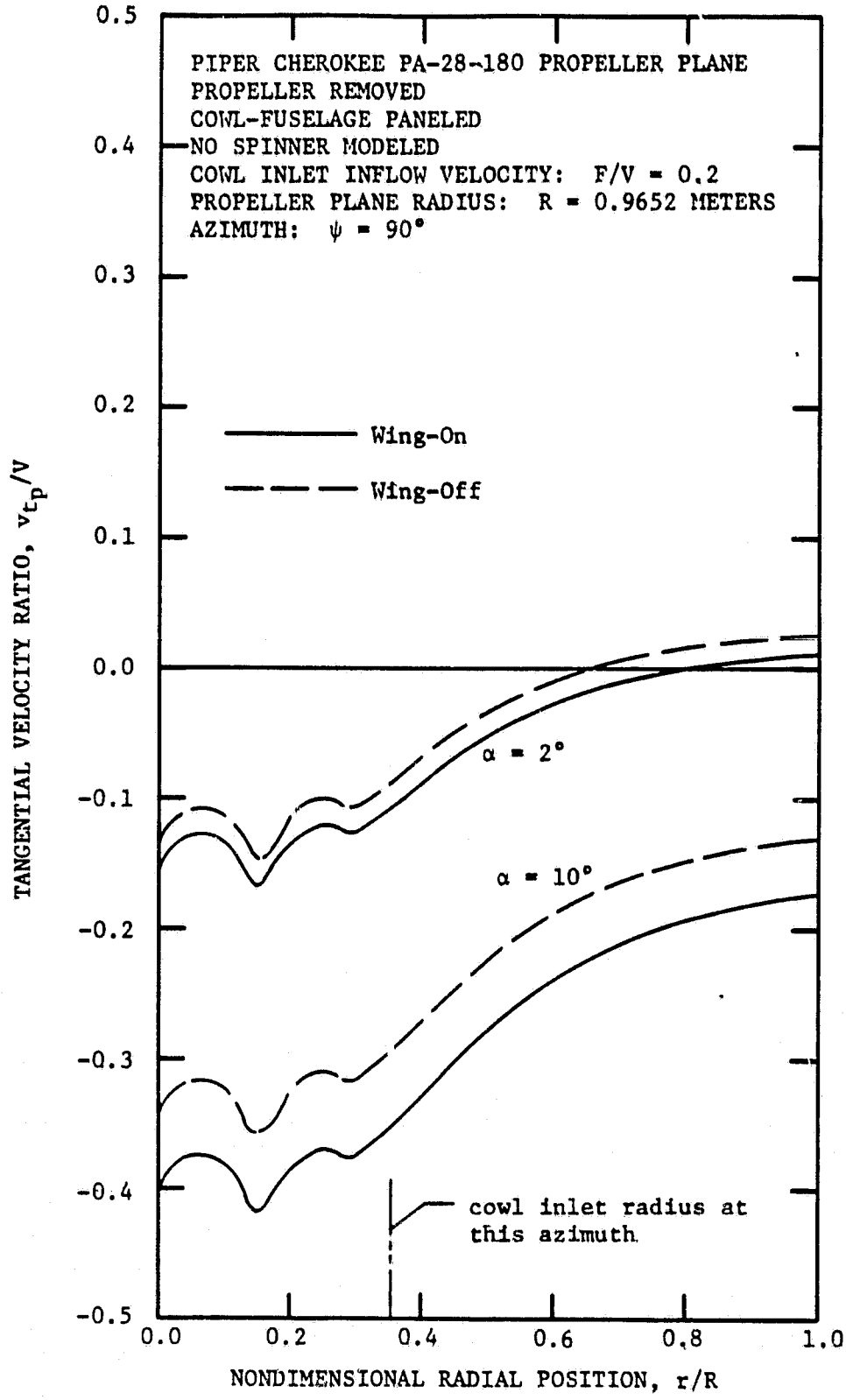

Figure 30a. Effect of Neglecting the Piper Cherokee 180 Wing on the Computed Radial Distribution of Tangential Velocity at the Propeller Plane

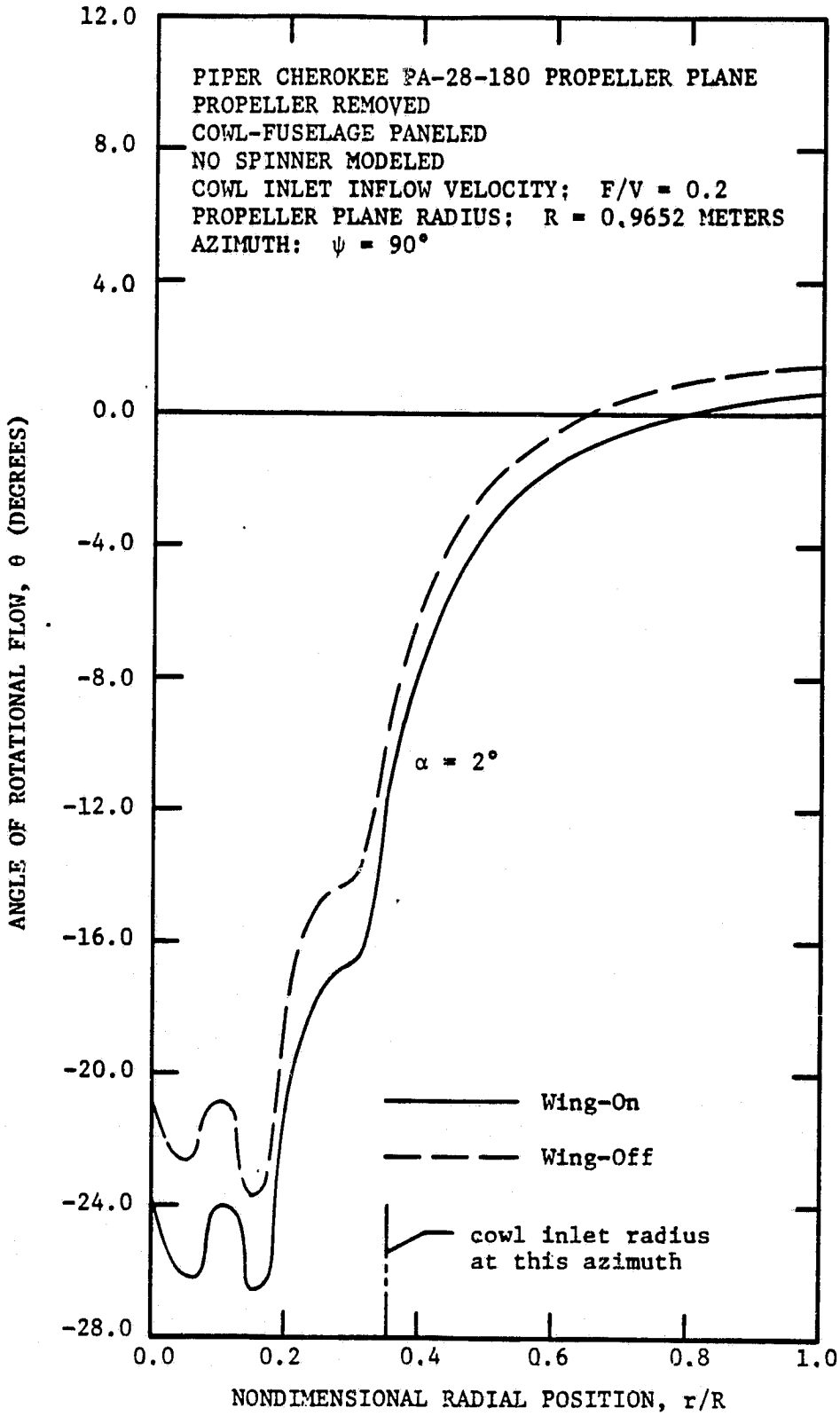

Figure 30b. Effect of Neglecting the Piper Cherokee 180 Wing on the Computed Radial Distribution of Flow Angularity at the Propeller Plane ($\alpha = 2°$ Case)

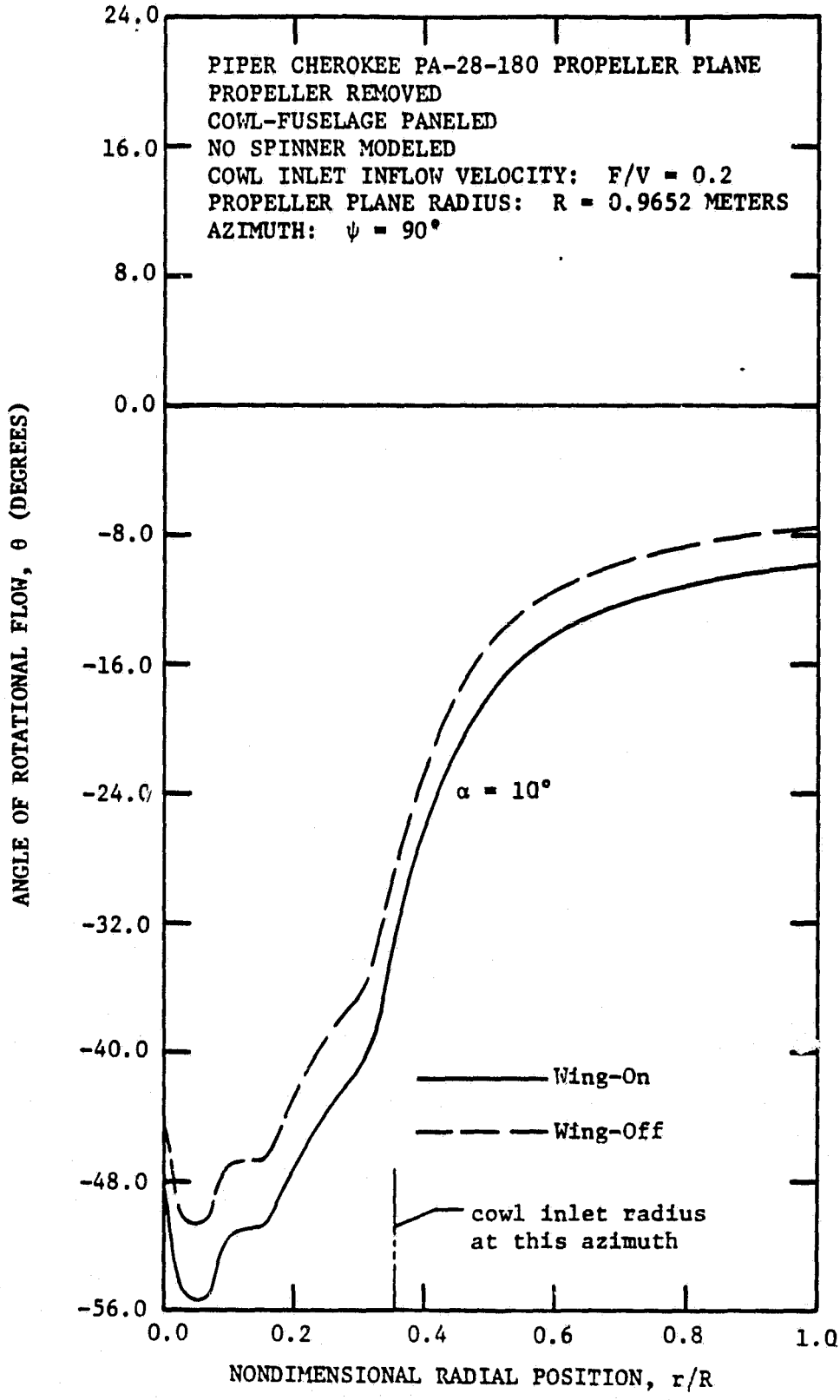

Figure 30c. Effect of Neglecting the Piper Cherokee 180 Wing on the Computed Radial Distribution of Flow Angularity at the Propeller Plane (α = 10° Case)

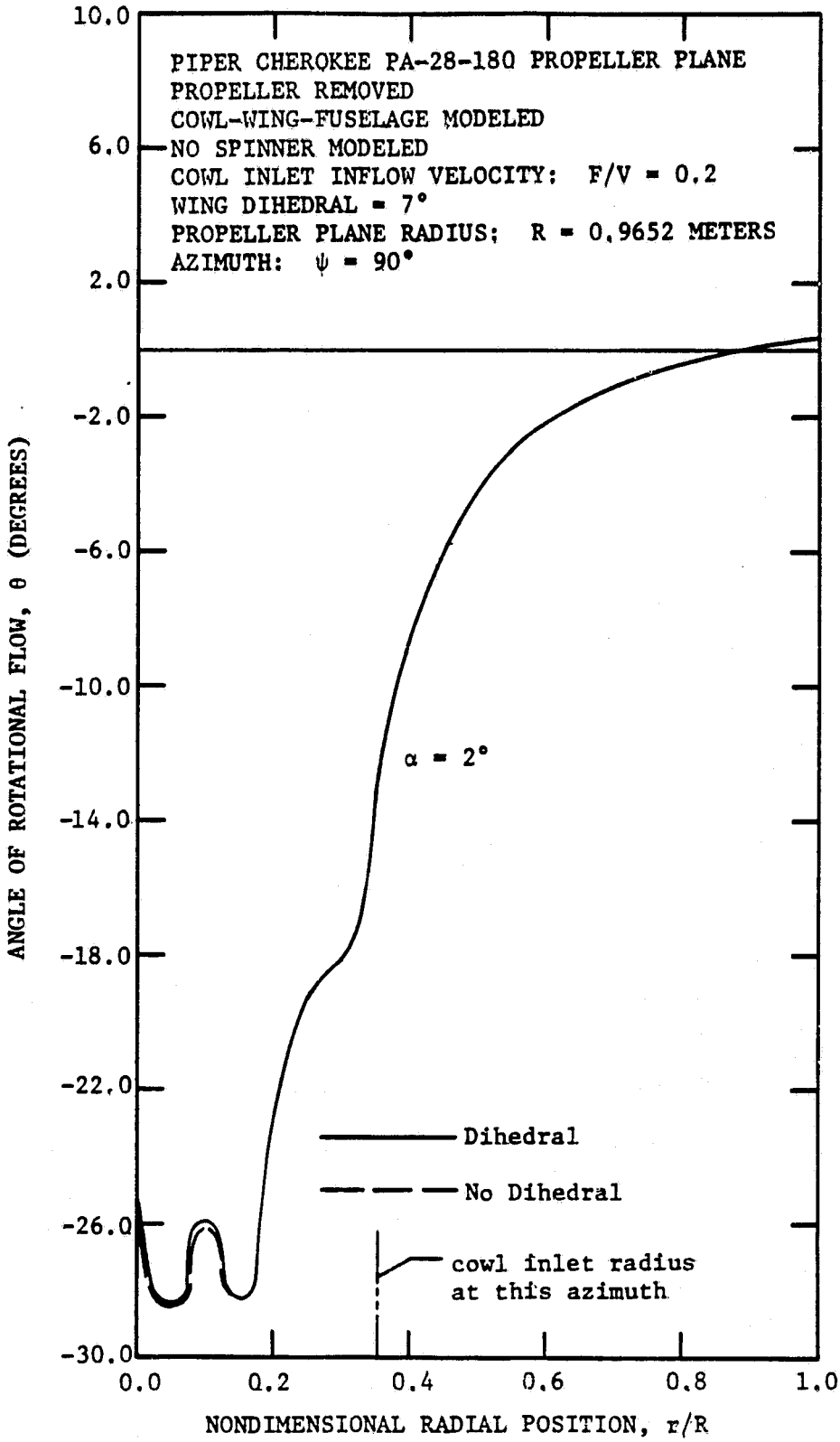

Figure 31a. Effect of Wing Dihedral on the Computed Radial Distribution of Flow Angularity at the Propeller Plane of the Piper Cherokee 180 (α = 2° Case)

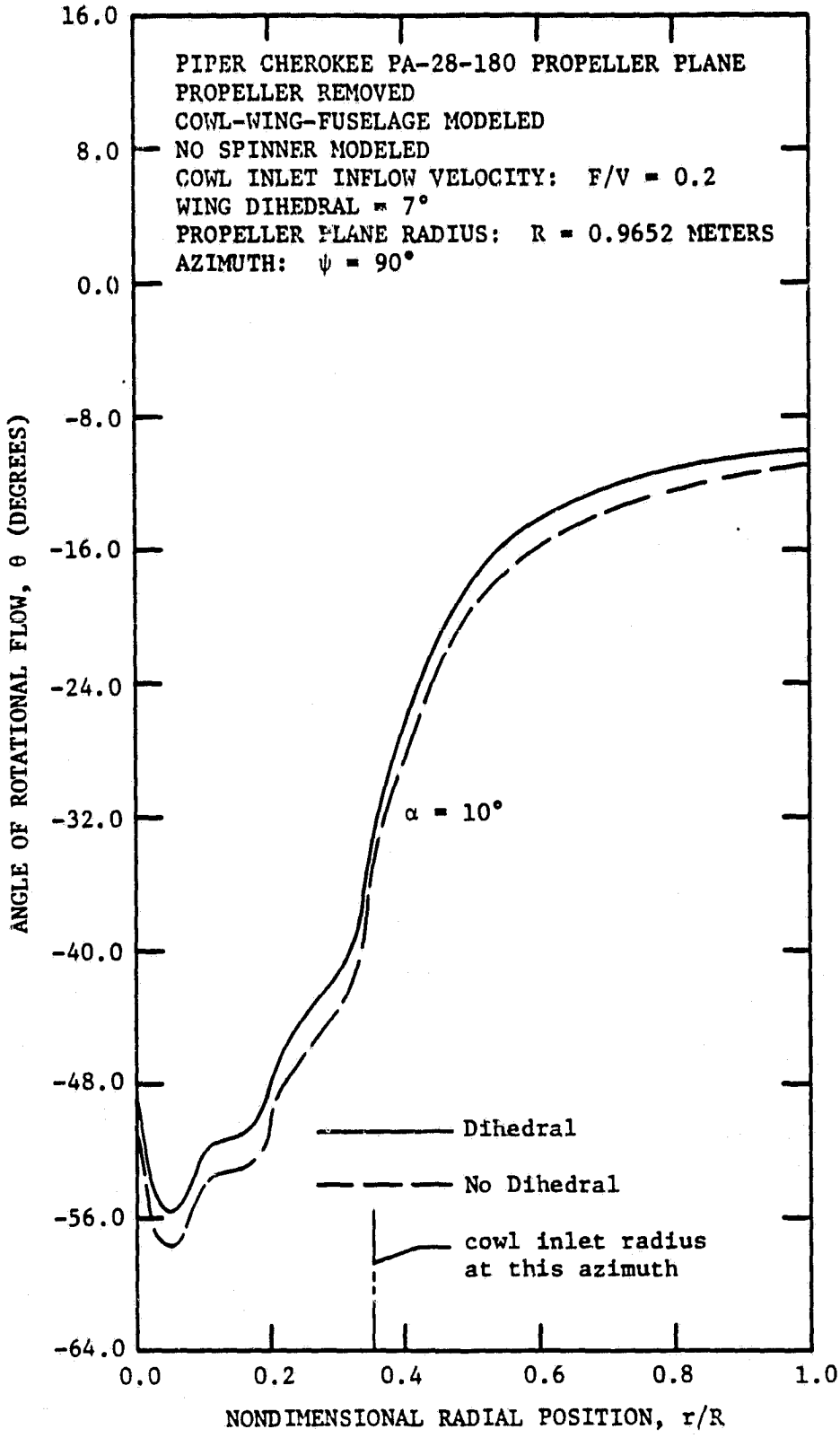

Figure 31b. Effect of Wing Dihedral on the Computed Radial Distribution of Flow Angularity at the Propeller Plane of the Piper Cherokee 180 (α = 10° Case)

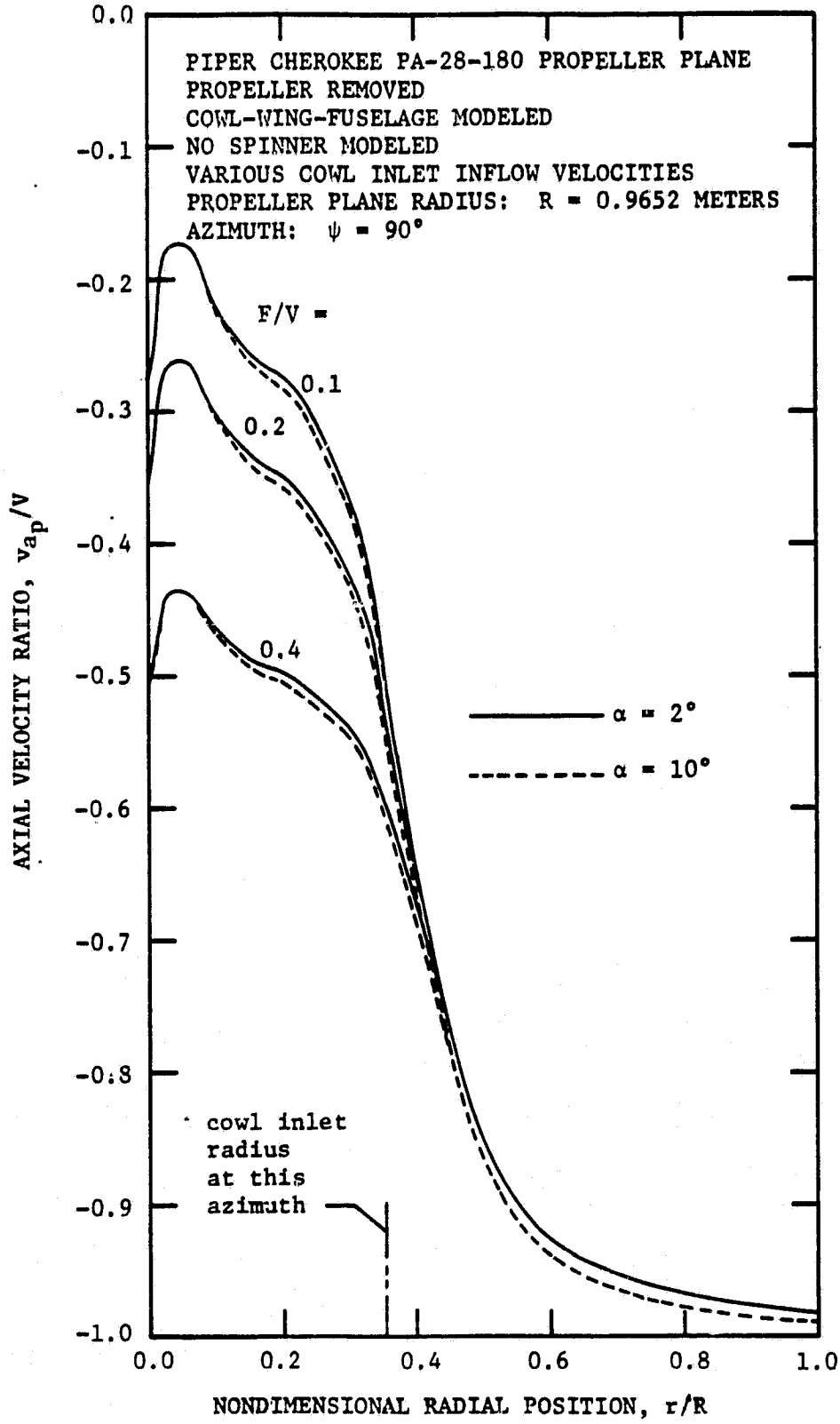

Figure 32a. Effect of Change in Cowl Inlet Inflow Velocity on the Computed Radial Distribution of Axial Velocity at the Propeller Plane of the Piper Cherokee 180

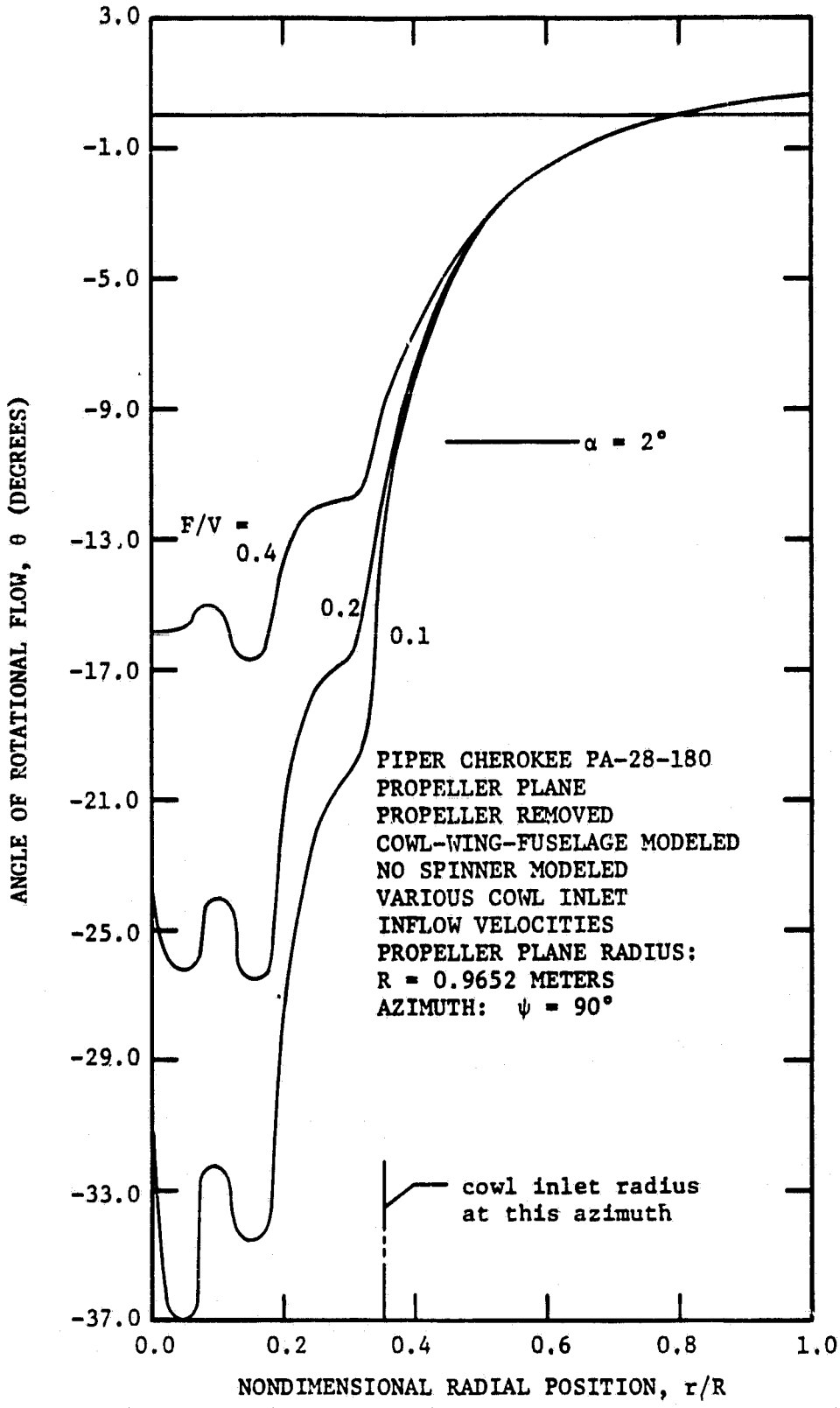

Figure 32b. Effect of Change in Cowl Inlet Inflow Velocity on the Computed Radial Distribution of Flow Angularity at the Propeller Plane of the Piper Cherokee 180 (α = 2° Case)

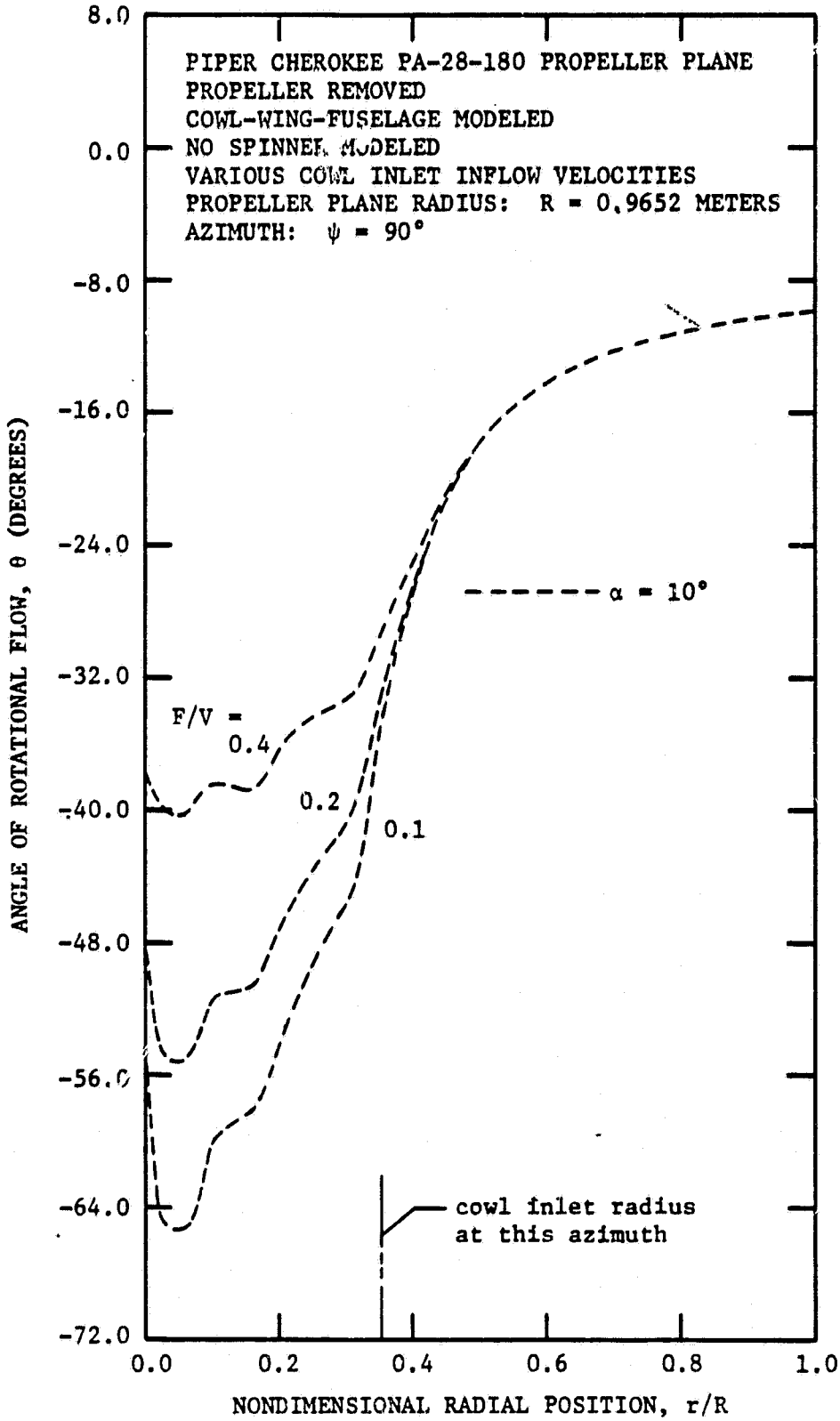

Figure 32c. Effect of Change in Cowl Inlet Inflow Velocity on the Computed Radial Distribution of Flow Angularity at the Propeller Plane of the Piper Cherokee 180 (α = 10° Case)

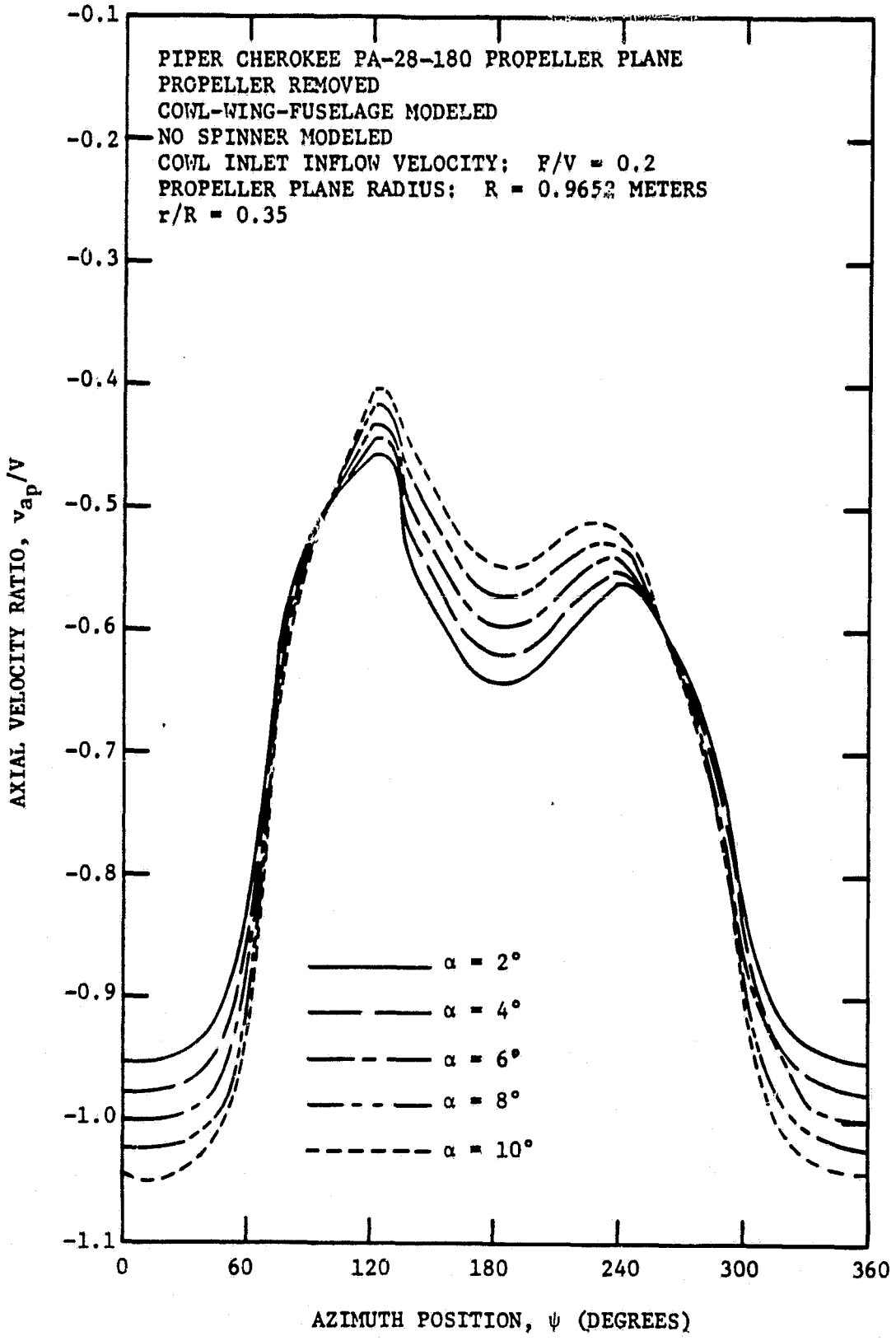

Figure 33a. Computed Azimuthal Distributions of Axial Velocity at the Propeller Plane of the Piper Cherokee 180 (at r/R = 0.35)

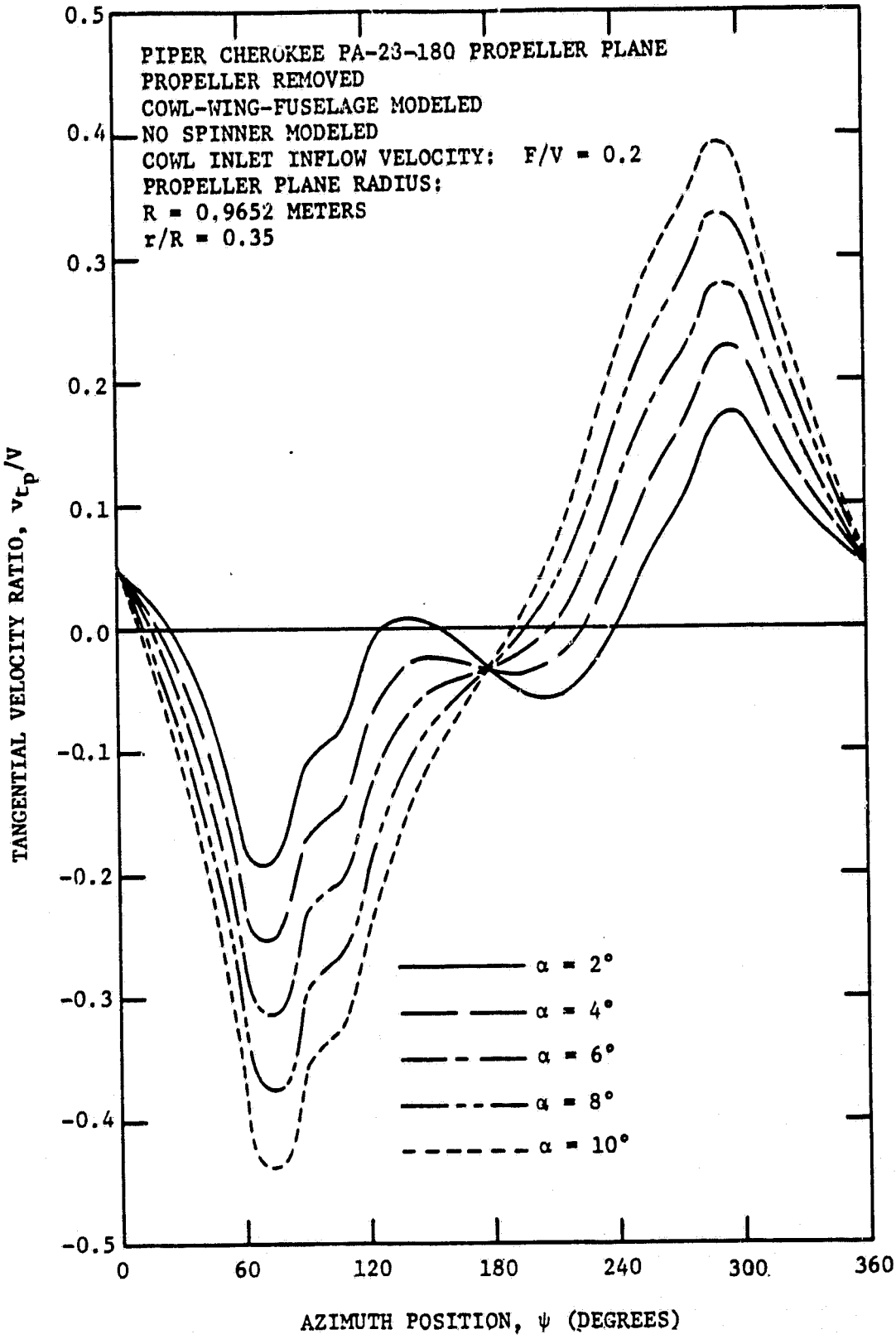

Figure 33h. Computed Azimuthal Distributions of Tangential Velocity at the Propeller Plane of the Piper Cherokee 180 (at r/R = 0.35)

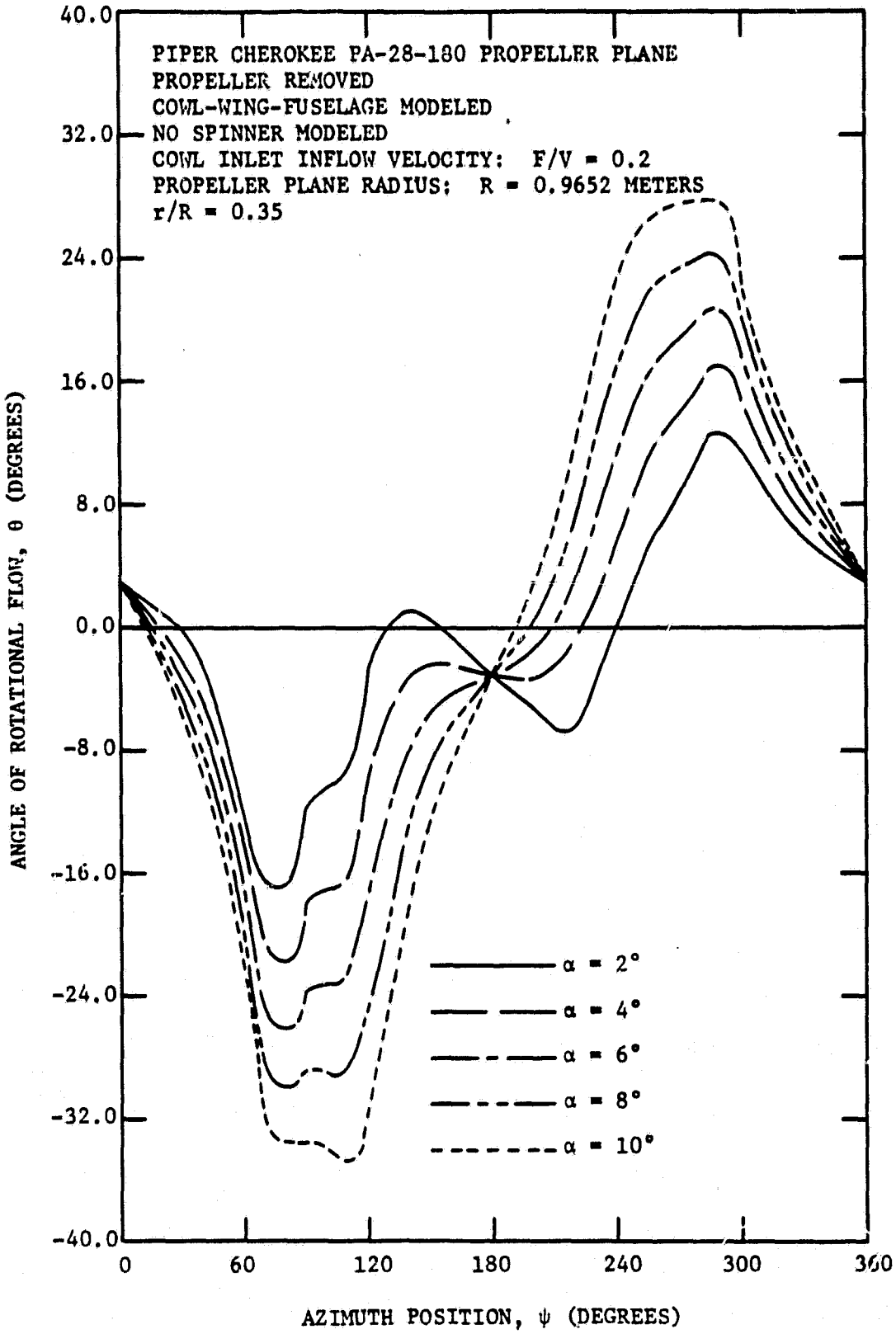

Figure 33c. Computed Azimuthal Distributions of Angle of Rotational Flow at the Propeller Plane of the Piper Cherokee 180 (at r/R = 0.35)

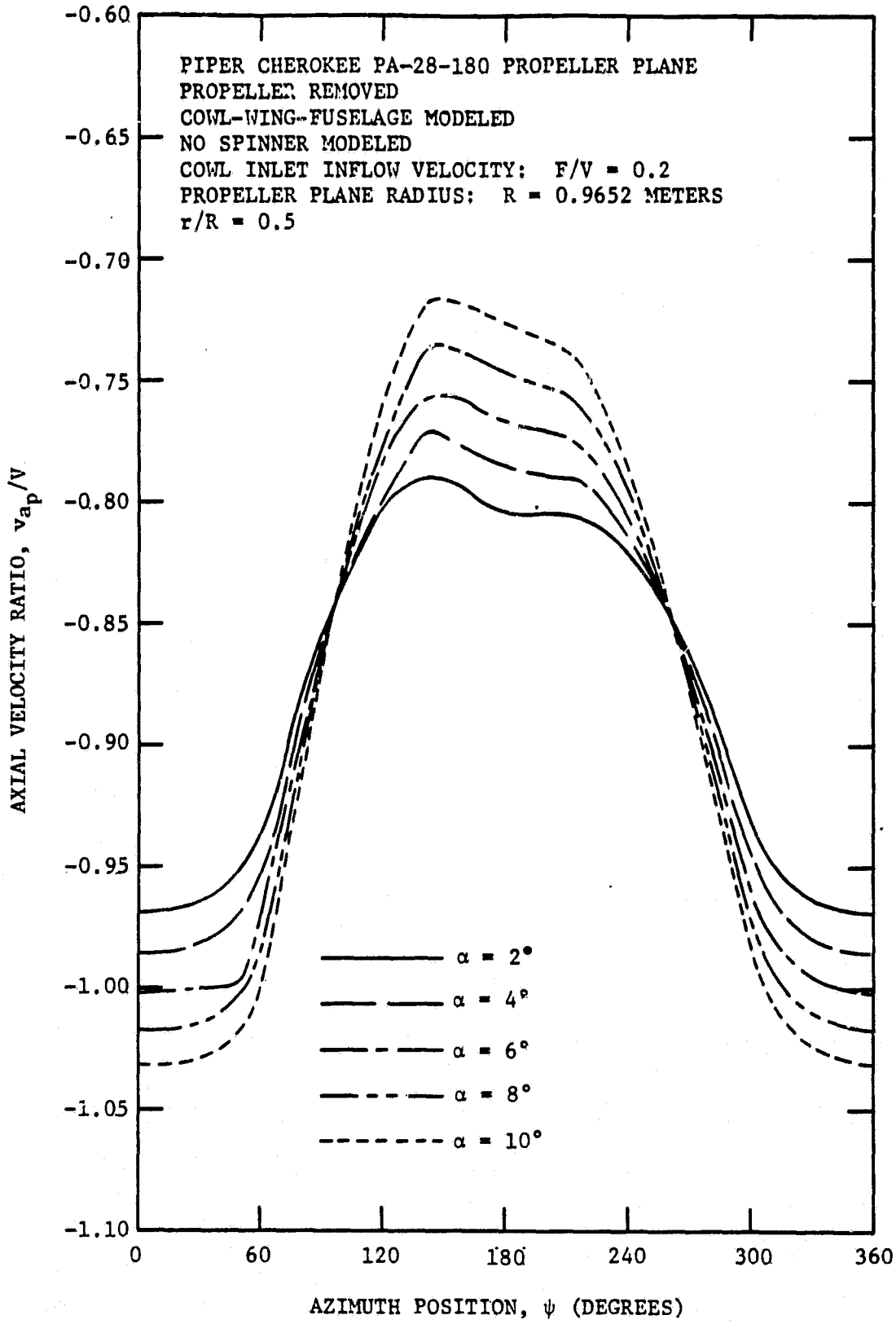

Figure 34a. Computed Azimuthal Distributions of Axial Velocity at the Propeller Plane of the Piper Cherokee 180 (at r/R = 0.5)

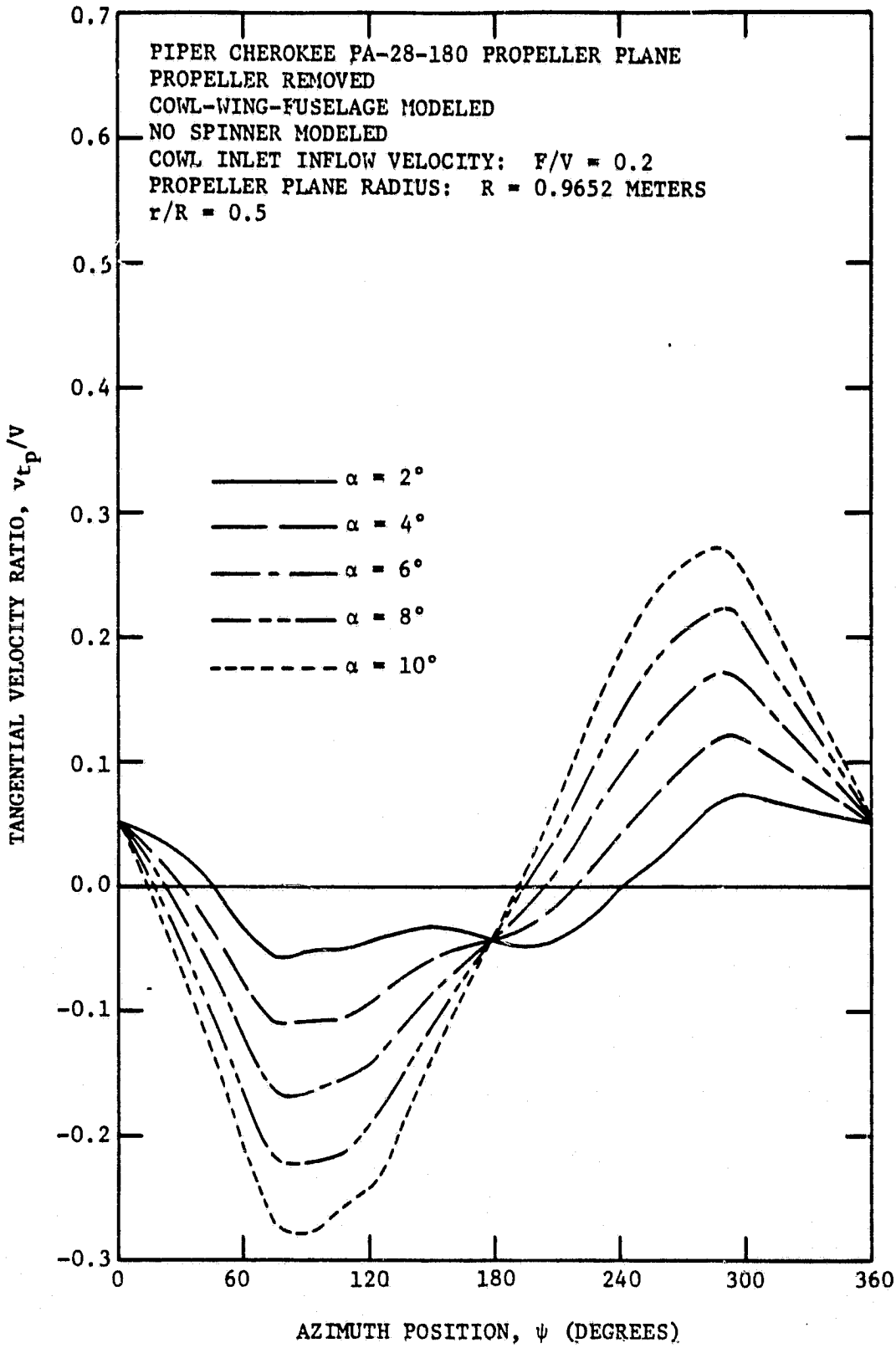

Figure 34b. Computed Azimuthal Distributions of Tangential Velocity at the Propeller Plane of the Piper Cherokee 180 (at r/R = 0.5)

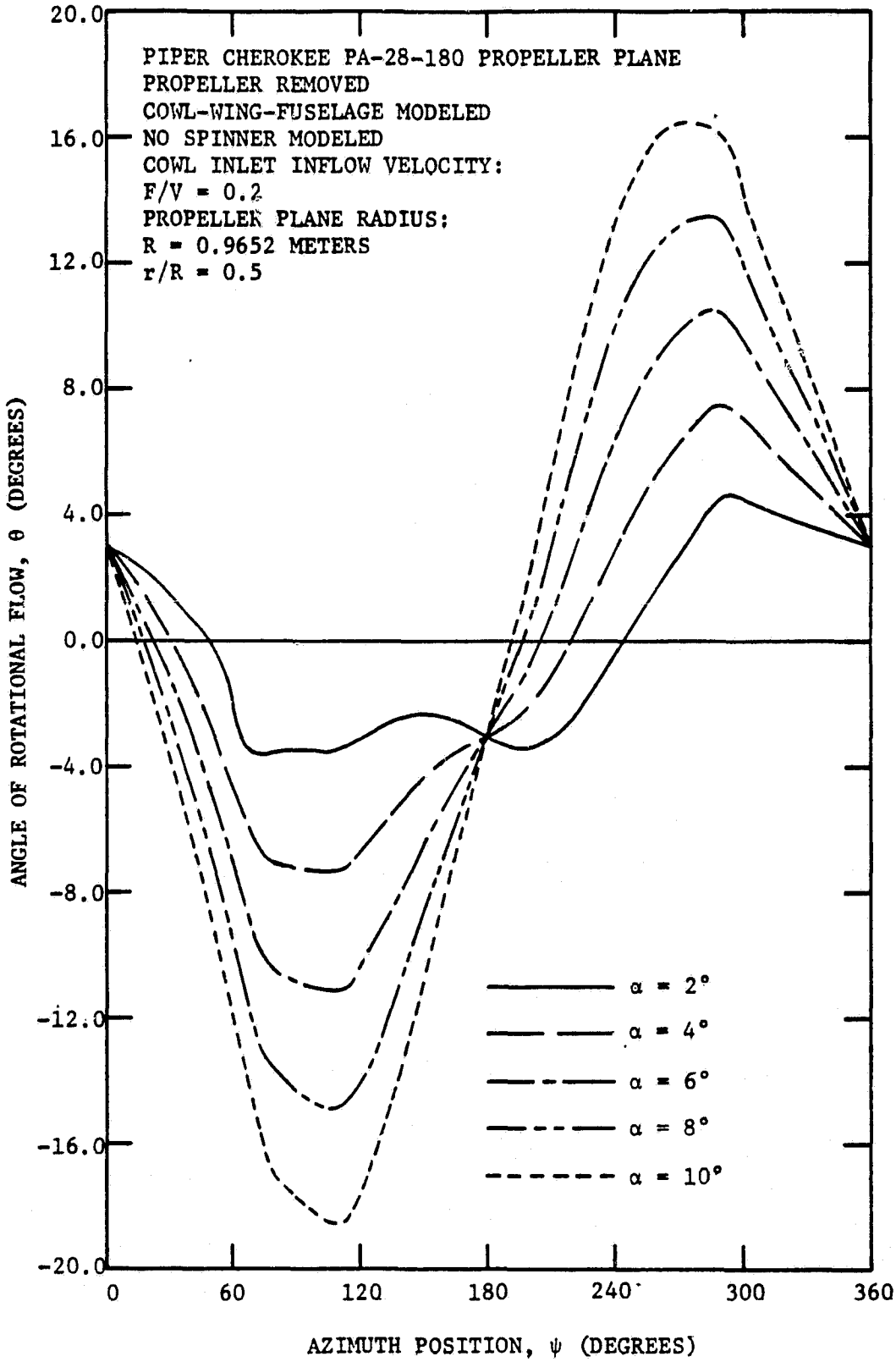

Figure 34c. Computed Azimuthal Distributions of Angle of Rotational Flow at the Propeller Plane of the Piper Cherokee 180 (at r/R = 0.5)

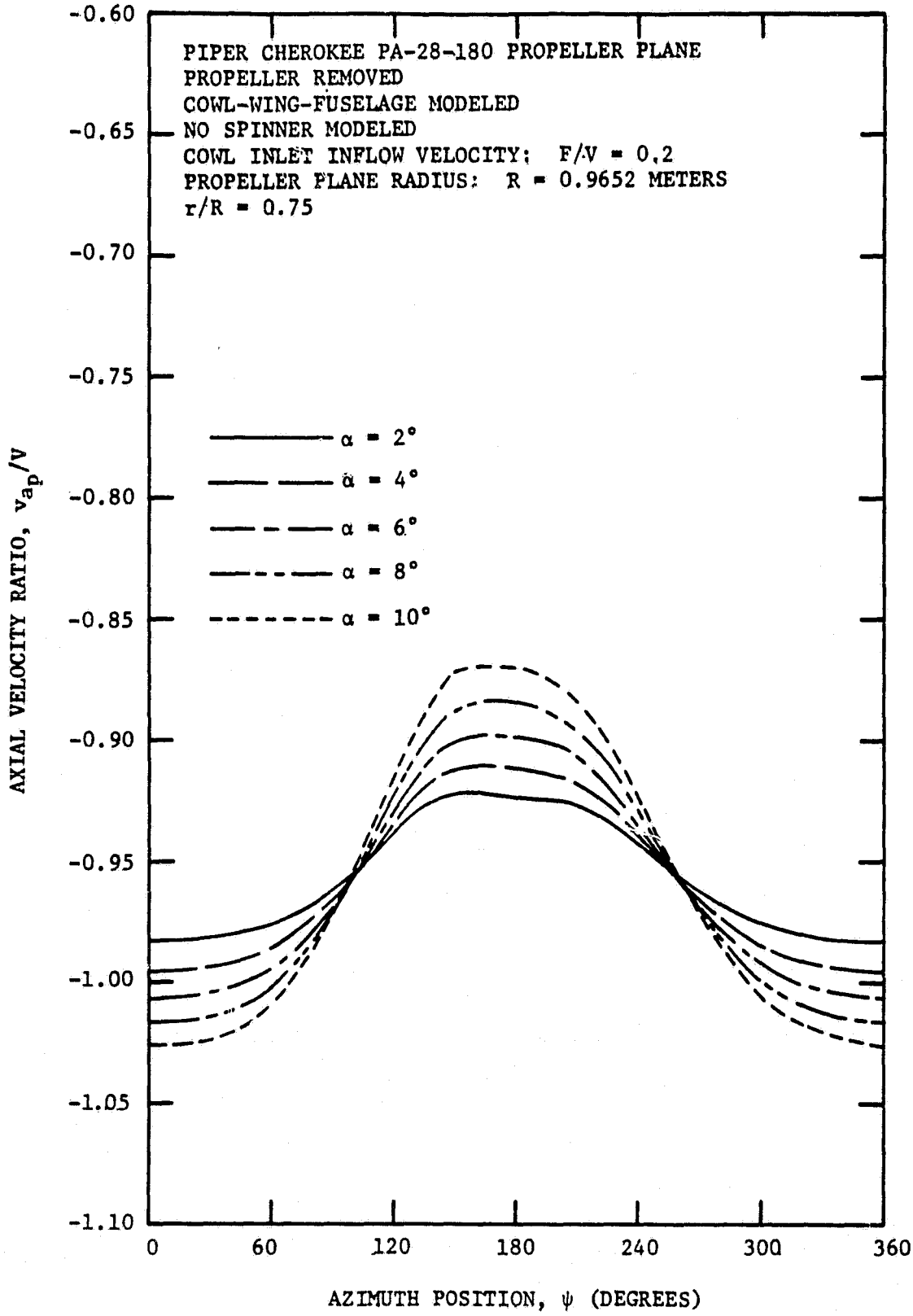

Figure 35a. Computed Azimuthal Distributions of Axial Velocity at the Propeller Plane of the Piper Cherokee 180 (at r/R = 0.75)

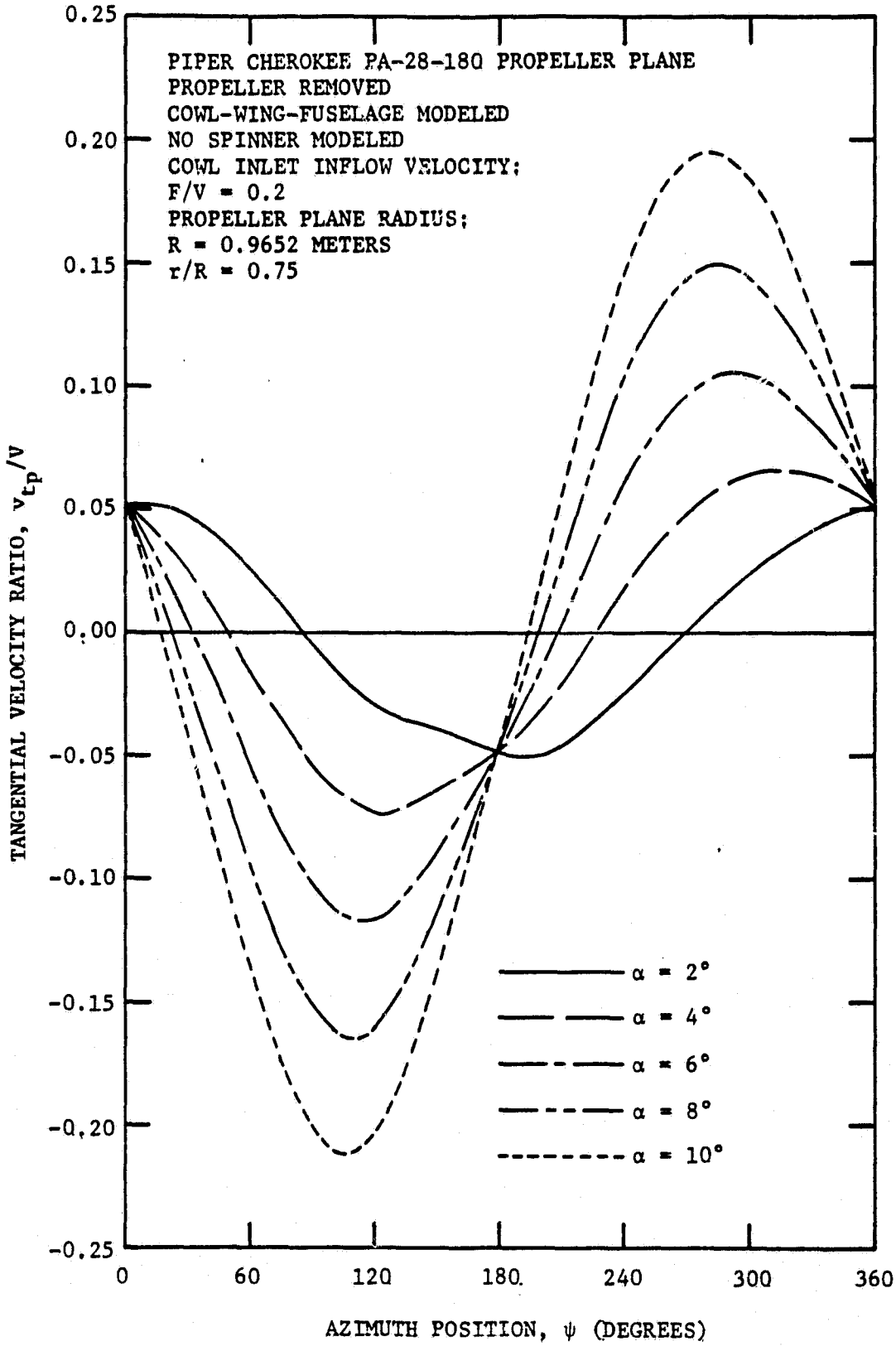

Figure 35b. Computed Azimuthal Distributions of Tangential Velocity at the Propeller Plane of the Piper Cherokee 180 (at r/R = 0.75)

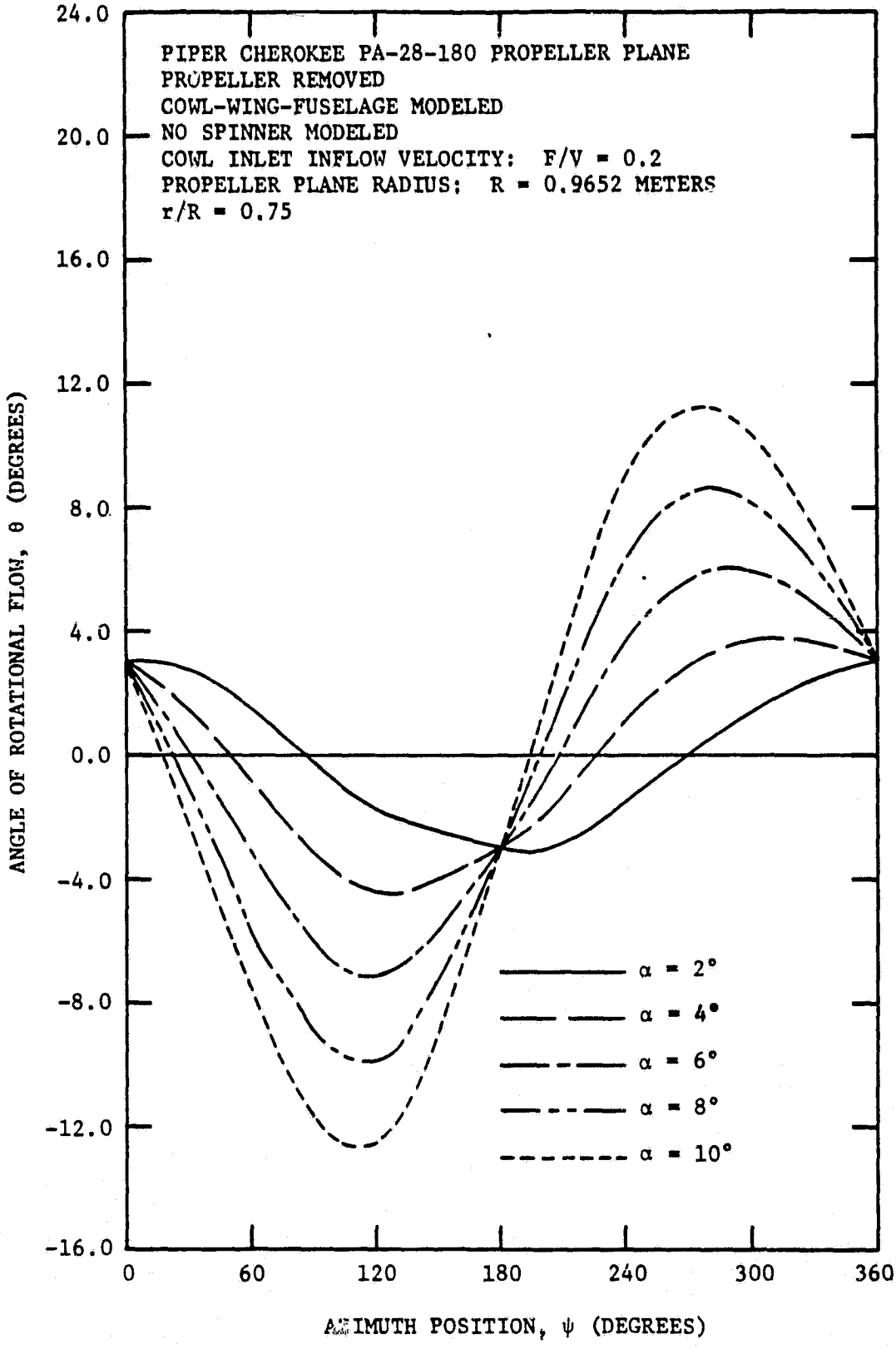

Figure 35c. Computed Azimuthal Distributions of Angle of Rotational Flow at the Propeller Plane of the Piper Cherokee 180 (at r/R = 0.75)

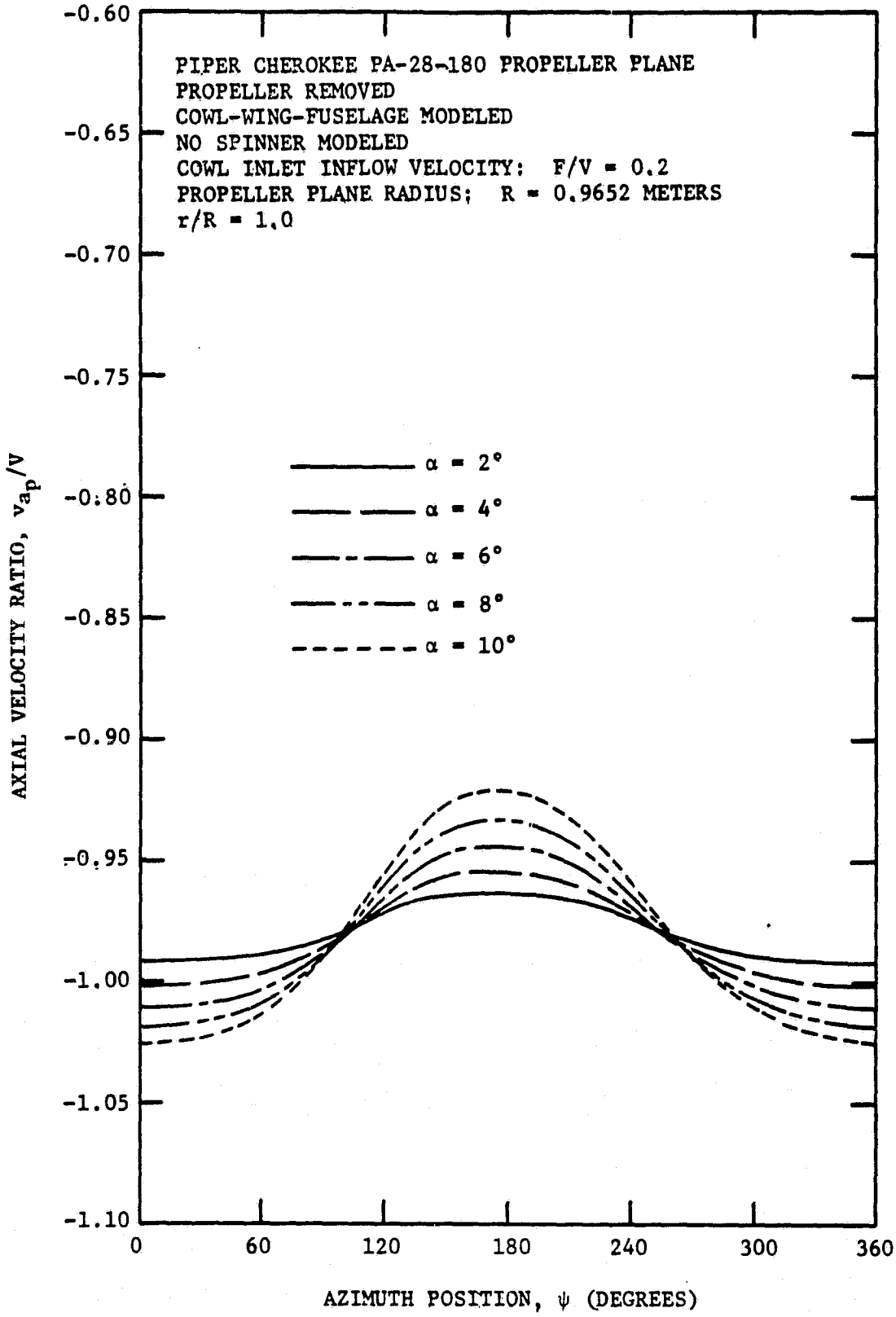

Figure 36a. Computed Azimuthal Distributions of Axial Velocity at the Propeller Plane of the Piper Cherokee 180 (at r/R = 1.0)

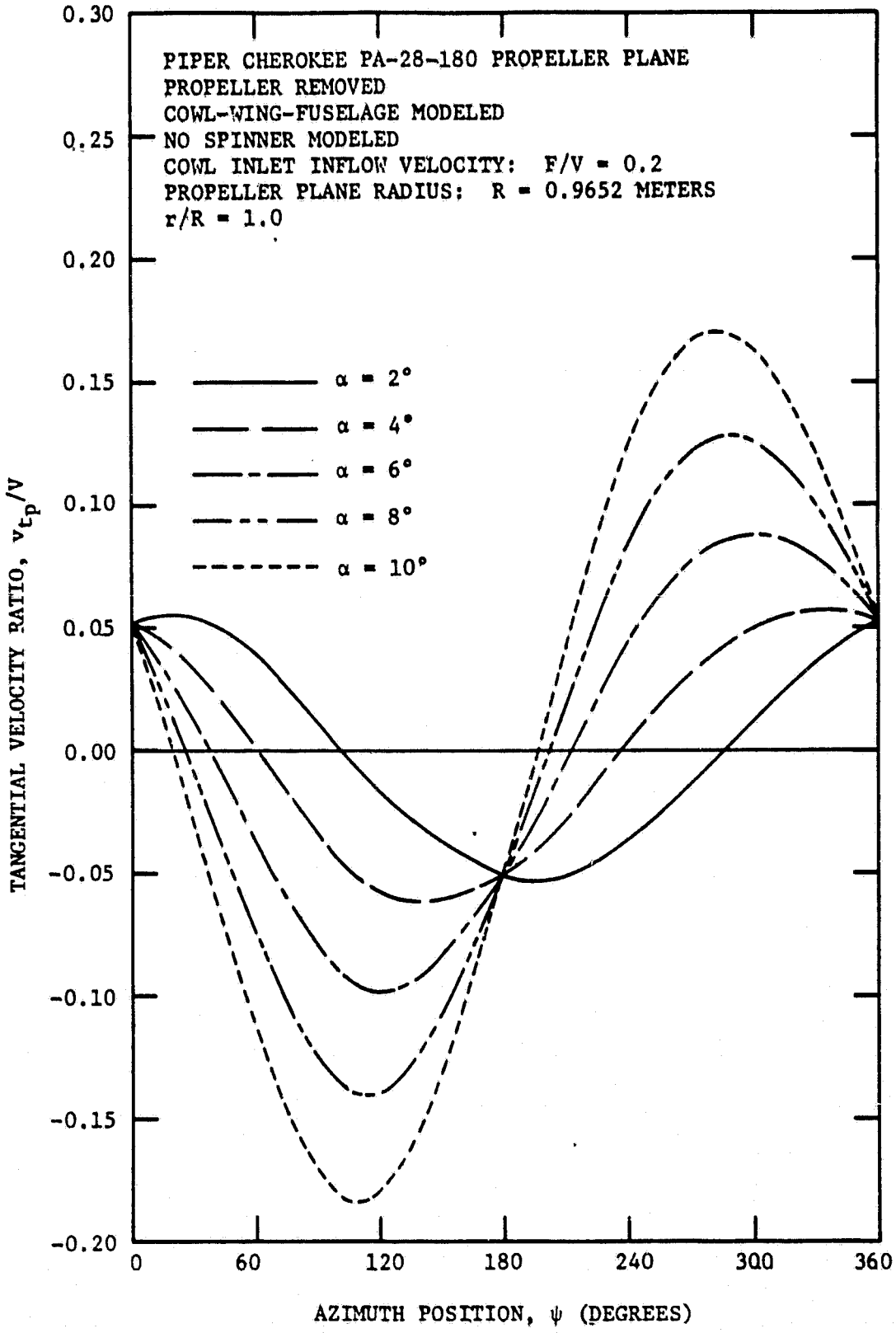

Figure 36b. Computed Azimuthal Distributions of Tangential Velocity at the Propeller Plane of the Piper Cherokee 180 (at r/R = 1.0)

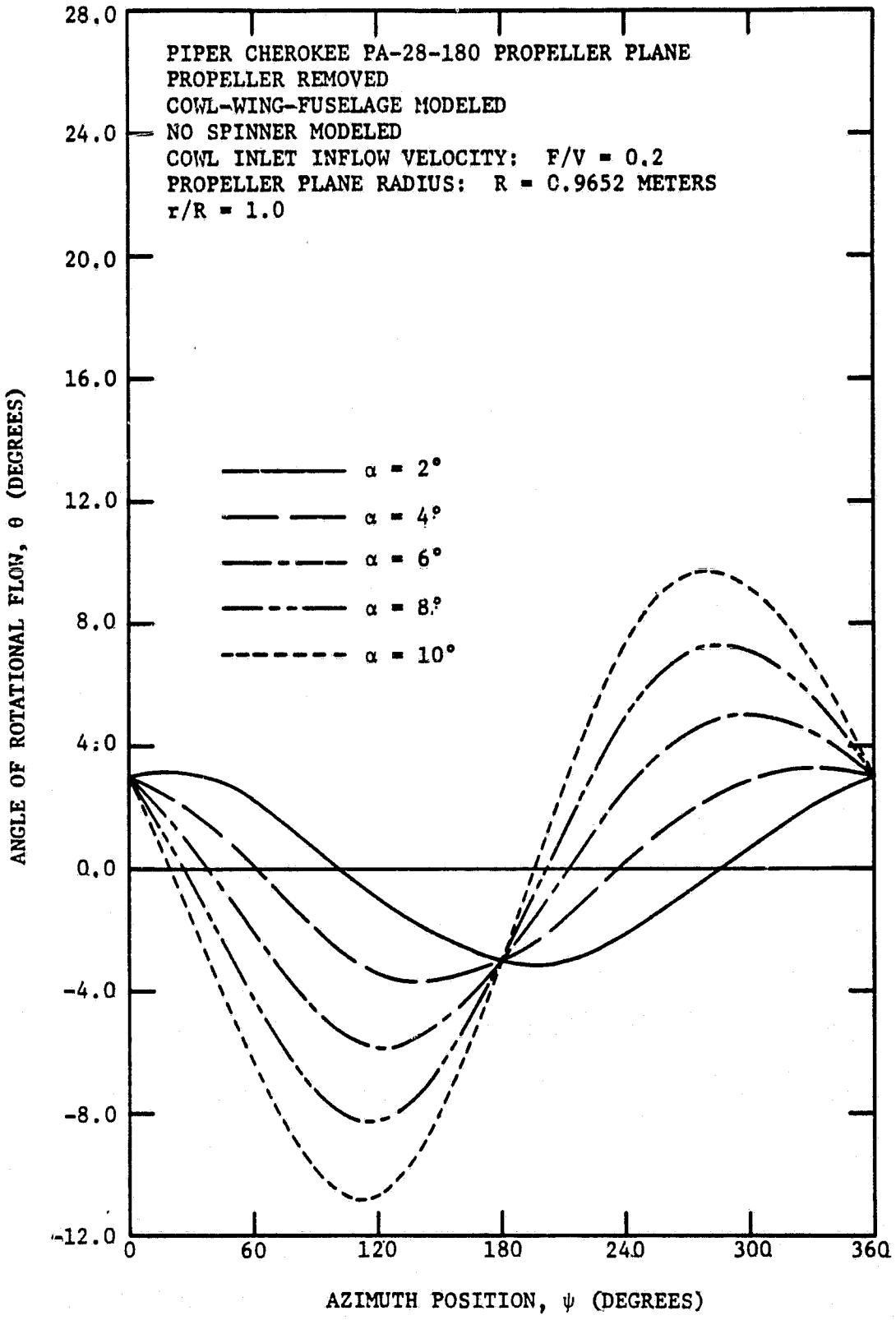

Figure 36c. Computed Azimuthal Distributions of Angle of Rotational Flow at the Propeller Plane of the Piper Cherokee 180 (at r/R = 1.0)

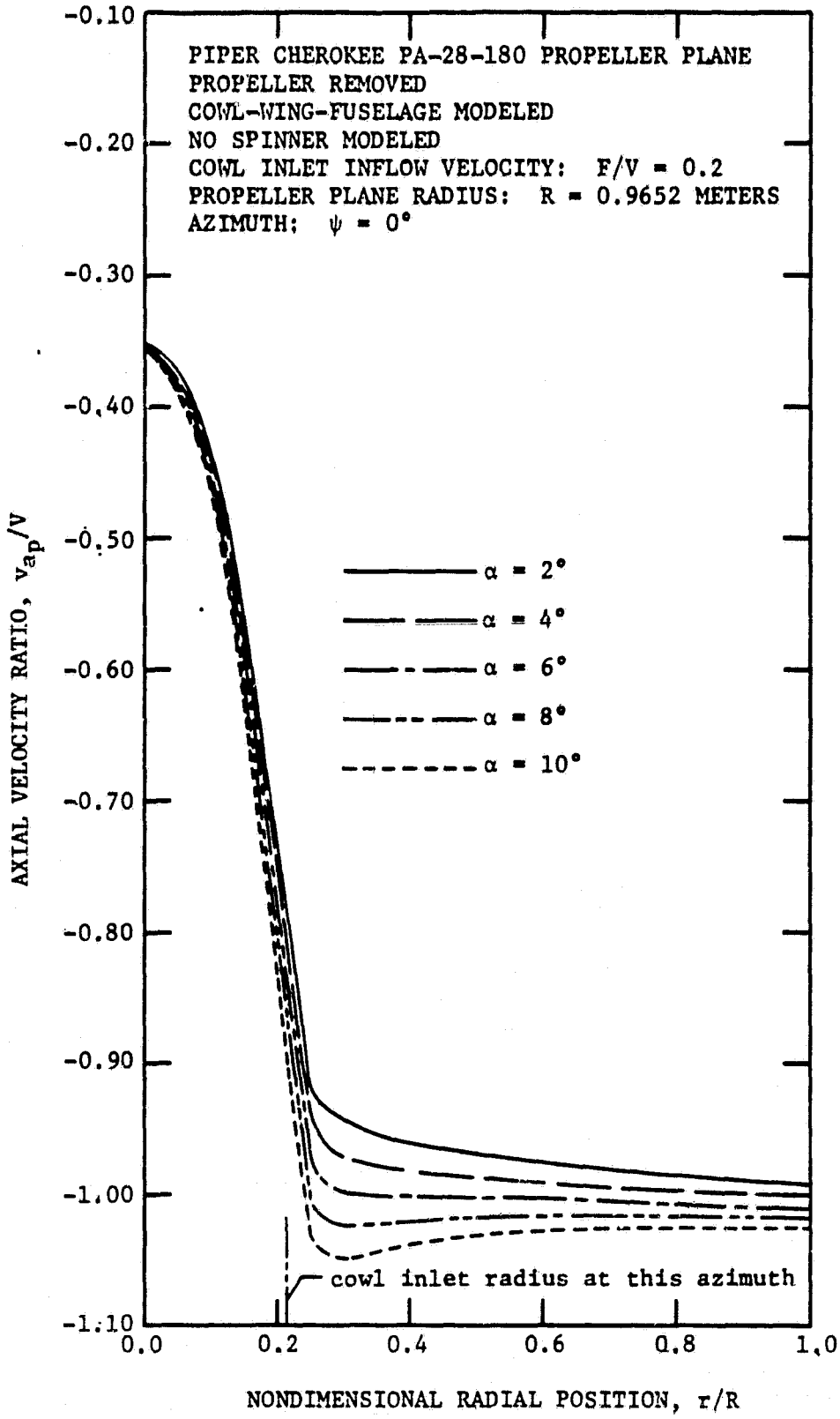

Figure 37a. Computed Radial Distributions of Axial Velocity at the Propeller Plane of the Piper Cherokee 180 (at $\psi = 0°$)

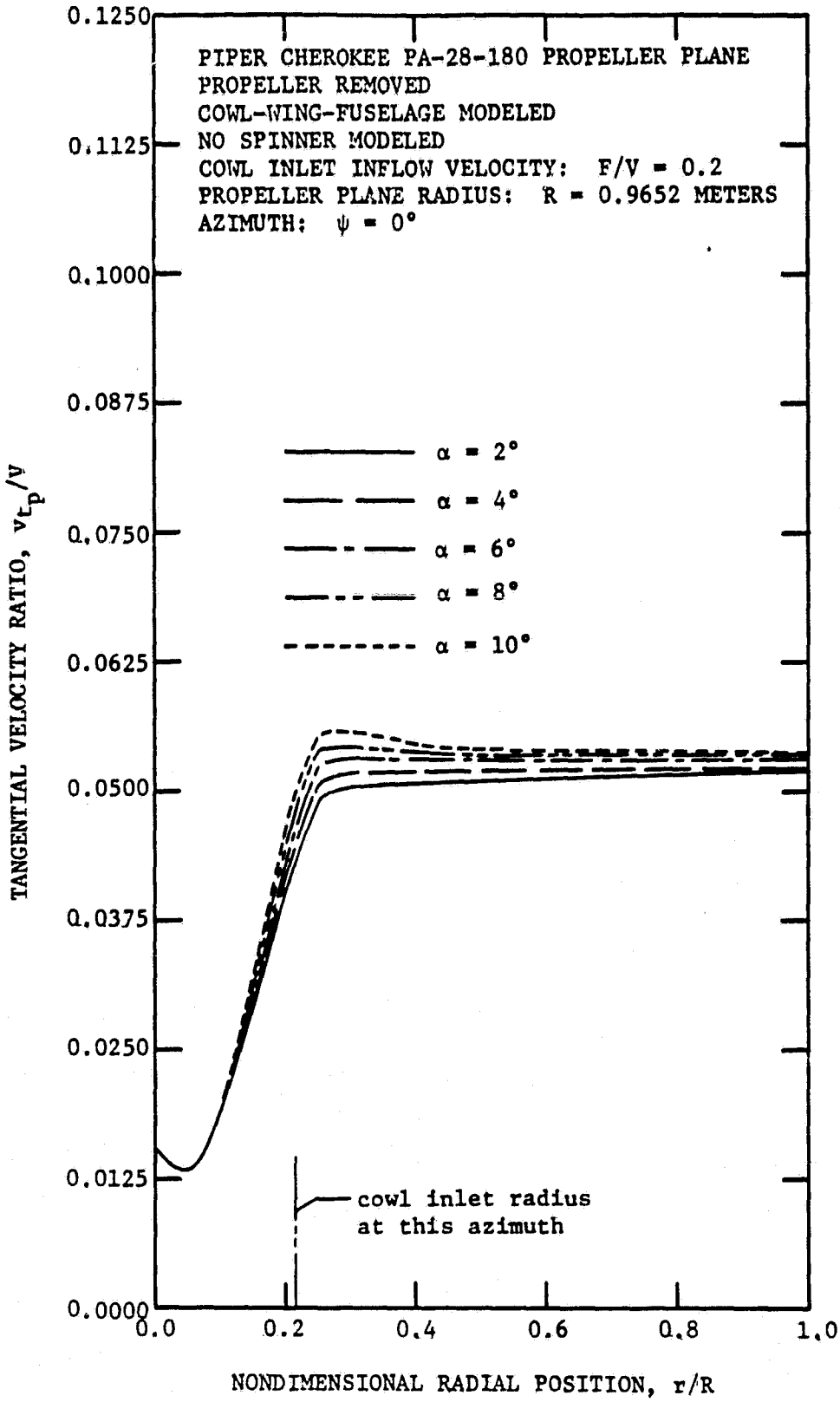

Figure 37b. Computed Radial Distributions of Tangential Velocity at the Propeller Plane of the Piper Cherokee 180 (at $\psi = 0°$)

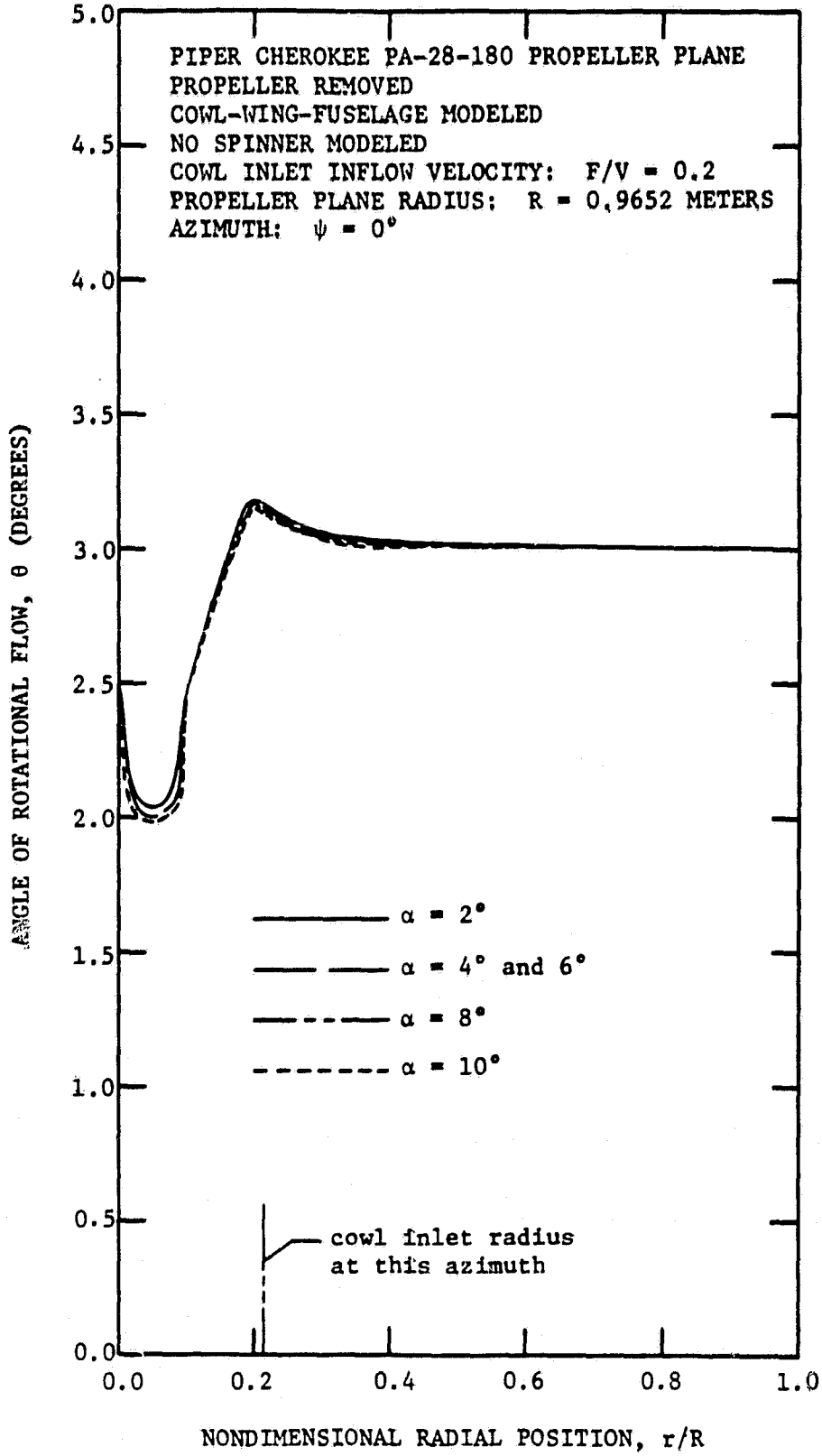

Figure 37c. Computed Radial Distributions of Angle of Rotational Flow at the Propeller Plane of the Piper Cherokee 180 (at $\psi = 0°$)

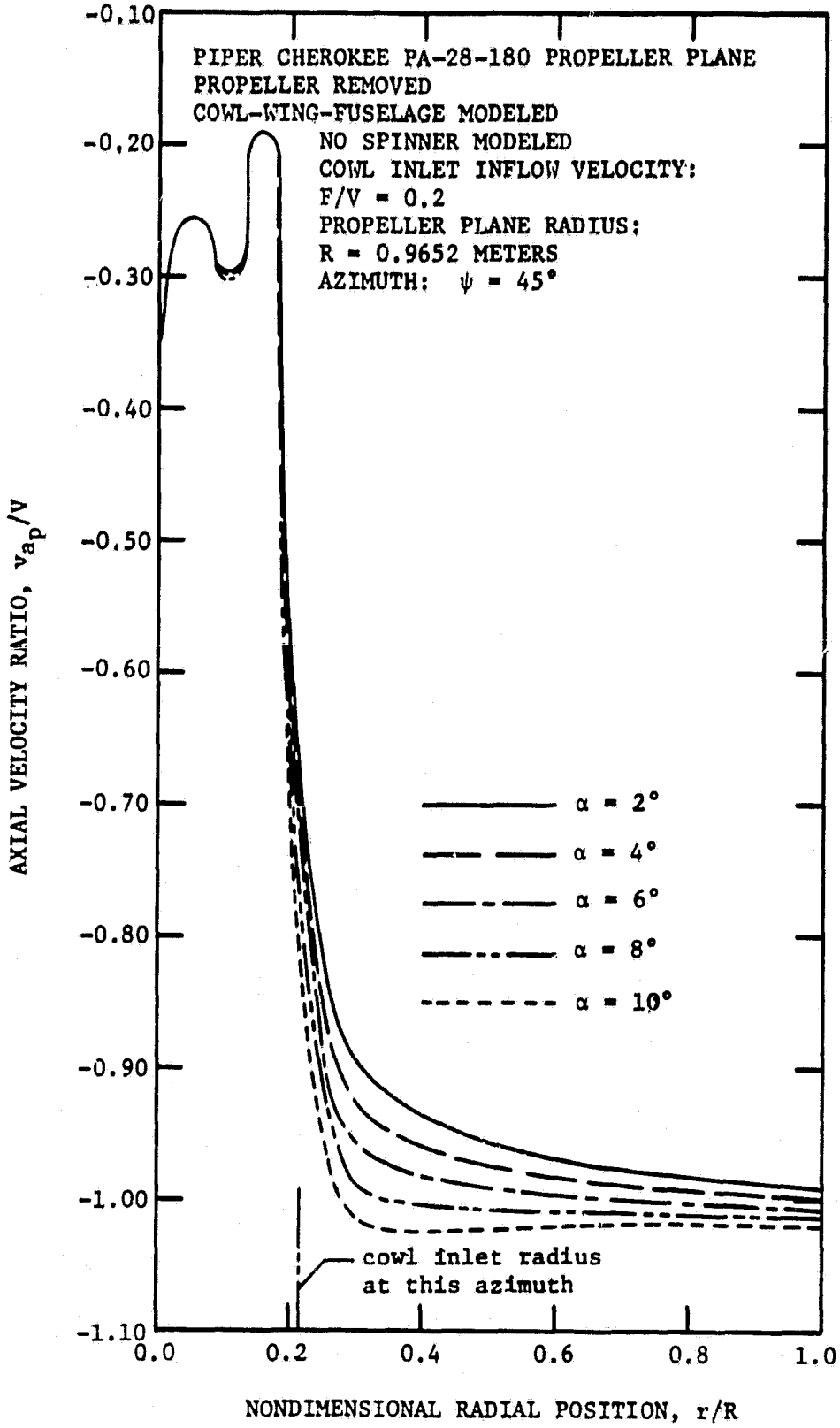

Figure 38a. Computed Radial Distributions of Axial Velocity at the Propeller Plane of the Piper Cherokee 180 (at ψ = 45°)

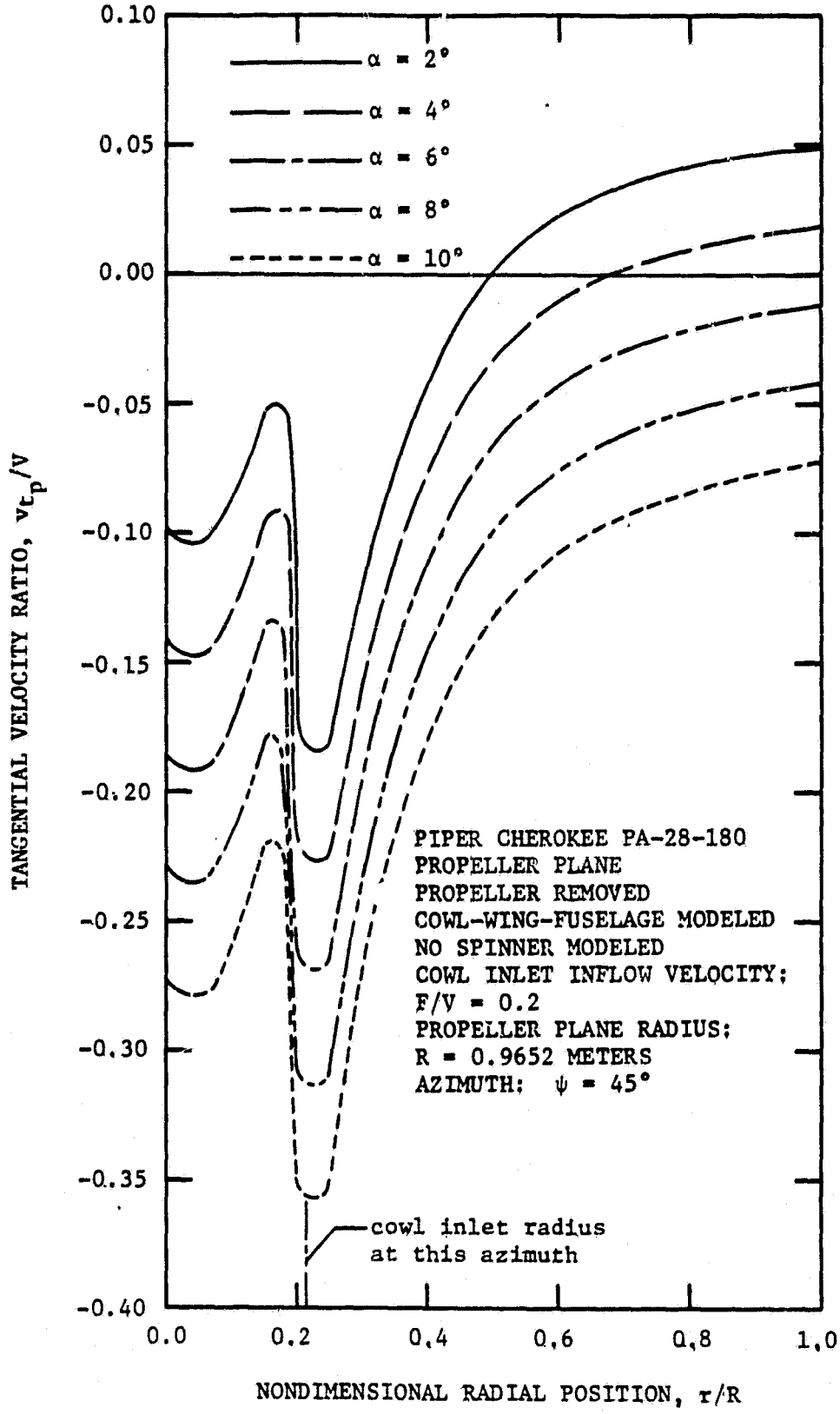

Figure 38h. Computed Radial Distributions of Tangential Velocity at the Propeller Plane of the Piper Cherokee 180 (at ψ = 45°)

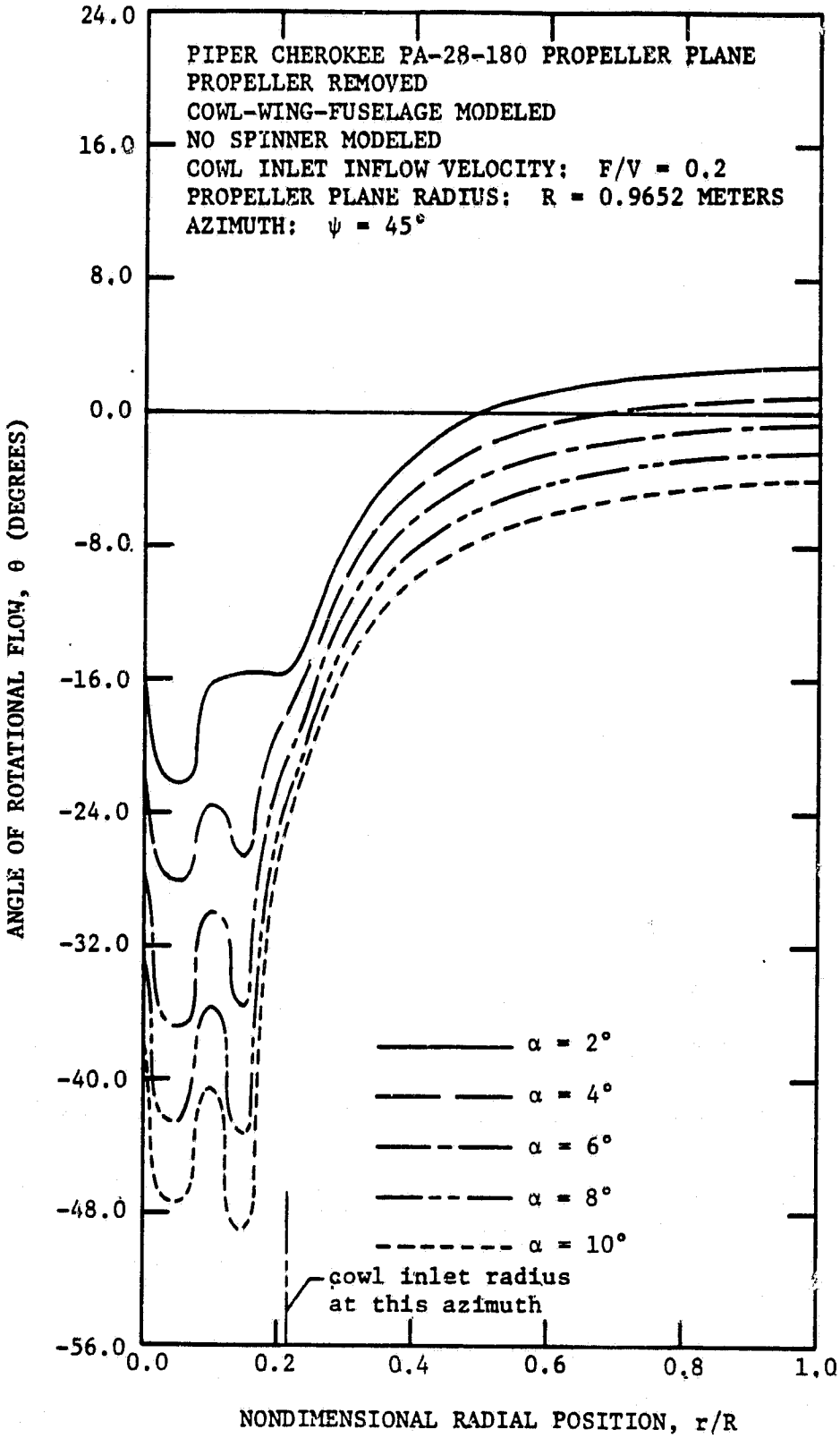

Figure 38c. Computed Radial Distributions of Angle of Rotational Flow at the Propeller Plane of the Piper Cherokee 180 (at $\psi = 45°$)

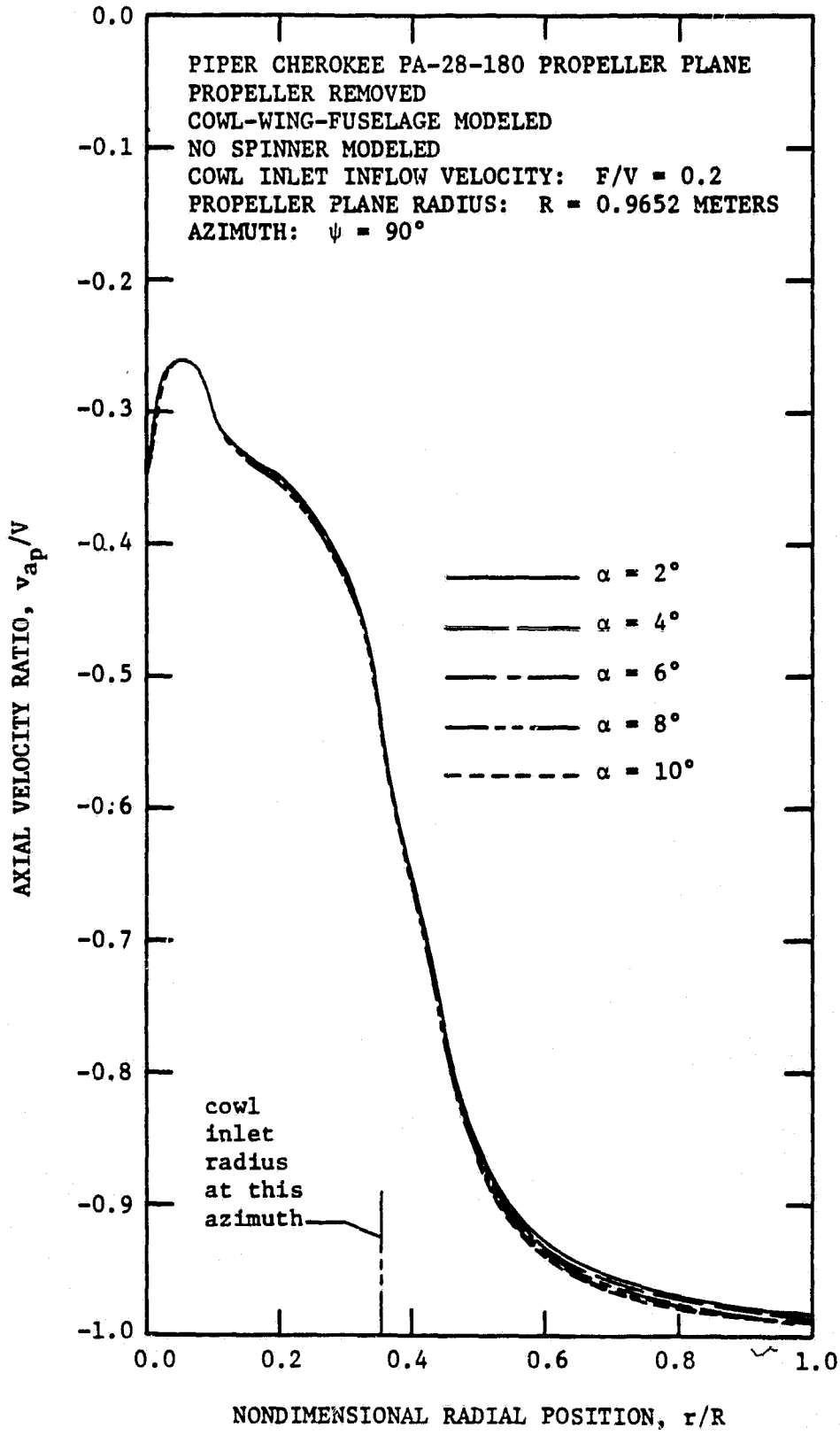

Figure 39a. Computed Radial Distributions of Axial Velocity at the Propeller Plane of the Piper Cherokee 180 (at $\psi = 90°$)

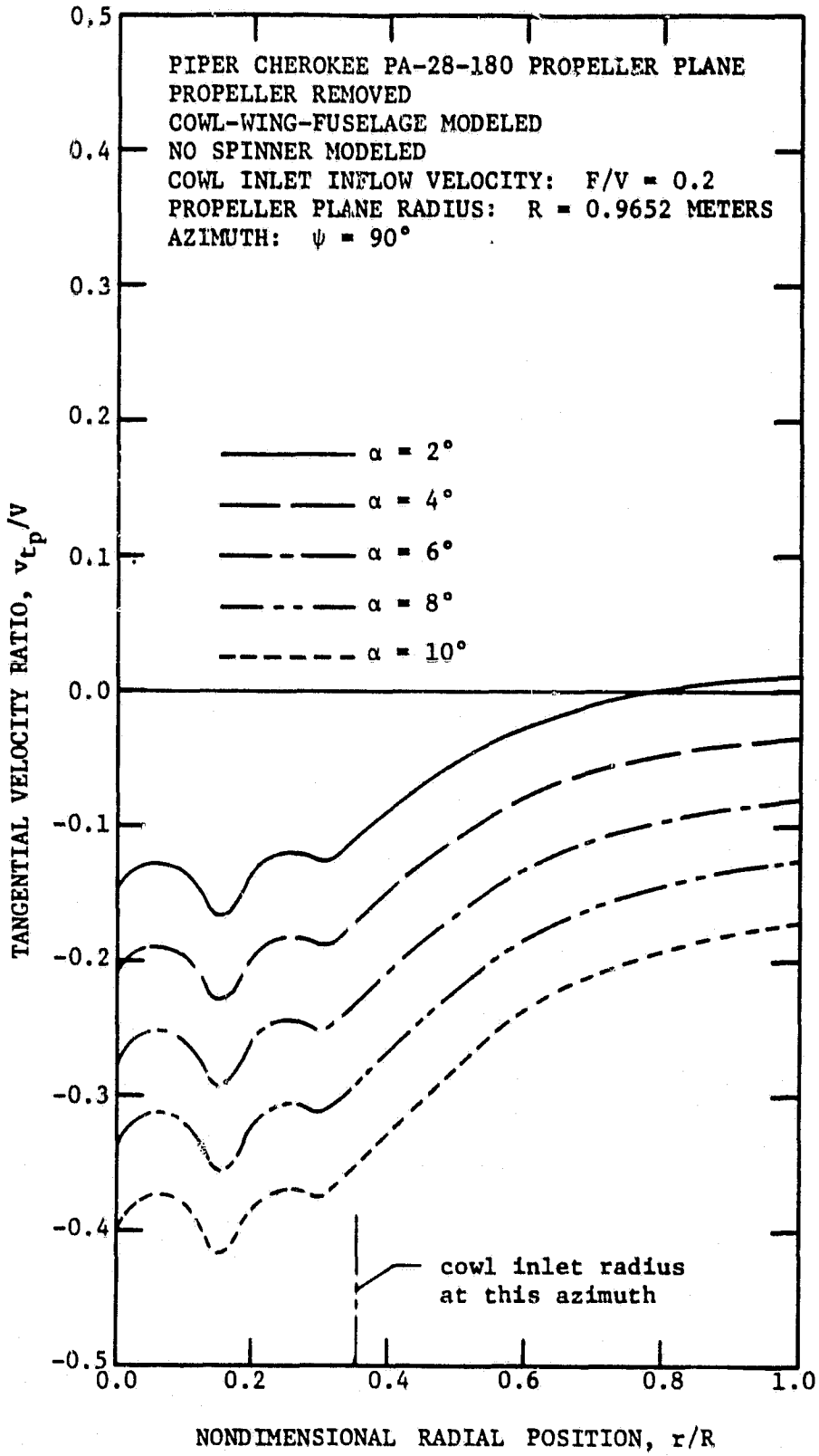

Figure 39b. Computed Radial Distributions of Tangential Velocity at the Propeller Plane of the Piper Cherokee 180 (at ψ = 90°)

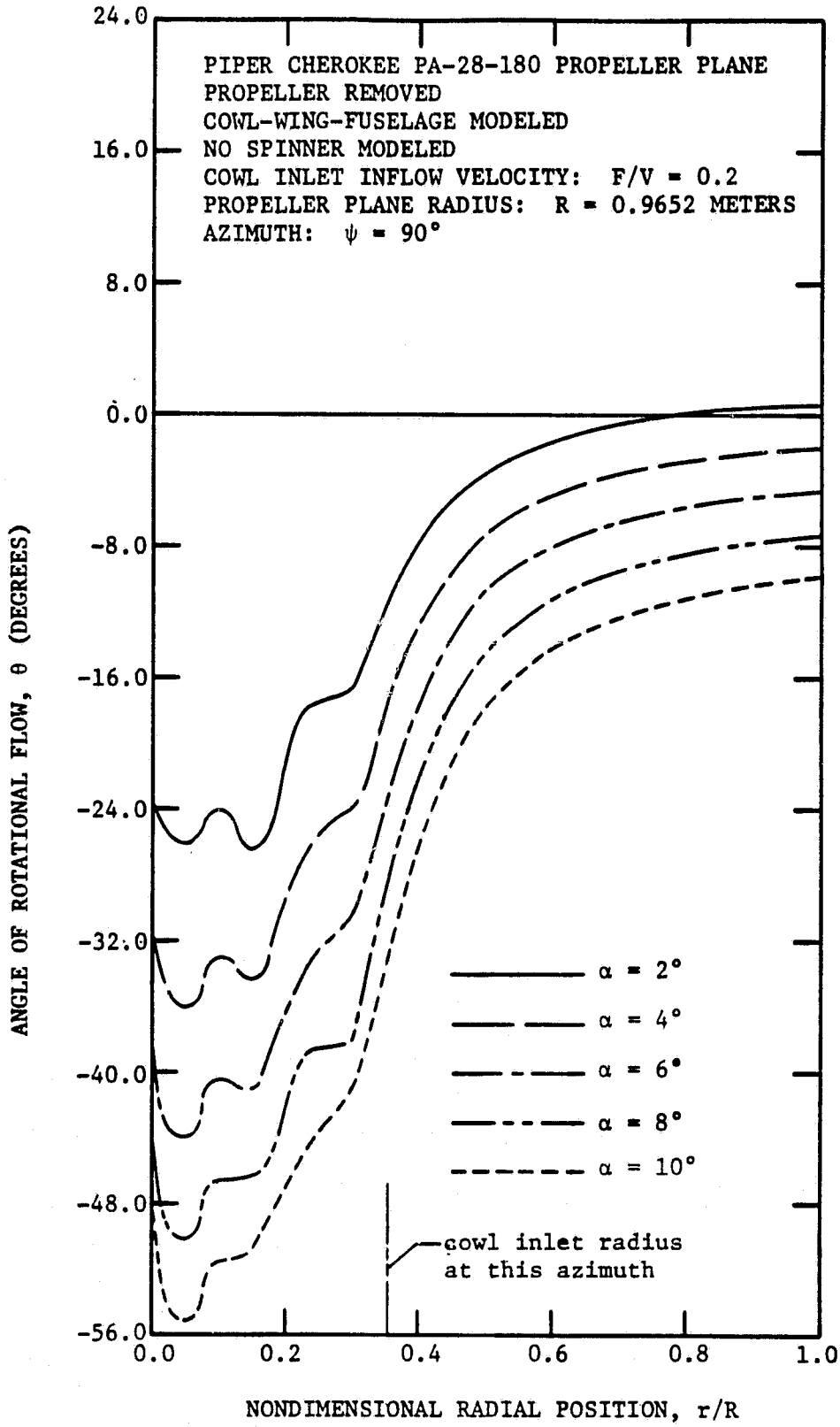

Figure 39c. Computed Radial Distributions of Angle of Rotational Flow at the Propeller Plane of the Piper Cherokee 180 (at $\psi = 90°$)

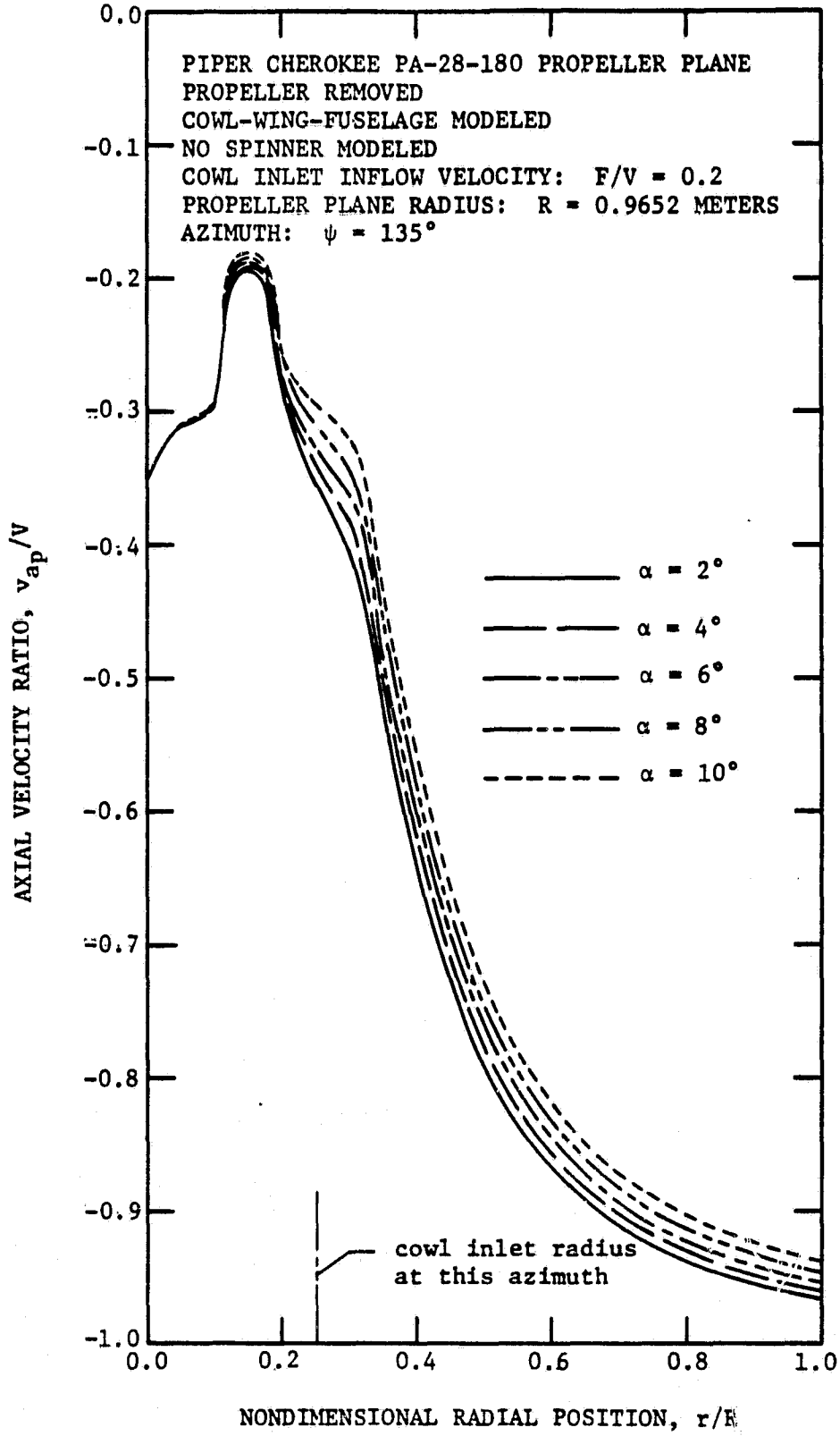

Figure 40a. Computed Radial Distributions of Axial Velocity at the Propeller Plane of the Piper Cherokee 180 (at ψ = 135°)

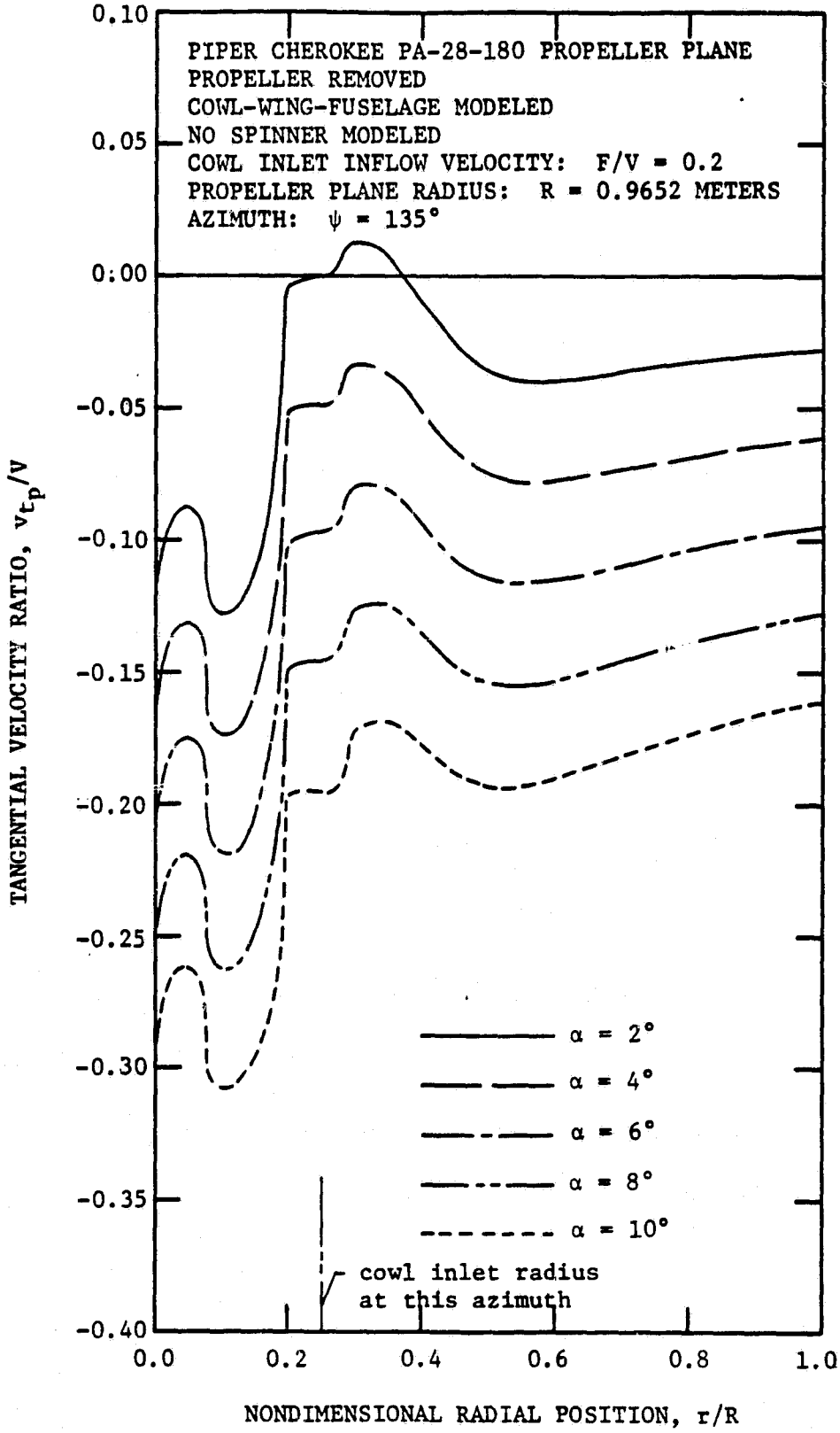

Figure 40b. Computed Radial Distributions of Tangential Velocity at the Propeller Plane of the Piper Cherokee 180 (at ψ = 135°)

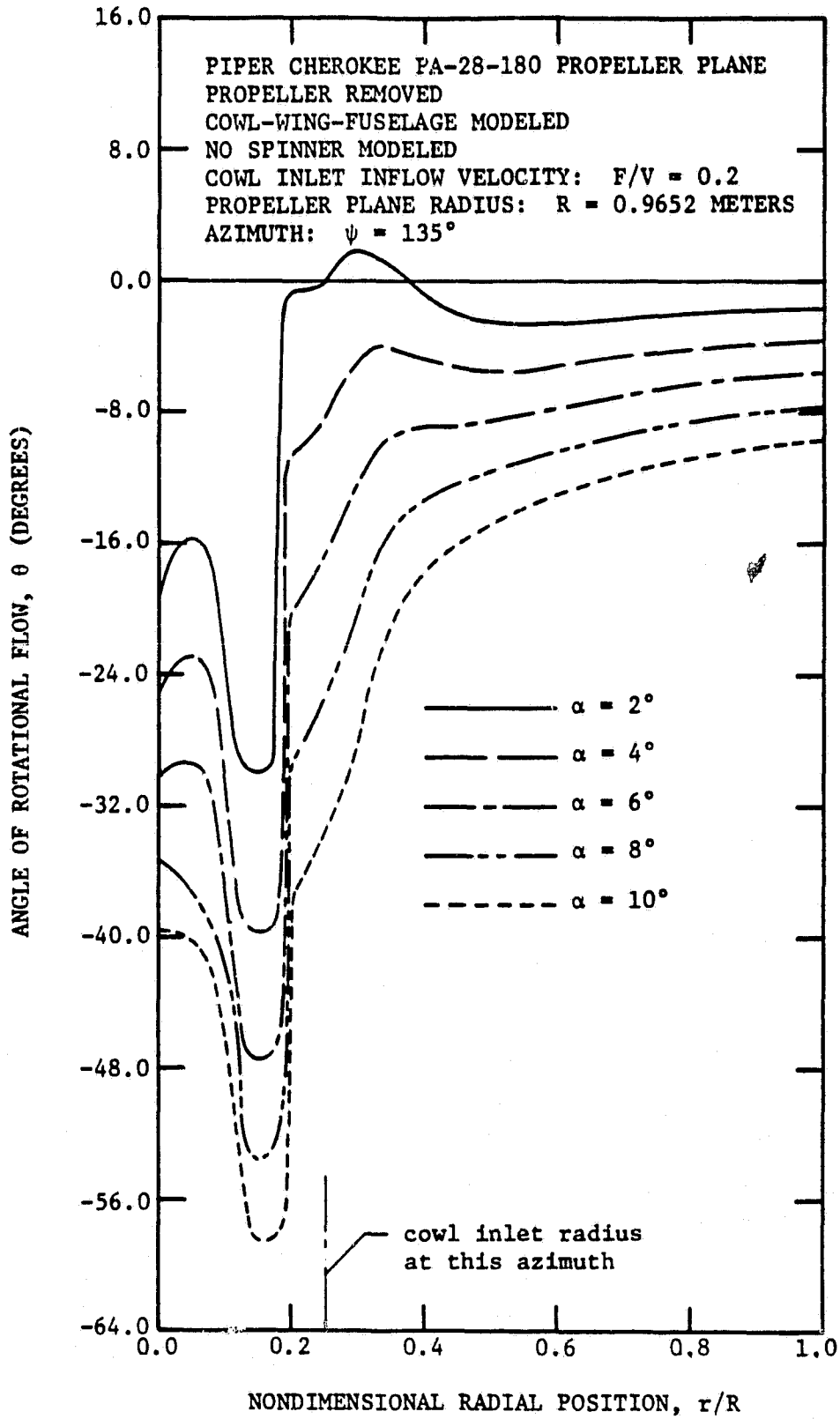

Figure 40c. Computed Radial Distributions of Angle of Rotational Flow at the Propeller Plane of the Piper Cherokee 180 (at $\psi = 135°$)

ORIGINAL PAGE IS
OF POOR QUALITY

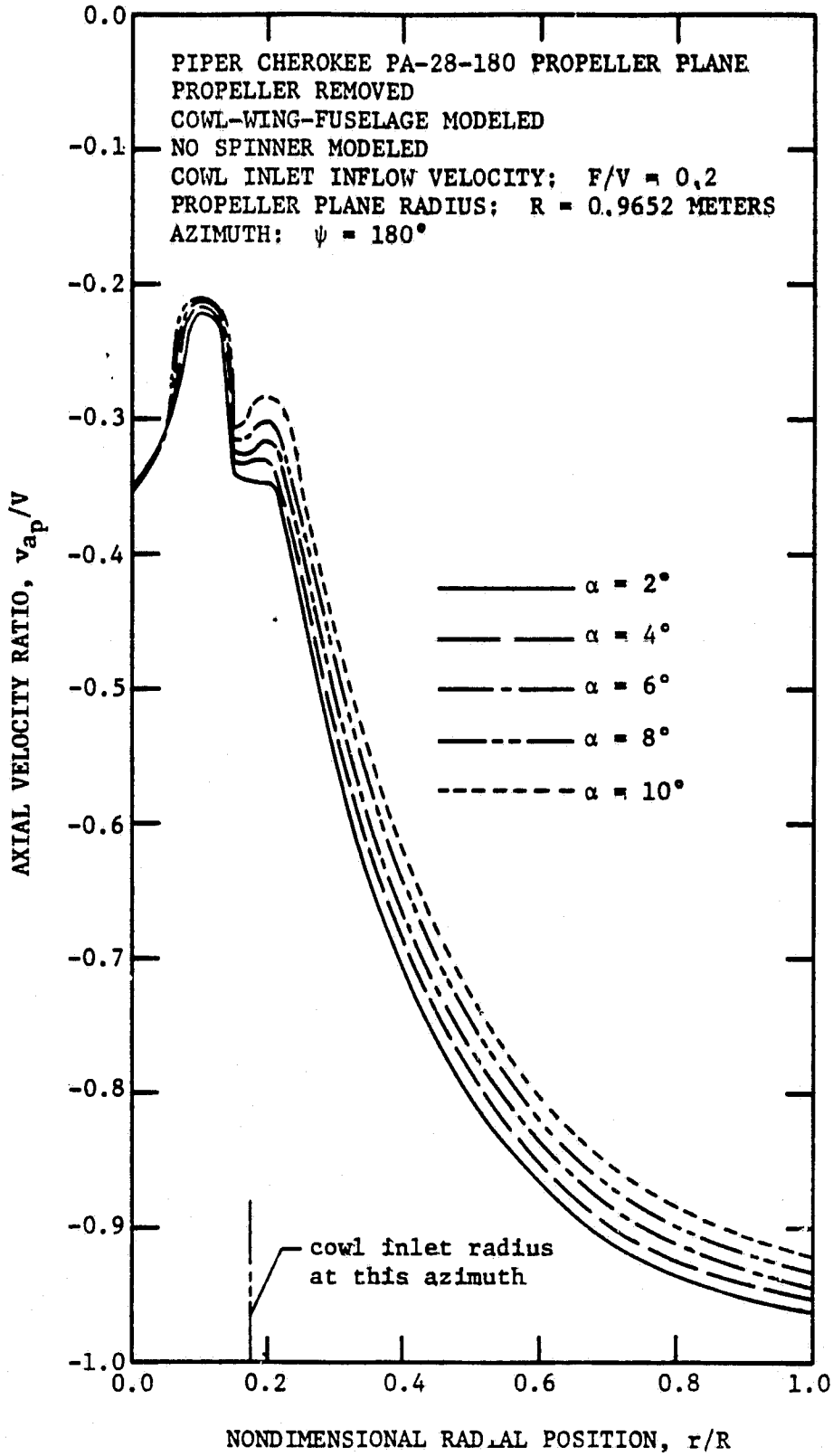

Figure 41a. Computed Radial Distributions of Axial Velocity at the Propeller Plane of the Piper Cherokee 180 (at ψ = 180°)

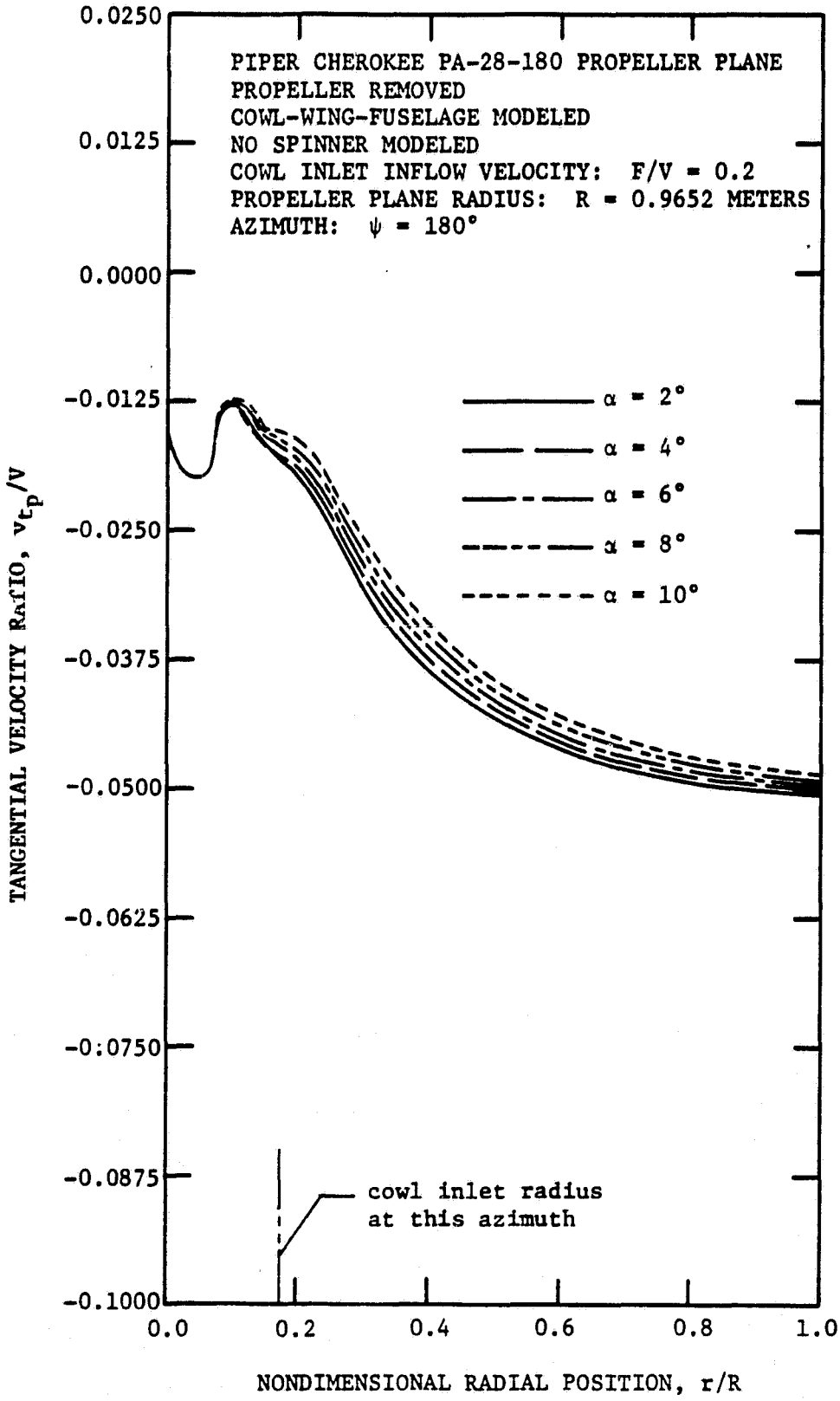

Figure 41b. Computed Radial Distributions of Tangential Velocity at the Propeller Plane of the Piper Cherokee 180 (at ψ = 180°)

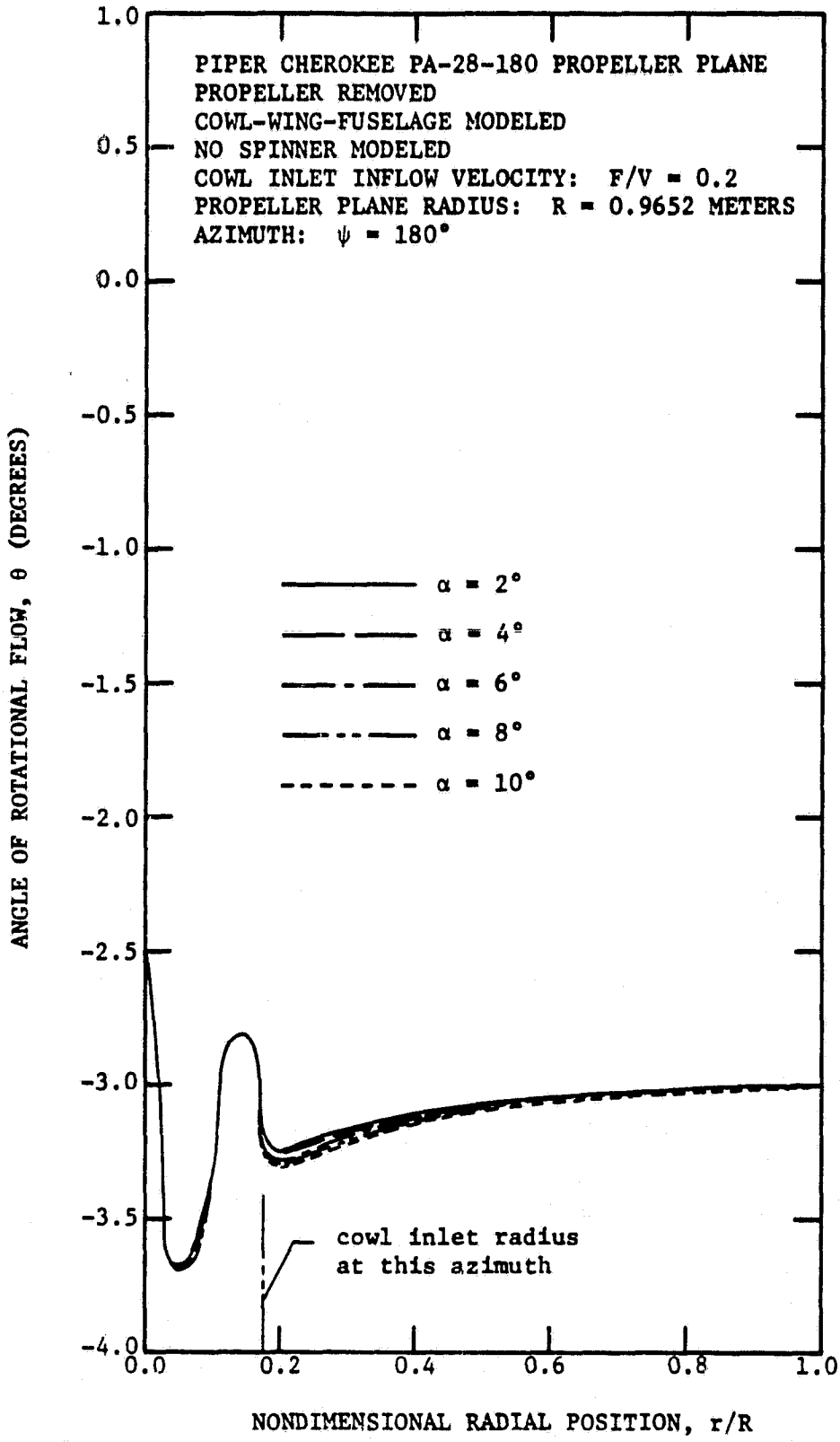

Figure 41c. Computed Radial Distributions of Angle of Rotational Flow at the Propeller Plane of the Piper Cherokee 180 (at $\psi = 180°$)

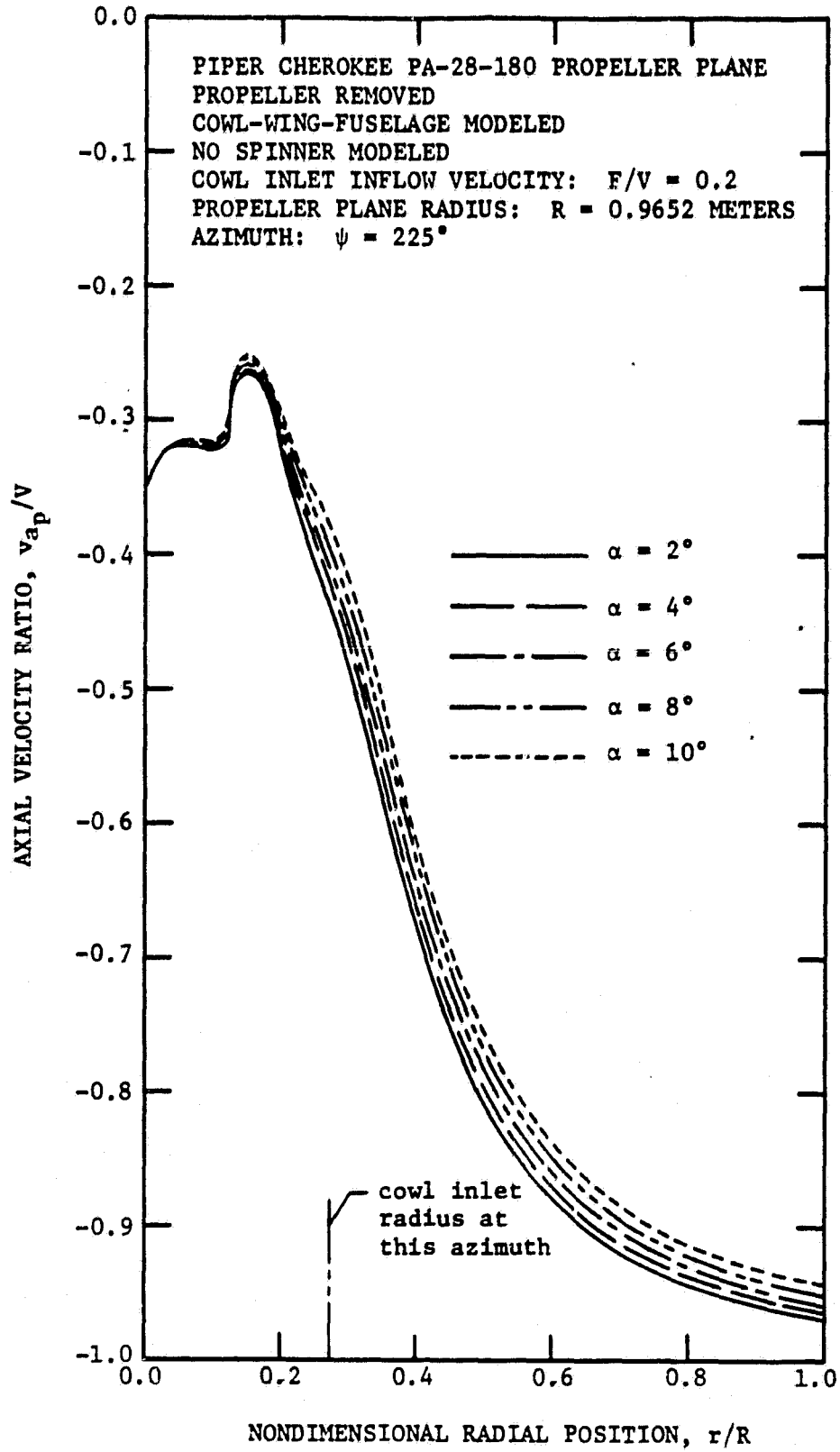

Figure 42a. Computed Radial Distributions of Axial Velocity at the Propeller Plane of the Piper Cherokee 180 (at ψ = 225°)

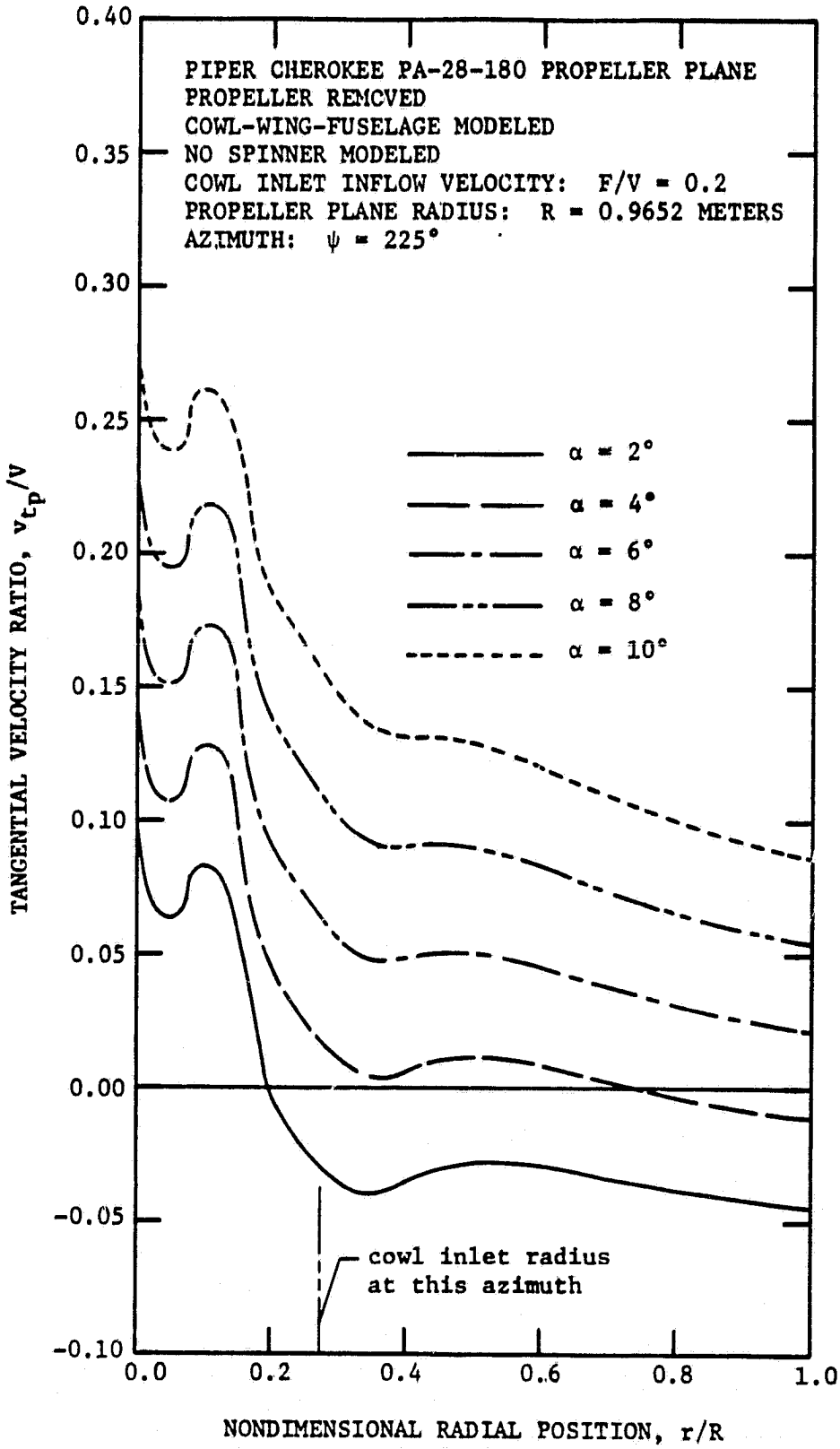

Figure 42b. Computed Radial Distributions of Tangential Velocity at the Propeller Plane of the Piper Cherokee 180 (at ψ = 225°)

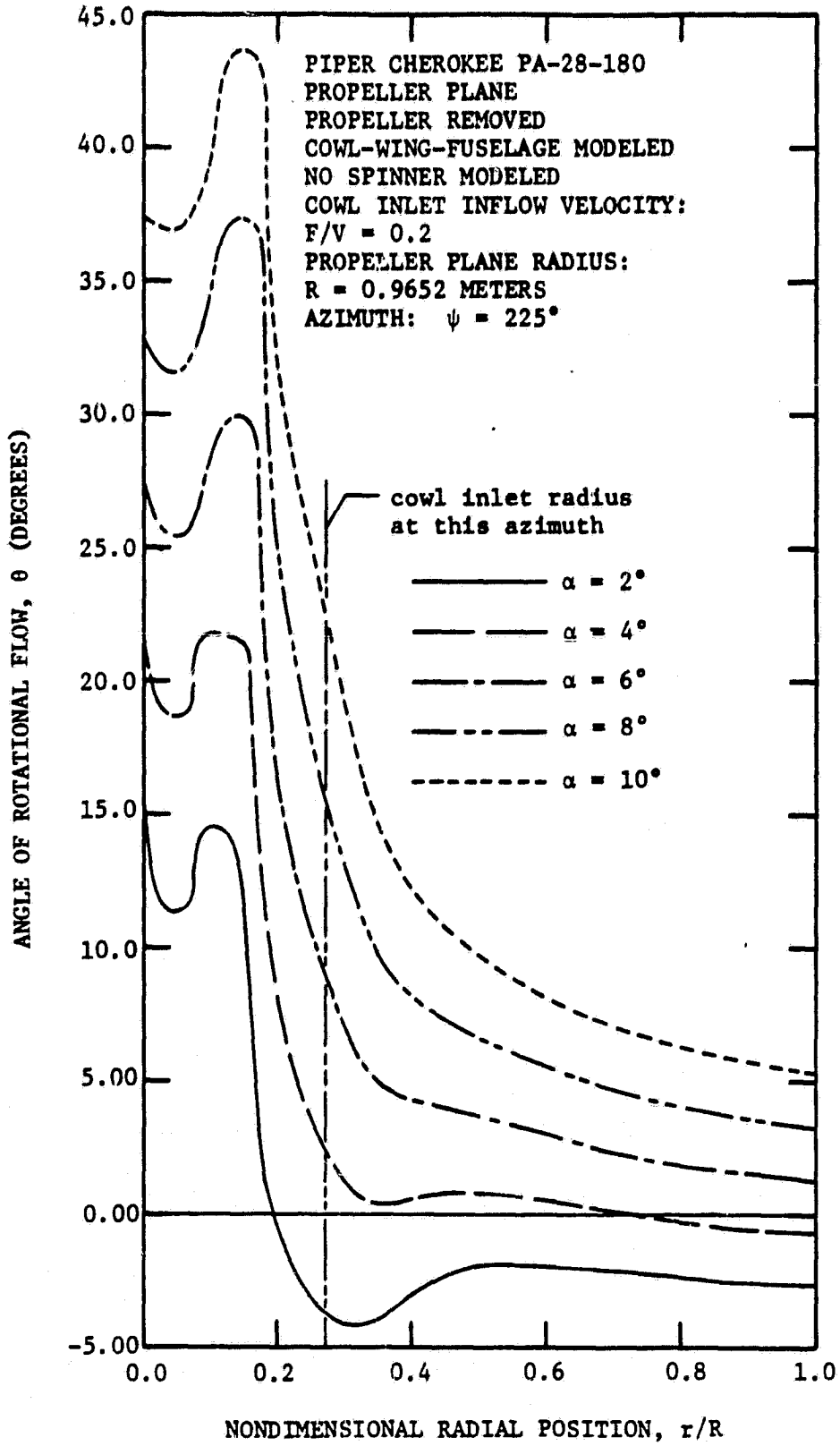

Figure 42c. Computed Radial Distributions of Angle of Rotational Flow at the Propeller Plane of the Piper Cherokee 180 (at ψ = 225°)

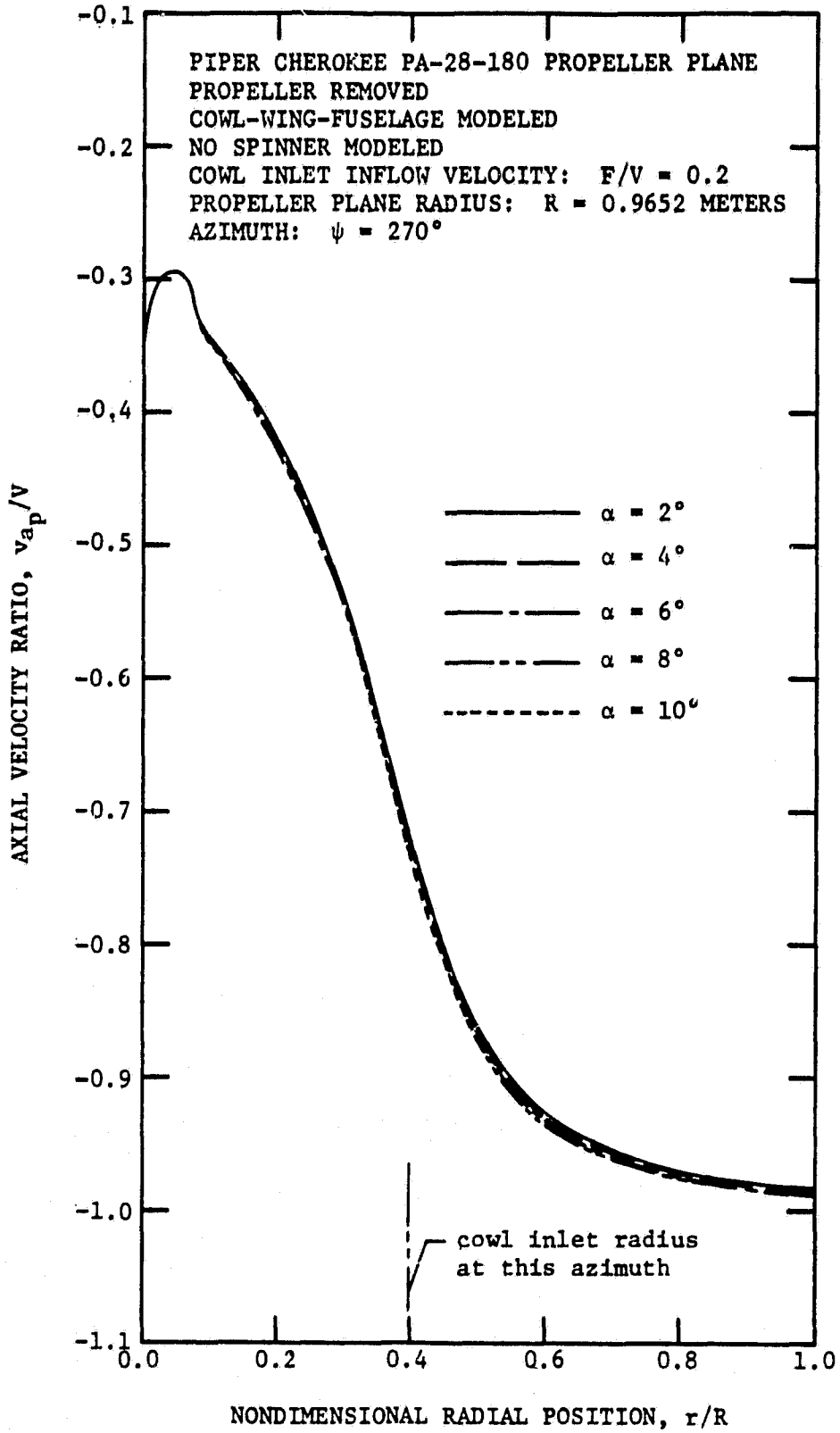

Figure 43a. Computed Radial Distributions of Axial Velocity at the Propeller Plane of the Piper Cherokee 180 (at ψ = 270°)

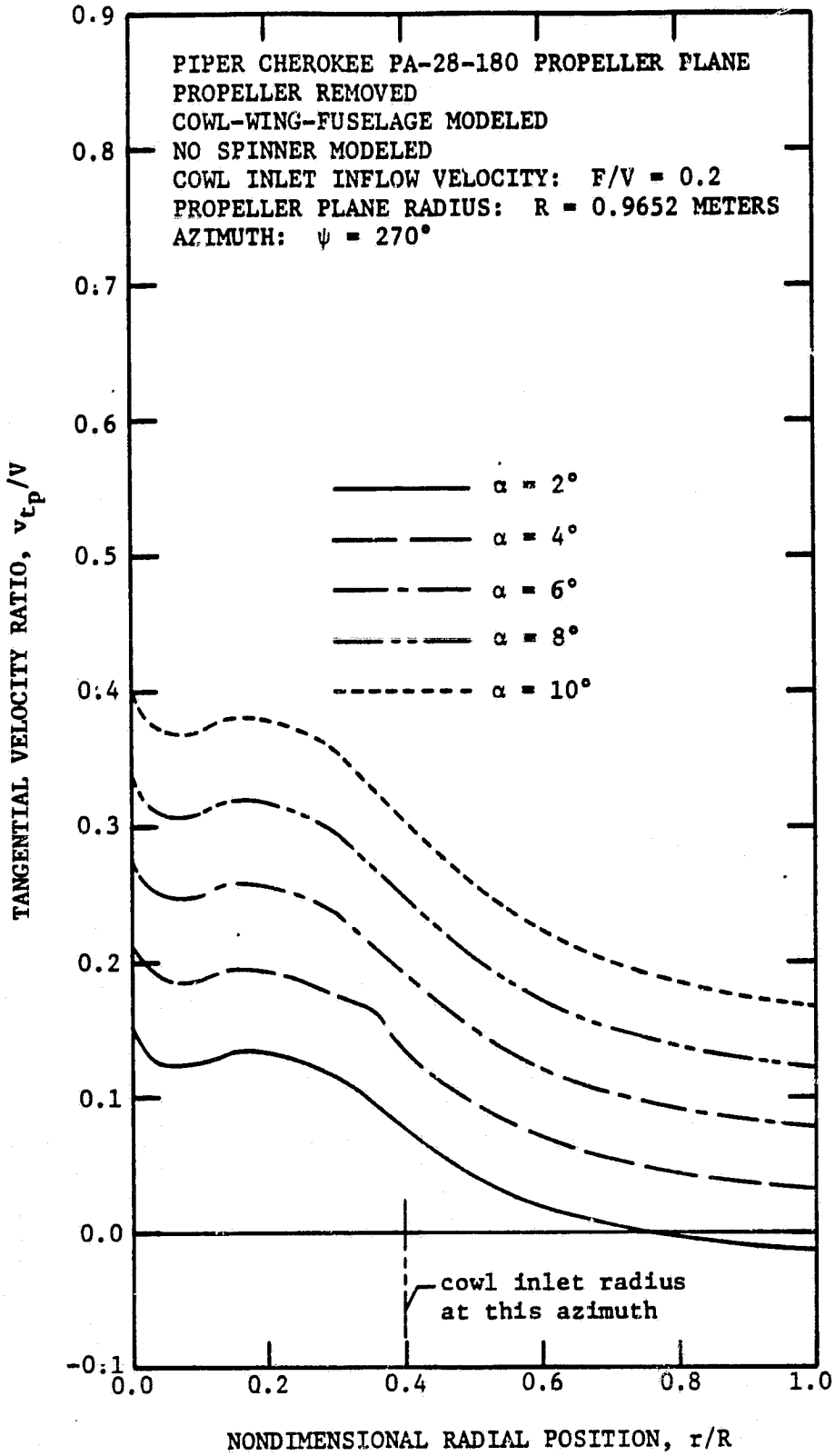

Figure 43b. Computed Radial Distributions of Tangential Velocity at the Propeller Plane of the Piper Cherokee 180 (at ψ = 270°)

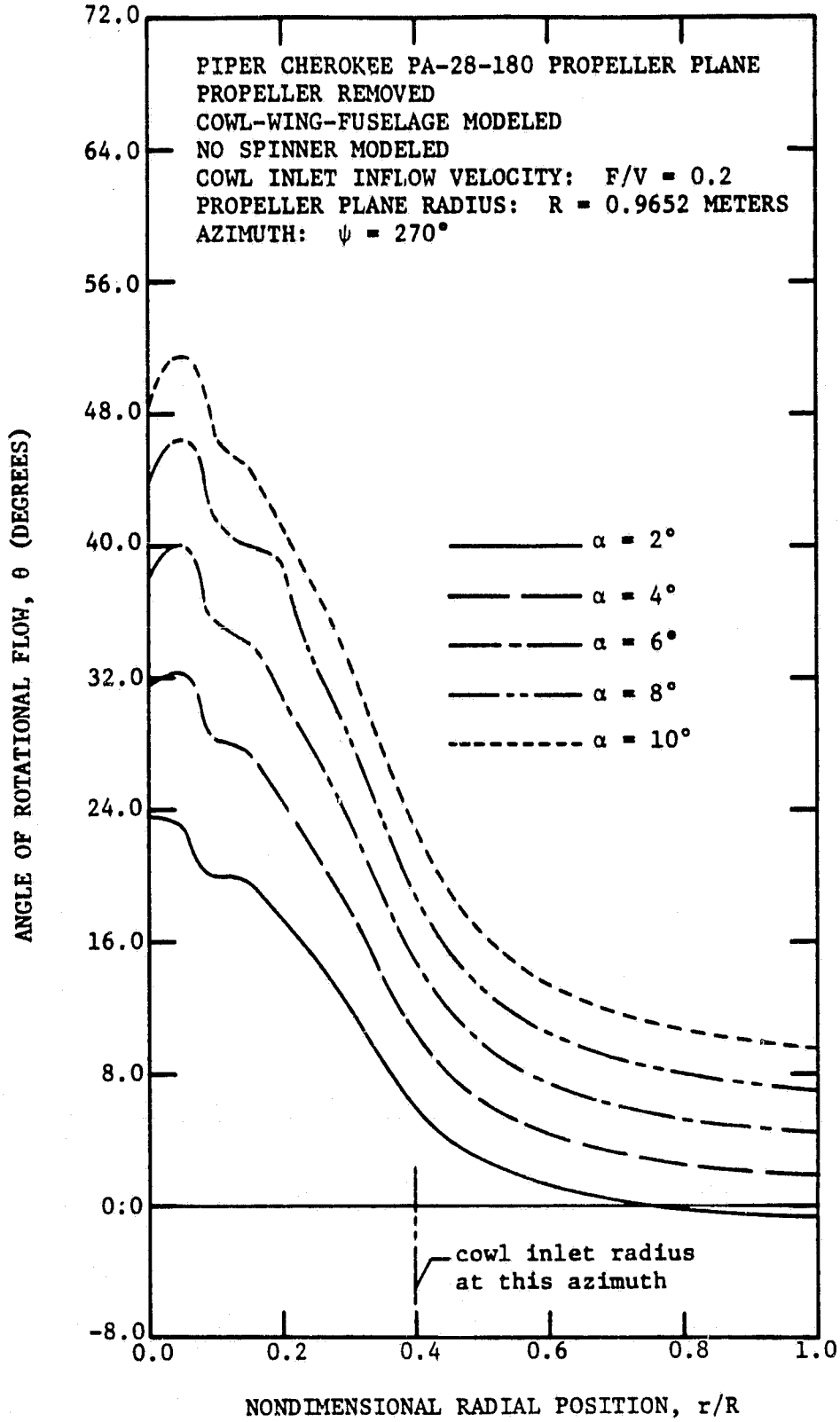

Figure 43c. Computed Radial Distributions of Angle of Rotational Flow at the Propeller Plane of the Piper Cherokee 180 (at $\psi = 270°$)

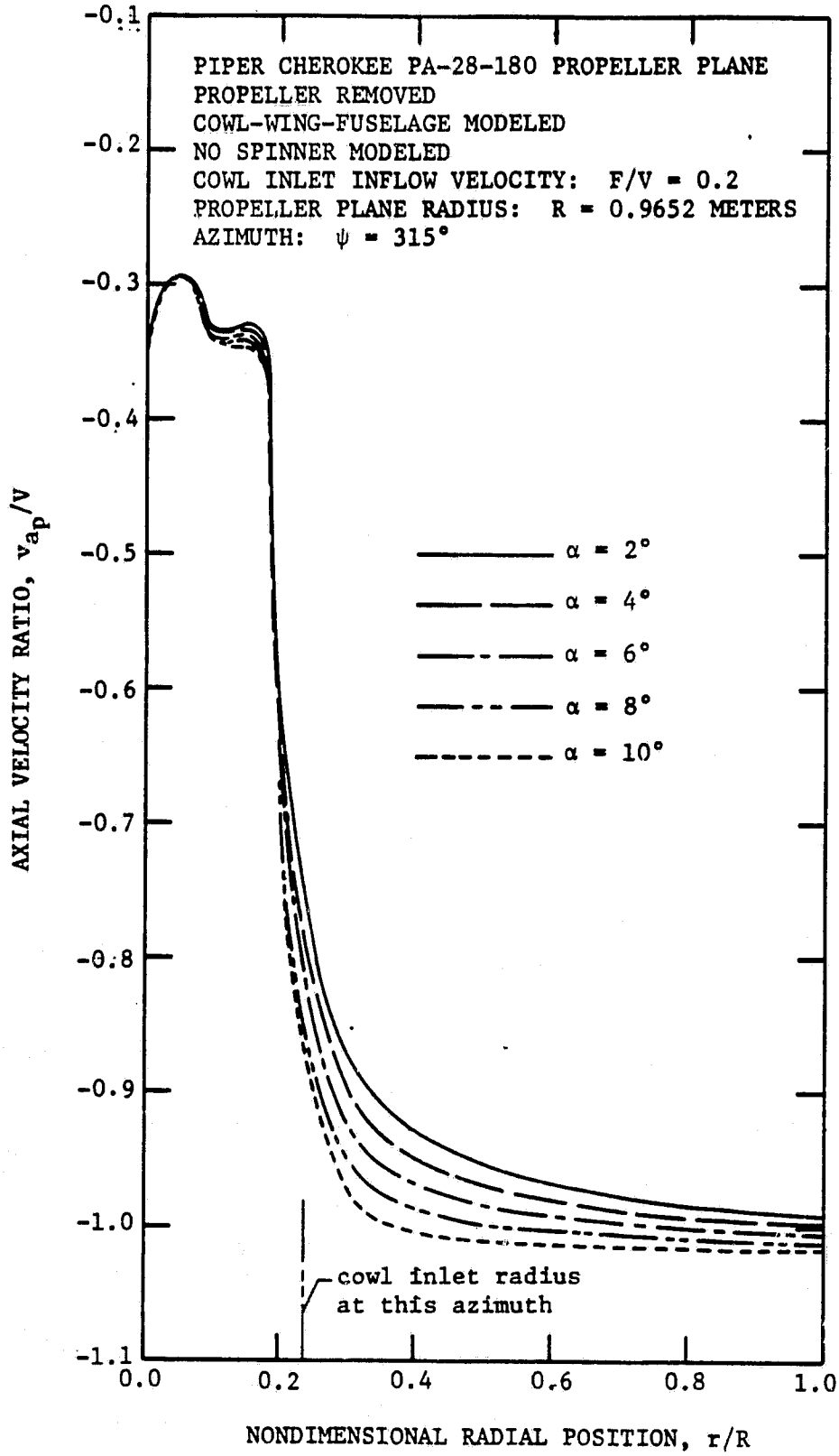

Figure 44a. Computed Radial Distributions of Axial Velocity at the Propeller Plane of the Piper Cherokee 180 (at ψ = 315°)

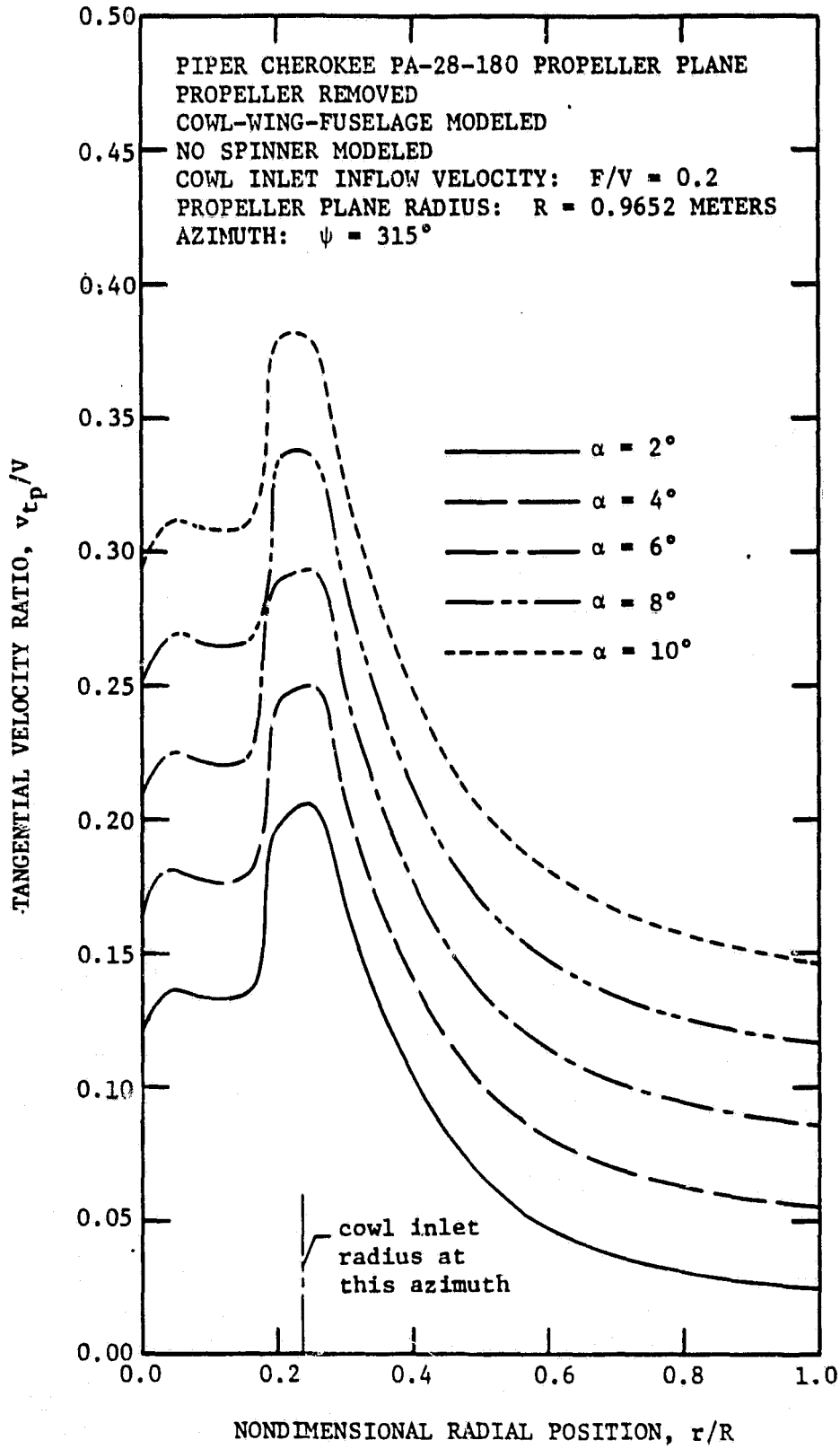

Figure 44b. Computed Radial Distributions of Tangential Velocity at the Propeller Plane of the Piper Cherokee 180 (at ψ = 315°)

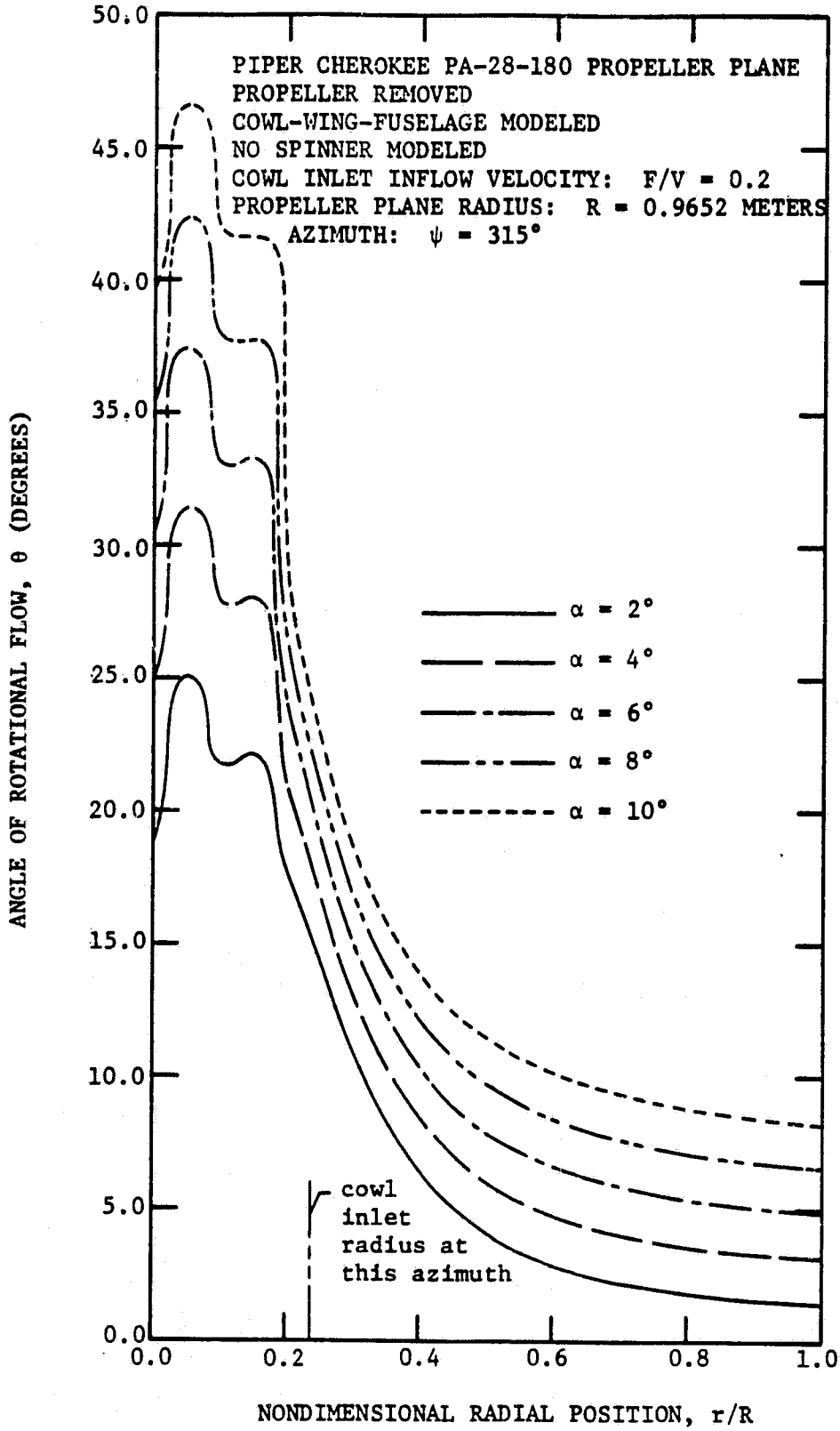

Figure 44c. Computed Radial Distributions of Angle of Rotational Flow at the Propeller Plane of the Piper Cherokee 180 (at ψ = 315°)

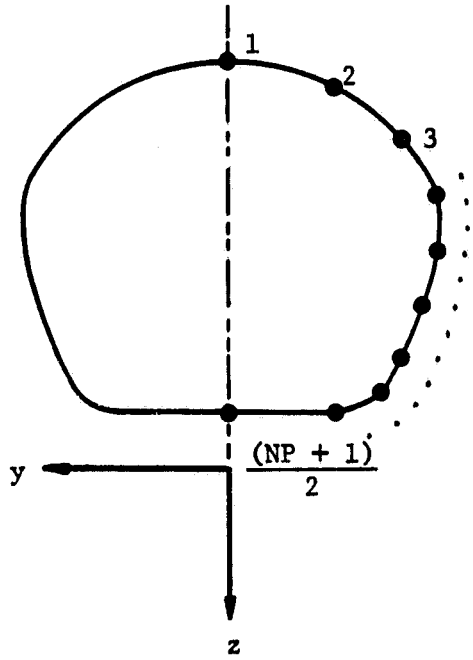

Figure A.1a. Periphery Point Input on a Symmetric Body Cross Section

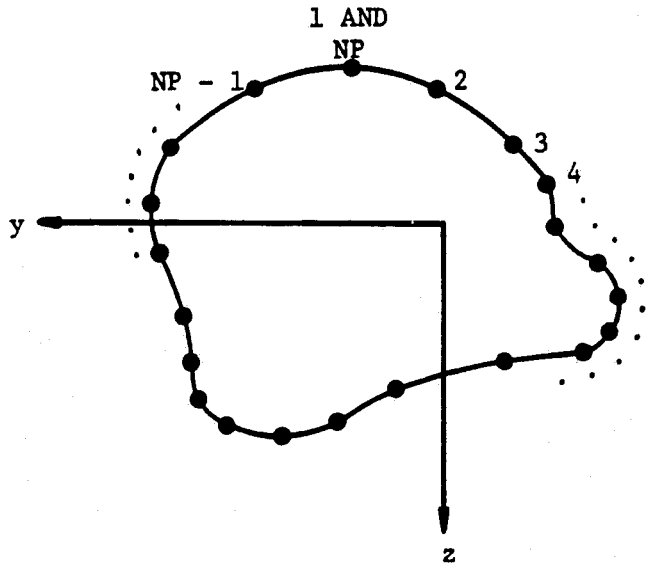

Figure A.1b. Periphery Point Input on a Nonsymmetric Body Cross Section

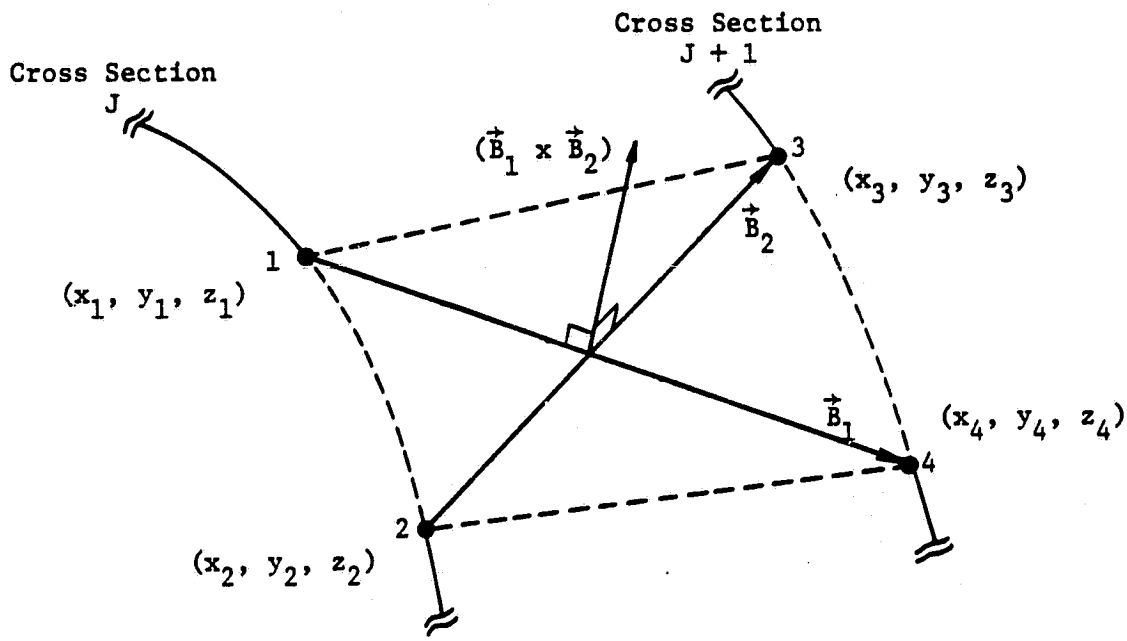

Figure A.2. Input Panel Corner Points and Creation of the Outward Normal Vector

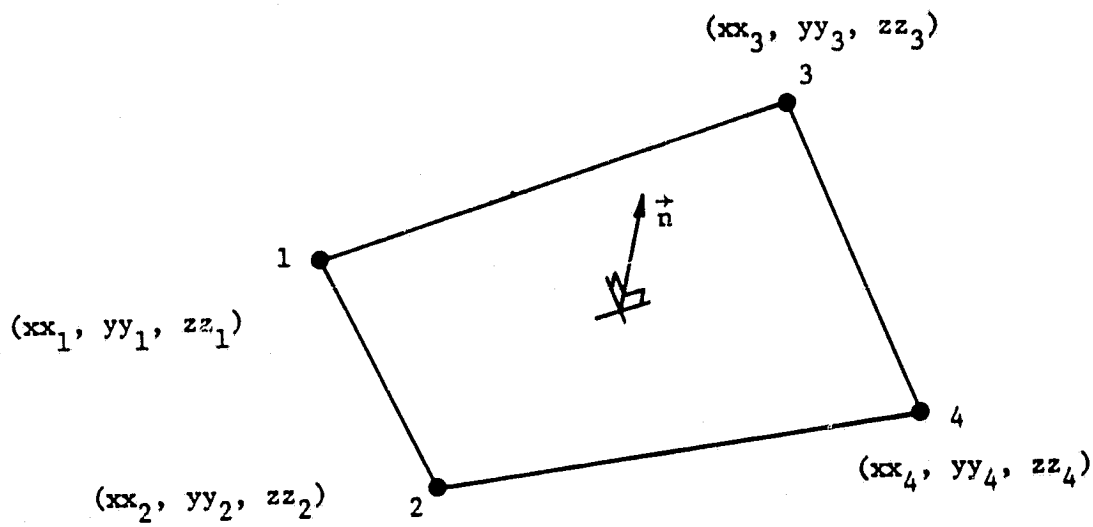

Figure A.3. Quadrilateral Element With New Coplanar Corner Points

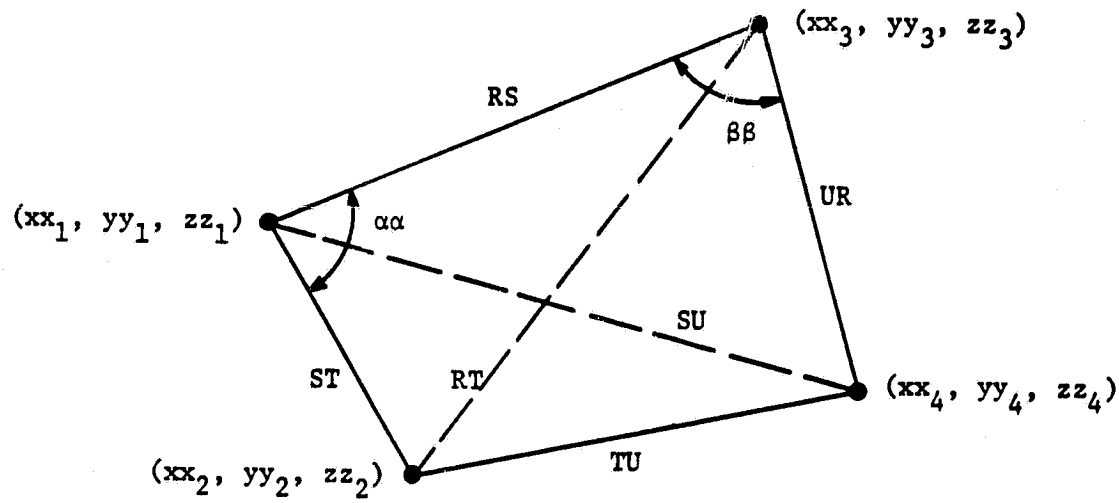

Figure A.4. Lengths and Angles Used to Calculate the Area of a Quadrilateral Panel

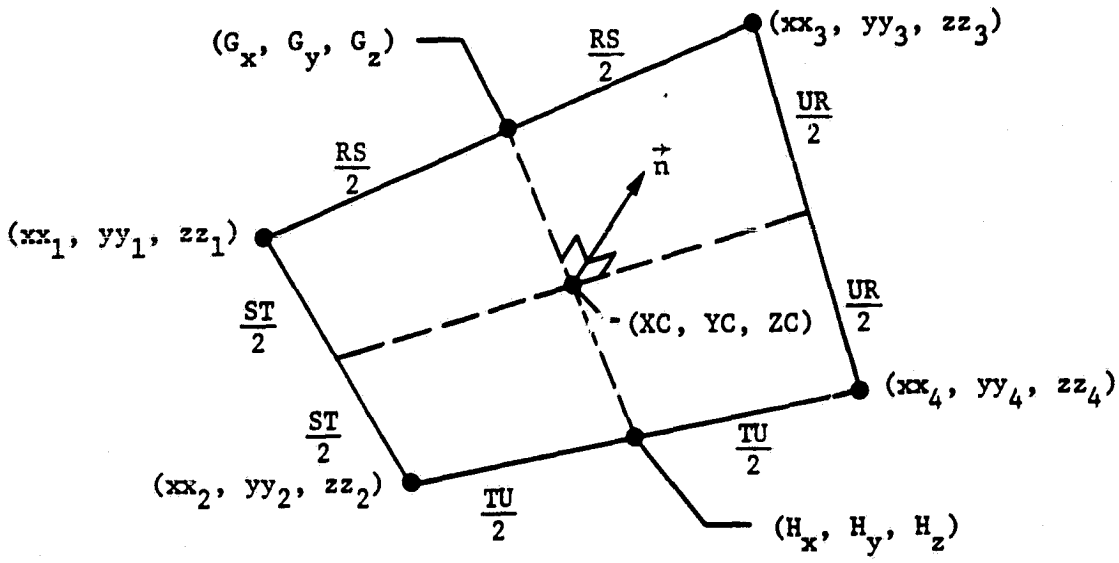

Figure A.5. Control Point Location on a Quadrilateral Panel

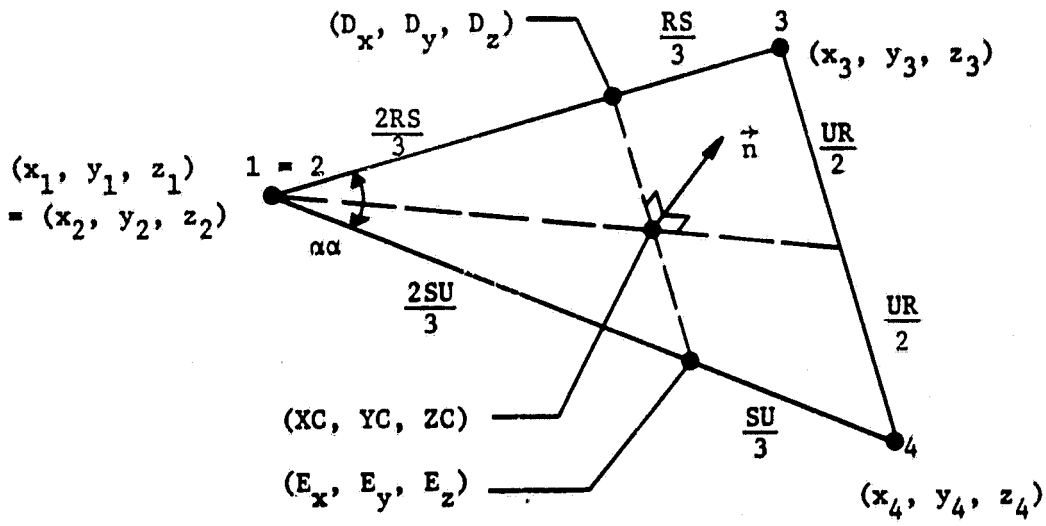

Figure A.6a. Triangular Panel With Input Points 1 and 2 Coincident (Case a)

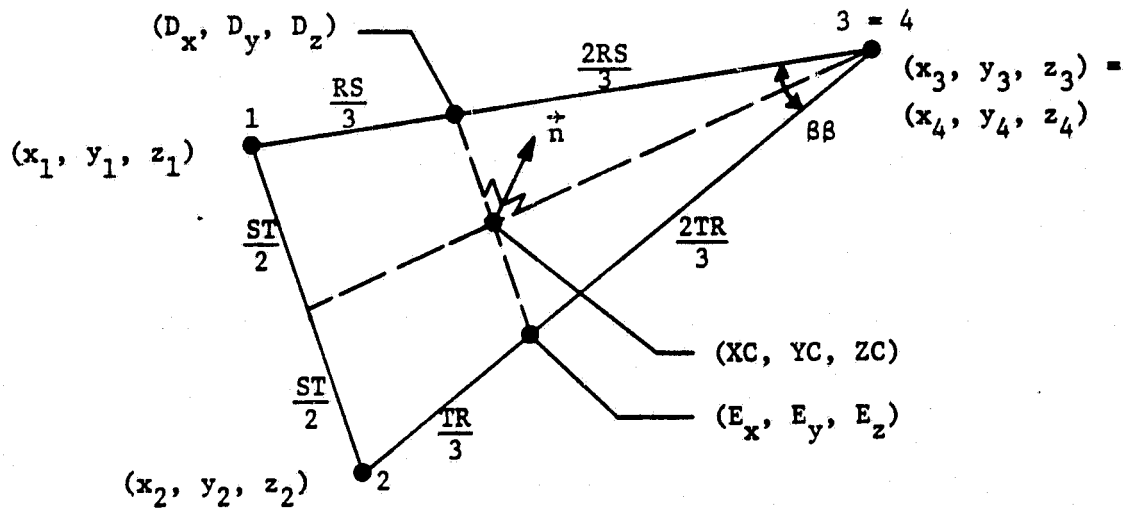

Figure A.6b. Triangular Panel With Input Points 3 and 4 Coincident (Case b)

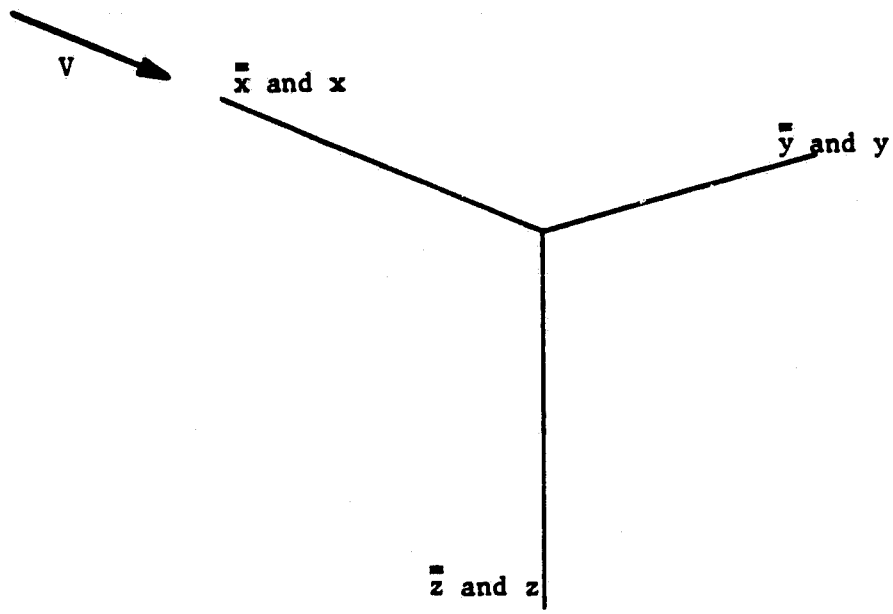

Figure B.1. Wind Axes and Body-Fixed Axes Initially Coincident

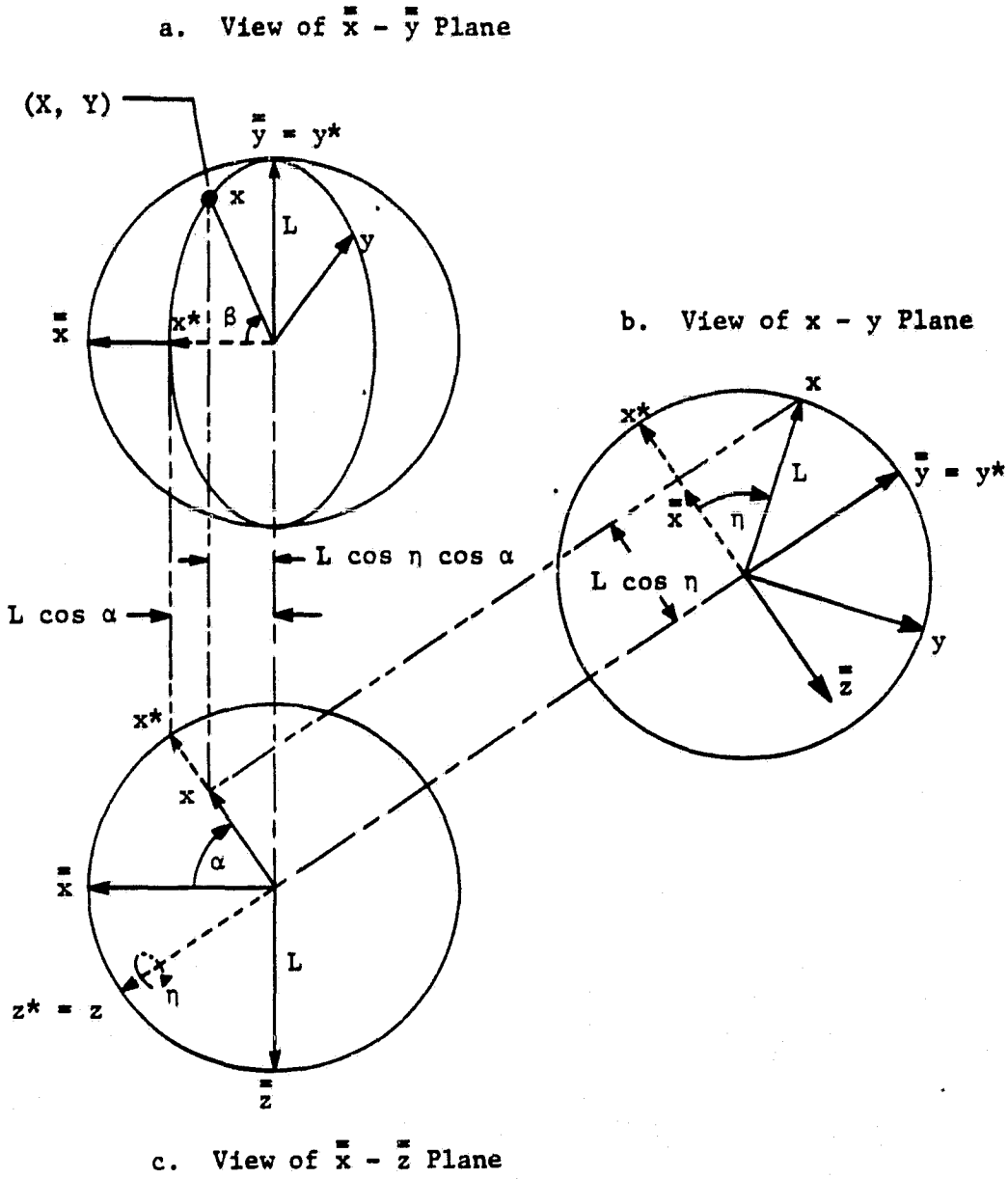

Figure B.2. Body-Fixed Axis System Rotations

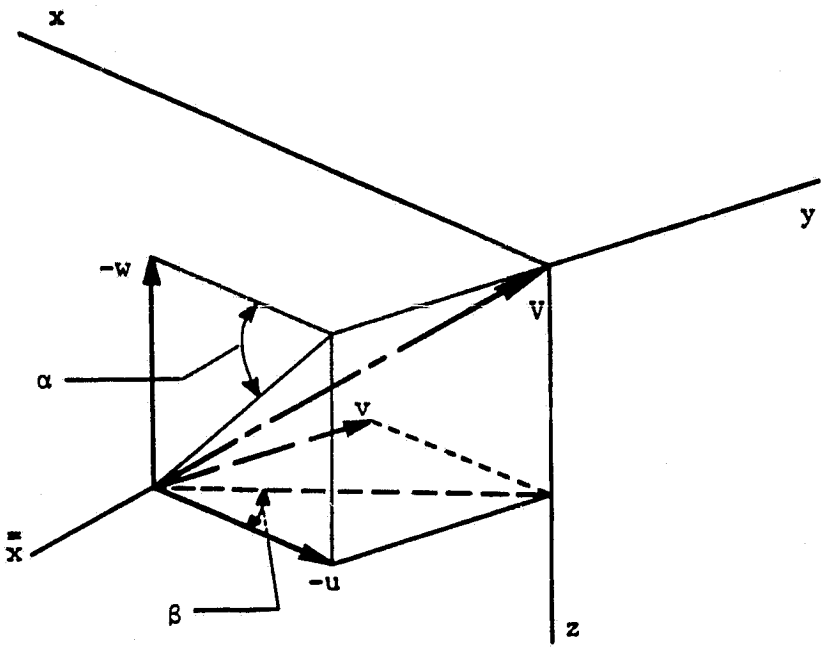

Figure B.3. Free Stream Velocity Components

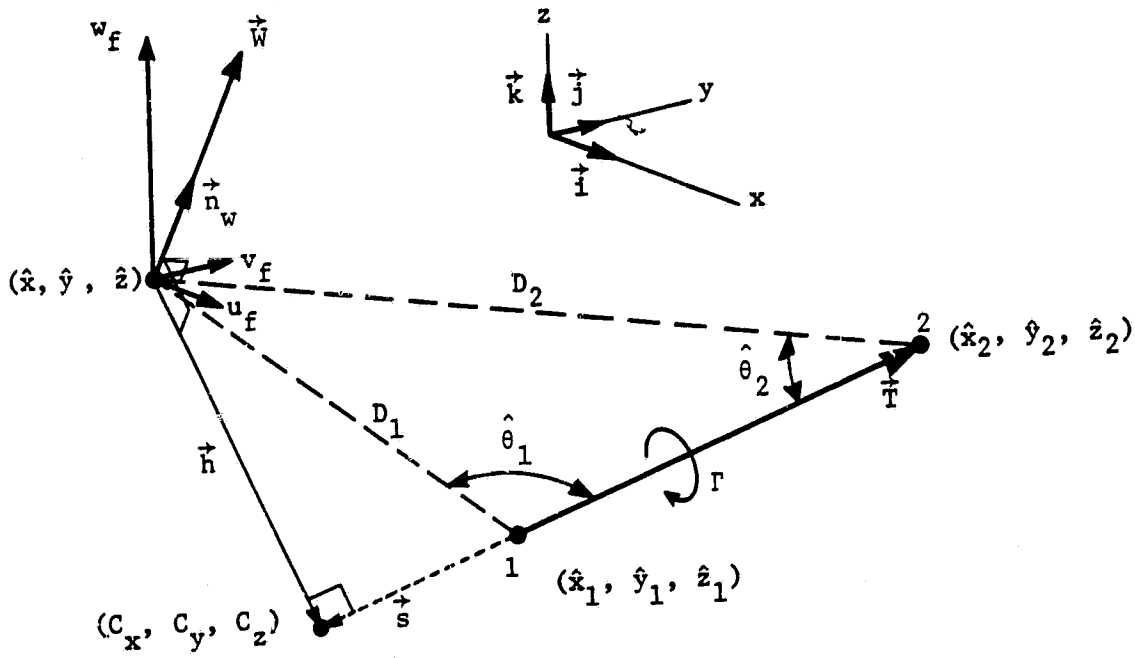

Figure C.1. Geometry and Induced Velocity of a Vortex Filament Having a Specified Location and Orientation in Space

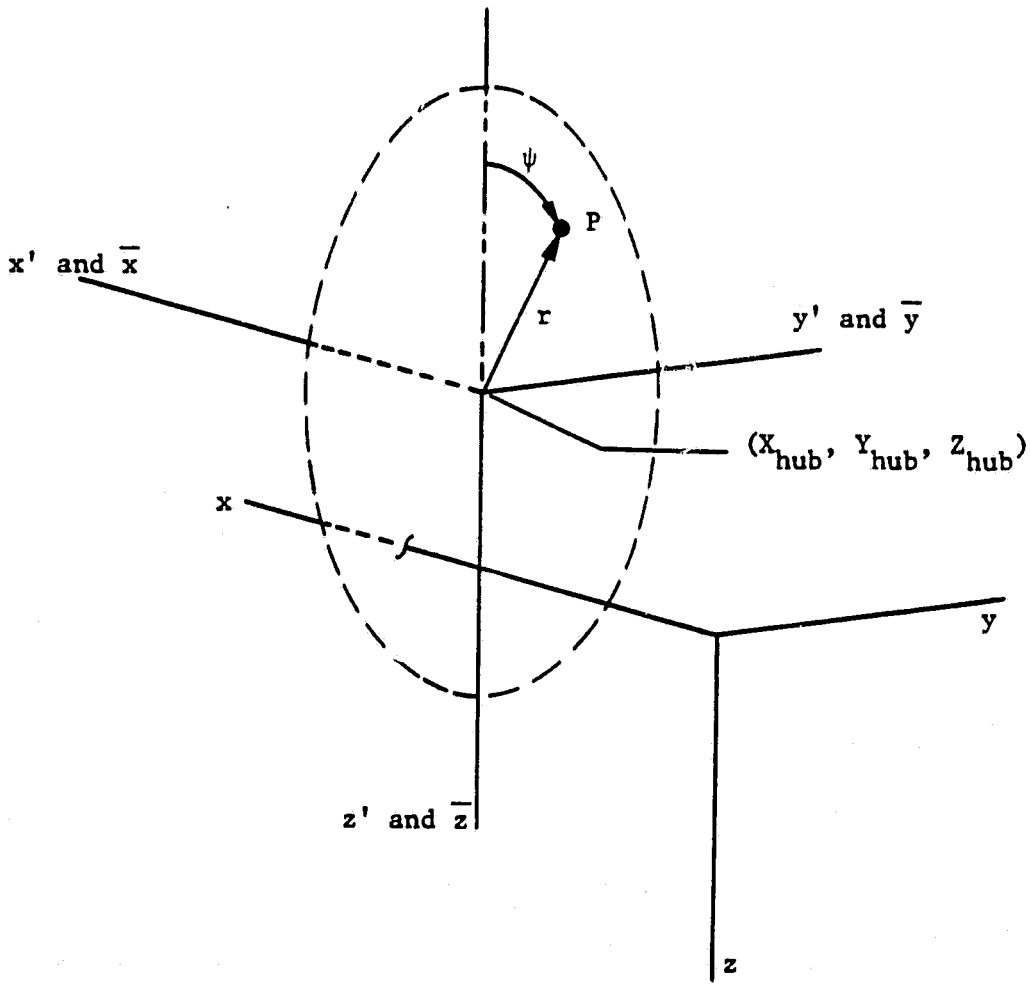

Figure D.1. Propeller Plane Shown Initially Noninclined With Respect to the Body-Fixed Axes

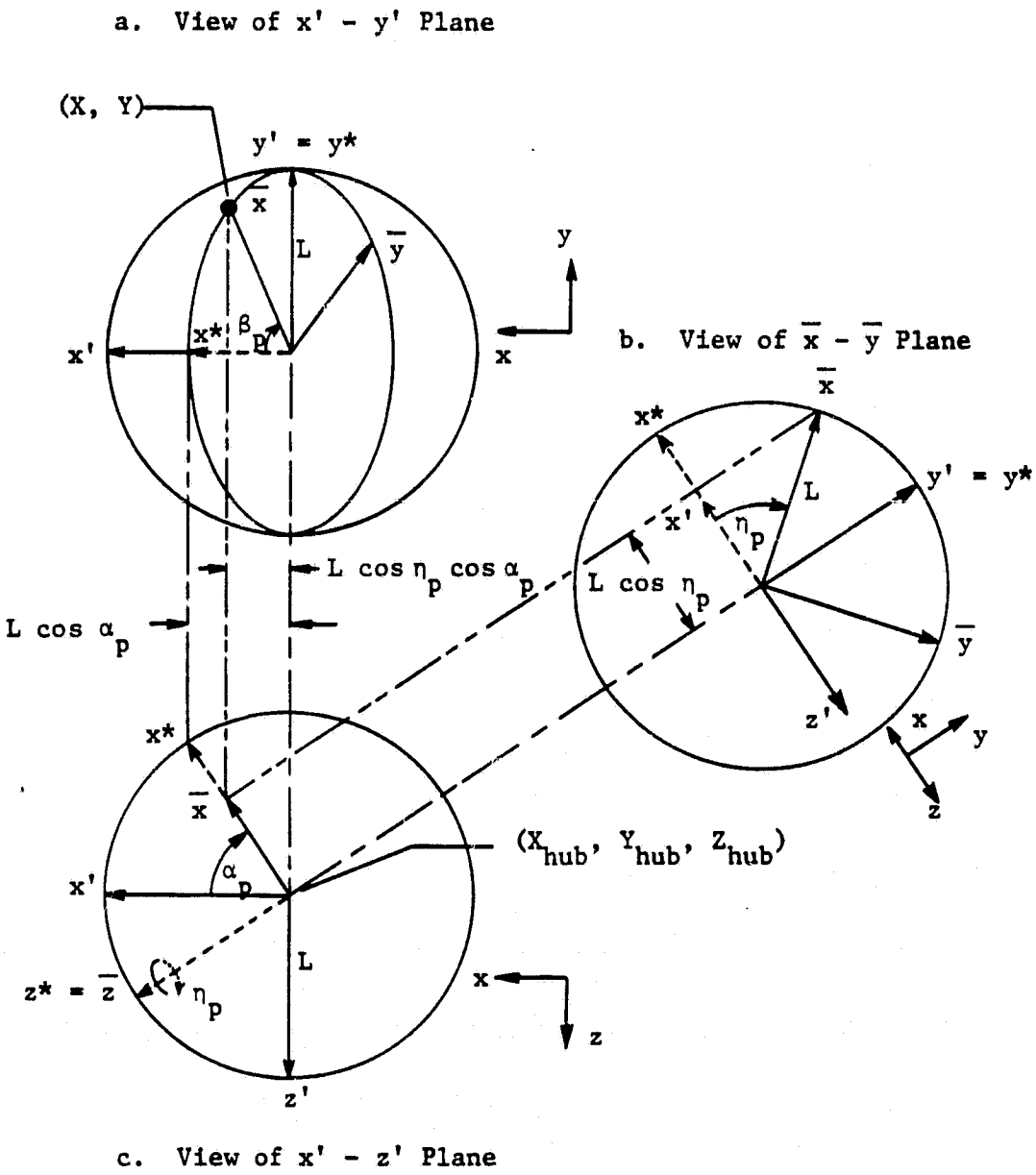

Figure D.2. Propeller Plane-Fixed Axis System Rotations

Note: Velocities $\bar{u}_p = v_{a_p}$ are positive in the direction of the view

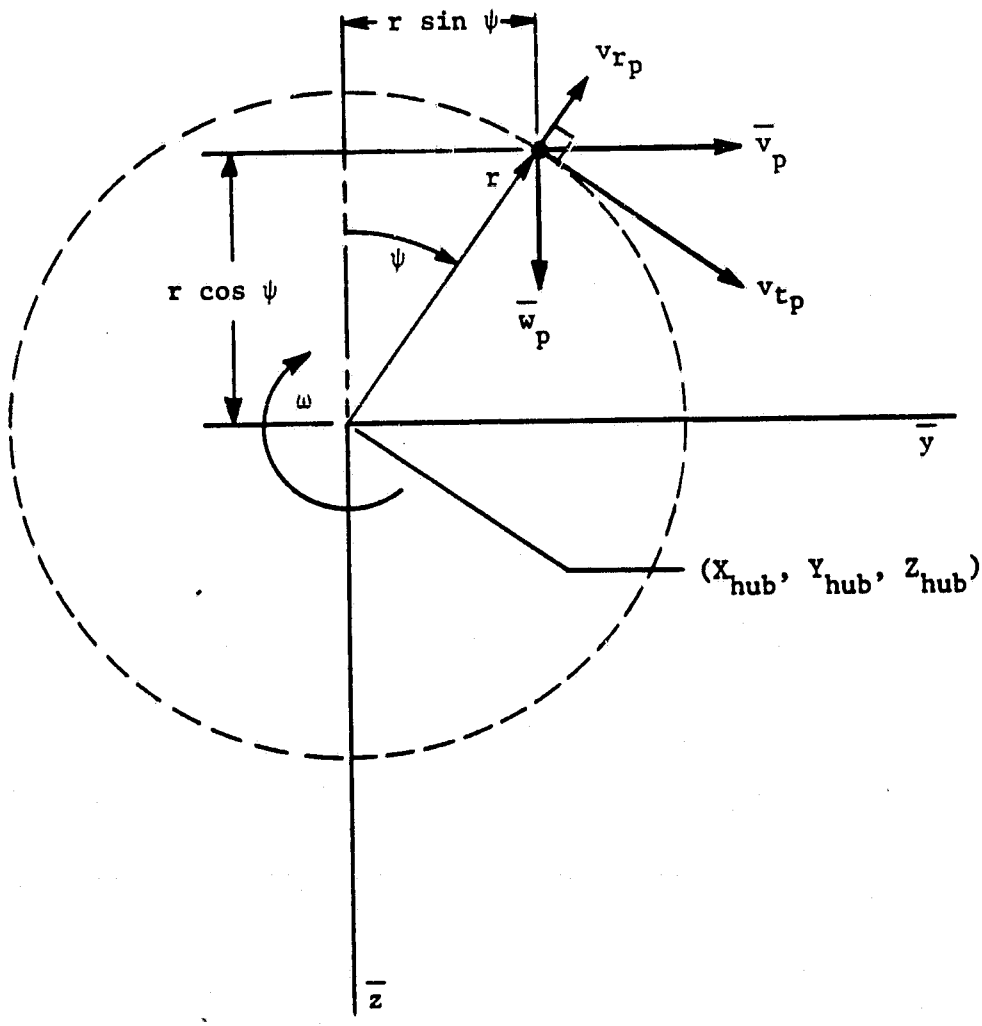

Figure D.3. View Normal to Propeller Plane in the Thrust Direction (Right-Hand Rotation, ω, of Propeller Assumed for Sign Convention)

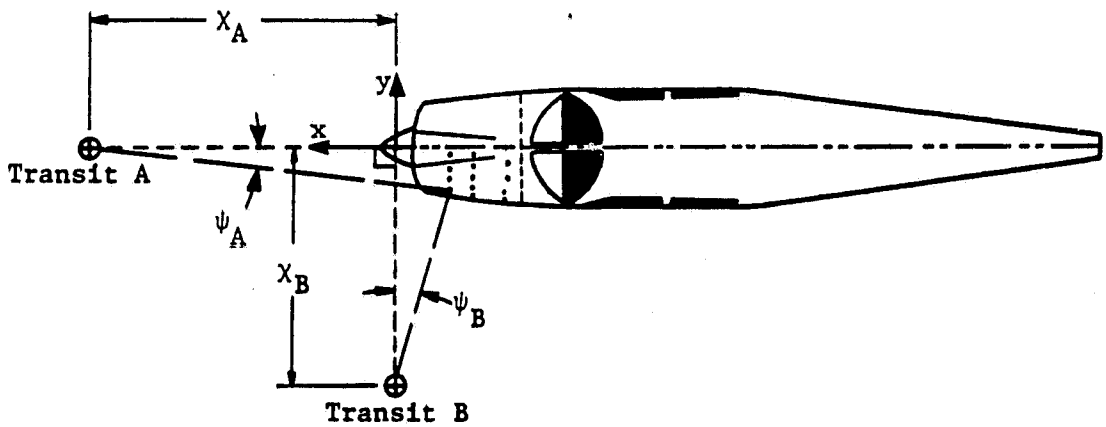

Figure E.1a. Optical Measurement of Cowl Surface Coordinates (Top View)

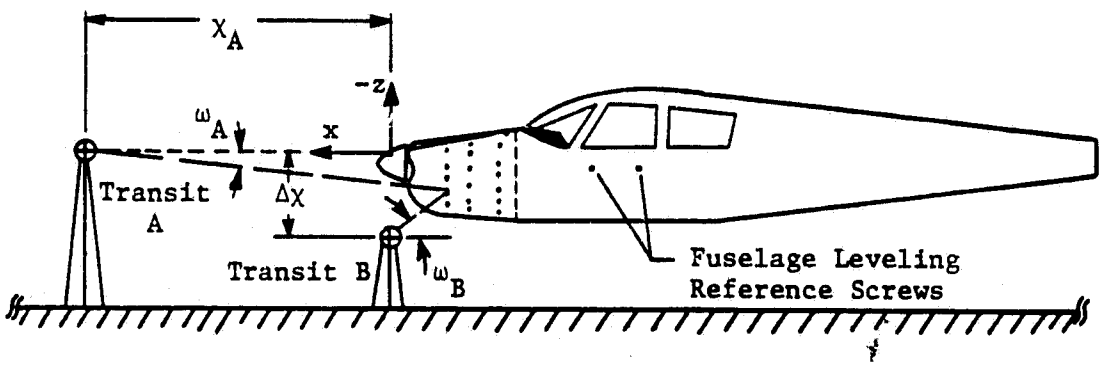

Figure E.1b. Optical Measurement of Cowl Surface Coordinates (Left Side View)